



HAL
open science

Prédétermination des hauteurs de départ d'avalanches. Modélisation combinée statistique-mécanique

Johan Gaume

► **To cite this version:**

Johan Gaume. Prédétermination des hauteurs de départ d'avalanches. Modélisation combinée statistique-mécanique. Sciences de la Terre. Université de Grenoble, 2012. Français. NNT : 2012GRENU019 . tel-00770156

HAL Id: tel-00770156

<https://theses.hal.science/tel-00770156>

Submitted on 4 Jan 2013

HAL is a multi-disciplinary open access archive for the deposit and dissemination of scientific research documents, whether they are published or not. The documents may come from teaching and research institutions in France or abroad, or from public or private research centers.

L'archive ouverte pluridisciplinaire **HAL**, est destinée au dépôt et à la diffusion de documents scientifiques de niveau recherche, publiés ou non, émanant des établissements d'enseignement et de recherche français ou étrangers, des laboratoires publics ou privés.

THÈSE

Pour obtenir le grade de

DOCTEUR DE L'UNIVERSITÉ DE GRENOBLE

Spécialité : **Sciences de la Terre et Univers, Environnement**

Arrêté ministériel : 7 août 2006

Présentée par

Johan GAUME

Thèse dirigée par **Mohamed NAAIM**
co-encadrée par **Guillaume CHAMBON** et **Nicolas ECKERT**

préparée au sein du **Laboratoire IRSTEA**
dans l'**École Doctorale Terre, Univers, Environnement**

Prédétermination des hauteurs de départ d'avalanches. Modélisation combinée statistique-mécanique

Thèse soutenue publiquement le **30 Octobre 2012**
devant le jury composé de :

M. Jürg SCHWEIZER

Directeur du SLF, Davos

Président du jury

M. Ali LIMAM

Professeur, INSA Lyon

Rapporteur

M. Jean Jacques BOREUX

Professeur, Université de Liège

Rapporteur

M. Jacques DESRUES

Directeur de recherche, CNRS

Examineur

M. Christophe ANCEY

Professeur, EPFL, Lausanne

Examineur

M. Mohamed NAAIM

Directeur de recherche, IRSTEA

Directeur de thèse

M. Guillaume CHAMBON

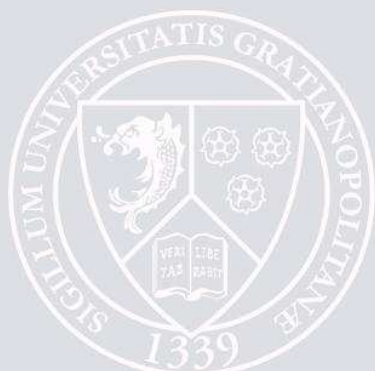
Chargé de recherche, IRSTEA

Co-encadrant

M. Nicolas ECKERT

Chargé de recherche IPEF, IRSTEA

Co-encadrant



IRSTEA
2 Rue de la Papeterie
38402 St Martin d'Hères



Evaluation of avalanche release depths.

Combined statistical – mechanical modeling



Johan Gaume

December 6, 2012



Photo: Vincent Denivet

"If I can make it, it ain't big enough."
Eric Labbé

Contents

Abstract	xi
Résumé	xiii
Remerciements	xv
1 Introduction	1
1.1 Avalanche formation	2
1.2 Risk management	4
1.2.1 Short-term forecast	4
1.2.2 Long-term prevention: hazard mapping	5
1.3 Problematic and objectives	9
1.3.1 Evaluation of the available snow depth in release zones	10
1.3.2 Evaluation of the release depth: statistical – mechanical modeling	11
1.3.3 Scientific questions and objectives	12
1.4 Summary of the main results and reading grid	13
2 Introduction (version française)	17
2.1 Problématique et objectifs	18
2.1.1 Prédétermination des hauteurs de neige en zone de départ	19
2.1.2 Prédétermination de la hauteur de départ: modélisation statistique – mécanique	20
2.1.3 Questions scientifiques et objectifs	21
2.2 Récapitulatif des résultats principaux et grille de lecture	23
3 State of the Art	27
3.1 Slab avalanche release	27
3.2 Avalanche release depth distributions	30
3.3 Physical and mechanical properties of snow	31
3.3.1 Snow metamorphism	31
3.3.2 Mechanical properties of snow	33

3.4	Slab avalanche release models	43
3.5	Extreme value statistics in a multivariate spatial context	47
3.5.1	Max-Stable Processes and spatial extremes	48
3.5.2	Likelihood-based inference	53
4	Influence of weak layer heterogeneity on snow slab avalanche release	55
4.1	Application to the evaluation of avalanche release depth	55
4.1.1	Introduction	57
4.1.2	Mechanically-based probabilistic model	58
	<i>Objectives</i>	58
	<i>Formulation of the model</i>	58
	<i>Constitutive relationships</i>	59
	<i>Spatial heterogeneity</i>	60
	<i>Loading</i>	60
	<i>Rupture mechanism</i>	60
	<i>Avalanche release criterion</i>	61
4.1.3	Mechanical validation	61
	<i>A single weak spot</i>	61
	<i>Two weak spots</i>	62
4.1.4	Results: Influence of weak layer heterogeneity	63
	<i>Simulation protocol</i>	63
	<i>Release angle and release factor distributions</i>	64
	<i>Average release factor</i>	64
	<i>Variability and heterogeneity smoothing</i>	64
4.1.5	Comparison with field data	65
	<i>La Plagne release depth data</i>	65
	<i>Release depth distributions obtained from mechanical model</i>	65
	<i>Coupling mechanical and snowfall distributions</i>	66
	<i>Results of the coupling and sensitivity analysis</i>	66
4.1.6	Conclusion and perspectives	67
	Appendix A: Model validation. Expression of the parameters	68
	Appendix B: Demonstration of the inversion of release factor distributions	68
4.2	Application to the evaluation of the position of avalanche release area	71
4.2.1	Introduction	73
4.2.2	Formulation of the model	73
4.2.3	Release types	74
4.2.4	Results	74
	<i>Influence of ϵ and σ_T</i>	74
	<i>Influence of h and σ_T</i>	74

<i>Influence of h and σ_c</i>	74
4.2.5 Statistical model	75
<i>Formulation of the model</i>	75
<i>Application of the model to our results</i>	76
4.2.6 Conclusion and discussion	78
5 Mapping extreme snowfalls in the French Alps using Max-Stable processes	81
5.1 Introduction	83
5.2 Extreme value statistics in the spatial case	84
5.2.1 Max-Stable Process (MSP)	84
5.2.2 Extremal coefficient	85
5.2.3 Spatial models for the GEV parameters	85
5.3 Empirical analysis	85
5.3.1 Data presentation	85
5.3.2 Altitude consideration	86
5.3.3 Pointwise GEV parameters	87
5.3.4 Extremal dependence	88
5.4 Application: Ajustment of a MSP to data	89
5.4.1 Composite likelihood	89
5.4.2 Model selection: TIC	89
5.4.3 Linear models	89
5.4.4 Spline models	92
5.4.5 Prediction accuracy: validation on non-used stations	94
5.5 Discussion	94
5.5.1 Comparison with previous work	94
5.5.2 Influence of the accumulation period	95
5.5.3 Joint analysis and conditional quantile evaluation	96
5.6 Conclusion	97
Appendix: Covariates for the spatial evolution of the GEV parameters	98
6 Coupling of mechanical and meteorological factors for the evaluation of avalanche release depth distributions	101
6.1 Introduction	103
6.2 Release depth data	103
6.3 Coupled mechanical–meteorological model	104
6.3.1 Theoretical framework	104
6.3.2 Mechanical probability density $p_m(h)$	104
<i>Formulation of the model</i>	104

<i>Release depth distributions for a fixed slope angle</i>	105
<i>Integration over all slopes</i>	105
6.3.3 Snowfall probability density $p_{sf}(h_{sf})$	105
6.3.4 Coupling result	106
6.4 Comparison with data and discussion	106
6.5 Conclusion	107
7 Conclusion	109
8 Conclusion (version française)	113
A Influence of weak layer friction heterogeneity on slab avalanche release	117
B Application of the max-stable model for the retro-analysis of the December 2008 avalanche cycle in the Eastern part of the French Alps	125
C Quasistatic to inertial transition in granular materials and the role of fluctuations	145

Abstract

The evaluation of avalanche release depth distributions represents a challenging issue for the mapping, zoning and long-term hazard management in mountaineous regions. The focus of this study is on slab avalanches which generally result from the rupture of a weak layer underlying a cohesive slab. In a first step, a mechanically-based statistical model of the slab – weak layer system is built to compute avalanche release depth distributions. Two key ingredients are taken into account for the mechanical description of such slab avalanche releases: the spatial heterogeneity of the weak layer and the redistribution of stresses via the elasticity of the slab. Several simulations for different realizations of the heterogeneity of the weak layer are carried out by increasing the slope angle until rupture. The influence of slab depth and heterogeneity correlation length on avalanche release angle distributions is then analyzed. We evidence in particular a heterogeneity smoothing effect caused by slab elasticity. The obtained release angle distributions are then inverted, yielding release depth distributions integrated over all slope angles. We also show the critical and major influence of morphological and topographical features on the localisation of the slab tensile failure.

However, a purely mechanical model is insufficient to compute accurate avalanche release depth distributions which also depend on snowfall frequency and intensity. Thus, in a second step, extreme snowfall data acquired in 40 meteorological stations in the French Alps since 1966 are deeply analysed using spatial extreme statistics. They are then modeled within the formal framework of max-stable processes which are the generalization of univariate extreme value theory to the spatial multivariate case. The three main max-stable processes now available are fitted on the data using composite likelihood maximisation, and the most flexible Brown-Resnick one is retained on the basis of the TIC criterion, taking into account anisotropy by space transformation. Different smooth linear and spline models for the spatial evolution of the GEV parameters are fitted and compared after altitudinal correction so as to separate spatial and orographic effects. The best max-stable model is used to produce snowfall maps for different return periods and we evidence, in particular, that the dependence of extreme snowfalls is stronger along the local orientation of the Alpin chain.

Finally, a rigorous formalism in which avalanche release depth distributions are expressed through a coupling of mechanical and meteorological factors is presented. Con-

sidering that an avalanche can occur only if the snowfall depth exceeds a critical value corresponding to a stability criterion, release depth distributions obtained from the slab–weak layer mechanically-based statistical model are coupled with the distribution of 3-day extreme snowfalls. We show that this coupled model is able to reproduce field data from 369 natural slab avalanches in La Plagne (France). Not only the power-law tail of the distribution, corresponding to large slab depths, but also the core of the distribution for shallow ones, are well represented. Small to medium-sized avalanches appear to be controlled mainly by mechanics, whereas large avalanches and the associated power-law exponent, are governed by a strong mechanical-meteorological coupling. We demonstrate that the obtained distribution is strongly space-dependent, and, using the results of the max-stable mapping, our coupled model is used to obtain release depth maps for given return periods at the whole French Alps scale.

Résumé

La prédétermination de la hauteur de départ des avalanches représente un défi majeur pour l'évaluation du risque en montagne. Cette hauteur constitue en effet un ingrédient d'entrée important des procédures de zonage et de cartographie du risque. Nous nous intéressons dans cette thèse au cas des avalanches de plaque qui résultent généralement de la rupture d'une couche fragile enfouie sous une plaque cohésive. Dans un premier temps, un modèle mécanique – statistique du système plaque – couche fragile est développé pour calculer des distributions de hauteur de départ d'avalanche. Deux ingrédients clés sont pris en compte pour la description mécanique de ces avalanches de plaque: l'hétérogénéité de la couche fragile et la redistribution des contraintes par élasticité de la plaque sus-jacente. Un grand nombre de simulations pour différentes réalisations de l'hétérogénéité de la couche fragile sont réalisées en augmentant progressivement l'angle de la pente jusqu'à la rupture. Nous analysons ensuite l'influence de l'épaisseur de la plaque et de la longueur de corrélation de l'hétérogénéité sur les distributions d'angle de départ d'avalanche. Nous mettons en évidence, en particulier, un effet de lissage de l'hétérogénéité induit par l'élasticité de la plaque. Les distributions d'angle de départ ainsi obtenues sont ensuite inversées pour donner des distributions de hauteur de départ intégrées sur tous les angles de pente. Nous montrons également l'influence critique et majeure des caractéristiques morphologiques et topographiques sur la localisation de la rupture en traction de la plaque.

Cependant, un modèle purement mécanique est insuffisant pour prédéterminer les distributions de hauteur de départ d'avalanche qui dépendent aussi de la fréquence et l'intensité des chutes de neige. Ainsi, dans un second temps, les données des chutes de neige extrêmes acquises dans 40 stations météorologiques des Alpes françaises depuis 1966 sont analysées à l'aide des statistiques des valeurs extrêmes dans un cadre spatial. Ces données sont ensuite modélisées dans le cadre formel des processus max-stables qui sont la généralisation de la théorie des valeurs extrêmes univariées au cas multivarié spatial. Les trois principaux processus max-stables actuellement disponibles sont ajustés aux données par maximisation de la vraisemblance composite, et le processus le plus flexible, celui de Brown-Resnick, est retenu sur la base du critère TIC, en prenant en compte l'anisotropie par transformation de l'espace. Différents modèles linéaires et splines pour l'évolution spatiale des paramètres de la GEV sont ajustés après correction altitudinale afin de séparer les effets spatiaux et orographiques. Le meilleur modèle max-stable obtenu est utilisé pour produire des cartes

des chutes de neige pour différentes périodes de retour. Nous mettons en évidence, en particulier, que la dépendance des chutes de neige extrêmes est plus forte selon l'orientation locale des Alpes.

Enfin, nous présentons un formalisme rigoureux dans lequel les distributions de hauteur de départ d'avalanche sont exprimées à travers un couplage des facteurs mécaniques et météorologiques. Considérant qu'une avalanche ne peut se produire que si la hauteur de chute de neige dépasse une hauteur critique correspondant à un critère de stabilité, les distributions de hauteur de départ obtenues à partir du modèle mécanique – statistique plaque - couche fragile sont couplées avec la distribution des chutes de neige extrêmes sur 3 jours. Nous montrons que ce modèle couplé est capable de reproduire des données de terrain de 369 avalanches naturelles de plaque à La Plagne (France). Non seulement la queue de la distribution en loi puissance, correspondant à des épaisseurs de plaque élevées, mais aussi le corps de la distribution pour les plaques moins épaisses, sont bien reproduits par le modèle. Les avalanches petites à moyennes semblent être essentiellement contrôlées par la mécanique, tandis que les grosses avalanches et l'exposant de la loi puissance associé, sont influencés par un couplage mécanique–météorologique fort. Par ailleurs, nous démontrons que la distribution obtenue est fortement dépendante de l'espace, et, en utilisant les résultats du modèle spatial max-stable, notre modèle couplé est utilisé pour obtenir des cartes de hauteur de départ d'avalanche pour différentes périodes de retour sur l'ensemble des Alpes françaises.

Remerciements

Ça y est, le manuscrit est enfin fini ! Voici donc venu le temps, des rires et des champs, des lourdes soirées et des remerciements. Alors commençons par le commencement, je remercie tout d'abord Albert Magnin, qui, au hasard d'un forum des masters, m'a convaincu que je pouvais faire de la recherche dans un domaine qui me passionne, la neige ! Grâce à lui, j'ai pu effectuer mon master puis ma thèse au CEMAGREF.

Ensuite, je dois dire que dans l'unité ETNA, les thésards sont bichonnés et chouchoutés par leurs encadrants, dans le sens où leur porte est toujours ouverte aux questions et à la discussion, scientifique ou non. Je souhaite donc remercier dans un premier temps Guillaume qui a eu le courage d'encadrer mon master et ma thèse, et qui m'a énormément appris du métier de chercheur. Perfectionniste et très pédagogue, il a, entre autres, été d'une aide précieuse sur l'analyse de mes résultats, sur les directions à prendre face aux problèmes rencontrés et sur la rédaction de mes articles scientifiques. Je remercie également Nicolas qui a eu la patience de me guider sur les concepts statistiques et probabilistes complexes auxquels j'ai été confronté pendant cette thèse. Mes remerciements vont aussi à Mohamed aka "Mo" qui a dirigé ma thèse, et qui, malgré la masse importante de travail qu'il doit assumer, est toujours resté très disponible. Encore un dernier gros Merci à vous trois pour l'aide, le soutien et la motivation que vous m'avez apporté, notamment sur la fin de la thèse et j'espère sincèrement qu'on sera amené à travailler à nouveau ensemble. Dans tous les cas, on reste en contact !

Je remercie par ailleurs tous les membres de mon comité de pilotage de thèse, Michael Brun, Margherita Maggioni, Philippe Naveau, Eric Parent et François Nicot, pour leur aide et leurs conseils avisés. Je remercie également Liliane Bel pour son aide soutenue et sa participation active sur les aspects statistiques de ma thèse et également Mathieu Ribatet qui m'a aidé à prendre en main le package SpatialExtremes qu'il a développé sous R.

Ma gratitude va également à Claude Schneider, nivologue à La Plagne, pour avoir mis à ma disposition sa base de données de hauteur de départ d'avalanche et pour sa vision d'expert de la montagne sur le déclenchement des avalanches.

Mes remerciements vont également aux rapporteurs Ali Limam et Jean-Jacques Boreux ainsi qu'aux autres membres du jury, Jürg Schweizer, Christophe Ancey, et Jacques Desrues, pour la lecture de ce manuscrit et pour la pertinence de leurs commentaires.

Je remercie Evgeny Podolsky aka "da Vinci", le wikipedia du déclenchement des avalanches,

pour le partage de ses connaissances bibliographiques impressionnantes, pour sa gentillesse et pour sa carte CTP ! D'ailleurs je suis désolé de te l'apprendre par ce biais mais il me semble que je l'ai perdu !

Merci également à Thierry, Hervé, Florence, Fred, Xavier, Manu, Stéphane, Didier, Alexandra, Christian et tout le personnel d'ETNA pour la bonne ambiance de travail, les discussions à la machine à café et au CTP, les conseils d'alpi, les barbecues, les fêtes, etc.

J'aimerais également remercier mes collègues de bureau Pascal et Nejib pour toutes nos discussions, les coups de mains, les bières, la clairette, et sans qui tout ça aurait été beaucoup moins fun. Je remercie notamment Nejib pour son humour décapant (© Pascal) et pour qui le travail n'est vraiment pas du second ordre ! Très bon partenaire de pétanque, il m'a également poussé à me dépasser pour faire des graphiques aussi beaux que les siens. Pascal, t'as manqué la lourde soirée de la soutenance, j'espère qu'on aura l'occasion de rattraper ça, allez, on remet ça, disons, pour fêter la soutenance de Nejib (on a le temps encore !).

En vrac, merci aussi à David Bertrand qui m'a initié au logiciel PFC2D, Franck Lominé et Emmanuel Jonas pour mon initiation à Linux, Fred Ousset pour la magnifique tablette à café inclinable pour zone de départ d'avalanche, mes stagiaires Anthony Calabro et Clémentine Guyon, Helene Castebrunet pour les données météo. Merci à Paolo, Nicolas, Caro, Pauline, Philo, Adeline, Josh, Assia, Sandrine, Mathieu et tous les autres thésards pour les bons moments passés lors des réunions de TR et autres ainsi que tout le personnel administratif.

Je voudrais remercier également mon père grâce à qui j'ai pu faire toutes ces études dans les meilleures conditions, mes grands parents pour m'avoir accueilli, choyé et si bien soigné pendant la rédaction de ma thèse, mon appendicite à 10 jours de la dead line pour rendre le manuscrit, c'était super sympa ça, ma cousine Angélique pour ses piqûres anti-phlébite en chantant Carly Rey Japsen, tout mes frères et soeurs, Luc et Alizée pour m'avoir un peu boosté quand c'était pas la joie, tous mes potes, mon wingman Max que j'ai du exaspérer à maintes reprises, et qui a toujours été là, notamment lors du clic final, les pieds dans le sable, et d'où s'en sont suivies de bien belles aventures ! Qu'est ce qu'on a rit ! Merci aussi à ma grand mère pour son courage et sa foi ainsi qu'à toute ma famille. Un gigantesque merci aussi à Laura pour tant de raisons qui ne s'énumèrent pas, t'es la meilleure.

Enfin, je tiens à dédier ma thèse à ma Maman, qui m'a donné les moyens, l'envie et la force de faire tout ça. J'espère que Mamie a raison et que tu seras un peu là pour voir ma présentation, de toute façon t'as ton invitation, il ne faudrait surtout pas que tu manques le pot de Laura, avec avalanche de saucisse de Morteau, comté et vin blanc du Jura, ça va être super sympa tu verras...

Chapter 1

Introduction

Source of wonder but also of terror, avalanches still hide many secrets, despite major recent scientific advances. An avalanche consists in a rapid gravitational flow of a snow mass on a mountaineous slope. Each year, avalanches are responsible for killing about 30 people in France and 150 in Europe (mainly hikers and backcountry skiers) with a total of about 1.5 million € of damage. In addition to this destructive aspect, avalanches have a strong mediatic impact, mainly due to the recent increase in the number of mountain practitioners, skiers and more particularly backcountry skiers. However, most avalanches are triggered naturally in the backcountry without human influence and become a significant issue only when human lives or material damage are potentially involved. The disastrous avalanche cycle of winter 1999 in the European Alps (12 deaths in Montroc, France; 12 deaths in Evolene, Switzerland; 39 deaths in Galtür, Austria; destruction of many settlements, roads and railways) recalled their destructive ability and urged to improve the scientific methods for hazard mapping. Hazard mapping and zoning consists, in bulk, to define the extent and the maximal impact pressure of an “exceptional” avalanche, where exceptional is defined by a high return period, 100 – 1000 year, typically.

Today, numerical models of avalanche propagation have acquired a central role in the current engineering practice for hazard mapping. Scientific studies conducted in recent years, helped to significantly increase the performance of these models, by taking into account the specific behavior of flowing snow, erosion and deposition, and the use of numerical schemes suitable for different situations (Barbolini et al., 2000; Lachamp et al., 2002; Naaim et al., 2003). In addition, several studies have validated the outputs of these models by comparing them with experimental results or field observations (Barbolini et al., 2000; Hutter et al., 2005; Naaim et al., 2008).

However, the systematic implementation of these models still faces a number of difficulties, among which the accurate assessment of the avalanche release volume. The release volume represents an input ingredient, to which the results can be strongly dependent, especially for small to medium-sized paths. There is currently no clear and well defined



Figure 1.1: Avalanche release types. Left: Loose snow avalanche release. Right: Slab avalanche release (©Remi Petit).

methodology allowing to evaluate the release volume of a potential avalanche for different return periods. Even for the best documented sites (e.g. Chamonix valley, Davos region), the evaluation of the initial volume is generally very difficult because of limited quantitative data available in release zones. The few existing methods are mostly empirical and generally consider that the release depth corresponds to the fresh snow accumulation over 3 days without taking into account mechanical effects. The release area is generally determined empirically according to geomorphological criteria (Maggioni et al., 2002; Maggioni and Gruber, 2003). Given the complexity and efficiency of propagation models, it seems necessary today to improve these oversimplified techniques for the estimation of the release depth and area by using more rigorous methods in order to improve the accuracy of hazard mapping procedures.

This introduction is dedicated to recalling the basis of avalanche formation and the current engineering practice for avalanche risk management in mountainous areas. The problematic, the objectives of this PhD thesis and the reading grid are then detailed in the last part of this introduction.

1.1 Avalanche formation

There are two types of avalanche releases: (1) Loose snow avalanches are formed in cohesionless snow and are very similar to the failure of granular materials like sand. This type of avalanche is initiated at a single point by the rupture of a snow mass which then propagates and mobilizes more and more snow, leading to a characteristic pear shape (Fig. 1.1a). These avalanches occur generally in spring, the temperature increase giving rise to a decrease of the cohesion (also called wet avalanche) or during the winter season after a snowfall accompanied by very low temperatures and no wind on relatively high slopes (also called “sluff”). (2) Slab releases are responsible for most of damage and fatalities related to avalanche activity. Jamieson and Johnston (1992) showed that 99% of avalanche fatal-

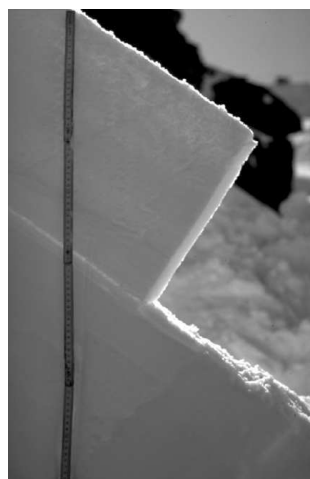


Figure 1.2: Thin weak layer of surface hoar crystals underlying a cohesive slab. From Schweizer et al. (2003).

ities between 1972 and 1991 in Canada occurred due to slab releases. These releases are characterized by a linear fracture of the snowpack (Figs. 1.1b and 1.4). These slabs can be constituted either by soft snow, even recent powder whose density can be lower than 100 kg.m^{-3} (soft slabs) or hard cohesive snow for which wind transport plays an important role in their formation. The release can occur on important surfaces, and can involve large quantities of snow, sometimes in areas far from the initial release. This typical behavior of fracture propagation over long distances has led snow experts and scientists to introduce the notion of weak layer. The presence of this layer under the slab is a necessary but not sufficient condition for slab avalanching (Bader and Salm, 1990). Its presence explains the large size of slab avalanche release zones. Jamieson and Schweizer (2000) showed that for 80% of slab releases, the weak layer was constituted of depth hoar (Fig. 1.3b), surface hoar (Fig. 1.3a), faceted crystals weak layers (Fig. 1.4) or interfaces.

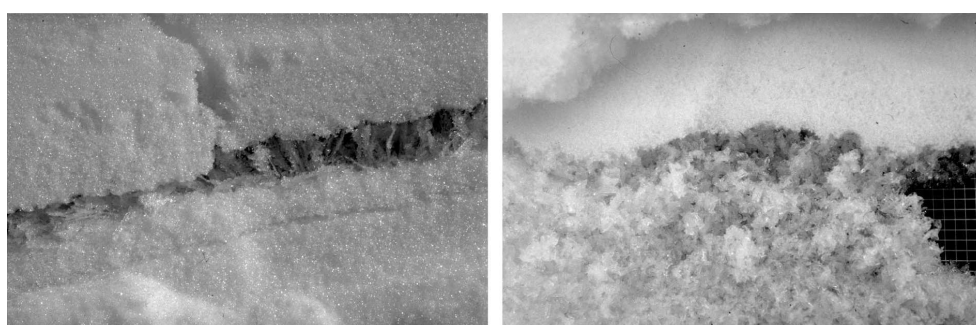


Figure 1.3: Typical configuration slab - weak layer suitable for avalanche release. (a) Surface hoar weak layer (©ASARC from Jamieson and Schweizer (2000)) intact on the right and partially ruptured on the left. (b) Depth hoar weak layer from Schweizer et al. (2003).



Figure 1.4: Four-meter crown fracture of a huge slab avalanche that occurred in Mt Baker in March 2012, consequence of a very important snowfall on a faced crystal weak layer. ©G.Gunderson

These slab avalanche releases are mainly influenced by weather and nivological conditions such as new snowfalls, wind, which can severely increase the local thickness of the snowpack, the structure of the snowpack with the presence of weak layers, etc, but also by the morphological characteristics of the path like the mean slope angle, the roughness (presence of forest, ridges, quality of the ground), the shape and the curvature of the release zone and the orientation of the path against the sun. However, the physical and mechanical quantities involved in the release phase are still poorly understood and still not fully characterized.

1.2 Risk management

To understand the objectives of this thesis, presented later, short-term avalanche forecast (prevision) and long-term prevention (avalanche control) have to be clearly distinguished. These are two approaches of avalanche risk management which involve completely different time and space scales but also seek different communities.

1.2.1 Short-term forecast

Avalanche forecasting consists in the estimation of avalanche activity within a short period (24 hours) at local and regional scales. It is intended primarily for mountain practitioners (skiers, snowboarders and hikers) and professionals who go to the backcountry.

Current techniques rely on monitoring weather conditions and predicting the evolution of the snowpack with the use of physically-based models for forecasting (SAFRAN / CROCUS / MEPRA for example in France, SNOWPACK in Switzerland). In France, these data are processed by MétéoFrance, which broadcasts every day, for each massif



Figure 1.5: European avalanche danger scale. Information from ski resort for backcountry practitioners.

($\approx 100 \text{ km}^2$), estimation bulletins of avalanche risk (BRA) which are based on a European scale of avalanche risk with 5 levels (Fig. 1.5).

1.2.2 Long-term prevention: hazard mapping

Hazard mapping aims at informing about the spatial extent of the risk. Idealistically, no human being or construction should be located in a dangerous zone. These zones are defined by the run-out distance of a high return period avalanche, typically equal or higher than 100-years. However in practice, it is often impossible to avoid any human activity and infrastructure in these areas. Consequently, it is also necessary to define the avalanche intensity in order to correctly design the endangered structures or to protect them with specific devices and structures.

Hazard maps

Hazard mapping criteria are different in each European country. Nevertheless, even if the final criterion differs, hazard levels are generally defined taking into account the same ingredients, namely the avalanche frequency (or return period) and/or the avalanche intensity (combination between the run-out distance and the pressure). In France, hazard maps contains two principal informations: the extent of the maximum observed event and the extent of the avalanche corresponding to a characteristic frequency, the $T=100$ years return period avalanche. Then three levels of hazard can be obtained by distinguishing avalanche intensity thresholds defined by the pressure $P = 0.5\rho_f C_D V^2$ (ρ_f being the flow density, V the avalanche speed and C_D the obstacle resistance coefficient). These maps are part of the PPR (Risk Prevention Plan, Fig. 1.6) and are widely used in avalanche engineering.

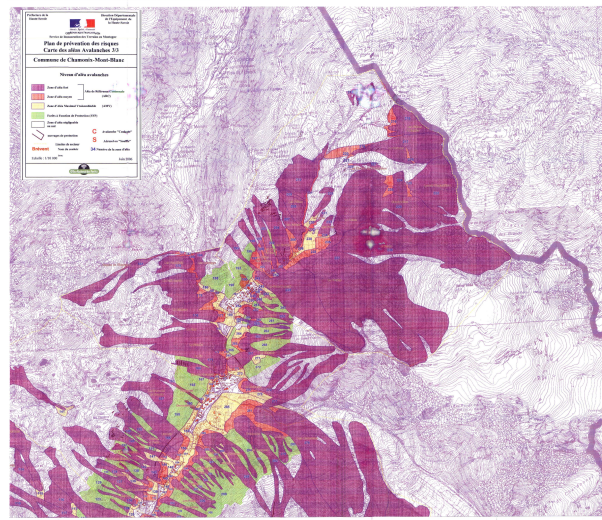


Figure 1.6: Example of hazard map (PPR) in Chamonix.

Coupled statistical–physical modeling

A few number of methods can be used to obtain an estimation of the intensity and the frequency of an avalanche for a given path. Historical data, such as direct observations constitutes a very relevant information for the evaluation of run-out distances. Vegetation analysis also provide a good approximation of avalanche maximum extents, since an avalanche can destroy trees and sometimes entire forest, leaving traces for many decades (Martinelli, 1974). However, to evaluate the hazards (decennial, centennial, tri-centennial) in a prospective approach, in the sense of predetermination, and to obtain probabilistic hazard map, physically/mechanically – based models are necessary. This methodology aims to treat the different phases of the phenomenon (snow formation, avalanche release, propagation) in a coupled statistical – deterministic framework instead of processing only a sample of past events (e.g. McClung and Lied (1987)). Such models have shown remarkable performances to evaluate run-out distances and pressures on obstacles.

Fig. 1.7 (Ancey et al., 2004) summarizes the different ingredients needed in these models to compute the run-out distance for different return periods:

- a hydrological sub-model to compute the snowfall involved,
- a mechanical sub-model describing avalanche release,
- an avalanche dynamic sub-model to compute the run-out distance and the pressure on an obstacle.

All these models must be integrated into a probabilistic framework, i.e. input probability distributions must be specified/infered in order to derive the probability distribution

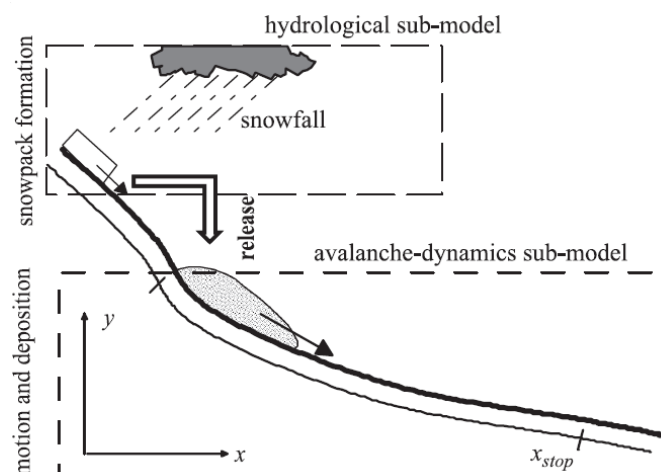


Figure 1.7: Illustration of the different ingredients necessary to compute avalanche run-out distances within a coupled statistical – physical approach. From Ancey et al. (2004)

of the outputs of interest, namely velocities, pressure, flow depth, etc, in the runout zone (Eckert et al., 2008).

Among these different sub-models, avalanche propagation codes are nowadays relatively well-established and validated (Salm et al., 1990; Perla et al., 1980; Naaïm and Naaïm-Bouvet, 1999; Bartelt et al., 2000). These models consist in modelling the flow of an avalanche taking into account the specific behavior of flowing snow, erosion and deposition (Barbolini et al., 2000; Naaïm et al., 2003). Their input data are: the digital terrain model, parameters for the description of snow rheology (e.g. friction angle, turbulent friction coefficient, etc) (Norem et al., 1989; Savage and Hutter, 1991; Naaïm and Ancey, 1992; Bartelt et al., 1997a,b) and the release depth and release area. Concerning the friction parameters, the current engineering practice consists in calibrating their probability distribution using historical data such as EPA (“Enquête Permanente sur les Avalanches”) or CLPA (Carte de Localisation des Phénomènes d’Avalanches). However, the evaluation of the probability distribution of the release area and the release depth (i.e. the formulation of the hydrological and release sub-models in Fig. 1.7) currently remains one of the main difficulty in avalanche engineering. These two ingredients, release depth and area distributions, have a strong influence on the final hazard assessment, namely the estimation of run-out-distance and pressure values for different return periods.

Snow input: Initial conditions

As stated before, avalanche propagation models used in hazard mapping procedures require the specification of both potential release area and release depth as initial conditions.

Release area It depends mainly on a combination of topographical, morphological, and vegetative features. Factors such as wind and sun exposure, surface roughness are generally considered as secondary factors that mainly affect avalanche activity and avalanche short-term forecasting. These latter factors are less important with respect to potential release areas for “extreme” avalanches used in hazard mapping procedures. Indeed, Maggioni and Gruber (2003) analyzed a well-documented database of avalanche events with respect to many topographic and morphologic characteristics. They showed that the mean slope angle, the curvature and the distance to the ridge are the most important parameters influencing avalanche release area distributions.

Release depth For slab avalanches, the release depth is generally assumed to be equal to the snowfall accumulation during the three days preceding the event, or three days snow fall, h_{3j} (Schweizer et al., 2003; Ancey et al., 2004). Since “extreme avalanches” are retained for hazard mapping procedures, the value of h_{3j} is taken as the annual maximum of the positive difference in snowfall depth calculated using a three days wide window, moving by one day steps (Barbolini et al., 2004). This is evaluated for a flat area and then empirically modified for local slope conditions and snow drift overloads (Salm et al., 1990; Barbolini et al., 2002, 2003). The Swiss Guidelines (Salm et al., 1990) suggest an empirical formula to estimate the release depth h of an avalanche for a given return period T , taking into account the snowfall depth h_{3j} , the wind snowdrift overload h_w , the slope angle θ and the rate of growth with the altitude z of the release area:

$$h(T, z) = (h_{3j}(T, z) + h_w) \frac{0.291}{\sin \theta - 0.202 \cos \theta} + \frac{0.05(z - 2000)}{100} \quad (1.1)$$

The distribution of h_{3j} is inferred by statistical analysis. Annual maximum values of h_{3j} are fitted to theoretical distributions, which are used to extrapolate from the recorded events beyond the highest observed values for the design event. Typically, the Gumbel or more recently the Generalized Extreme Value (GEV) distributions are considered for this purpose. The wind snowdrift overloads, h_w , is usually determined empirically. For instance, in the Swiss Guidelines values in the range 30 – 50 cm are proposed in the case of situations appropriate for wind snowdrift processes.

Other authors have studied the correlations between the release depth and the deposit volume and propose a deterministic transformation to give an evaluation of the release depth (Meunier and Ancey, 2004; Eckert et al., 2010).

However, all these approaches are purely empirical and oversimplified, and generally require considerable poorly-formalized expertise. Besides, even if it is true that slab avalanches are mostly snowfall driven (Fig. 1.8a), unlike wet snow avalanches which are mostly driven by the increase of temperature and snow metamorphism (Fig. 1.8b), other factors may influence slab avalanche releases such as the evolution with time of the mechanical properties of snow which can result in the creation of weak layers. This is also

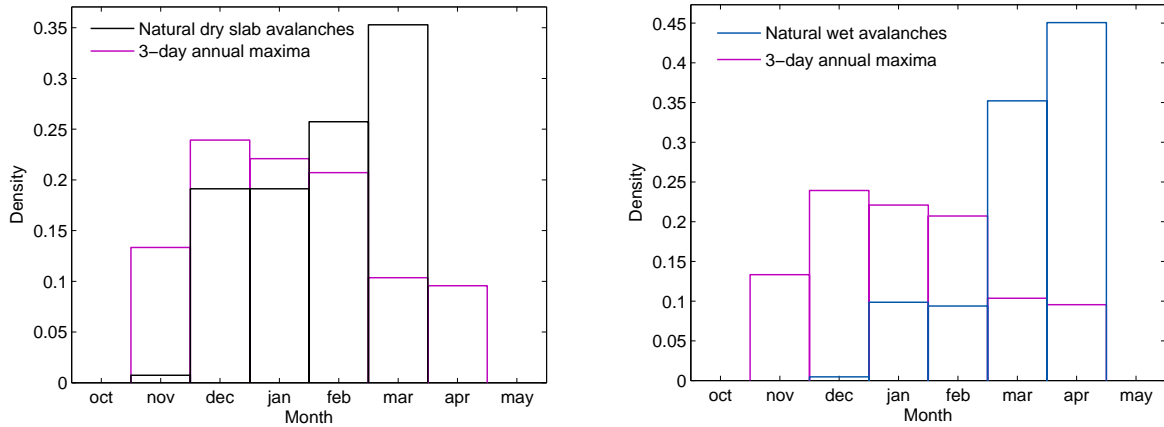


Figure 1.8: Comparison between the occurrence distribution of avalanches and 3-day annual maxima. Data from La Plagne, France. Left: Dry-snow slab avalanches. Right: Wet-snow avalanches.

what suggests Fig. 1.8a since the occurrence of slab avalanche releases is not completely in agreement with the occurrence of 3-day extreme snowfalls, especially in march, when strong temperature gradients are generally observed giving rise to new weak layers. This highlights the necessity of taking into account the influence of mechanics in these evaluations, by introducing a mechanical stability criterion in a probabilistic framework.

1.3 Problematic and objectives

The statistical distribution of avalanche release volumes at a given site can be expressed as a combination of statistical distributions of areas and release depths, including a coupling term since these two variables are not completely independent. In this study, we will focus on the evaluation of the release depth distributions. The release depth results from two factors: the available snow depth in the release area and a mechanical stability criterion coming from the topographical and morphological features of the release zone (e.g. slope angle) and mechanical properties of snow. Consequently, it seems possible to split the problem in two subproblems:

- Evaluation of the available snow depth,
- Evaluation of a probabilistic critical depth corresponding to a mechanical stability criterion.

Then, a coupling between the obtained distributions should be performed to obtain the global release depth distribution.

1.3.1 Evaluation of the available snow depth in release zones

Conceptually, the evaluation of snow depth distributions in any potential release zone should be made by interpolation of data acquired by the snow and weather monitoring stations located in the concerned region. In practice, however, the difficulties are numerous, since, in mountaineous regions, available data are few and generally incomplete:

- Data are limited mostly to rainfall chronics measured in water equivalent. The distinction rain / snow is not always done, which requires the joint analysis of temperature series.
- Measurement stations are usually located far from the starting zones of avalanches. It is therefore necessary to use spatial interpolation methods adapted to the heterogeneity of data, such as kriging (Cressie, 1993).
- In addition, these stations are usually located in the valleys rather than at high altitudes, making it necessary to take into account an orographic precipitation gradients for the quantification of water equivalents in release areas.
- Avalanches being rare events, extreme snow depths have to be characterized, which requires an extrapolation beyond the highest observed values in the available series that are generally short. This requires the implementation of methods for statistical analysis of extreme (Coles, 2001).
- Finally the stationarity of the underlying phenomenon, which is almost always assumed, is a questionable assumption, particularly in the context of climate change (Marty and Blanchet, 2011; Eckert et al., 2010).

In the current practice of avalanche engineering, all these difficulties are usually circumvented at the cost of very strong assumptions. The problems of interpolation techniques and orographic gradient are generally treated via the definition of “homogeneous zones by altitude band” (Salm et al., 1990; Bocchiola et al., 2006). This method, besides the difficulty in defining these zones, introduces discontinuities at the borders that are incompatible with the natural phenomenon. Nevertheless, it has the main advantage of increasing the number of data and enables to predict high return levels. The treatment of the extreme character of the values to interpolate remains also generally very imperfect, since most current methods use almost systematically Gumbel laws rather than a more general GEV model. This may lead to systematic underestimations of the most extreme precipitations (Parent and Bernier, 2003; Bacro and Chaouche, 2006). Recently, a solid formalism has been proposed to characterize the spatial dependence of extreme values. Applied to a whole series of data around a series of reference, maps of spatial dependence can thus be obtained (Coles et al., 1999; Heffernan and Tawn, 2004). In line with this

work, the concept of variogram, which is central to any kriging process, was adapted to extreme values spatial fields under the form of an extremal function (Cooley et al., 2006, 2007). At the cost of estimation difficulties, sometimes very heavy, this generalized variogram allows the interpolation of spatial fields of extreme values and the definition of a range, distance to which the interpolation provides information. This formalism is now beginning to be successfully applied to rainfall data (Bel et al., 2008). It opens up quite promising for data analysis and interpolation of snow depth data, without the need of the simplifying assumptions made to date. The main obstacle is related to the consideration of altitude, which adds an extra dimension to an already complex modeling problem. The use of this formal framework of extreme value theory generalized to the multivariate spatial case (Max-Stable Processes, Brown and Resnick, 1977; DeHaan, 1984) seems for us to be the best choice, for the mapping of extreme snowfalls in the French Alps, and constitutes one of the objectives of this thesis.

1.3.2 Evaluation of the release depth: statistical – mechanical modeling

Various authors have studied release depth statistical distributions across several paths, or even over an entire region (Rosenthal and Elder, 2002; McClung, 2003; Failletaz et al., 2004). They highlighted, in particular, power-law-type distributions without characteristic scales. These results have motivated the development of different mechanical models like cellular automata (Failletaz et al., 2004; Fyffe and Zaiser, 2004, 2007; Bair et al., 2008). These models incorporate a source of stochastic variability (usually a heterogeneity of mechanical properties or snow depth) and are therefore able to provide statistical distributions of the release depth. Interestingly, they have proven capable of reproducing, under certain conditions, power law distributions.

The good results obtained by these cellular automata models highlight two basic ingredients that are essential for the mechanical description of avalanche releases, namely the heterogeneity of the weak layer and the effects of stress redistribution by the elasticity of the overlying slab.

Based on the results presented above, it is now possible to go further, and to develop mechanical models adapted to the evaluation of the statistical distributions of the release depth at the path scale. To do this, we propose to abandon the cellular automata approach, while retaining the essential ingredients of pre-existing models, and to move towards a full finite element mechanical modeling of the weak layer – slab system which could further take into account the influence of topography and geomorphology. A major difficulty that must be addressed is the specification of the constitutive law of the weak layer, which must include the ingredients for instability (softening behavior) while remaining simple enough not to multiply the parameters. There are very few experimental data on this subject, but

different forms of plausible constitutive laws were nevertheless proposed in the literature based on considerations of fracture mechanics (McClung, 1979b; Louchet, 2001; Fyffe and Zaiser, 2004, 2007; McClung, 2009).

The coupling of all the elements listed above – description of the mechanical behavior of the weak layer and the overlying slab, taking into account the spatial heterogeneity of snow cover in a well-defined mechanical–statistical model using current numerical methods and the coupling with snowfall distributions – has, to our knowledge, never been done before. Yet, in the absence of sufficient data rendering obsolete any purely statistical approach, such a coupled statistical–mechanical model is, from our point of view, the only way forward that would produce reliable results for the evaluation of avalanche release depth distributions.

1.3.3 Scientific questions and objectives

The principal objective of this thesis is to obtain statistical distributions of avalanche release depths. These distributions must be valid over a long time scale (several decades) and must be obtainable for any path in the French Alps. This work is thus clearly intended to long-term risk management and prevention. This objective is far from trivial given the current state of knowledge about snow and the numerous remaining unknowns. Consequently, this complex problem of avalanche release has to be simplified. First, we will focus in this thesis on slab avalanches, more destructive than loose-snow avalanches and generally more relevant for hazard mapping. It is commonly accepted that slab avalanches are triggered by the rupture of a weak snow layer buried under one or many slab layers, generally denser and more cohesive. Thus, the complex stratigraphy of snow will be simplified into a bi-layer slab – weak layer system. This system is the simplest situation to model the phenomenon of slab avalanche release. Moreover, let us recall that, besides the scientific interest of this thesis, the obtained distributions are aimed at serving as inputs of avalanche propagation models. These models are also very simplified, and generally assume that the flow is characterized by a depth and a mean velocity integrated over the flow depth. Consequently, the modeling level of the input must be compatible with that of flow models, which justifies the assumptions that will be made.

In this thesis, we have focused our efforts on the three following main scientific questions:

- What is the influence of weak layer heterogeneity on snow slab avalanche release? To answer this question, the idea is to develop a mechanical modeling of avalanche release in a framework of continuum mechanics. The modeling will be based on the consideration of the ingredients essential to the onset of instability: softening of the weak layer, spatial heterogeneities and spatial stress coupling induced by the elasticity of the slab. Integrated in a probabilistic framework, this model will allow to obtain avalanche release depth distributions independently of the available snowfall.

- How to map extreme snowfalls and high return period quantiles? The development of a framework of statistical interpolation of snowfall using the latest methods of spatial analysis of extreme values, taking into account, in particular, the spatial dependence between extreme values, will give an answer to this question.
- How to couple the release depth distributions coming from the mechanical analysis and snowfall distributions to obtain the global release depth distribution? A rigorous formalism using conditional probabilities will be proposed to solve this point.

The ultimate goal of this thesis is to develop an operational tool to evaluate, at the path scale, avalanche release depths for different return periods. This is an ambitious goal, but crucial for avalanche engineering. The approach we propose, based on a combined use of statistical and mechanical models, is for us the most suitable to provide answers to the problem given the current status of scientific knowledge and available data. From a broader perspective, this thesis addresses one of the major scientific obstacles currently impeding the modeling of avalanches, i.e. the initiation phase.

1.4 Summary of the main results and reading grid

This PhD thesis is organized around four main articles which are either already published, submitted or still in preparation.

Chapter 3 presents the current state of the art regarding the many different concepts used and studied in this thesis. A first section is dedicated to a review of slab avalanche release processes, then in a second section the existing studies dealing with statistical analyzes of release depth data are presented. The third section describes the physical and mechanical properties of snow. In particular, a graphical compilation of the mechanical parameters of snow reported by many authors and relevant in this study is performed. In the fourth section, the different mechanical models for slab avalanche release which have been proposed in the literature are recalled. Finally, the last section gives the necessary background on extreme value statistics and their application in the multivariate case using max-stable processes.

In **Chapter 4**, we study the influence of weak-layer cohesion heterogeneity on slab avalanche release using a finite element model. This chapter is composed of two articles. The first one is entitled “Influence of weak layer heterogeneity on snow slab avalanche release: Application to the evaluation of avalanche release depths.” and was submitted to *Journal of Glaciology*. In this paper, a shear-softening interface underlying an elastic slab is modeled and the system is loaded by increasing the slope angle until failure and avalanche release. Release angle distributions are analyzed and a heterogeneity smoothing effect due to redistributions of stresses by elasticity of the slab is highlighted. This smoothing effect induces a reduction of the release angle variance compared to the case of a fully rigid slab.

However, the average release angle is almost unaffected by this effect. The obtained release angle distributions are then inverted, yielding a release depth distribution integrated over all slopes.

The second paper is entitled “Influence of tensile strength and weak layer heterogeneity on slab tensile rupture.” and is still in preparation for a submission to *Journal of Glaciology*. In this paper, we analyze two different rupture types observed in the simulations. (1) Full-slope releases for which the heterogeneity is not sufficient to trigger a tensile failure. These releases are influenced by the topography and the morphology of the path. For instance, the tensile failure will be very sensitive to the presence of trees, rocks, ridges and local curvature. (2) Partial-slope releases for which the local variations of weak-layer cohesion is substantial and can trigger the slab tensile crack on its own. Importantly, for both release types, the primary rupture process observed is always the basal shear failure of the weak layer. Hence, slab rupture systematically constitutes a secondary process. We have shown that the proportion between these two types of rupture is extremely dependent on the mechanical model parameters. Besides, we present a simple statistical model capable of reproducing the proportion between release types as a function of the model parameters. We demonstrate that, for realistic values of the parameters, the releases are mainly full-slope, which highlights the major influence of slope morphology on the position of the tensile failure within the slab and thus on the extent of the release area.

Chapter 5 is composed of one article entitled “Mapping extreme snowfalls in the French Alps using Max-Stable processes.” submitted to *Water Resources Research*. In this paper, extreme snowfalls are mapped in the French Alps by spatial interpolation of snowfall water equivalent annual maxima of 40 measurement stations. To do so, Max-Stable Processes, a mathematical formalism generalizing extreme value theory to the multivariate spatial context are used. Orographic gradients from Durand et al. (2009) were used to transform our data to a unique altitude level of 2000 m. Using an efficient transformation of space, anisotropy can be modeled. It appears that the spatial extremal dependence depends strongly on the local orientation of the alpine axis and the presence of large valleys. Linear and spline models for the spatial evolution of the GEV parameters were used and compared. This smooth modelling of GEV (Generalized Extreme Value) parameters within max-stable processes and associated with a nested model selection procedure constitutes the methodological strong point of the work. We evidence, in particular, that, at a constant altitude (2000m), the highest location parameters μ are very North (Mont-Blanc, Aravis and Bauges), but significant values are also observed far South. The highest scale parameters σ are in the Southeast (extreme Southern Alps), which corresponds to the Mediterranean effect that tends to bring variability. The shape parameter is mainly positive in the Northern, Central and Southern Alps, showing a Frechet attraction domain, and becomes negative in the extreme Southern Alps (Weibull domain). This model also allows, the computation of high return level maps of extreme snowfalls, which constitutes

a powerful operational tool for long-term managing of avalanche risk.

A complementary article entitled “Cross-comparison of meteorological and avalanche data for characterising avalanche cycles: The example of December 2008 in the eastern part of the French Alps.”, published in *Cold Region Science and Technology* is presented in appendix. A part of this paper, to which I contributed, is dedicated to the application of the previous Max-Stable model to the avalanche cycle of December 2008 in the eastern part of the French Alps. A retro-analysis of this event is performed using different techniques which are cross-compared. It is shown that the 3-day snowfall return period calculated using the Max-Stable approach globally corresponds to the one derived from Safran outputs at the massif scale. The relatively good agreement between the two approaches is very encouraging and emphasizes the ability of our model to achieve retro-expertise of past extreme snowfall events.

Chapter 6 is composed of an article entitled “Relative influence of mechanical and meteorological factors on avalanche release depth distributions: An application to the French Alps.” published in *Geophysical Research Letters*. In this paper, we present a rigorous formalism in which release depth distributions are expressed through a coupling of mechanical and meteorological factors. Considering that an avalanche can occur only if the snowfall depth exceeds a critical value corresponding to a stability criterion, release depth distributions obtained from the slab–weak layer mechanical model are coupled with the distribution of 3-day extreme snowfalls. We show that this coupled model is able to reproduce field data from 369 natural slab avalanches in La Plagne (France). Not only the power-law tail of the distribution, corresponding to large slab depths, but also the core of the distribution for shallow slab depths, are well represented. Small to medium-sized avalanches appear to be controlled mainly by mechanics, whereas large avalanches and the associated power-law exponent, are influenced by a strong mechanical-meteorological coupling. Finally, we demonstrate that the obtained distribution is strongly space-dependent, and, using the consistent interpolation formalism presented above, our model is used to obtain release depth maps for given return periods.

In Appendix, a conference proceeding entitled “Influence of weak layer heterogeneity on slab avalanche release using a finite element method” published in *Springer Series in Geomechanics and Geoengineering* is presented. This paper shows the influence of the heterogeneity of the weak-layer friction coefficient on release angle distributions and on the rupture type.

A last article entitled “Quasistatic to inertial transition in granular materials and the role of fluctuations” published in *Physical Review E*, whose subject lies outside of the main scope of this PhD thesis but which was written during the same period, is also provided.

Chapter 2

Introduction (version française)

Source d'émerveillement mais aussi de crainte et de terreur, les avalanches cachent encore bien des mystères, malgré d'importants progrès scientifiques récents. Une avalanche consiste en un écoulement gravitaire rapide d'une masse de neige sur une pente montagneuse. Chaque année, les avalanches sont responsables de la mort d'environ 30 personnes en France et 150 en Europe (principalement randonneurs et skieurs hors piste) avec un total d'environ 1,5 million d'euros de dommages matériels. En plus de cet aspect destructeur, les avalanches ont un fort impact médiatique, principalement en raison de l'augmentation récente du nombre de pratiquants de montagne, skieurs, snowboarders et plus particulièrement les skieurs de randonnée. Cependant, la plupart des avalanches sont déclenchées naturellement en hors-piste sans influence humaine et deviennent un enjeu important seulement lorsque des vies ou des dégâts matériels sont potentiellement impliqués. Le cycle avalancheux catastrophique de l'hiver 1999 dans les Alpes européennes (12 décès à Montroc, France; 12 décès à Evolène, Suisse; 39 décès à Galtür, Autriche; destruction de nombreuses structures, routes et chemins de fer) a rappelé leur capacité destructrice et a poussé à améliorer les méthodes scientifiques pour la cartographie du risque avalanche. La cartographie du risque et le zonage consistent à définir l'étendue maximale et la pression d'impact d'une avalanche de référence, associée à une période de retour élevée, de 100 ans, typiquement.

Aujourd'hui, les modèles numériques de propagation des avalanches de neige ont acquis un rôle central dans les méthodes d'ingénierie pour la cartographie et le zonage du risque. Les travaux scientifiques menés au cours de ces dernières années, ont permis d'accroître significativement la performance de ces modèles, grâce à la prise en compte du comportement spécifique de la neige en écoulement, à la prise en compte des phénomènes d'érosion et de dépôt par la coulée, ainsi qu'à l'utilisation de schémas numériques adaptés aux différentes situations traitées (Barbolini et al., 2000; Lachamp et al., 2002; Naaim et al., 2003). En outre, plusieurs études ont permis de valider les sorties de ces modèles en les confrontant à des résultats expérimentaux ou à des observations de terrain (Barbolini et al., 2000; Hutter

et al., 2005; Naaim et al., 2008).

Pour autant, la mise en oeuvre systématique de ces modèles reste confrontée à un certain nombre de difficultés, parmi lesquelles l'évaluation précise du volume de départ des avalanches. Le volume de départ constitue en effet une donnée d'entrée des modèles, et les résultats en dépendent très fortement, en particulier pour les couloirs de taille petite à moyenne. Or, il n'existe pas à l'heure actuelle de méthodologie claire et bien définie permettant, dans un couloir donné, de prédéterminer le volume de départ des avalanches potentielles pour différentes périodes de retour. Même pour les sites les mieux documentés (ex: vallée de Chamonix, région de Davos), l'évaluation du volume initial est généralement très délicate en raison du peu de données quantitatives disponibles dans les zones de déclenchement. Les quelques méthodes existantes sont pour la plupart empiriques et considèrent généralement que la hauteur de départ de l'avalanche correspond à l'accumulation de neige fraîche sur 3 jours, sans tenir compte des effets mécaniques. La surface de départ est généralement déterminée de manière empirique également, à l'aide de critères géomorphologiques. Compte tenu de la complexité et de l'efficacité des modèles de propagation, il semble aujourd'hui nécessaire d'améliorer ces techniques empiriques pour l'estimation de la hauteur et de la surface de départ en utilisant des méthodes plus rigoureuses afin d'améliorer la qualité de ces procédures de zonage et de cartographie du risque.

2.1 Problématique et objectifs

Le problème de la prédétermination du volume initial d'une avalanche exige à la fois l'évaluation de la hauteur et de la surface potentielle de départ. En effet, la distribution statistique des volumes de départ d'avalanche sur un site donné peut être exprimé comme une combinaison des distributions statistiques de hauteur et de surface de déclenchement, en prenant en compte un terme de couplage étant donné que ces deux variables ne sont pas totalement indépendantes. Dans cette étude, nous allons nous concentrer sur l'évaluation de la hauteur de départ. Cette hauteur fait intervenir deux facteurs: la hauteur de neige disponibles dans la zone de départ et un critère de stabilité mécanique provenant des caractéristiques topographiques et morphologiques de la zone de départ (angle de la pente par exemple) et des propriétés mécaniques de la neige. Par conséquent, il semble possible de diviser le problème en deux sous-problèmes:

- Prédétermination de la distribution de hauteur de neige disponible,
- Prédétermination d'une hauteur critique correspondant à un critère de stabilité mécanique, dans un cadre probabiliste.

Ensuite, un couplage entre les distributions obtenues par ces deux approches devra être réalisé pour obtenir la distribution globale de hauteur de déclenchement.

2.1.1 Prédétermination des hauteurs de neige en zone de départ

Conceptuellement, la prédétermination des hauteurs de neige dans toute zone de départ potentielle devrait pouvoir être réalisée par interpolation des données nivo-météorologiques acquises dans les stations de mesure de la région concernée. En pratique, cependant, les difficultés sont multiples car, en zone de montagne, les données disponibles sont peu nombreuses et généralement incomplètes :

- Les données se limitent le plus souvent à des chroniques de précipitations mesurées en hauteur d'eau. La distinction pluie/neige n'est pas toujours effectuée, ce qui nécessite l'analyse conjointe des séries de température.
- Les postes nivologiques et pluviométriques sont situés en général assez loin des zones de départ d'avalanches. Il est donc nécessaire d'employer des méthodes d'interpolation spatiale adaptées à la forte hétérogénéité des données, de type krigage (Cressie, 1993).
- En outre, ces postes sont généralement situés dans les vallées plutôt qu'à des altitudes élevées, ce qui rend nécessaire la prise en compte d'un gradient orographique de température et de précipitation pour la quantification de l'équivalent en eau tombé au niveau des zones de départ.
- Les avalanches étant des événements rares, ce sont des hauteurs de neige extrêmes qui doivent être caractérisées, ce qui nécessite d'extrapoler au-delà des plus fortes valeurs observées dans les séries généralement courtes qui sont disponibles. Cela nécessite la mise en oeuvre de méthodes de statistique des extrêmes de type analyse des maximas ou renouvellement (Coles, 2001).
- Enfin la stationnarité du phénomène sous-jacent, qui est pratiquement toujours postulée, est une hypothèse questionnable notamment dans le contexte du changement climatique (Marty and Blanchet, 2011; Eckert et al., 2010).

Dans la pratique actuelle de l'ingénierie paravalanche, toutes ces difficultés sont généralement contournées au prix d'hypothèses très fortes. Ainsi les problèmes liés aux techniques d'interpolation et au gradient orographique sont traités via la définition de "zones homogènes par bande d'altitude" (Salm et al., 1990; Bocchiola et al., 2006). Cette méthode, outre les difficultés liées à la définition des zones, introduit des discontinuités au niveau des frontières qui sont incompatibles avec le phénomène naturel. Néanmoins, elle a l'avantage principal d'augmenter le nombre de données et permet ainsi de prédire des niveaux de retour élevés. Le traitement du caractère extrême des valeurs à interpoler reste également très imparfait, puisque la plupart des méthodes actuelles utilisent quasi-systématiquement des lois de Gumbel plutôt qu'un modèle plus général de type GEV mieux adapté à la

description des queues de distribution. Ceci a pour effet de sous-estimer systématiquement les précipitations les plus extrêmes (Parent and Bernier, 2003; Bacro and Chaouche, 2006). Récemment, un formalisme solide a été proposé afin de caractériser la dépendance spatiale des valeurs extrêmes. Appliqué à un ensemble de séries de données autour d'une série de référence, des cartes de dépendance spatiale peuvent ainsi être obtenues (Coles et al., 1999; Heffernan and Tawn, 2004). Dans la lignée de ces travaux, la notion de variogramme, qui est centrale dans toute procédure de krigage, a été adaptée aux champs spatiaux de valeurs extrêmes sous la forme d'une fonction extrémale (Cooley et al., 2006, 2007). Au prix de difficultés d'estimation parfois très lourdes, ce variogramme généralisé permet l'interpolation des champs spatiaux de valeurs extrêmes et la définition d'une portée, distance jusqu'à laquelle l'interpolation apporte de l'information. Ce formalisme commence aujourd'hui à être appliqué avec succès aux données de pluviométrie (Bel et al., 2008). Il ouvre des perspectives tout à fait prometteuses pour l'analyse des données nivologiques et l'interpolation des hauteurs de neige sans recourir aux hypothèses simplificatrices réalisées jusqu'à présent. Le principal verrou est lié à la prise en compte de l'altitude, ce qui rajoute une dimension supplémentaire à un problème de modélisation déjà complexe. L'utilisation de ce cadre formel de la théorie des valeurs extrêmes généralisée au cadre multivarié spatial (processus max-stables, Brown and Resnick, 1977; DeHaan, 1984) semble être le meilleur choix selon nous, pour la cartographie des chutes de neiges extrêmes dans les Alpes Françaises, et constitue un des objectifs de cette thèse.

2.1.2 Prédétermination de la hauteur de départ: modélisation statistique – mécanique

Différents auteurs se sont intéressés aux distributions statistiques de hauteur de départ à l'échelle de plusieurs couloirs, voire du massif (Rosenthal and Elder, 2002; McClung, 2003; Failletaz et al., 2004). Ils mettent en évidence, en particulier, des distributions de type loi puissance sans échelle caractéristique. Ces résultats ont motivé le développement de différents modèles mécaniques de type automates cellulaires (Failletaz et al., 2004; Fyffe and Zaiser, 2004, 2007). Ces modèles intègrent une source de variabilité stochastique (en général une hétérogénéité des propriétés mécaniques ou des hauteurs de neige) et sont donc à même de fournir des distributions statistiques de tailles de déclenchements. De manière très intéressante, ils se sont avérés capables de reproduire, dans certaines conditions, des distributions en loi puissance.

Les bons résultats obtenus par ces modèles de type automates cellulaires permettent de mettre en évidence deux des ingrédients de base qui sont essentiels pour la description mécanique du déclenchement des avalanches, à savoir l'hétérogénéité de la couche fragile et les effets de redistribution des contraintes par l'élasticité de la plaque sus-jacente.

Sur la base des résultats présentés ci-dessus, il apparaît aujourd'hui possible d'aller plus

loin, et de développer des modèles mécaniques adaptés à la prédétermination des distributions statistiques des tailles de zones de départ à l'échelle du couloir. Pour ce faire, nous proposons d'abandonner l'approche automate cellulaire et, tout en conservant les ingrédients essentiels des modèles pré-existants, d'aller vers une modélisation mécanique complète par éléments finis du système couche fragile – plaque élastique qui pourrait ultérieurement prendre en compte l'influence de la topographie et de la géomorphologie. Une difficulté importante qu'il faudra résoudre réside dans la spécification de la loi de comportement de cette couche fragile, laquelle doit intégrer les ingrédients nécessaires à l'instabilité (c'est-à-dire un comportement adoucissant) tout en restant suffisamment simple pour ne pas multiplier les paramètres. Il existe très peu de données expérimentales sur ce sujet, mais différentes formes de lois de comportement plausibles ont néanmoins été proposées dans la littérature sur la base de considérations de mécanique de la rupture (McClung, 1979b; Louchet, 2001; Fyffe and Zaiser, 2004, 2007).

Le couplage de tous les éléments cités ci-dessus – description du comportement mécanique de la couche fragile et de la plaque sus-jacente, prise en compte de l'hétérogénéité spatiale du manteau neigeux et le couplage avec les distributions de chutes de neige, au sein d'un modèle mécanique-statistique bien posé et en utilisant les moyens de simulation numérique actuels – n'a, à notre connaissance, jamais été réalisé. Pourtant, en l'absence de données en nombre suffisant rendant caduque toute approche purement statistique, une telle modélisation mécanique constitue à notre sens la seule voie de progrès qui permettrait d'obtenir des résultats fiables quant à la distribution des hauteurs de départ d'avalanche.

2.1.3 Questions scientifiques et objectifs

L'objectif principal de cette thèse est d'obtenir des distributions statistiques de hauteur de départ d'avalanche. Ces distributions doivent être valides sur une échelle de temps longue (plusieurs décennies) et doivent pouvoir être obtenues pour tout couloir des Alpes Françaises. Ce travail est donc clairement destiné à la gestion du risque à long terme et à la prévention. Cet objectif est loin d'être trivial étant donné l'état actuel des connaissances sur la neige et les avalanches et les nombreuses inconnues en jeu. Par conséquent, ce problème complexe du déclenchement de l'avalanche doit être simplifié. Tout d'abord, nous allons nous concentrer dans cette thèse sur les départs d'avalanches en plaques, généralement plus destructrices que les avalanches ponctuelles et donc plus pertinentes pour la cartographie du risque. Il est communément admis que les avalanches de plaques sont déclenchées par la rupture d'une couche de neige fragile ensevelie sous une ou plusieurs plaques, généralement plus denses et plus cohésives. Ainsi, la stratigraphie complexe manteau neigeux sera simplifiée en un système bi-couche plaque – couche fragile. Ce système est la situation la plus simple pour modéliser le phénomène d'avalanche de plaque. Par ailleurs, rappelons que, outre l'intérêt scientifique de cette thèse, les distributions obtenues

sont destinées à servir en entrée des modèles de propagation. Ces modèles sont aussi très simplifiés, et supposent généralement que l'écoulement est caractérisé par une épaisseur et une vitesse moyenne intégrée sur l'épaisseur de l'écoulement. Par conséquent, le niveau de modélisation en entrée doit être compatible avec celui des modèles d'écoulement, ce qui justifie les hypothèses qui seront faites. Dans cette thèse, nous avons concentré nos efforts sur les trois principales questions scientifiques suivantes:

- Quelle est l'influence de l'hétérogénéité de la couche fragile sur le déclenchement des avalanches de plaque ? Pour répondre à cette question, l'idée est de développer une modélisation mécanique du phénomène de déclenchement d'avalanche dans le cadre de la mécanique des milieux continus. La modélisation sera basée sur la considération des ingrédients essentiels à l'apparition de l'instabilité: l'adoucissement en cisaillement de la couche fragile, l'hétérogénéité spatiale, le couplage spatial des contraintes induit par l'élasticité de la plaque. Intégré dans un cadre probabiliste, ce modèle permettra d'obtenir des distributions de départ d'avalanches indépendamment des chutes de neige disponibles.
- Comment cartographier les valeurs extrêmes de chutes de neige et calculer des niveaux de retour élevés ? Le développement d'un cadre d'interpolation statistique des chutes de neige en utilisant les dernières méthodes d'analyse spatiale des valeurs extrêmes, en prenant en compte, en particulier, la dépendance spatiale entre les valeurs extrêmes, apportera une réponse à cette question.
- Comment coupler les distributions de hauteur de départ provenant de l'analyse mécanique et les distributions des chutes de neige afin d'obtenir la distribution globale de hauteur de départ ? Un formalisme rigoureux en utilisant les probabilités conditionnelles sera proposé pour résoudre ce point.

L'objectif final de cette thèse est de développer un outil opérationnel permettant de prédéterminer, à l'échelle du couloir, la hauteur de départ d'avalanche pour différentes périodes de retour. Il s'agit d'un objectif ambitieux, mais crucial pour l'ingénierie par-avalanche. L'approche que nous proposons, fondée sur une utilisation combinée de modèles statistiques et mécaniques, nous semble la plus appropriée pour apporter des réponses au problème posé au vu de l'état d'avancement actuel des connaissances scientifiques et des données disponibles. D'un point de vue plus général, cette thèse s'attaque à l'un des verrous scientifiques majeurs entravant actuellement la modélisation des avalanches, à savoir la phase de déclenchement.

2.2 Récapitulatif des résultats principaux et grille de lecture

Cette thèse est organisée autour de quatre articles principaux qui sont soit déjà publiés, soumis ou en cours de préparation.

Le **chapitre 3** présente l'état actuel des connaissances sur les nombreux concepts différents utilisés et étudiés dans cette thèse. Une première section est consacrée à une revue des processus d'initiation des avalanches de plaque, puis dans une deuxième section, les études existantes portant sur des analyses statistiques de données de hauteur de départ d'avalanche sont présentées. La troisième section décrit les propriétés physiques et mécaniques de la neige. En particulier, une compilation graphique des paramètres mécaniques de la neige pertinents pour cette étude est réalisée. Dans la section 4, les différents modèles mécaniques pour le déclenchement des avalanches de plaque qui ont été proposés dans la littérature sont rappelés. Enfin, la dernière section donne les bases nécessaires sur les statistiques des valeurs extrêmes et leur application dans le cas multivarié en utilisant les processus max-stables.

Dans le **chapitre 4**, nous étudions l'influence de l'hétérogénéité de cohésion de la couche fragile sur le départ des avalanches de plaque en utilisant un modèle mécanique simulé par éléments finis. Ce chapitre est composé de deux articles. Le premier est intitulé "Influence de l'hétérogénéité de la couche fragile sur le départ des avalanches de plaque: Application à l'évaluation de la hauteur de départ d'avalanche" et a été soumis à *Journal of Glaciology*. Dans cet article, on modélise une interface adoucissante en cisaillement sous une plaque élastique et le système est chargé en augmentant l'angle d'inclinaison jusqu'à la rupture et le départ de l'avalanche. Les distributions d'angle de départ sont analysées et un effet de lissage de l'hétérogénéité du aux redistributions de contraintes par élasticité de la plaque est mis en évidence. Cet effet de lissage engendre une réduction de la variance de l'angle de départ par rapport au cas d'une plaque complètement rigide. L'angle de départ moyen, en revanche, n'est quasiment pas affecté par cet effet. Les distributions d'angle de départ obtenues sont ensuite inversées, ce qui donne une distribution de hauteur de départ intégrée sur toutes les pentes.

Le deuxième article est intitulé "Influence de la résistance à la traction et de l'hétérogénéité de la couche fragile sur la rupture en traction de la plaque." et est en cours de finalisation pour une soumission dans *Journal of Glaciology*. Dans cet article, nous analysons deux types de ruptures différents observés dans les simulations. (1) Les départs complets pour lesquels l'hétérogénéité n'est pas suffisante pour déclencher une rupture en traction. Ces départs sont influencés par la topographie et la morphologie du couloir. Par exemple, dans ce cas, la rupture en traction sera très sensible à la présence d'arbres, de rochers, de crêtes, de ruptures de pentes et à la courbure locale. (2) Les départs partiels pour lesquels les variations locales de la cohésion de la couche fragile sont importantes et peuvent déclencher

la rupture en traction de la plaque à elles-seules. Il est important de noter que, pour les deux types de départs, le processus de rupture primaire observé est toujours la rupture en cisaillement de la couche fragile basale. Ainsi la rupture en traction de la plaque constitue systématiquement un processus secondaire. Nous avons montré que la proportion entre ces deux types de départ était extrêmement dépendante des paramètres du modèle mécanique. En outre, nous présentons un modèle statistique simple capable de reproduire la proportion entre les différents types de départs. Nous démontrons que pour des valeurs réalistes des paramètres, les départs sont principalement de type complet ce qui met en évidence l'influence majeure de la morphologie et de la topographie du couloir sur la position de la rupture en traction de la plaque et donc sur l'étendue de la zone de départ.

Le **chapitre 5** est composé d'un article intitulé "Cartographie des chutes de neige extrêmes dans les Alpes françaises en utilisant les processus max-stables." soumis à *Water Resources Research*. Dans cet article, les chutes de neige extrêmes sont cartographiées dans les Alpes Françaises par interpolation spatiale des maxima annuels de chutes de neige en équivalent en eau provenant de 40 stations de mesure. Pour ce faire, les processus max-stables, un formalisme mathématique généralisant la théorie des valeurs extrêmes au contexte multivarié spatial sont utilisés. Les gradients orographiques de l'étude de Durand et al. (2009) ont été utilisés pour transformer nos données à une altitude unique de 2000 m. En utilisant une transformation elliptique de l'espace, l'anisotropie des chutes de neige extrêmes a pu être modélisée. Il semble que la dépendance spatiale des extrêmes soit fortement influencée par l'orientation locale de l'axe alpin et la présence des grandes vallées intra-alpines. Des modèles linéaire et spline pour l'évolution spatiale des paramètres de la GEV (Generalized Extreme Value) ont été utilisés et comparés en utilisant le critère TIC. Cette modélisation lisse des paramètres de la GEV en utilisant les processus max-stables constitue le point méthodologique fort du travail. Nous mettons en évidence, en particulier, que, à altitude constante (2000m), les valeurs les plus élevées du paramètre de localisation μ sont situées très au Nord, mais des valeurs significatives sont également observées dans les Alpes extrême-sud. Les valeurs les plus importantes du paramètre d'échelle σ se trouvent dans le Sud-Est, ce qui correspond à l'effet méditerranéenne qui tend à amener de la variabilité. Le paramètre de forme ξ est globalement positif montrant un domaine d'attraction de Fréchet et est seulement négatif dans les Alpes extrême-sud (domaine de Weibull). Ce modèle permet notamment, d'établir des cartes de chutes de neige pour des niveaux de retour élevés, ce qui constitue un outil opérationnel puissant pour la gestion à long terme du risque d'avalanche.

Un article complémentaire intitulée "Comparaison croisée de données météorologiques et d'avalanches pour caractériser les cycles avalancheux: L'exemple de Décembre 2008 dans la partie Est des Alpes Françaises.", publié dans *Cold Region Science and Technology* est présenté en annexe. Une partie de cet article, à laquelle j'ai contribué, est dédiée à l'application du modèle max-stable précédent au cycle avalancheux de Décembre 2008

dans la partie Est des Alpes Françaises. Une rétro-analyse de cet événement est réalisée en utilisant différentes méthodes qui sont comparées entre elles. Il est montré que la période de retour du cumul de neige sur 3 jours calculée en utilisant les résultats de l'approche max-stable correspond globalement à celle calculée en utilisant les sorties du modèle Safran par massif. L'accord relativement bon entre les deux approches est très encourageant et met en évidence les capacités de notre modèle pour la rétro-expertise d'événements extrêmes.

Le **chapitre 6** est composé d'un article intitulé "Influence relative des facteurs mécaniques et météorologiques sur les distributions de départ d'avalanche: Application aux Alpes françaises" et publié dans *Geophysical Research Letters*. Dans cet article, nous présentons un formalisme rigoureux dans lequel les distributions de hauteur de départ sont exprimées à travers un couplage des facteurs mécaniques et météorologiques. Considérant qu'une avalanche ne peut se produire que si la hauteur des chutes de neige dépasse une valeur critique correspondant à un critère de stabilité, les distributions de hauteur de départ obtenues à partir du modèle mécanique plaque-couche fragile sont couplées avec la distribution des chutes de neige extrêmes sur 3 jours. Les distributions de hauteur de départ prédites par ce modèle couplé sont ensuite comparées à une base de données bien documentée englobant 369 avalanches naturelles de plaques à La Plagne, France. On montre qu'avec seulement un paramètre ajustable, un excellent accord avec les données peut être obtenu à la fois pour la queue en loi de puissance de la distribution, correspondant à des hauteurs de plaques importantes, et pour son corps correspondant à de faibles hauteurs. Deux conclusions importantes peuvent être tirées: (1) Les avalanches petites à moyennes sont principalement contrôlées par la mécanique, tandis que les grosses avalanches sont influencées par un couplage mécanique-météorologique important. (2) Les distributions de hauteur de départ, y compris la valeur de l'exposant de la loi de puissance observée pour les hauteurs de plaques élevées, sont très variables dans l'espace et ne peuvent pas être considérées comme universelles. Enfin, le modèle est étendu en utilisant les résultats du modèle max-stable dans le but de produire des cartes de hauteur de départ d'avalanche pour différentes périodes de retour.

En **annexe**, un acte de colloque intitulé "Influence de l'hétérogénéité de la couche fragile sur le départ des avalanches de plaque en utilisant la méthode des éléments finis", publié dans *Springer Series in Geomechanics and Geoengineering* est présenté. Ce document montre l'influence de l'hétérogénéité du coefficient de frottement de la couche fragile sur les distributions d'angle de départ d'avalanche et sur le type de rupture.

Enfin, un dernier article intitulé "Transition quasi-statique inertielle dans les milieux granulaires et le rôle des fluctuations" publié dans *Physical Review E* sortant du sujet principal de cette thèse mais également écrit au cours de cette période, est aussi présenté.

Chapter 3

State of the Art

In this chapter, the current state of knowledge about the different concepts and notions used in this study is recalled. In the first section, slab avalanche release processes are recalled, then in a second section the existing studies dealing with statistical analyzes of release depth data are presented. In the third section, the physical and mechanical properties of snow are reviewed. In particular, a graphical collection of the mechanical parameters of snow relevant for this study is done. In the fourth section, the different mechanical models for slab avalanche release which have been proposed in the literature are recalled. Finally, in the last section, extreme value statistics and their application in the multivariate case using max-stable processes are detailed.

3.1 Slab avalanche release

It is now commonly accepted that slab avalanches are initiated by a shear failure in a weak snow layer (or at a weak interface) followed by tensile crown failure of the overlying slab (McClung, 1979b; Schweizer et al., 2003). Fig. 3.1 (from Perla (1977) and adapted by Schweizer et al. (2003)) shows slab avalanche nomenclature. The shear failure is caused by a local loss of cohesion inside the weak layer that may be due to (1) a localized surface loading such as skiers or explosives (artificial release), (2) uniform loading due to a new snowfall (natural release), or (3) changes in the snowpack properties due to weather changes (natural release). In addition, some recent studies (Johnson et al., 2004; van Herwijnen and Heierli, 2009) relying on field data show that the initial shear failure of the weak layer tend to be systematically accompanied by a normal collapse. These authors argued that slope normal and slope parallel displacements occur simultaneously during release. Anticrack analytical models have been developed and proved capable of reproducing these data (Heierli and Zaiser, 2007; Heierli et al., 2008). However, the issue of the influence of normal collapse on avalanche release is still a matter of debate. Some authors (Jamieson and Schweizer, 2000; Johnson et al., 2004) suggest that the simultaneous occurrence of

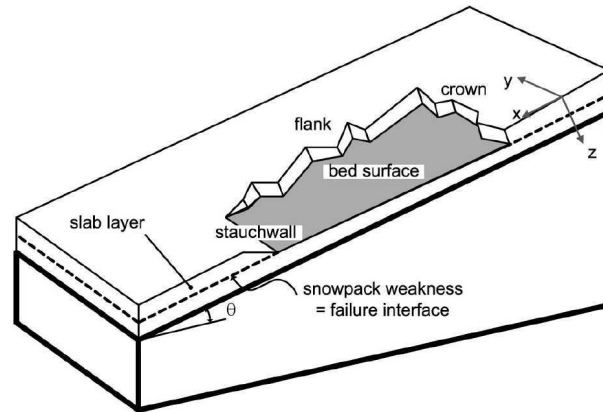


Figure 3.1: Nomenclature for slab avalanche release. From Perla (1977) and adapted by Schweizer et al. (2003).

weak-layer collapse and shear failure may facilitate fracture propagation due to bending effects. McClung (2011), on the contrary, showed that a model that does not account for slope-normal failure can reasonably reproduce critical length measurements obtained in field saw-cut tests. Hence, he argued that the slope-parallel propagation is very little influenced by the interaction between slope-normal displacement and stress.

A conceptual model for slab avalanche release has been proposed by Schweizer et al. (2003) and is represented in Fig. 3.2. A localized failure, or weak-spot, grows until it reaches a critical size and then becomes self-propagating. A slab can thus be released after a tensile rupture at the top (crown). The critical size for self-propagation of the basal failure is of the order of 0.1 – 10 m, with the longer lengths for rapid surface loading and shorter lengths for natural releases. The localized failure may be due to different slow mechanisms such as damage at the microscopic scale but also to the structural spatial heterogeneity of snow. Very little experimental studies on fracture initiation and propagation involved in slab avalanche release were conducted until now. These processes are only documented

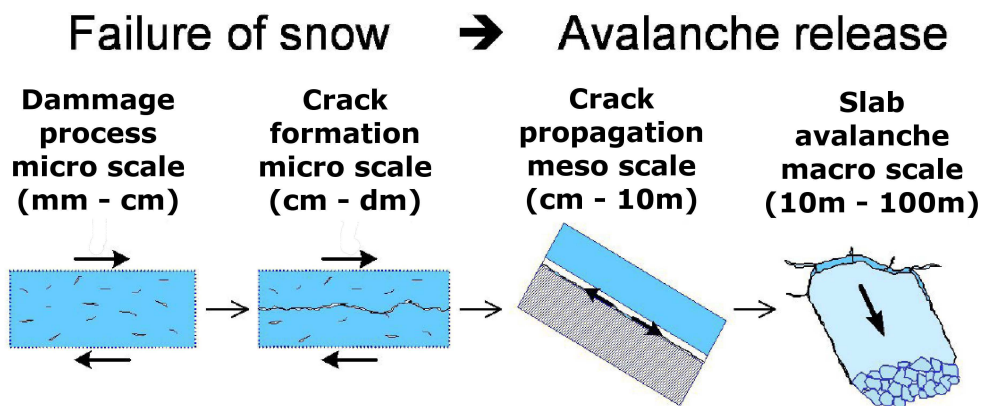


Figure 3.2: Conceptual model of snow slab avalanche release (from Schweizer et al., 2003)

in the case of artificially triggered slab avalanches (van Herwijnen and Jamieson, 2005; van Herwijnen and Heierli, 2009) but has never been done for natural avalanches for which the processes still remain poorly understood.

In their review about avalanche formation, Schweizer et al. (2003) described five essential contributing factors for slab avalanche release:

(1) Terrain which is an essential and constant-over-time factor. Generally, a slope angle $> 30^\circ$ is required for slab avalanching. Fig. 3.3 represents an histogram of slope angle in release zones for human-triggered slab avalanches (Schweizer et al., 2003) but is also representative of natural avalanche releases (Perla, 1977). In addition to the slope angle, Maggioni and Gruber (2003) showed the crucial influence of the curvature of the release zone and the distance to the ridge on avalanche release. Other terrain aspects such as roughness and forest density can also play an important role.

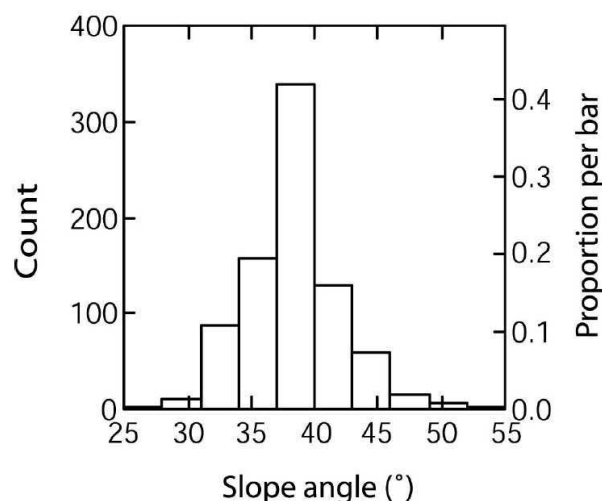


Figure 3.3: Slope angle in release zones of 809 human-triggered avalanches. The mean depth of the slabs was 0.49 m. From Schweizer et al. (2003)

(2) New snow is generally the most important factor for forecasting catastrophic avalanches. Generally, natural avalanches can be released for new snow depths about 30 – 50 cm and extreme avalanches can be initiated for new snow depths higher than 1 m, typically.

(3) Wind is the second most important factor after snowfalls and may contribute to a very significant increase in local thickness of the snowpack and thus very important stress concentrations. It also contributes to the formation of hard slabs which facilitates the propagation of the basal fracture over long distances which can cause avalanches of very large size.

(4) Snow cover stratigraphy is critical for slab avalanche release. The presence of a weak layer or a weak interface is a necessary but not sufficient condition for slab avalanching (Bader and Salm, 1990; Schweizer, 1999; Schweizer et al., 2003)

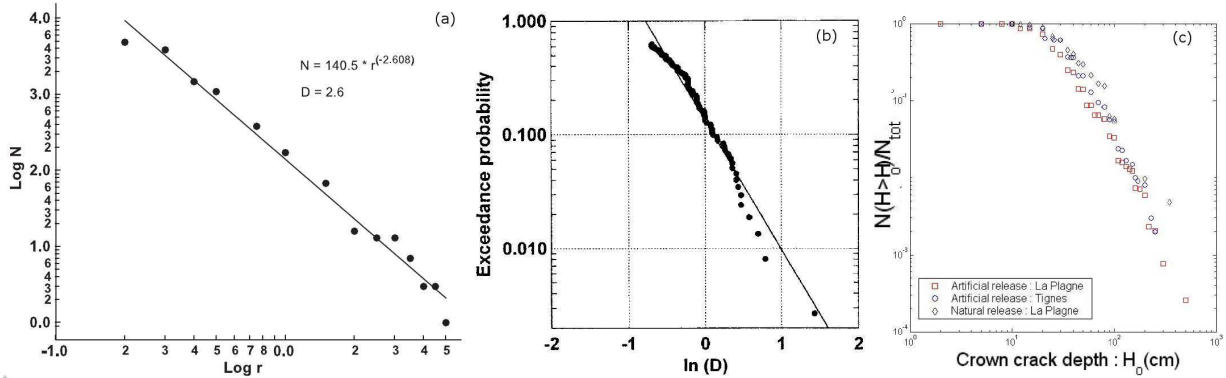


Figure 3.4: Avalanche release depth cumulative exceedence distributions. (a) 8000 avalanches with a mix of triggers (Rosenthal and Elder, 2002). (b) 187 avalanches in British Columbia with a mix of triggers (McClung, 2003). (c) 3450 avalanches in Tignes and La Plagne with the distinction between natural and artificial releases (Failletaz et al., 2006).

(5) Temperature is an important factor which can contribute to avalanche release even a long time after the snowfall (see Fig. 1.8). Depending on the rate of change, it can lead to the formation of new weak layers or to the weakening of existing ones and thus to instability.

3.2 Avalanche release depth distributions

The evaluation of avalanche release depth distributions represents a challenging issue for the mapping, zoning and long term management of hazard in mountainous regions. In particular, these distributions constitute one of the essential ingredients (besides friction, terrain, and erosion) to predict accurate run-out distance distributions using coupled statistical-dynamical numerical simulations (Meunier and Ancey, 2004; Eckert et al., 2010). Until now, very little research has been undertaken to understand and more importantly to predict these distributions.

Currently, a strong debate is ongoing concerning the existence of a possible universal behavior for these distributions. In their pioneering work, Rosenthal and Elder (2002) studied a set of 8000 avalanches mixing artificial and natural triggers at Mammoth Mountain (USA), and showed that the release depth cumulative exceedence distribution (CED) appears to follow a power-law of exponent -2.6 (Fig. 3.4a). This led them to postulate that avalanche release depths are scale-invariant and behave as a chaotic process. They argued that this behavior may be due to the deposition and evolution of snow layers and to the mechanics of slab avalanche release.

McClung (2003) reported the same behavior and power-law exponent for a set of 187 slab avalanches in British Columbia (mix of triggers, Fig. 3.4b), and pointed out the

possible role of fracture toughness distributions and mechanical size effects. This author also analyzed separately artificial and natural avalanche releases to study the effect of the triggering mechanism. A scale-invariant CED tail was also found on the set of 56 natural avalanches, although on a relatively small range of depths in this case and with an apparent power-law exponent of -4.4 .

Failletaz et al. (2006) studied 3450 avalanches in Tignes and La Plagne (France) and also reported a power-law CED with a characteristic exponent of -2.4 for artificially released avalanches (Fig. 3.4c). Given the similarity of this result with previous studies carried out in different areas, they concluded on the universality of this power-law exponent.

Finally, a more recent study by Bair et al. (2008) compares the adjustment of different statistical distributions on release depth data from different mountainous areas, and show that GEV (Generalized Extreme Value) of Frechet type seem to provide better fits than power-law distributions for all the analyzed datasets. They also showed a significant spatial variation in the power-law exponents of the CED tails and concluded, on the contrary, on a non-universal behavior of avalanche release depth distributions.

3.3 Physical and mechanical properties of snow

3.3.1 Snow metamorphism

Snow forms in the atmosphere by cloud-droplet freezing induced by freezing nuclei and water vapor deposition. Different shape and size of crystals can develop depending on the degree of water vapor supersaturation and snow crystals temperature. The most common shape is the stellar dendrite, which is characterized by a hexagonal symmetry (Fig. 3.5a).

When the snow crystals reach the ground or an existing snowpack, they start to bind together by sintering, the snowpack densifies (settlement) and the snow crystals change shape as a function of meteorological conditions (solar radiation, wind, air temperature, temperature gradients...).

Two main different types of snow metamorphisms lead to different grain shapes: equilib-

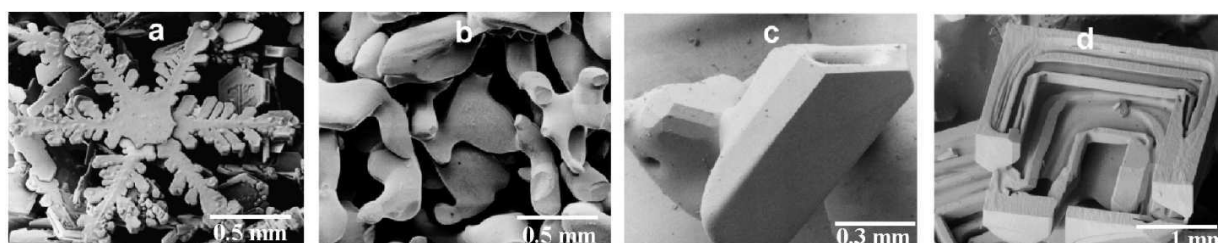


Figure 3.5: Examples of snow crystals: a) Stellar snow crystal, b) Rounded snow crystals, c) Faceted snow crystal, d) Depth hoar. Low temperature scanning electron microscope images from <http://emu.arsusda.gov/>.

<i>Class</i>	<i>Symbol</i>	<i>Code</i>
Precipitation Particles	+	PP
Machine Made snow	⊙	MM
Decomposing and Fragmented precipitation particles	/	DF
Rounded Grains	●	RG
Faceted Crystals	□	FC
Depth Hoar	^	DH
Surface Hoar	v	SH
Melt Forms	○	MF
Ice Formations	■	IF

Table 3.1: Main morphological grain shape classes from the Fierz et al. (2009) classification.

rium (or rounding) and kinetic (or faceting) metamorphisms. Equilibrium metamorphism is driven by low temperature gradients which produces rounded grains (Fig. 3.5b). The initial form (generally dendritic) evolves in few days into rounded particles, in order to reduce their specific surface. The vapour pressure gradient is the cause of this rounding process, since it generates a vapour flux from surfaces with high curvature to low curvature zones (Schneebeli and Sokratov, 2004; Kaempfer et al., 2007; Pinzer, 2009). This process, is associated with intergranular bonding (sintering cohesion) and thus, generally increases the stability of the snowpack (Perla and Sommerfeld, 1987). In contrast, kinetic metamorphism is driven by strong temperature gradients (usually greater than $10^{\circ}.\text{m}^{-1}$ (Akitaya, 1974) which induces high vapor diffusion in the snowpack. This leads water vapour to move from the warm surface of one snow crystal (at the top) to the cold surface of another crystal (at the bottom). Hence, grains with angular shapes, sharp edges and flat faces or facets (Fig. 3.5d) form in a few hours or days. This type of metamorphism is responsible for the creation of unstable weak snow layers within the snowpack such as depth hoar (Fig. 3.5d) and faceted crystals (Fig. 3.5c). Indeed, with this characteristic shape, the grains cannot bind together. This metamorphism is therefore often associated with a loss of strength and thus of stability. This explains the formation of weak layers within the snowpack. Weak layers can also form at the surface of the snowpack. Surface hoar crystals generally form during cold and clear conditions, particularly at night. The cooling of the snow surface due to radiation may lead to a condensation of water vapor on the snow surface producing surface hoar crystals (McClung and Schaerer, 2006). Once buried, it is a particularly thin, fragile and persistent weak layer in the snowpack (similar to a “house of cards” layers) which is responsible for a number of avalanche deaths each season. Fierz et al. (2009) compiled a classification of all snow types and various snow properties. The symbols and code of the different types of grains according to this classification are represented in Tab. 3.1.

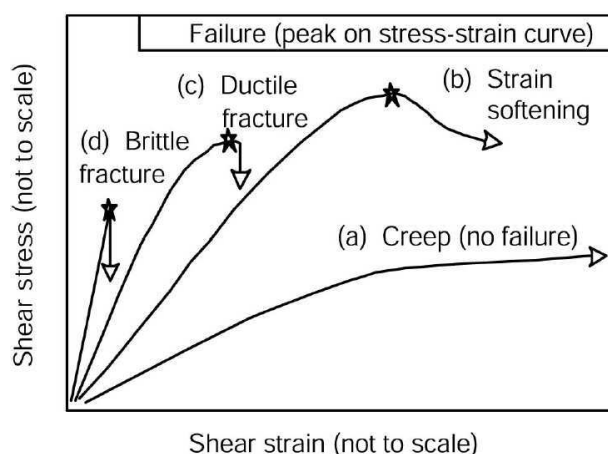


Figure 3.6: Schematic of failure behaviour of snow under shear at different shear strain rates (from Schweizer et al., 2003). Note that the strain rate increases from a to d, i.e. $\dot{\epsilon}_a < \dot{\epsilon}_b < \dot{\epsilon}_c < \dot{\epsilon}_d$. Figure based on data of Fukuzawa and Narita (1993); McClung (1977); Narita (1980); Schweizer (1998).

3.3.2 Mechanical properties of snow

Snow is a very complex material whose mechanical behavior is still not fully understood. Mechanical properties of snow vary with time and space and they depend a lot on the crystal type, snow density, temperature, the applied strain rate, etc. In particular, snow deformation and rupture are strongly strain-rate dependent. This has been first shown with tension tests on homogeneous snow (Narita, 1980, 1983). Shear strength of snow decreases with increasing strain rate and temperature. A ductile to brittle transition occurs at a strain rate $\dot{\epsilon}$ of about 10^{-3} – 10^{-4} s^{-1} depending on temperature and pressure (Fukuzawa and Narita, 1993; McClung, 1977; Narita, 1980; Schweizer, 1998, 1999; Schweizer et al., 2003). A brittle rupture implies that virtually none or very little permanent deformation occurs before fracture (Fig. 3.6d). On the contrary, ductile behaviour means large irreversible deformations before failure (Fig. 3.6bc) or no failure at all (Fig. 3.6a). Snow behaves as a brittle material for high strain rates ($\dot{\epsilon} > 10^{-3}$ s^{-1}) or fast loading, while it is ductile under low loading or deformation rates ($\dot{\epsilon} < 10^{-4}$ s^{-1}) (Fig. 3.6).

Although many laboratory experiments (Mellor, 1975; McClung, 1977; Narita, 1980; Navarre et al., 1992; Schweizer, 1998) and field measurements (Roch, 1965; De Montmollin, 1978; Jamieson and Johnston, 1990; Föhn et al., 1998; McClung and Schweizer, 2006) have been carried out for homogeneous snow, only few studies (McClung, 1977, 1979b; Föhn et al., 1998; McClung and Schweizer, 2006; McClung, 2009) have been undertaken to characterize the mechanical behaviour of weak layers. The main outcome of these latter studies is that weak snow layers behave, at high loading rates, as strain-softening (or quasi-brittle) materials (Fig. 3.7). The softening is caused by the break of ice bridges at the microscopic scale. The value of the associated characteristic strain-softening displacement

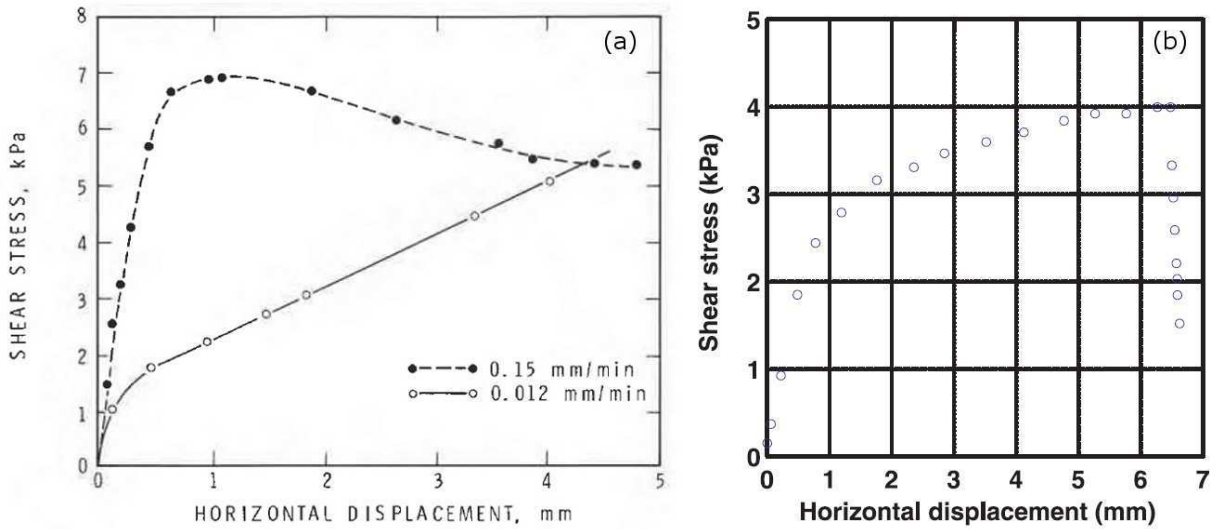


Figure 3.7: Direct simple shear results for shear stress (kPa) versus horizontal displacement. (a) Low density samples of 180 kg/m^3 sheared with different strain rates (From McClung (1977)). The lower strain rate sample shows strain hardening and the higher strain rate sample shows strain softening with a characteristic softening displacement $\delta \approx 2 \text{ mm}$. (b) Sample of faceted snow. Density is 165 kg/m^3 , test temperature is -15° and grain size is $0.2\text{-}0.5 \text{ mm}$. The characteristic strain-softening displacement after peak stress is $\delta \approx 0.1 \text{ mm}$. (From McClung, 2009).

δ is still a matter of debate. It was first found to be close to 2 mm (Fig. 3.7a, McClung, 1977), but estimated lower close to 0.1 mm in more recent experiments (Fig. 3.7b, McClung, 2009). Because of the heterogeneous character of these weak layers, these micro-cracks are generally localized, they develop almost uniformly and concentrate progressively to form a macro-crack (or weak-spot), which can eventually propagate until global rupture.

Experimental studies on homogenous snow samples being relatively numerous and those on weak layers being sparse, I collected and compiled in graphics most of the existing data on snow mechanical properties required in the present study. The mechanical parameters presented below depend on several factors, such as snow density, the applied strain rate, temperature, etc. We chose to represent elasticity and rupture parameters of snow mainly as a function of density since it appears to be the dominant factor. The strain rate also plays a very important role on the type of constitutive law (ductile or brittle) but has a less significant influence than density on the values of the different mechanical quantities. However, the important variability observed in the following 2D figures can probably be explained by the multi-factorial dependence of the presented quantities.

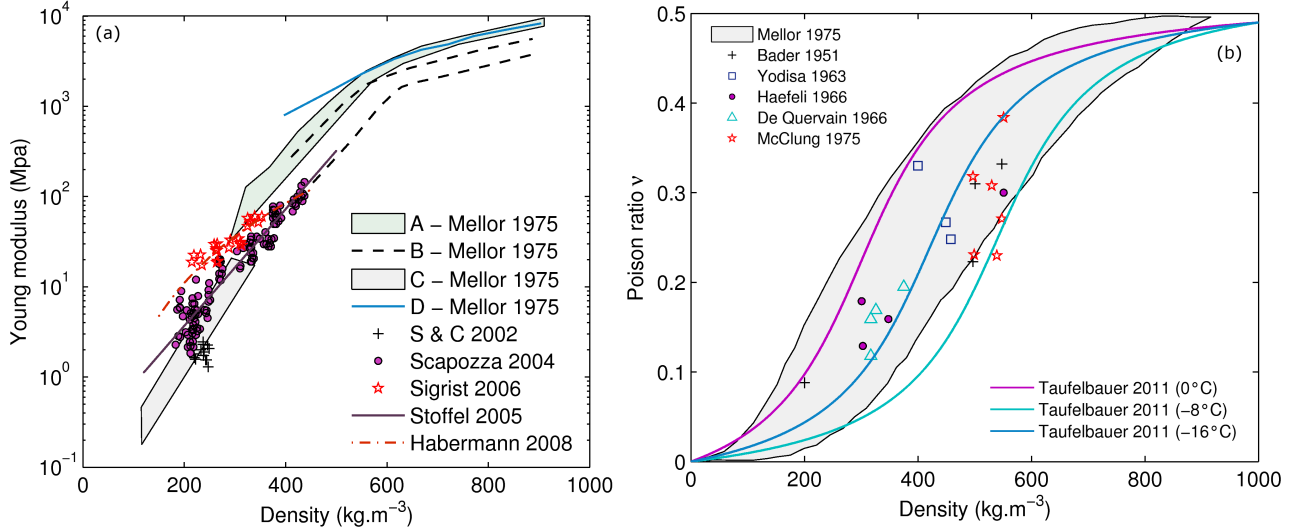


Figure 3.8: (a) Summary of existing values of Young modulus plotted against density. (b) Summary of existing values of Poisson ratio plotted against density. See text for details.

Elasticity parameters

Young modulus Snow elasticity is known for a long time, since Mellor (1975). Fig. 3.8a is a compilation of Young moduli from different studies and measured with different methods:

- Mellor (1975) already made an important compilation of Young Moduli and classified them into 4 zones corresponding to different measurement techniques and different strain rates: (A) Pulse propagation or flexural vibration at high frequencies, -10° to -25°C . (B) Uniaxial compression, strain rate approximately 3×10^{-3} to $2 \times 10^{-2} \text{ s}^{-1}$, temperature -25° . (C) Uniaxial compression and tension, strain rate approximately 8×10^{-6} to $4 \times 10^{-4} \text{ s}^{-1}$, temperature -12° to 25°C and static creep test, -6.5° to -19°C . (D) Complex modulus, 10^3 Hz , -14°C .

- Dynamic torsional shear experiments of Schweizer and Camponovo (2002) converted to Young modulus values.

- Quasi-static compression experiments by Scapozza (2004). Stoffel (2005) adjusted an exponential law to Scapozza (2004) data for densities between 180 and 450 kg.m^{-3} :

$$E_0(\rho) = 1.873 \times 10^5 e^{0.0149\rho}. \quad (3.1)$$

- Dynamic Young modulus measured in a cyclic loading experiment, strain rate $\dot{\epsilon} = 2.7 \times 10^{-2}$, from Sigrist (2006). Habermann (2008) fitted a power law to Sigrist (2006) data for densities between 100 and 300 kg.m^{-3} :

$$E_1(\rho) = 9.68 \times 10^8 \left(\frac{\rho}{\rho_{ice}} \right)^{2.94}, \quad (3.2)$$

with $\rho_{ice} = 917 \text{ kg.m}^{-3}$.

It can be noted from Fig. 3.8a that Young modulus increases with density almost exponentially and seem to tend asymptotically to a limit. In the present study, we will be interested in the Young modulus of slabs whose density is generally between 100–300 kg.m⁻³ (Schweizer, 1999). This leads to Young modulus values between 0.3 and 30 MPa.

Poisson ratio Fig. 3.8b summarizes the available data for quasistatic and dynamic determinations of the Poisson ratio ν from the experimental studies of Bader et al. (1951); Yosida (1963); Haefeli (1966); De Quervain (1966) and McClung (1975) (shear creep test, $\dot{\epsilon} \approx 10^{-8} \text{ s}^{-1}$) with the envelop of Mellor (1975). Poisson ratio also increases with density and slab values are in the 0–0.3 range.

Rupture parameters

Tensile strength σ_T Several field and laboratory experiments have been conducted up to now to determine tensile strength of snow. Fig. 3.9 summarizes tensile strength σ_T values from these different studies which have been performed with different methods:

- Mellor (1975) summarized data of tensile strength of dry snow under rapid loading ($\dot{\epsilon} \in 10^{-4} - 10^{-2} \text{ s}^{-1}$) in uniaxial stress states from Bucher (1948); Butkovich (1956); Haefeli (1939); Hawkes and Mellor (1972); Keeler (1969); Keeler and Weeks (1967); Kovacs and Weeks (1969); Mellor and Smith (1966); Ramseier (1963); Smith (1963, 1965). According to Mellor (1975), this domain is relevant for brittle failure only.

- Roch (1966) measured the tensile strength under uniaxial tension and high loading rates directly at the crown of 35 slab avalanches using rectangular and cylindrical measurement devices. Tensile strength values are averages of tensile tests repeated every 50 mm down the face of slab crown fractures.

- Perla (1969) estimated the tensile strength from 250 cantilever beam tests on a very recent snowpack.

- McClung (1979a) made 38 *in situ* tests on large sample size using a tilting-table at low loading rates and under uniaxial tension. As his results were not affected by the notches shape, he argued that the failure was ductile.

- Conway and Abrahamson (1984) identified *in situ* slab weak layer systems and performed tensile tests at high rates and uniaxial tension by isolating a column from effects of side shear and compressive hold-up with a saw, and inserted the frames of their device on each side of the tested sample.

- Rosso (1987) tensile measurements are very similar to those of Conway and Abrahamson (1984), the main difference being the use of a trapezoid frame instead of a rectangular one.

- Jamieson and Johnston (1990) made 450 tensile tests using the same method as Conway and Abrahamson (1984) with large cross-sections. Jamieson and Johnston (1990)

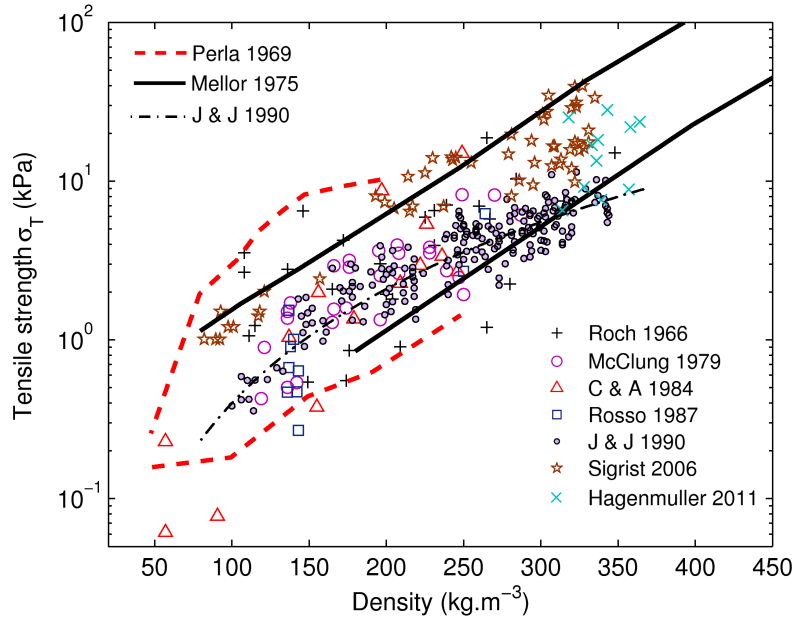


Figure 3.9: Density dependence of the tensile strength for several different studies and methods. See text for details.

also made a first review of these tensile strength values. They proposed the following empirical fit to relate the tensile strength to the density:

$$\sigma_{T0}(\rho) = 7.97 \times 10^4 \left(\frac{\rho}{\rho_{ice}} \right)^{2.39}. \quad (3.3)$$

- More recently Sigrist (2006) used the three-point bending laboratory test (3PB) to calculate the tensile strength of homogeneous snow samples under dynamic conditions. This test requires a beam specimen which is notched on one side with a cut, placed on two supporter and then loaded in the middle. This author also proposed an empirical relation with density:

$$\sigma_{T1}(\rho) = 2.4 \times 10^5 \left(\frac{\rho}{\rho_{ice}} \right)^{2.44}. \quad (3.4)$$

- Hagenmuller et al. (2012) made cold laboratory uniaxial tests to measure the tensile strength ($\dot{\epsilon} \in 10^{-4} - 10^{-3} \text{ s}^{-1}$) and compared it to finite element calculations of the microstructure of the sample captured using a tomograph. The tested snow was homogeneous samples of rounded grains with a density of 350 kg.m^3 .

As one can note, there is an important dispersion of tensile strength values from these different studies. However, recent measurements (Sigrist, 2006; Hagenmuller et al., 2012) still belong to the domain speculated by Mellor (1975). Globally, σ_T increases with increasing density. For slab densities in the $100\text{--}300 \text{ kg.m}^{-3}$, tensile strength values belong to the $0.3\text{--}20 \text{ kPa}$ interval, with a mean value around 2 kPa .

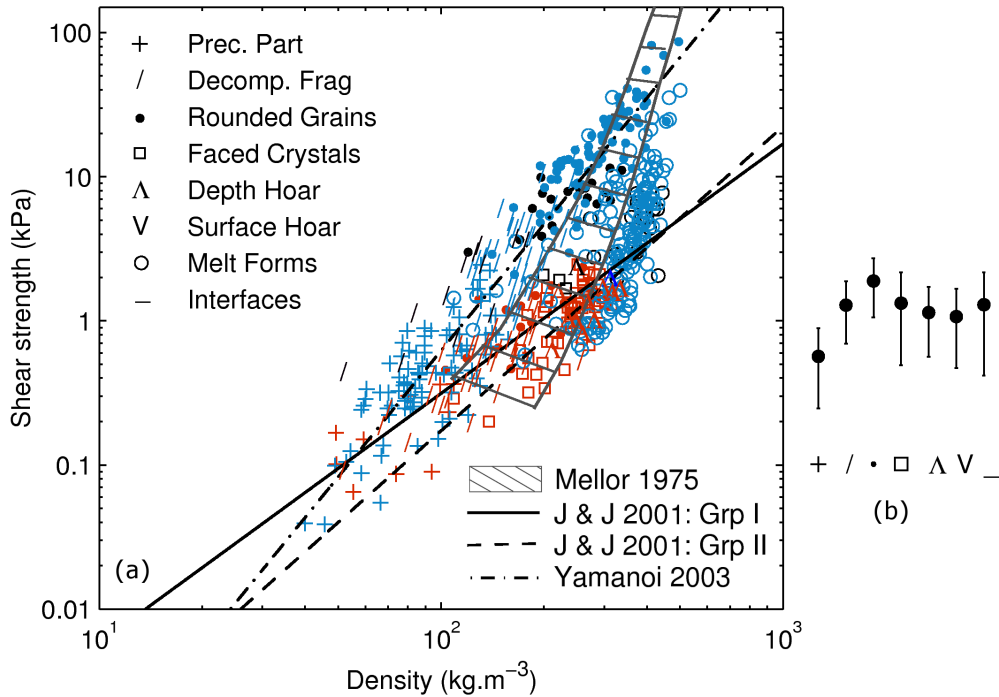


Figure 3.10: (a) Compilation of shear strength values plotted against density for different types of grains (see Tab. 3.1). Data from Mellor (1975) (hatched domain), Navarre et al. (1992) (black symbols), Jamieson and Johnston (2001) (orange symbols) and Yamanoi and Endo (2003) (blue symbols). See text for fit equations. (b) Shear strength as a function of the grain type from Föhn et al. (1998).

Shear strength τ_p We have seen before that slab avalanche releases are generally initiated by the shear rupture of a weak layer underlying a cohesive slab. In that sense, shear properties of snow such as shear strength τ_p are of major importance to study initiation mechanisms. Several authors measured shear strength of homogeneous snow *in situ* (Mellor, 1975; Conway and Abrahamson, 1988; Navarre et al., 1992; Yamanoi and Endo, 2003) or during laboratory experiments (Schweizer, 1998; Podolskiy et al., 2010). However, only few studies attempted to measure weak layers shear strength (Föhn et al., 1998; Jamieson and Johnston, 2001; Reiweger, 2010; Podolskiy et al., 2010; Reiweger, 2011). Fig. 3.10 is a collection of shear strength values for different types of grains and different studies:

- Mellor (1975) summarized shear strength values from direct measurements of Bailard and McGaw (1965); Butkovich (1956); Haefeli (1939); Keeler (1969); Keeler and Weeks (1967) but also avalanche release data from various sources summarized by Keeler (1969).
- Navarre et al. (1992) made *in situ* shear strength measurements for different types of snow grains.

- Föhn et al. (1998) measured shear strength of different weak snow layer *in situ* with different strain rates ($\dot{\epsilon} \in 10^{-2} - 1 \text{ s}^{-1}$) corresponding to the brittle domain. They report shear strength values between 0.2 and 2.8 kPa.

- Jamieson and Johnston (2001) made approximatively 800 sets of 10 shear frame tests to evaluate the shear strength of different types of weak layers *in situ*. When the weak layer was thick enough for density measurements, they could plot the shear strength as a function of the density. They distinguished two main groups of different grain shapes. Group I for precipitation particles, decomposing and fragmented precipitation particles and rounded grains. For this group, Jamieson and Johnston (2001) adjusted the following empirical relationship to density:

$$\tau_p^I(\rho) = 1.45 \times 10^4 \left(\frac{\rho}{\rho_{ice}} \right)^{1.73}. \quad (3.5)$$

Group II is composed of depth hoar and faceted crystals (most unstable weak layers). The following empirical relation was fitted to the data of this group:

$$\tau_p^{II}(\rho) = 1.85 \times 10^4 \left(\frac{\rho}{\rho_{ice}} \right)^{2.11}. \quad (3.6)$$

- Yamanoi and Endo (2003) made *in situ* shear frame tests for different frame sizes, normal load, strain rates and different types of grains. They showed the minor effect of size and normal load on their results. For dry snow (melted forms excluded), they exhibited a power law evolution of shear strength with density:

$$\tau_p^Y(\rho) = 2.075 \times 10^5 \left(\frac{\rho}{\rho_{ice}} \right)^{2.91}. \quad (3.7)$$

Hence, shear strength of snow increases with density. In this thesis, we will be interested in weak layers shear strength which generally have low densities ($< 200 \text{ kg.m}^{-3}$). According to Fig. 3.10, weak layer shear strengths belong to the 0.1–3 kPa range, with an average around 1 kPa.

Besides, in order to further characterize the ductile–brittle transition highlighted before, I also reported in Fig. 3.11, shear strength values from different studies as a function of the shear strain rate $\dot{\gamma}$:

- Schweizer (1998) used a direct simple-shear apparatus in a cold laboratory to measure shear strength of homogeneous samples (small rounded particles, density: 290 kg.m^{-3}). Experiments were performed at a temperature of -10°C . He found the shear strain rate of the brittle–ductile transition around 10^{-3} s^{-1} .

- Fukuzawa and Narita (1993) carried out simple shear experiment in cold laboratory on weak layers of depth hoar (density: 190 kg.m^{-3}) at a temperature of -6°C . These author found the ductile–brittle transition around $2 \times 10^{-4} \text{ s}^{-1}$. For very low shear rates in the ductile regime, these autors found relatively large shear strength values ($\approx 10 \text{ kPa}$).

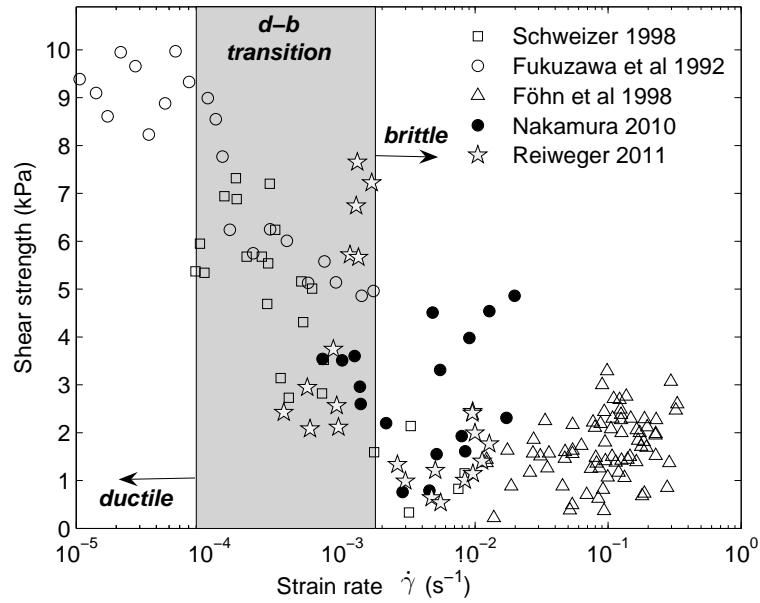


Figure 3.11: Shear strength strain rate dependence from different studies (see text for details). The transition between ductile and brittle regimes is between 10^{-4} and $2 \times 10^{-3} \text{ s}^{-1}$.

- As stated before, Föhn et al. (1998) measured shear strength of weak snow layer at high loading rates corresponding to a brittle regime.
- Nakamura et al. (2010) used a vibration apparatus in a cold laboratory to measure shear strength of dense homogeneous snow layers. These authors found opposite trends compared to almost all previous studies, namely increasing shear strength with increasing strain rate. The complexity of their measurement device may be one of the reasons of this discrepancy.
- Reiweger (2011) made cold laboratory experiments with natural samples including a weak layer of buried surface hoar. According to her results, she estimated the ductile–brittle transition around $2 \times 10^{-3} \text{ s}^{-1}$.

These results stress out that this transition between ductile and brittle regimes is still poorly known and not well characterized. Nevertheless, one can give a range of the transition strain rate between 10^{-4} and $2 \times 10^{-3} \text{ s}^{-1}$.

Friction coefficient $\mu = \tan \phi$ The general practice is to define and determine the shear strength τ_p according to the Mohr-Coulomb failure criterion for biaxial stress fields: $\tau_p = c + \sigma_n \tan \phi$ where c is the cohesion and ϕ the friction angle. Friction thus represent a contribution to the shear strength. Very little data are available on snow friction coefficient. The friction coefficient μ is the ratio between shear stress and normal stress of a solid material while it undergoes deformation. The static (or rupture) friction coefficient is the

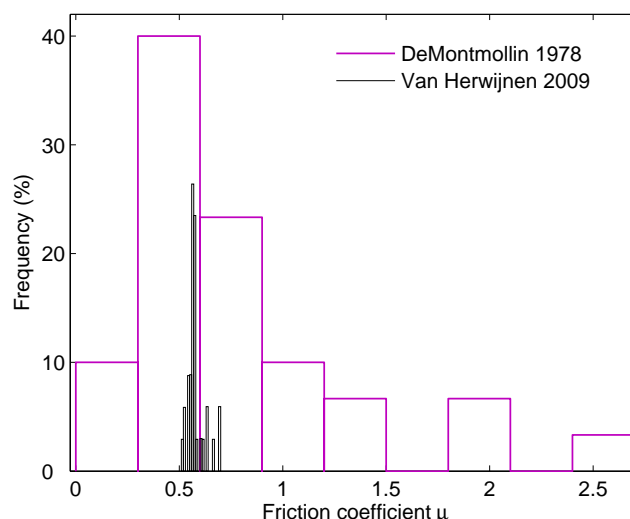


Figure 3.12: Distribution of rupture (De Montmollin, 1978) and residual (van Herwijnen and Heierli, 2009) friction coefficients.

ratio between the shear stress required to produce the sliding between two surfaces and the normal stress. Once the surfaces move, it is called dynamic (or residual) friction coefficient. Fig. 3.12 is an histogram of friction coefficient from different studies:

- De Montmollin (1978) measured the static friction coefficient as a function of snow density *in situ* using a manual “bévamètre”. Internal friction coefficient ranged from 0 to 2.7 corresponding to friction angles between 0 and 70°.
- van Herwijnen and Heierli (2009) were able to compute the evolution of static (rupture) and dynamic (residual) friction coefficients from *in situ* saw cut tests on slab - weak layer systems using video sequences and markers. Values of the residual friction coefficient for 34 experiments are reported in Fig. 3.12.

This figure shows that rupture friction coefficient values have a wide disparity with a mean around 0.6. On the contrary, residual friction coefficient values from van Herwijnen and Heierli (2009) do not show a strong variation. The measured values of μ ranged from 0.52 to 0.68 with a mean value of 0.57. This corresponds to friction angles ranging from 28 to 34° with a mean of 30°.

Spatial variability

Results obtained from *in situ* mechanical tests, suggest the existence of an important variability of mechanical properties of snow that can be due to the measurement protocol (samples sizes, loading rate, temperature, snow type, etc), but also to the spatial heterogeneity of the snow cover. Schweizer et al. (2008) stated that this spatial variability and particularly its characteristic range may have a very important influence on avalanche formation. Geostatistical analysis (Cressie, 1993; Kronholm, 2004) has been introduced

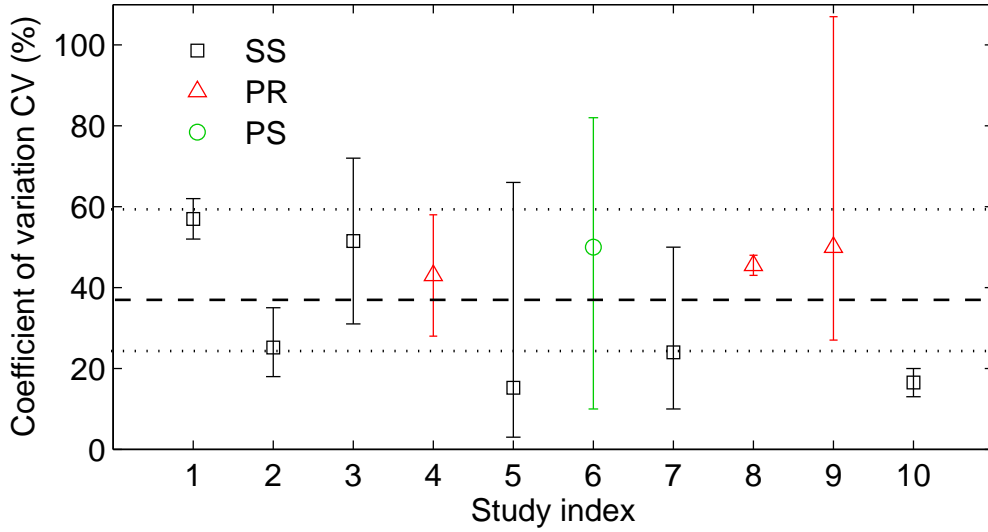


Figure 3.13: Coefficient of variation CV (minimum, mean and maximum value) from different studies (see text). SS = Shear strength measurement, PR = Point resistance measurement, PS = Point stability measurement.

and used to determine the correlation length (ϵ) and the coefficient of variation (CV) of field data. Schweizer et al. (2008) made an extensive review of all the existing field studies that analyzed snowcover spatial variability. Fig. 3.13 is a graphical summary of the coefficients of variation already reviewed by Schweizer et al. (2008). The index of the graphic corresponds to the following different studies:

- (1) Sommerfeld and King (1979) computed the CV of shear strength (SS) for 3 slopes approximately 24 h after the avalanche.
- (2) Föhn (1989) studied the CV of stability index derived from shear strength measurements (shear frame) for stable slopes (support of 0.025 m^2 , minimum spacing of $\approx 10 \text{ m}$ with a spatial extent of 30–300 m).
- (3) Conway and Abrahamson (1988) also analyzed the CV of stability index (derived from shear strength measurements) for 5 slopes (support of 0.09 m^2 , minimum spacing between 0.6 and 0.9 m with a spatial extent of $\approx 200 \text{ m}$). They suggested that the measurements should be spaced less than 0.5 m apart to capture the spatial variability and should span at least 3 m.
- (4) Birkeland (1990); Birkeland et al. (1995) made penetration resistance (PR) tests (support of 0.001 m^2 , minimum spacing of 1 m and spatial extent of 50 m). They studied the CV of PR on two slopes.
- (5) Jamieson and Johnston (2001) made approximately 800 sets of 10 shear frame tests (supports of 0.01, 0.025 and 0.05 m^2 , minimum spacing of 0.3 m and spatial extent of 6 m) on different weak snowpack layers. They shown that shear strength measurements were normally distributed.

- (6) Stewart (2002); Stewart and Jamieson (2002); Campbell (2004); Campbell and Jamieson (2007) made point stability (PS) tests using the drop hammer test on 39 slopes (support of 0.09 and 3 m², minimum spacing of 0.6 to 2.5 m and spatial extent of 10–50 m). They showed that CV values depend on the support size.

- (7) Landry (2002); Landry et al. (2004) derived the stability index from shear strength measurements for 11 slopes (support of 0.09 m², minimum spacing of 0.5 m and spatial extent of 42 m).

- (8) Birkeland et al. (2004) used the snow micro-pen (SMP) to determine the CV of penetration resistance of a buried surface hoar layer slope (two sets of measurements from two part of the slope six days apart, support of 2×10^{-5} m², minimum spacing of 0.5 m and spatial extent of 30 m).

- (9) Kronholm (2004) made penetration resistance measurements with the SMP over 21 slopes (support of 2×10^{-5} m², minimum spacing of 0.5 m and spatial extent of 30 m).

- (10) Logan (2005); Logan et al. (2007) made shear frame tests to derive shear strength and point stability on 2 uniform slopes (support of 0.025 m², minimum spacing of 0.5 m and spatial extent of 14–30 m).

From all these studies, the average CV is ranged between 23 and 60% with an overall average value of 37%. Note however, that for some of the mentioned studies, the CV values may be influenced by spatial correlations. Finally, concerning the correlation length ϵ (spatial range of the variability), it was found to be highly variable from < 0.5 to > 10 m (Kronholm, 2004; Birkeland et al., 2004). Hence, Schweizer et al. (2008) recommended that two tests should be spaced out on the order of at least 10 m in order to get independent results.

3.4 Slab avalanche release models

A slab avalanche is the result of four rupture types: (1) a shear rupture (that may be accompanied by a normal collapse) of a buried weak layer or interface; (2) A tensile rupture at the top of the slab (crown); (3) two lateral shear ruptures on both sides of the slab (flanks); (4) a compressive rupture at the bottom of the slab (stauchwall) (Schweizer et al., 2003) (Fig. 3.1).

Most of the existing avalanche release models are based on the assumption first made by Palmer and Rice (1973) for an overconsolidated clay and then taken up for snow by McClung (1979b) that a weak spot or shear band, i.e. a zone of zero shear strength, pre-exists inside the weak layer. Fracture mechanics is then applied to study the conditions for shear-band propagation. Based on an energy budget at the tip of the band where the stress concentrates (Fig. 3.14), the rapid propagation occurs when a critical length L is

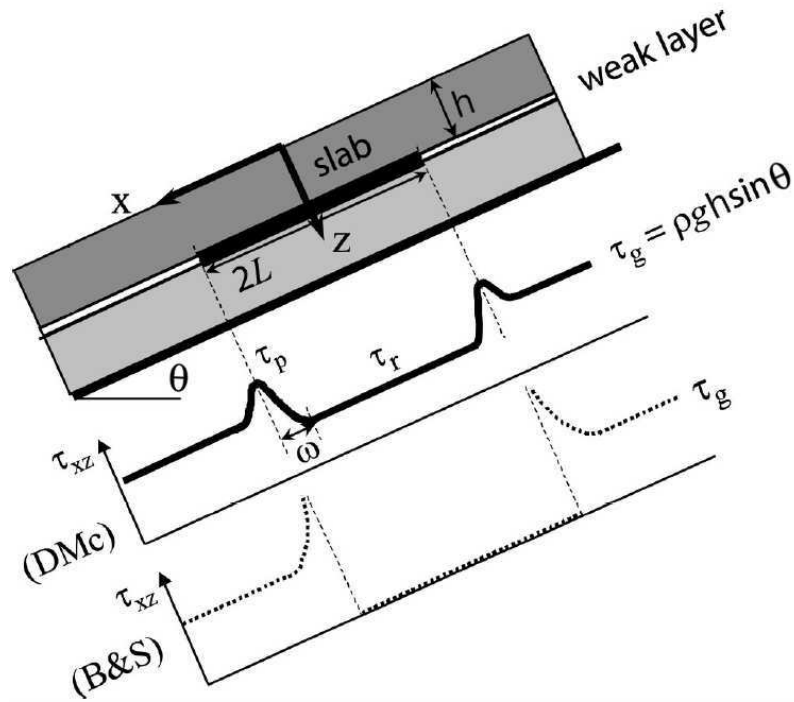


Figure 3.14: Snow slab release models with preexisting weak spots. A uniform 2D slope inclined with a slope angle θ , a slab depth h . The two graphics show the evolution of the shear stress at the interface between the slab and the substratum for two models: McClung (1979b) and Bader and Salm (1990), with $\tau_g = \rho g h \sin \theta$ the body weight shear stress, τ_p the peak stress and τ_r the residual stress. From Schweizer et al. (2003).

reached after a phase of slow strain softening. The propagation criterion is given by:

$$\frac{h(1-\nu)}{4G} \left((\tau_g - \tau_r) \frac{L}{h} \right)^2 = (\tau_p - \tau_r) \delta, \quad (3.8)$$

where h is the slab depth, ν the Poisson ratio of the slab, G the shear modulus of the slab, $\tau_g = \rho g h \sin \theta$ the body-weight stress, with ρ the density of the slab, θ the slope angle and δ the softening displacement in the weak spot required for the stress to pass from peak stress τ_p to residual stress τ_r . The right-hand term of Eq. (3.8) represents the resistance to the extension of the weak spot; the left-hand term is a driving term which provides the energy for the weak spot to propagate. For realistic values of the different parameters, the critical length can vary in the 1–20 m range. The size of the end zone (or plastic zone) ω (Fig. 3.14) is the characteristic length in which the shear stress decreases from the peak to the residual stress. It is considered as the minimal length to initiate any progressive failure process.

Following McClung (1979b), Bader and Salm (1990) also analyzed weak layer shear rupture propagation (Fig. 3.14) but taking into account snow strain-rate dependency. Based on continuum mechanics under small deformations and using simple linear visco-elastic constitutive laws, they proposed expressions for stress and strain at the edge of the

weak spot (called super weak zone). One of the main outcome of their study is that a weakness inside the snowpack is required for avalanche release even with a local increase of stress such as a skier. Besides, their model is able to predict the critical length for brittle and ductile fracture propagations. Using more realistic values of snow properties than Bader and Salm (1990), Schweizer (1999) determined the critical length using their model. For ductile failure propagation, the critical length is between 0.1 and 3.1 m. For brittle propagation, it is found to be between 5 and 35 m.

Louchet (2001) developed an analytical micromechanical model in which the weak layer was treated as an open cell ice foam of an array of ice bonds. These bonds were prone to break under stress, but broken bonds may reconstruct if in contact with each other for some time. Hence, this author described creep in relation to the bond-breaking rate and the bond-rewelding rate. Depending on the load and the balance between breaking and rewelding rates, the system can lead to stable, unstable (natural avalanche release), or critical conditions of slope stability. He argued that the critical situation is equivalent to a ductile to brittle transition.

Schweizer (1999) made a review of the existing mechanical models for slab release and concluded that the critical length for fracture propagation should be between 0.1 and 10 m. The 1 – 10 m range corresponds to rapid loading such as a skier, whereas the lower range 0.1 – 1 m corresponds to slow loading.

More recently, Chiaia et al. (2008) showed that a simple stress failure criterion coming from equilibrium equations could also be sufficient to predict shear-band propagation with a good accuracy when accounting for the thickness of the weak layer.

Nevertheless, as already noted by Schweizer (1999), the very concept of weak-spot is questionable since, even if we can imagine how local weak zones could appear (for instance from a progressive damage process at the micro-scale (Fig. 3.2) or around dark spots such as rocks, where the snow depth is reduced and thus the temperature gradient is increased), it is probably too simplistic, in general, to represent the complex heterogeneity of weak-layer mechanical properties. Besides, “because of the stochastic nature of some of the meteorological processes acting on the snow cover, a purely deterministic approach to the questions of where and when will have limited success” (quoted from Schweizer et al., 2003).

Several studies (Conway and Abrahamson, 1988; Jamieson and Johnston, 2001; Birke-land et al., 2004; Kronholm, 2004; Schweizer et al., 2008; Bellaire and Schweizer, 2011) have shown that snow mechanical properties present considerable spatial variability. From field data, this variability is generally described as following Gaussian distributions with spatial correlations. Hence, the concept of weak-spot may be replaced by mechanical models taking into account spatial stochastic processes to represent the heterogeneity. Such models would not only explain failure initiation in weak zones, but also fracture arrest in stronger zones (Schweizer, 1999). Besides, as pointed out by Schweizer et al. (2008), a

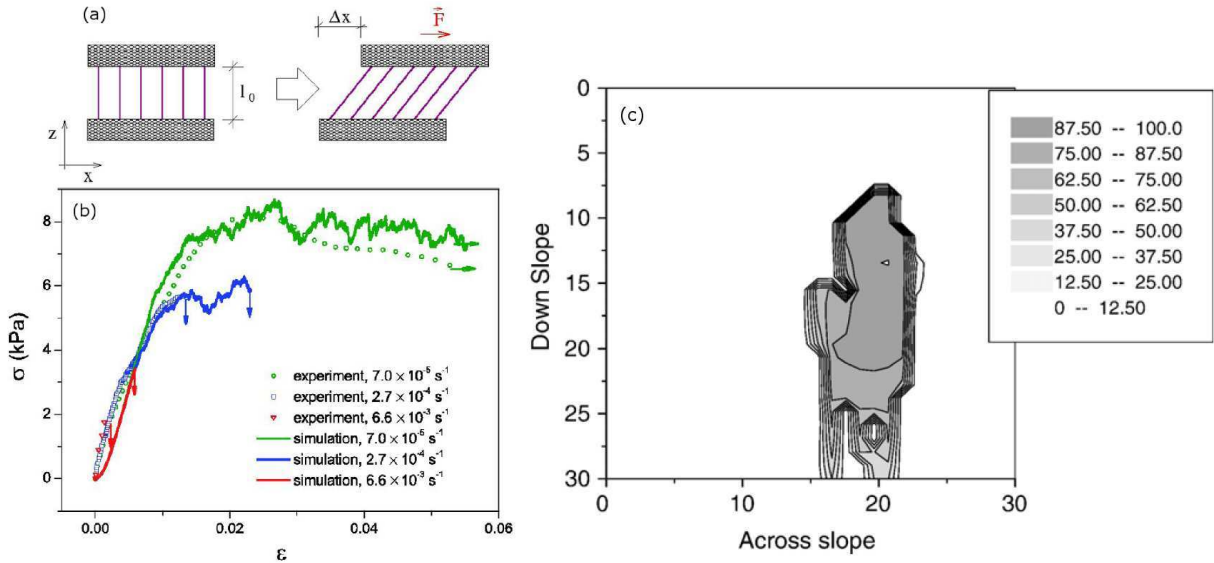


Figure 3.15: (a) Schematic representation of the FBM (Reiweger et al., 2009). (b) Comparison of the FBM simulations with experimental results (Reiweger et al., 2009). (c) Displacement profile for a failed slope; A cohesive area of slab has ruptured, the crown and side walls of the avalanche are marked by the thick black lines (Fyffe and Zaiser, 2007).

key factor in avalanche formation would be the relation between the critical length of the initial failure L (generally belonging to the 0.1–10 m range; Schweizer, 1999) to the spatial scale of the variability ϵ . For example, if $\epsilon/L < 1$ then it is suggested that the variability has a stabilizing effect (Kronholm et al., 2004). Recently, several studies attempted to include this heterogeneity in mechanical models. These studies can be classified as follows, according to the numerical method used:

(i) Fiber Bundle Model (FBM) are simple statistical fracture models that are well adapted for representing spatially heterogeneous systems, including possibly time-dependent effects such as sintering. Hence, Reiweger et al. (2009) model the weak snow layer as a discrete set of parallel brittle-elastic fibers (Fig. 3.15a). Spatial variability is accounted for by assigning to each fiber an initial strength taken within a Weibull distribution. Despite the simplicity of the model, these authors are able to quantitatively reproduce laboratory shearing experiments on homogeneous snow samples (Fig. 3.15b). However, redistribution effects by elasticity of the slab cannot be taken into account in such models which are therefore unable to reproduce full-scale avalanche release.

(ii) Cellular-Automata Models (CAM) consist of a regular grid of cells characterized by a state that can change over time and as a function of the neighboring cells' state. Fyffe and Zaiser (2004, 2007) and Kronholm and Birkeland (2005) applied such approaches to slab avalanche release with a heterogeneous shear strength of the weak layer represented by Weibull or Gaussian distributions. Via neighboring elements their models account for stress redistribution between weak and strong regions. They also included mode-II (shear)

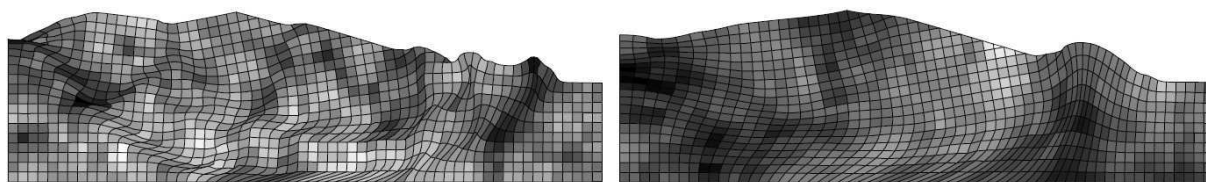


Figure 3.16: Examples of spatial heterogeneity of a cohesive slope using a log-normal random field for two correlation lengths and simulated using a Finite Element Method. Deformed mesh at slope failure. From Griffiths and Fenton (2004).

rupture of the weak layer with a strain-softening law, and mode-I (tensile) rupture of the slab as in Failletaz et al. (2004). These studies demonstrated the influence of spatial variability characteristics (variance, nugget effect, etc) on release depth distributions. Fyffe and Zaiser (2007) were also able to reproduce (under certain conditions) release depth distributions following power laws, as in field studies (Rosenthal and Elder, 2002; McClung, 2003; Failletaz et al., 2004). Besides and interestingly, Fyffe and Zaiser (2007) model allows to mark out the boundaries of avalanche release areas (Fig. 3.15c). However, stress elastic redistribution effects are oversimplified in these models whose applicability is limited to the case of a shear strength correlation length lower than the slab depth.

(iii) Finite Element Models (FEM) rely on the resolution of the complete mechanical equations of the problem. One of the main advantages of FEM compared to CAM is that it is able to capture large-scale stress redistribution effects due to elasticity. FEM has already been successfully applied to modeling the mechanical response of sandwich specimens including weak-snow layers with homogeneous properties (e.g. Bader and Salm, 1990; Stoffel, 2005; Mahajan and Joshi, 2008; Mahajan et al., 2010). However, only few studies coupled FEM with a stochastic representation of the spatial variability. Recently, such a model has been introduced by Griffiths and Fenton (2004) to study soil stability (Fig. 3.16). To our knowledge, the same type of approach has never been undertaken for snow.

3.5 Extreme value statistics in a multivariate spatial context

The objective of this section is to present the application of extreme value theory in the multivariate spatial case using max-stable processes which will enable the mapping of extreme snowfalls. In a first part, the three main max-stable processes are presented and the extremal coefficient is defined. Then, in a second part, a likelihood-based method for fitting a max-stable process to data is shown.

3.5.1 Max-Stable Processes and spatial extremes

Definition: Max-Stable Process

$\{Z(x)\}_{x \in \mathcal{X}}$ is a max-stable process if there exist positive sequences $a_n(x)$ and $b_n(x)$, such that if for all n and $(Z_i)_{i=1,n}$ independent copies of Z , $\{Z(x)\}_{x \in \mathcal{X}}$ has the same distribution as

$$\left\{ \frac{\max_{i=1,n} Z_i(x) - a_n(x)}{b_n(x)} \right\}_{x \in \mathcal{X}}.$$

As a consequence, all finite dimensional marginal distributions are max-stable and, in particular, the univariate marginal $Z(x)$ distribution belongs to the GEV family:

$$P(Z(x) \leq z) = \begin{cases} \exp \left[- \left(1 + \frac{\xi(x)(z - \mu(x))}{\sigma(x)} \right)^{-1/\xi(x)} \right] & \text{if } 1 + \frac{\xi(x)(z - \mu(x))}{\sigma(x)} > 0 \\ 1 & \text{otherwise} \end{cases} \quad (3.9)$$

where $\mu(x)$, $\sigma(x)$ and $\xi(x)$ are respectively the location, scale and shape parameters at location x . According to the sign of $\xi(x)$, $Z(x)$ distribution belongs to three different families of distributions known as Fréchet ($\xi(x) > 0$), Weibull ($\xi(x) < 0$) and Gumbel ($\xi(x) \rightarrow 0$).

Usually it is convenient to transform the univariate marginals setting:

$$Z^*(x) = \left(1 + \xi(x) \frac{(Z(x) - \mu(x))}{\sigma(x)} \right)^{1/\xi(x)}. \quad (3.10)$$

Z^* is thus a max-stable process with unit Fréchet margins. Models of max-stable processes have been proposed by several authors. The most popular are those of Smith (extremal Gaussian Smith, 1991), a particular case of DeHaan (1984) construction, Schlather (Schlather, 2002), and Brown-Resnick (Brown and Resnick, 1977) generalized by Kabluchko (Kabluchko et al., 2009).

Smith MSP The Smith Max-Stable Process (Smith, 1991) with unit Fréchet margins is defined as:

$$Z(x) = \max_i (\xi_i f(y_i, x)) \quad x \in \mathcal{X}, \quad (3.11)$$

where $(\xi_i, y_i), i \geq 1$ are the points of a Poisson process on $(0, +\infty) \times \mathcal{X}$ with intensity measure $\xi^{-2} d\xi \nu(dy)$, where $\nu(dy)$ is a positive measure on \mathcal{X} . The function f is non-negative such that

$$\int_{\mathcal{X}} f(x, y) \nu(dy) = 1, \quad x \in \mathcal{X}, \quad (3.12)$$

This process is often called rainfall-storm process. Eq. (3.11) is general but Smith considered a particular setting in which $\nu(dy)$ is the Lebesgue measure and $f(x, y) = f_0(y - x)$ a multivariate normal density with zero mean and covariance matrix Σ . In this case (and still

under the unit Fréchet margin assumption), one can show that the bivariate cumulative distribution function (CDF) is expressed as:

$$P(Z(x_1) \leq z_1, Z(x_2) \leq z_2) = \exp \left[-\frac{1}{z_1} \Phi \left(\frac{a}{2} + \frac{1}{a} \log \frac{z_2}{z_1} \right) - \frac{1}{z_2} \Phi \left(\frac{a}{2} + \frac{1}{a} \log \frac{z_1}{z_2} \right) \right] \quad (3.13)$$

where Φ is the standard normal cumulative distribution function, $a^2 = h^t \Sigma^{-1} h$ the Maha-

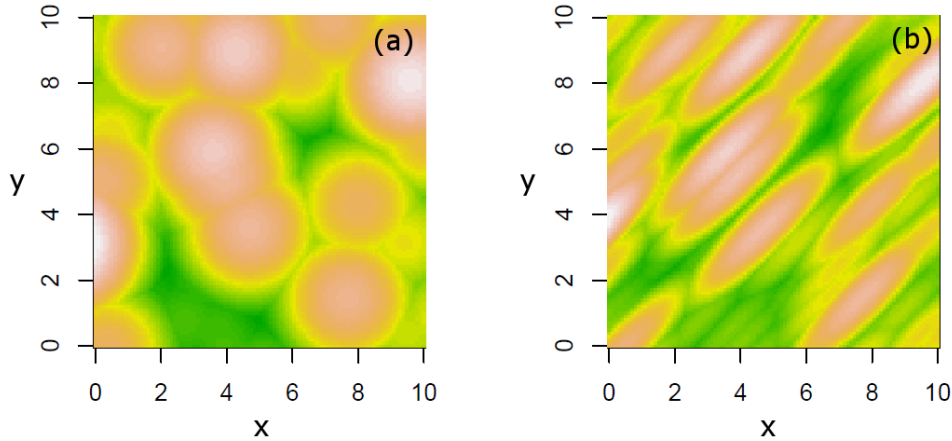


Figure 3.17: Two simulations of the Smith model with different covariance matrices Σ . (a) $\sigma_{11} = \sigma_{22} = 9/8$ and $\sigma_{12} = 0$. (b) $\sigma_{11} = \sigma_{22} = 9/8$ and $\sigma_{12} = 1$. The max-stable processes are transformed to unit Gumbel margins for viewing purposes. From Ribatet (2009).

lanobis distance between locations x_1 and x_2 and

$$\Sigma = \begin{pmatrix} \sigma_{11} & \sigma_{12} \\ \sigma_{12} & \sigma_{22} \end{pmatrix} \text{ in a 2D space, or } \Sigma = \begin{pmatrix} \sigma_{11} & \sigma_{12} & \sigma_{13} \\ \sigma_{12} & \sigma_{22} & \sigma_{23} \\ \sigma_{13} & \sigma_{23} & \sigma_{33} \end{pmatrix} \text{ in a 3D space.}$$

Fig. 3.17 represents two realizations of Smith MSP for two different covariance matrices. As one can notice, the covariance matrix Σ plays a major role since it defines the shape of the storm events and the main direction of anisotropy. Due to the use of a multivariate normal distribution, the storms have an elliptical shape.

Schlather MSP The Schlather Max-Stable Process (Schlather, 2002) with unit Fréchet margins is defined as:

$$Z(x) = \max_i \xi_i \max(0, Y_i(x)) \quad x \in \mathcal{X}, \quad (3.14)$$

where Y_i are i.i.d copies of a stationary process on \mathcal{X} such that $\mathbb{E}[\max(0, Y(x))] = 1$ and $\xi_i, i \geq 1$ the points of a Poisson process on \mathbb{R}_*^+ with intensity $\xi^{-2} d\xi$.

To obtain a model usable in practice, Schlather proposed to take Y_i as a stationary standard Gaussian process with correlation function $\rho(\|h\|)$. With this new assumption,

one can derive the bivariate CDF from Eq. (3.14):

$$P(Z(x_1) \leq z_1, Z(x_2) \leq z_2) = \exp \left[-\frac{1}{2} \left(\frac{1}{z_1} + \frac{1}{z_2} \right) \left(1 + \sqrt{1 - 2(\rho(\|h\|) + 1) \frac{z_1 z_2}{(z_1 + z_2)^2}} \right) \right] \quad (3.15)$$

where $\|h\| \in \mathbb{R}^+$ is the Euclidian distance between locations x_1 and x_2 . Usually, $\rho(\|h\|)$

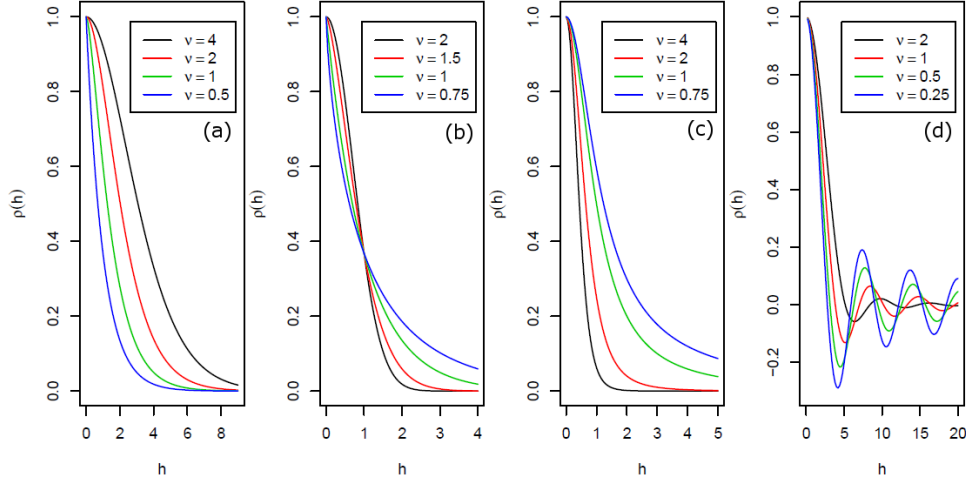


Figure 3.18: Plots of the Whittle-Matern (a), the powered exponential (b), the Cauchy (c) and the Bessel (d) correlation functions. The sill and range parameters are $c_1 = c_2 = 1$ while the smooth parameters are given in the legends. From Ribatet (2009).

is chosen from the following valid correlation functions:

$$\textbf{Whittle-Matern:} \quad \rho(h) = c_1 \frac{2^{1-\nu}}{\Gamma(\nu)} \left(\frac{h}{c_2} \right)^\nu K_\nu \left(\frac{h}{c_2} \right), \nu > 0$$

$$\textbf{Cauchy:} \quad \rho(h) = c_1 \left[1 + \left(\frac{h}{c_2} \right)^2 \right]^{-\nu}, \nu > 0$$

$$\textbf{Powered Exponential:} \quad \rho(h) = c_1 \exp \left[- \left(\frac{h}{c_2} \right)^\nu \right], 0 < \nu \leq 2$$

$$\textbf{Bessel:} \quad \rho(h) = c_1 \left(\frac{2c_2}{h} \right) \Gamma(\nu + 1) J_\nu \left(\frac{h}{c_2} \right), \nu > \frac{p-2}{2} \quad (3.16)$$

where $c_2 > 0$ and ν are the range and the smooth parameters of the correlation function. Γ is the gamma function and J_ν and K_ν are the Bessel and the modified Bessel functions of the third kind with order ν and p is the dimension of the random fields.

Fig. 3.18 is a plot of these different correlation functions for different values of the parameters. Fig. 3.19 represents two realizations of Schlather MSP with the powered exponential and Whittle-Matern correlations functions.

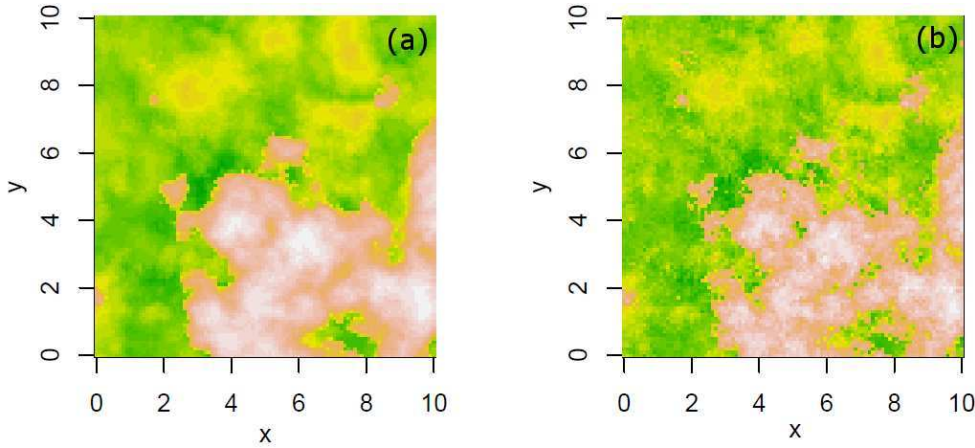


Figure 3.19: Two simulations of the Schlather model with different correlation functions having approximately the same practical range. (a) Whittle-Matern with $c_1 = c_2 = \nu = 1$. (b) Powered exponential with $c_1 = \nu = 1$ and $c_2 = 1.5$. The max-stable processes are transformed to unit Gumbel margins for viewing purposes. From Ribatet (2009).

Brown-Resnick MSP The Brown-Resnick model (Brown and Resnick, 1977), generalized by Kabluchko et al. (2009) is defined as:

$$Z(x) = \max_i (\xi_i \exp(W_i(x) - \sigma^2(x)/2)) \quad x \in \mathcal{X}, \quad (3.17)$$

where ξ_i is a Poisson process on \mathbb{R}^{**} of intensity $\frac{1}{\xi^2} d\xi$ and W_i are independent Gaussian fields, with stationary increments, variance $\sigma^2(x)$ and variogram $\gamma(h)$.

The expression of the bivariate cumulative distribution function (CDF) is nearly the same as for the Smith MSP [Eq. (3.13)]:

$$P(Z(x_1) \leq z_1, Z(x_2) \leq z_2) = \exp \left[-\frac{1}{z_1} \Phi \left(\frac{d}{2} + \frac{1}{d} \log \frac{z_2}{z_1} \right) - \frac{1}{z_2} \Phi \left(\frac{d}{2} + \frac{1}{d} \log \frac{z_1}{z_2} \right) \right], \quad (3.18)$$

except that the Mahalanobis distance a is replaced by $d = \sqrt{2\gamma(h)}$. Fig. 3.20 shows realizations of Brown-Resnick MSPs with a power variogram $\gamma(h) = \|h\|^\alpha$ for different values of α .

Extremal coefficient

Spatial dependence of maxima at two locations x and x' is characterized by the extremal coefficient denoted $\theta(x, x')$. If Z^* is the limiting process of maxima with unit Fréchet margins, then (Brown and Resnick, 1977):

$$\begin{aligned} P(Z^*(x) \leq z, Z^*(x') \leq z) &= P(Z^*(x) \leq z)^{\theta(x, x')} \\ &= \exp(-\theta(x, x')/z) \end{aligned} \quad (3.19)$$

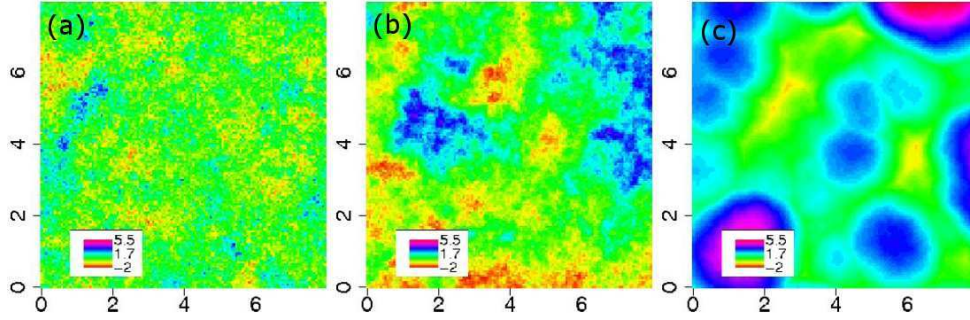


Figure 3.20: Three simulations of the Brown-Resnick model with a power variogram $\gamma = \|h\|^\alpha$. (a) $\alpha = 0.4$, (b) $\alpha = 1.0$, (c) $\alpha = 1.95$. The max-stable processes are transformed to unit Gumbel margins for viewing purposes. From Schlather (2010).

Thus, if $\theta(x, x') = 1$ there is perfect dependence of the maxima at stations x and x' and, on the contrary, if $\theta(x, x') = 2$ the maxima are independent. For Smith, Schlather and Brown-Resnick models the extremal coefficient can be calculated explicitly. According to these models, the processes are stationary, and the related extremal coefficient only depends on $h = x - x'$. The Smith's model extremal coefficient θ_{Sm} is given by:

$$\theta_{Sm}(h) = 2\Phi(a(h)/2), \quad (3.20)$$

with $a(h) = (h^t \Sigma h)^{1/2}$ the Mahalanobis distance, Σ a covariance matrix with three parameters σ_{11} , σ_{12} , σ_{22} and Φ the cumulative normal distribution.

The Schlather's extremal coefficient θ_{Sc} is given by:

$$\theta_{Sc}(h) = 1 + \sqrt{1 - \frac{1}{2}(\rho(\|h\|) + 1)} \quad (3.21)$$

with $-1 \leq \rho(\|h\|) \leq 1$, a valid correlation function (Wittle-Matern, Cauchy, exponential, Bessel ...). In our study, we generally used the exponential correlation function $\rho(h) = \exp(-\|h\|/c_1)$ where c_1 is the range parameter.

Finally, the Brown-Resnick's extremal coefficient θ_{BR} is given by:

$$\theta_{BR}(h) = 2\Phi\left(\sqrt{\frac{\gamma(\|h\|)}{2}}\right). \quad (3.22)$$

The behaviour of the extremal coefficient may give an indication for the choice of the model. For instance, the Schlather's MSP cannot achieve full independence ($\theta = 2$). This can be useful for applications with extremal dependence that remains strong even at very important distances, but is a major flaw in other cases. Instead, the Smith's MSP imposes full independence at long distances ($\theta_{Sm} \xrightarrow{\infty} 2$) but is quite rigid at short distances. The Brown-Resnick's MSP is more flexible as the variogram may take a great variety of shapes near 0 and allows for full independence ($\theta_{BR} \xrightarrow{\infty} 2$) at long distances [Eq. (3.22)].

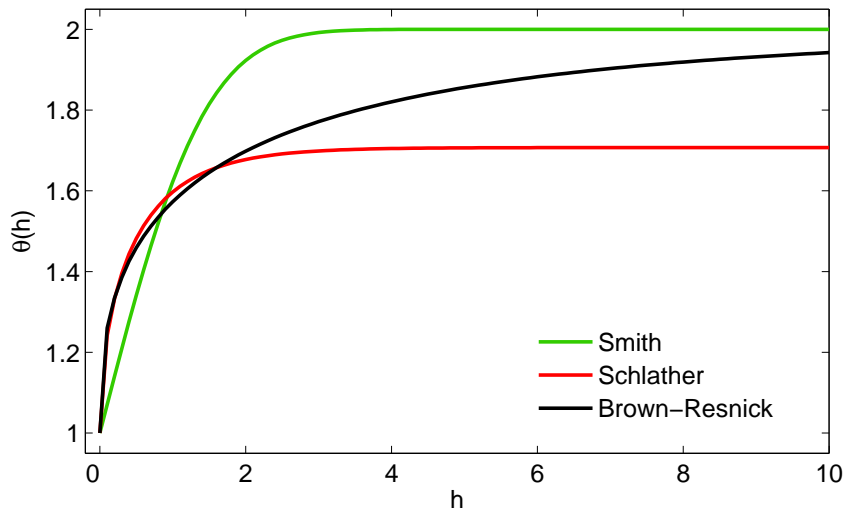


Figure 3.21: Example of extremal coefficients of Smith, Schlather and Brown-Resnick MSPs.

The Smith's MSP can directly model the anisotropy in the extremal coefficient by using a modified distance (Mahalanobis), function of the covariance matrix Σ . As already noted before, this covariance matrix plays a very important role because it determines the elliptical shape of the extremal dependence. On the contrary, Schlather's and Brown-Resnick's MSP are primarily isotropic as they involve the Euclidean distance. Thus, to take into account possible directional effects in the case of Schlather's and Brown-Resnick's MSP, we must modify the standard space (Ribatet, 2009; Blanchet and Lehning, 2010) while inferring the extremal dependence. To do this, we set $\tilde{E} = VE$ with $E = [x \ y]^t$ the Euclidean coordinates in 2D for instance and V the rotation matrix defined below:

$$V = \begin{pmatrix} \cos \psi & \sin \psi \\ -\rho \sin \psi & \rho \cos \psi \end{pmatrix}, \quad (3.23)$$

where ψ represents the anisotropy angle of the transformation and ρ its intensity.

3.5.2 Likelihood-based inference

Composite likelihood

In order to fit a max-stable process to data, likelihood maximisation is used. However, we cannot calculate the complete likelihood since we only know analytically the expression of the different bivariate distributions according to Eqs. ((3.13),(3.15),(3.18)). Padoan et al. (2009) showed that, for MSP, the full log-likelihood can be advantageously replaced by a special case of composite likelihood (Lindsay, 1988): the pairwise log-likelihood l_p defined

as:

$$l_p(\beta, z) = \sum_{n=1}^N \sum_{i=1}^K \sum_{j=i+1}^{K-1} \log f(z_{n,i}, z_{n,j}; \beta), \quad (3.24)$$

with z the data available on the whole region, N the number of observations (typically the number of years of measurements), K the number of measurement stations, β the vector of parameters to estimate and f the bivariate density of the unit Frechet MSP used (Smith, Schlather or Brown-Resnick). In the case of annual block maxima data, $z_{n,i}$ represents the annual maximum of the quantity to be analyzed for year n and station i . One can then find the parameters $\hat{\beta}$ that maximize the composite likelihood by solving the partial differential equation:

$$\frac{\partial}{\partial \beta} l_p(\hat{\beta}, z) = 0. \quad (3.25)$$

Under appropriate conditions (Lindsay, 1988; Ribatet, 2009) the maximum composite likelihood estimator is consistent and asymptotically ($n \rightarrow \infty$) distributed as $\hat{\beta}_{MCLE} \xrightarrow{n \rightarrow \infty} N(\hat{\beta}, H(\hat{\beta})J(\hat{\beta})^{-1}H(\hat{\beta}))$, where $H(\hat{\beta})$ and $J(\hat{\beta})$ are the Hessian and Jacobian information matrices of l_p .

Under the pairwise setting for extreme, one can derive the associate standard errors from H and J estimated by:

$$H(\hat{\beta}) = - \sum_{n=1}^N \sum_{i=1}^K \sum_{j=i+1}^{K-1} \frac{\partial^2 \log f(z_{n,i}, z_{n,j}; \hat{\beta})}{\partial \beta \partial \beta^t}, \quad (3.26)$$

and

$$J(\hat{\beta}) = \sum_{n=1}^N \sum_{i=1}^K \sum_{j=i+1}^{K-1} \frac{\partial \log f(\hat{\beta}, z_i)}{\partial \beta} \frac{\partial \log f(z_{n,i}, z_{n,j}; \hat{\beta})}{\partial \beta^t}. \quad (3.27)$$

Model selection: TIC

To compare different models, a criterion weighting the value of the likelihood by the number of model parameters to estimate can be used. The classic AIC (Akaike Information Criterion Akaike, 1981) cannot be applied when composite likelihood maximisation is used. A derivative of AIC suitable for composite likelihood is the TIC (Takheuchi Information Criterion) (Takeuchi, 1976):

$$\text{TIC}(\hat{\beta}) = -2l_p(\hat{\beta}, z) + 2\text{tr} \left(J(\hat{\beta})H(\hat{\beta})^{-1} \right), \quad (3.28)$$

The best model is the one that minimizes the TIC [Eq. (3.28)]. Composite likelihood maximisation and TIC computations can be carried out under the SpatialExtreme R package (Ribatet, 2009).

Chapter 4

Influence of weak layer heterogeneity on snow slab avalanche release

4.1 Application to the evaluation of avalanche release depth

This section is composed of an article entitled “Influence of weak layer heterogeneity on snow slab avalanche release: Application to the evaluation of avalanche release depths.” which was **submitted** to *Journal of Glaciology* with the contribution of Guillaume Chambon, Nicolas Eckert and Mohamed Naaim.

The objective of this article is to compute avalanche release depth distributions from a mechanically-based statistical model. To do so, a shear-softening interfacial weak layer underlying an elastic slab is modeled and the system is loaded by increasing the slope angle until failure and avalanche release. We first study the influence of a single weak spot in the weak layer in order to validate the model against analytical solutions. The interaction between two weak spots is also examined. The case of heterogeneous weak layers represented through Gaussian distributions of the cohesion with a spherical spatial covariance is then studied. The obtained release angle distributions are analyzed and a heterogeneity smoothing effect due to redistributions of stresses by elasticity of the slab is highlighted. This smoothing effect induces a reduction of the release angle variance compared to the case of a fully rigid slab. The obtained release angle distributions are then inverted, yielding a release depth distribution integrated over all slopes. A coupling with extreme snowfall distributions is performed and a sensitivity analysis of the final distributions to the mechanical parameters is done. Note that the coupling equation presented in this paper is an approximation of the formal coupling equation presented in more details in Chapter 6 (paper published in *Geophysical Research Letters*).

Influence of weak-layer heterogeneity on snow slab avalanche release: Application to the evaluation of avalanche release depths.

Johan GAUME,¹ Guillaume CHAMBON,¹ Nicolas ECKERT,¹ Mohamed NAAIM¹

¹*Irstea, UR ETNA, 2 rue de la Papeterie, 38400 St Martin d'Heres.
E-mail: johan.gaume@gmail.com*

ABSTRACT. The evaluation of avalanche release depths constitutes a great challenge for risk assessment in mountaineous areas. This study focuses on slab avalanches which generally result from the rupture of a weak layer underlying a cohesive slab. We use the finite element code Cast3M to build a mechanical model of the slab-weak layer system taking into account two key ingredients for the description of avalanche releases: weak-layer heterogeneity and stress redistribution via slab elasticity. The system is loaded by increasing the slope angle until rupture. We first examine the cases of one single and two interacting weak spots in the weak layer in order to validate the model. We then study the case of heterogeneous weak layers represented through Gaussian distributions of the cohesion with a spherical spatial covariance. Several simulations for different realizations of weak layer heterogeneity are carried out and the influence of slab depth and heterogeneity correlation length on avalanche release angle distributions is analyzed. We show in particular a heterogeneity smoothing effect caused by slab elasticity. Finally, this mechanically-based probabilistic model is coupled with extreme snowfall distributions. A sensitivity analysis of the predicted distributions enables to determine the values of mechanical parameters providing the best adjustment to field data.

1. INTRODUCTION

The evaluation of avalanche release depths is of major importance for all the applications related to hazard mapping or zoning. In particular, avalanche release depths represents a crucial input ingredient for dynamical runout models (Barbolini and others, 2000; Naaïm and others, 2003) and are required for implementing statistical-dynamical simulations (Meunier and Ancey, 2004; Eckert and others, 2010). It has been shown in different studies (Hutter, 1996; Bartelt and others, 1999; Jamieson and others, 2008) that the outputs of these models in terms of run-out distances and impact forces are strongly dependent on the release mass, as well as on other ingredients such as friction, deposition and erosion.

It is commonly accepted that dry-snow slab avalanches are initiated by a shear failure in a weak-snow layer (or at a weak interface) followed by tensile crown failure of the overlying slab (McClung, 1979; Schweizer and others, 2003). The shear failure is caused by a local loss of cohesion inside the weak layer that may be due to (1) a localized surface loading such as skiers or explosives (artificial release), (2) uniform loading due to a new snowfall (natural release), or (3) changes in the snowpack properties due to weather changes (natural release).

Most of the existing avalanche release models are based on the assumption first made by Palmer and Rice (1973) for an overconsolidated clay and then taken up for snow by McClung (1979) that a weak spot or shear band, i.e. a zone of zero shear strength, pre-exists inside the weak layer. Fracture mechanics is then applied to study the conditions for shear-band propagation. Based on an energy budget at the tip of the band, the rapid propagation occurs when a critical length is reached after a phase of slow strain softening.

Schweizer (1999) produced a complete review of these fracture mechanics models and gave critical length values as a function of snow characteristics. More recently, Chiaia and others (2008) showed that a simple stress failure criterion coming from equilibrium equations could also be sufficient to predict shear-band propagation with a good accuracy. Nevertheless, as already noted by Schweizer (1999), the very concept of weak-spot is questionable since, even if we can imagine how local weak zones could appear (for instance around rocks, where the snow depth is reduced and thus the temperature gradient is increased), it is probably too simplistic, in general, to represent the complex heterogeneity of weak-layer mechanical properties.

Several studies (Conway and Abrahamson, 1988; Jamieson and Johnston, 2001; Birkeland and others, 2004; Kronholm, 2004; Schweizer and others, 2008; Bellaire and Schweizer, 2011) have shown that snow mechanical properties present considerable spatial variability. From field data, this variability is generally described as following Gaussian distributions with spatial correlations. Hence, the concept of weak-spot may be replaced by mechanical models taking into account spatial stochastic processes to represent the heterogeneity. Such models would not only explain failure initiation in weak zones, but also fracture arrest in stronger zones (Schweizer, 1999). Recently, several studies attempted to include this heterogeneity in mechanical models. These studies can be classified as follows, according to the numerical method used:

(i) Fiber Bundle Models (FBM) are simple statistical fracture models that are well adapted for representing spatially heterogeneous systems, including possibly time-dependent effects such as sintering. Using this framework, Reiweger and

others (2009) model the weak snow layer as a discrete set of parallel brittle-elastic fibers. Spatial variability is accounted for by assigning to each fiber an initial strength taken within a Weibull distribution. Despite the simplicity of the model, these authors are able to quantitatively reproduce laboratory shearing experiments on homogeneous snow samples. However, complex stress redistribution effects by elasticity of the slab cannot be taken into account in such models, which are therefore unable to reproduce full-scale avalanche release.

(ii) Cellular-Automata Models (CAM) consist of a regular grid of cells characterized by a state that can change over time and as a function of the neighboring cells' state. Fyffe and Zaiser (2004, 2007) and Kronholm and Birkeland (2005) applied such approach to slab avalanche release with a heterogeneous shear strength of the weak layer represented by Weibull or Gaussian distributions. Via neighboring elements their models account for stress redistribution between weak and strong regions. They also included mode-II (shear) rupture of the weak layer with a strain-softening law, and mode-I (tensile) rupture of the slab as in Failletaz and others (2004). These studies demonstrated the influence of spatial variability characteristics (variance, nugget effect, etc) on release depth distributions. Fyffe and Zaiser (2007) were also able to reproduce (under certain conditions) release depth distributions following power laws, as in field studies (Rosenthal and Elder, 2002; McClung, 2003; Failletaz and others, 2004). However, stress elastic redistribution effects are oversimplified in these models whose applicability is limited to the case of a shear strength correlation length lower than the slab depth.

(iii) Finite Element Models (FEM) rely on the resolution of the complete mechanical equations of the problem. One of the main advantages of FEM compared to CAM is that it is able to capture large-scale stress redistribution effects due to elasticity. FEM has already been successfully applied to modeling the mechanical response of sandwich specimens including weak-snow layers with homogeneous properties (e.g. Bader and Salm, 1990; Stoffel, 2005; Mahajan and Joshi, 2008; Mahajan and others, 2010). However, only few studies coupled FEM with a stochastic representation of the spatial variability. Recently, such a model has been introduced by Griffiths and Fenton (2004) to study soil stability. To our knowledge, the same type of approach has never been undertaken for snow.

In addition, some recent studies (Johnson and others, 2004; van Herwijnen and Heierli, 2009) relying on field data show that the shear failure of the weak layer tend to be systematically accompanied by a normal collapse. These authors argued that slope normal and slope parallel displacements occur simultaneously during release. Anticrack analytical models have been developed and proved capable of reproducing these data (Heierli and Zaiser, 2007; Heierli and others, 2008). However, the issue of the influence of normal collapse on avalanche release is still a matter of debate. Some authors (Jamieson and Schweizer, 2000; Johnson and others, 2004) suggest that the simultaneous occurrence of weak-layer collapse and shear failure may facilitate fracture propagation due to bending effects. McClung (2011), on the contrary, showed that a model that does not account for slope-normal failure can reasonably reproduce critical length measurements obtained in field saw-cut tests. Hence, he argued that the slope-parallel propagation is very little influenced by the interaction between slope-normal displacement and stress. In the present study, the effect of normal collapse is not considered.

The present paper uses a finite element method to build a mechanically-based probabilistic model of the slab-weak layer system taking into account the two key ingredients mentioned above, namely the redistribution effects by elasticity of the slab and the heterogeneity of weak-layer mechanical properties. The objective of this study is the evaluation of avalanche release depth statistical distributions, distributions that could be later coupled to propagation models for hazard mapping and zoning. In sections 2 and 3, we present the considered system and validate the model using the well-known weak-spot case. This validation is also used to highlight a characteristic length of the system associated to the elastic redistribution of stresses. In section 4, results obtained with a realistic spatial heterogeneity based on field data are presented. We analyze in particular how slab stability depends on slab depth and on the spatial correlation length of weak-layer properties. Finally, in section 5, the obtained release depth distributions are combined with snowfall extreme value distributions and compared to field data of avalanche crown depths.

2. MECHANICALLY-BASED PROBABILISTIC MODEL

2.1. Objectives

As already mentioned, the objective of the model developed in this study is the evaluation of probability distributions of avalanche release depths, in particular in the context of absent or scarce data. More precisely, the aim is to produce a tool capable of predicting release depth distributions that are meaningful over relatively long time scales (typically several decades), and that could be used as inputs for hazard mapping procedures such as statistical-dynamical approaches (Keylock and others, 1999; Eckert and others, 2008, 2010). Hence, the objective is not to develop a complete mechanical model of slab avalanche release accounting for all the complex processes at play. Both the geometry and the mechanical behavior of the system will be drastically simplified such as to reduce the number of poorly-known parameters, while keeping the ingredients essential to describe the mechanics of slab release. Moreover, to be compared with field data, the predictions of this model will then need to be coupled with a description of snowfall distributions, as shown in Gaume and others (2012). In the present paper, we focus only on the formulation and validation (numerical consistency) of the mechanical part of the model. In the last section, however, the sensitivity of the predicted distributions (after coupling with snowfalls) to several mechanical parameters is presented.

2.2. Formulation of the model

The model is based on the finite element code Cast3m (Verpeaux and others, 1988). The resolution procedure used ("Pasapas" Charras and Di Paola, 2011) enables considering non linear models with an implicit integration scheme based on the weighted residuals method. The momentum conservation equations, including inertial terms, are solved under the small deformations hypothesis:

$$\underline{M} \cdot \ddot{\underline{u}} + \underline{D} \cdot \dot{\underline{u}} + \text{div} \cdot (\underline{\sigma}) = \underline{F}, \quad (1)$$

$$\underline{\epsilon} = \frac{1}{2} \left(\underline{\text{grad}}(\underline{u}) + \underline{\text{grad}}^t(\underline{u}) \right), \quad (2)$$

with \underline{M} the mass matrix, \underline{u} the node displacement vector, $\underline{\sigma}$ the stress tensor, $\underline{\epsilon}$ the deformation tensor, \underline{F} the integrated

Parameter	Typical value	Range	Reference
Slab density ρ	250kg/m ³	100 – 300kg/m ³	Schweizer (1999)
Slab Young modulus E	1MPa	0.2 – 12MPa	Schweizer (1999)
Slab Poisson ratio ν	0.2	0.1 – 0.4	Schweizer (1999)
Slab viscosity η	10 ⁸ Pa.s	0.2 – 5 × 10 ⁸ Pa.s	Mellor (1975); Camponovo (1998)
W. l. cohesion c	1kPa	0.5 – 2.5kPa	Föhn and others (1998); Jamieson and Johnston (2001)
W. l. friction angle Φ	30°	20 – 40°	De Montmollin (1978); van Herwijnen and Heierli (2009)
W. l. displacement to failure u_p	2mm	1 – 10mm	McClung (1977)
W. l. residual displacement u_r	4mm	1 – 10mm	McClung (1977)
Correlation length ϵ of w.l. cohesion variations	0.5 – 40m	0.5 – 10m	Schweizer and others (2008)
Coefficient of variation $CV = \sigma_c / \langle c \rangle$	30%	15 – 50%	Schweizer and others (2008)

Table 1. Mechanical parameters used in this study and typical ranges of variation. (w.l.: weak layer)

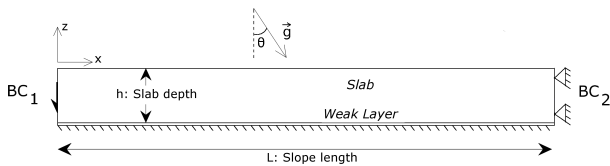


Fig. 1. Geometry of the system: a weak layer interface under a cohesive slab of depth h .

force vector at nodes and \underline{D} the damping matrix. In our study, the matrix \underline{D} is taken as zero.

The system considered is a 2D (plane stress conditions) uniform slope inclined at an angle θ , of length $L = 50\text{m}$ (Fig. 1). The x -axis is in the slope-parallel direction and the z -axis is orthogonal to the slope. The system consists of a slab of thickness h overlying a weak layer modeled as an interface of zero thickness. The mesh is composed of 100 elements in the slope-parallel direction x , and six elements in direction z . We used quadrilateral elements for the slab (QUA4: four nodes with 2 dof/node) and joint elements for the weak layer interface (JOI2: four nodes with 2 dof/node). We checked that the mesh resolution is fine enough so that it does not influence the results to be presented (see in particular section 3.1).

The boundary conditions applied to slab are the following: At the upper end of the slope ($BC1$) a shear stress $\sigma_{xz} = -\rho g(z + h) \sin \theta$ is applied in order to avoid bending of the slab linked to finite size effects. At the lower end ($BC2$), a nil displacement in slope-parallel direction x is imposed. The upper surface of the slab is free and the base is subjected to an interface law, i.e. a law relating shear stress to tangential displacement, which represents the weak layer.

2.3. Constitutive relationships

Snow is a very complex material whose mechanical behavior is still not fully understood. In the present model, only the ingredients necessary to produce realistic instability of the system, namely strain-softening of the weak layer and elasticity of the slab, are taken into account. Table 1 summarizes

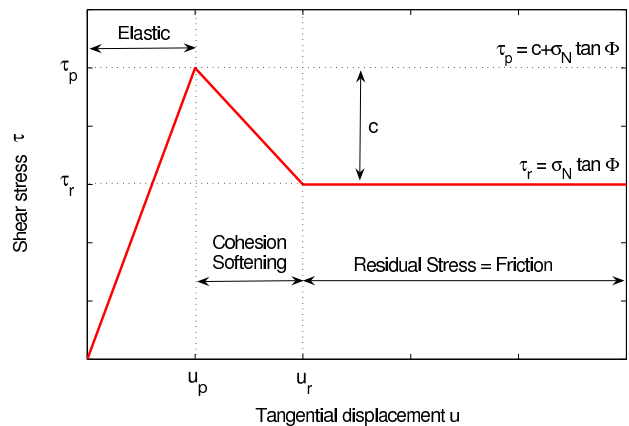


Fig. 2. Weak layer constitutive law.

the value of the different mechanical parameters used in this study.

Weak Layer

Various studies (McClung, 1979; Föhn and others, 1998; McClung and Schweizer, 2006) have shown that weak snow layers behave as strain-softening (or quasi-brittle) materials. The softening is caused by the break of ice bridges at the microscopic scale. In existing mechanical models (McClung, 1979; Bazant and others, 2003; Fyffe and Zaiser, 2004, 2007; Mahajan and Joshi, 2008; Mahajan and others, 2010; Gaume and others, 2011), weak layers are generally characterized by a rupture displacement u_p and a critical softening displacement δ . The pre-peak behavior is considered to be elastic, but stiffness values are very difficult to obtain since these layers are generally very thin and unstable.

In the present study, the weak layer is modeled as a displacement-softening interface with a simple, linear piecewise relationship between shear stress τ and tangential displacement u (Fig. 2). The value of the shear stress peak τ_p is governed by the Mohr-Coulomb criterion: $\tau_p = c + \sigma_n \tan \Phi$, with c the weak layer cohesion, σ_n the normal stress and Φ the friction angle. The friction angle has been chosen as constant $\Phi = 30^\circ$ (De Mont-

mollin, 1978; van Herwijnen and Heierli, 2009) and the cohesion c is spatially heterogeneous, as will be described below. The tangential stiffness of the weak layer during the pre-peak phase is given by $k_s = \tau_p/u_p$ (Fig. 2). After the peak, the shear stress decreases (shear softening) until reaching a residual value $\tau_r = \sigma_n \tan \Phi$. This residual value corresponds to the situation where ice bridges are completely broken and only the friction between the slab and the underlying layer remains. Following McClung (1977), both the characteristic peak and softening displacement u_p and δ are taken equal to 2mm (see also Bazant and others, 2003; Fyffe and Zaiser, 2004, 2007). Hence, the displacement to reach residual stress $u_r = u_p + \delta = 4\text{mm}$. Note that, according to recent studies (McClung, 2009, 2011), the softening displacement δ under high loading rates actually tends to be smaller than the value assumed in this study, in the 0.1–0.3 mm range. However, as will be shown later, the precise value of this parameter does not influence the outcomes of our model.

Slab

At high loading rates such as those characteristic of slab avalanche release, laboratory experiments (Mellor, 1975; McClung, 1977; Narita, 1980; Navarre and others, 1992; Schweizer, 1998) and field measurements (Roch, 1965; De Montmollin, 1978; Jamieson and Johnston, 1990; Föhn and others, 1998; McClung and Schweizer, 2006) have shown that cohesive snow behaves as a brittle-elastic material. In the present study, as will be explained below (see section 2.6), the possible tensile rupture of the slab is not directly modeled. Therefore, the mechanical behavior of the slab is modeled by an isotropic elastic law:

$$\underline{\underline{\epsilon}} = \frac{1}{E}\underline{\underline{\sigma}} - \frac{\nu}{E}(\text{tr}(\underline{\underline{\sigma}}) - \underline{\underline{\sigma}}) \quad (3)$$

where E is the Young modulus and ν the Poisson ratio. The following values have been used: $E = 1\text{MPa}$, $\nu = 0.2$, and $\rho = 250\text{kg.m}^{-3}$ for the slab density. In addition, in order to stabilize the computations, it has been necessary to slightly enrich the above constitutive law by the addition of a viscous term. All viscosity values within the range $10^4 - 10^9\text{Pa.s}$ have been found to yield satisfactory results. We retained the value $\eta = 10^8\text{Pa.s}$ which is in agreement with real snow viscosity measurements (Mellor, 1975; Camponovo, 1998; Schweizer, 1999).

2.4. Spatial heterogeneity

The spatial heterogeneity of the weak layer is modeled through a stochastic distribution of cohesion c . Following Jamieson and Johnston (2001) and Kronholm and Birkeland (2005), we consider a Gaussian distribution of average $\langle c \rangle$ and standard deviation σ_c , with a spherical covariance function $\mathcal{C}(d)$:

$$\mathcal{C}(d) = \sigma_c^2 \left(1 - \frac{3d}{2\epsilon} + \frac{1}{2} \left(\frac{d}{\epsilon} \right)^3 \right) \mathcal{I}_{[0,\epsilon]}(d), \quad (4)$$

where d is the distance between two points, ϵ is the spatial correlation length and the $\mathcal{I}_{\mathcal{A}}(d)$ function is 1 if $d \in \mathcal{A}$, 0 otherwise. The correlation length ϵ represents the distance over which the cohesion values are significantly correlated. Note that in the present model, no nugget effect is considered (i.e. $\mathcal{C}(d) \rightarrow 0$ when $d \rightarrow 0$). The effect of the nugget on avalanche size has been investigated by Kronholm and Birkeland (2005) using a CAM model.

Fig. 3 shows examples of cohesion field realizations with different values of the correlation length ϵ . These fields were generated using the turning bands method (Chilès and Delfiner,

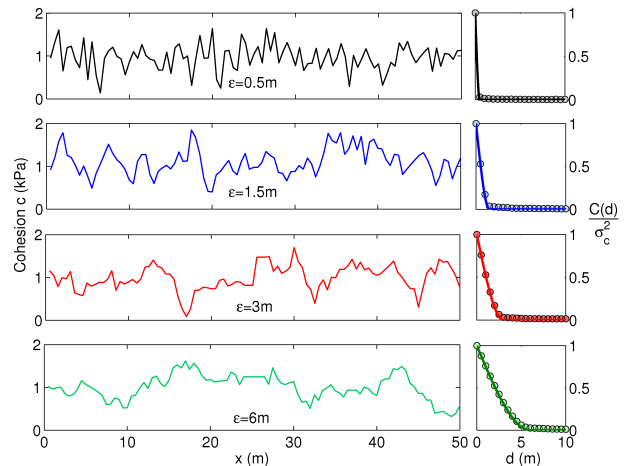


Fig. 3. Left: Examples of the heterogeneity of the cohesion for different values of the correlation length ϵ . Right: Comparison between the empirical normalized covariance function of the cohesion fields (computed from 100 independent realizations: circles) and the theoretical expression given by Eq. (4) (lines).

1999) and we checked that, with the used mesh size, the obtained empirical covariance functions are in good agreement with the predictions of Eq. (4) for all the values of ϵ investigated. Existing studies are not conclusive on the typical correlation length scale (Jamieson and Johnston, 2001; Schweizer and others, 2008; Bellaire and Schweizer, 2011) relevant for weak-snow layers. Schweizer and others (2008) recommended spacing out snow pits at least 10m apart in order to have independent results, thus suggesting that the correlation length ϵ varies approximately within the 0.5–10m range. In our study, ϵ was varied between 0.5 and 40m (the lower limit $\epsilon = 0.5\text{m}$ being imposed by our mesh size), but due to finite size effects, only the results with $\epsilon \leq 10\text{m}$ can be cross compared (for $\epsilon > 10\text{m}$, the average cohesion $\langle c \rangle$ begins to evolve with ϵ). Lastly, the average cohesion $\langle c \rangle$ was taken equal to 1kPa and cohesion standard deviation σ_c to 0.3kPa.

2.5. Loading

Gravity is the only applied external force and the system is loaded by progressively increasing the slope angle θ at constant slab depth until rupture. As will be shown, this loading procedure is equivalent to a progressive increase of the slab depth h at constant slope angle. The loading curve is represented in Fig. 4. After an initial stage during which gravity is increased from zero to 9.81m.s^{-2} , the loading is applied in two phases (Fig. 4). First, the slope angle is increased from zero to $\theta_1 = \Phi = 30^\circ$ with a fast loading speed of 0.4° per time-step since no failure can occur during this stage ($\tau < \tau_p$). Then, the loading speed is reduced to 0.04° per time-step until rupture occurs. We checked that, with this two-phase procedure, the chosen loading speed values do not influence the results to be presented. This simple loading is sufficient to study avalanche releases triggered by a progressive accumulation of snow. We emphasize that our model is not meant to account for the slow processes (snow metamorphism, viscous stress redistributions) active during the formation of the snowpack.

2.6. Rupture mechanism

Avalanche releases observed in our simulations are always induced by a local shear rupture inside the weak layer, which

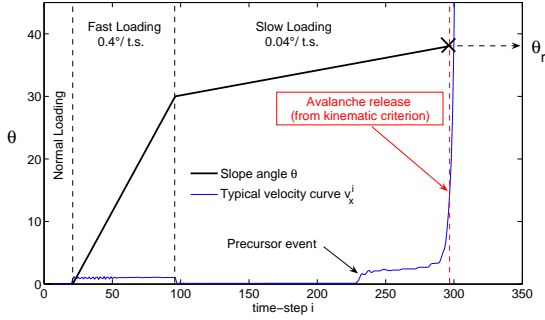


Fig. 4. Applied loading curve. The time-step value is 0.1s. The blue curve represents a typical velocity evolution showing a marked precursor event.

then propagates to both extremities of the slope. With reference to real avalanche releases, this would correspond to the case where the weak layer heterogeneity is not sufficient to induce a tensile rupture within the slab, and slab rupture is thus triggered by morphological features such as ridges, slope breaks, rocks, trees, or other defects within the slab. We also performed simulations using a brittle-elastic constitutive law for the slab. These simulations showed that for a realistic tensile strength value $\sigma_t = 2\text{kPa}$ (Mellor, 1975; Jamieson and Johnston, 1990; Sigrist, 2006), effectively no tensile failure occurred within the slab (the slab remained elastic) and the rupture mechanism was identical to the one reported in this study. Note, however, that other sets of parameters may lead to tensile ruptures within the slab, which constitutes the subject of a further study (see also Gaume and others, 2011).

2.7. Avalanche release criterion

We consider that an avalanche occurs in our simulations when the following kinematic release criterion is met:

$$\text{Release} \Leftrightarrow v_x^i \geq N \times \bar{v}_x^{i,m} = \frac{N}{m} \sum_{k=1}^m v_x^{i-k}. \quad (5)$$

Hence, an avalanche is detected when the weak-layer velocity v_x^i is higher than N times the average velocity recorded over m previous time-steps $\bar{v}_x^{i,m}$. The values of $N = 10$ and $m = 10$ were chosen in order to ensure that the criterion is not sensitive to small velocity variations triggered by potential precursor events (Fig. 4), which could lead to wrong release angle values.

3. MECHANICAL VALIDATION

In this section, the finite element model presented above is validated against the classical case of release induced by a single weak spot. For this simple case, analytical solutions can be derived following the approach presented by Chiaia and others (2008). The interaction between two weak spots will also be considered in order to illustrate the influence of an important characteristic length of the system that emerges from the analysis.

3.1. A single weak spot

Analytical solution

We follow here the same approach as Chiaia and others (2008), but considering a non-zero residual stress inside the weak spot due to friction (Fig. 2). Let us consider a weak spot of

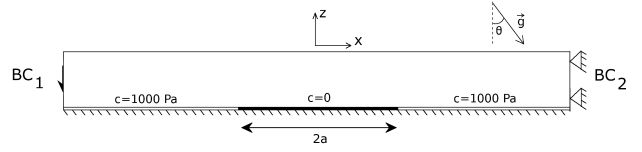


Fig. 5. Geometry of the system with one weak spot of half-length a with a nil cohesion.

nil cohesion ($c = 0$), half length a , inside a weak layer of homogeneous cohesion $c = 1\text{kPa}$ underlying a cohesive slab of depth h (Fig. 5). The equilibrium equation in the slope-parallel direction integrated over the slab depth writes:

$$\frac{\partial}{\partial x} \int_{-h}^0 \sigma_{xx} dz - \tau = -\tau_g, \quad (6)$$

with $\tau_g = \rho g h \sin \theta$ the body weight shear stress, σ_{xx} the normal stress in the slope-parallel direction and τ the shear stress in the weak layer. The shear stress τ is related to the tangential displacement u according to the interface constitutive law (Fig. 2). Two cases have to be distinguished: $\theta < \Phi$ for which the shear stress τ depends on the tangential displacement u both inside and outside the weak spot; and $\theta > \Phi$ for which the shear stress τ depends on the tangential displacement u only outside the weak spot.

Case 1: $\theta < \Phi$

For $\theta < \Phi$, the shear stress writes $\tau(x) = \tau_p u / u_p$ outside the weak spot ($|x| > a$) and $\tau(x) = \tau_{ws} = \tau_r u / u_p$ inside the weak spot ($|x| < a$). Eq. (6) and the linear elastic behavior of the slab lead to the following equation:

$$\frac{\partial^2 u}{\partial x^2} - \frac{u}{\Lambda(x)^2} = -\frac{\tau_g}{E'h}, \quad (7)$$

with $E' = E/(1 - \nu^2)$ (plane stress hypothesis) and

$$\Lambda(x) = \Lambda_{ws} = \sqrt{\frac{E'h u_p}{\tau_r}} \text{ for } |x| \leq a, \quad (8)$$

$$\Lambda(x) = \Lambda = \sqrt{\frac{E'h u_p}{\tau_p}} \text{ for } |x| > a. \quad (9)$$

Considering in addition the continuity of displacement and velocity at the interface between the weak layer and the weak spot, and the fact that the slope-parallel normal stress σ_{xx} vanishes far away from the weak spot, displacement and stress profiles can be determined by integrating Eq. (7):

Outside the weak spot ($|x| > a$):

$$\begin{cases} u(x) = \frac{\Lambda^2 \tau_g}{E'h} \left(1 - r e^{-\frac{|x|-a}{\Lambda}} \right) \\ \tau(x) = \tau_g \left(1 - r e^{-\frac{|x|-a}{\Lambda}} \right) \end{cases}, \quad (10)$$

Inside the weak spot ($|x| \leq a$):

$$\begin{cases} u(x) = \frac{\Lambda_{ws}^2 \tau_g}{E'H} \left[1 + r' \left(\alpha e^{x/\Lambda_{ws}} + \beta e^{-x/\Lambda_{ws}} \right) \right] \\ \tau(x) = \tau_g \left[1 + r' \left(\alpha e^{x/\Lambda_{ws}} + \beta e^{-x/\Lambda_{ws}} \right) \right] \end{cases}, \quad (11)$$

where expressions of the constants r , r' , α , and β are given in Appendix A.

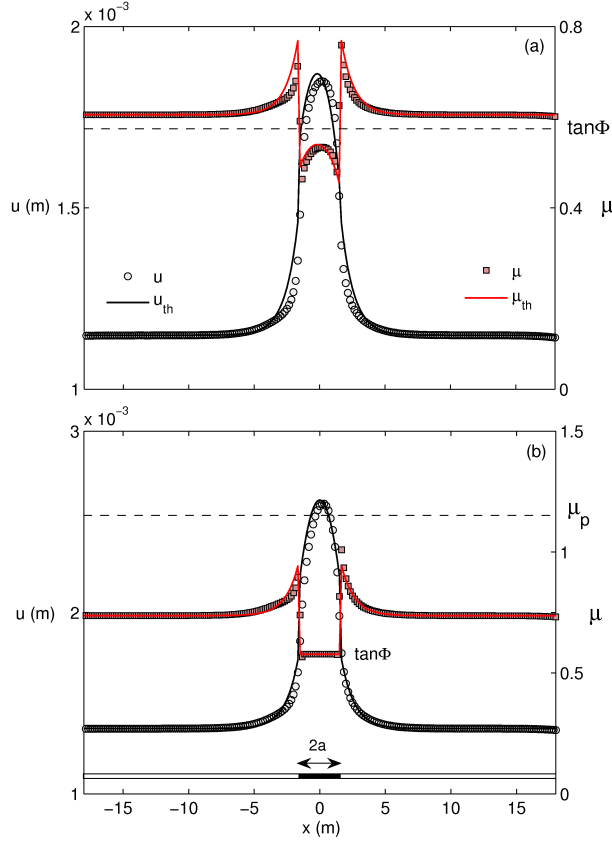


Fig. 6. (a) Displacement u and apparent friction coefficient $\mu = \tau/\sigma_n$ profiles for a slab depth $h = 1\text{m}$, a weak spot half length $a = 4.5\text{m}$, and for the case $\theta < \Phi$. Symbols: finite element results. Solid lines: Analytical model. (b) Idem for the case $\phi < \theta < \theta_r$, where θ_r is the release angle.

Case 2: $\theta > \Phi$

If $\theta > \Phi$, the shear stress inside the weak spot ($|x| \leq a$) meets the frictional criterion and thus no longer depends on displacement u : $\tau(x) = \tau_r = \sigma_N \tan \Phi$. Eq. (6) then becomes:

$$\frac{\partial^2 u}{\partial x^2} = \frac{\tau_r - \tau_g}{E'h}, \quad (12)$$

for $|x| \leq a$, and Eq. (7) remains valid for $|x| > a$. Similarly to the previous case, the displacement and stress profiles can be determined again:

Outside the weak spot ($|x| > a$):

$$\begin{cases} u(x) = \frac{\Lambda^2 \tau_g}{E'h} \left(1 - r_2 e^{-\frac{|x|-a}{\Lambda}} \right) \\ \tau(x) = \tau_g \left(1 - r_2 e^{-\frac{|x|-a}{\Lambda}} \right) \end{cases}, \quad (13)$$

Inside the weak spot ($|x| \leq a$):

$$\begin{cases} u(x) = \frac{\Lambda^2 \tau_g}{E'h} \left[\frac{1}{2} \frac{\Lambda}{a} r_2 \left(\left(\frac{x}{\Lambda} \right)^2 - \left(\frac{a}{\Lambda} \right)^2 \right) + 1 - r_2 \right] \\ \tau(x) = \tau_r \end{cases}, \quad (14)$$

where expression of the constant r_2 is given in Appendix A.

We note that both the shear stress and the displacement present decreasing exponential profiles outside of the weak spot [Eqs. (10) and (13)]. The characteristic length associated with these exponential decreases is the parameter Λ which

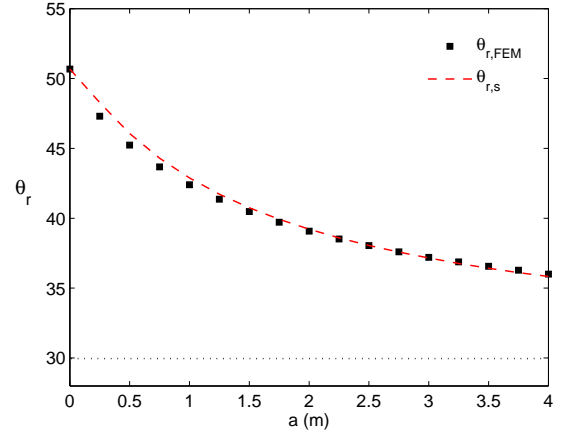


Fig. 7. Evolution of the release angle θ_r as a function of the half-length a of the weak spot. Black squares: Finite element results. Red dashed line: theoretical stress rupture threshold.

depends both on the slab and weak layer characteristics [Eq. (9)]. Far from the weak spot ($|x| - a \gg \Lambda$), the shear stress tends to its body weight value τ_g and the displacement tends to $u = u_p \tau_g / \tau_p$ (elastic behavior).

The shear band becomes unstable when the maximum stress τ_{max} at $|x| = a$ reaches $\tau_p = c + \sigma_N \tan \Phi$. Using Eq. (13), the theoretical critical stress $\tau_{g,s}$ for weak spot propagation can thus be expressed as follows:

$$\tau_{g,s} = \frac{1}{1 + \frac{a}{\Lambda}} \left[c + \sigma_N \tan \Phi \left(1 + \frac{a}{\Lambda} \right) \right]. \quad (15)$$

From this expression, the critical release angle $\theta_{r,s}$ can then be derived using:

$$\tau_{g,s} = \rho g h \sin \theta_{r,s}. \quad (16)$$

Comparison with simulations

As shown in Figs. 6a and 6b the overall agreement between theoretical predictions and FEM numerical results is very satisfactory, both for $\theta < \Phi$ and for $\theta > \Phi$. In particular, the stress concentration at the weak spot tip and the exponential decrease of stress outside of the weak spot are very well reproduced. Similarly, the displacement profiles, which present a maximum at the center of the weak spot, are also well captured. Note, however, that the numerical model indicates the existence of slight variations with x of the normal stress σ_n that are not accounted for in the theoretical analysis.

Fig. 7 shows a comparison between the release angles obtained by the FEM calculations and those predicted by the stress rupture criterion [Eqs. (15)–(16)]. Here also, the agreement between the theory and numerical results is excellent for all values of weak-spot half-lengths. This agreement also holds for all tested values of slab depth h . Globally, the results shown in Figs. 6 and 7 constitutes a validation of the various mechanical ingredients taken into account in our finite element model. In particular, these results prove that the used mesh size is fine enough to account for cohesion heterogeneities with typical length scales (in this case, the weak-spot half-length) as small as 0.5 m.

3.2. Two weak spots

In order to illustrate the influence of the characteristic length Λ introduced above, we conducted simulations to investigate

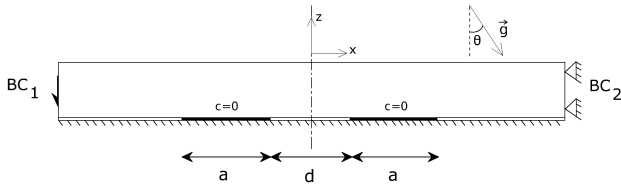


Fig. 8. Geometry of the system with two weak spots of length a separated by a distance d .

the interaction between two weak spots of length a separated by a distance d (Fig. 8). Different values of the distance d were simulated and the effect of this parameter on the release angle was examined. Note that for $d = 0$ the problem is the same as the one presented previously with one weak spot of half length a .

Fig. 9 shows the evolution of the release angle as a function of distance d . Typical displacement profiles illustrating the behavior for different values of d/Λ are also shown. If the distance between the weak spots is high compared to Λ (typically for $d/\Lambda \gtrsim 10$), then the displacement profiles generated by the weak spots do not interact between each other. The release thus occurs for the same angle as for the case of only one weak spot of total length a . If now the distance d between weak spots decreases to values of the same order as Λ (i.e. if $1 < d/\Lambda \lesssim 10$), the displacement profile still keeps a bimodal shape but the two peaks progressively coalesce. As a consequence of this interaction, the release angle θ_r progressively decreases as d decreases. Empirically, the evolution of θ_r for $d/\Lambda > 1$ can be adjusted by an exponential function: $\theta_r = \theta_\infty(1 - \gamma e^{-d/(k\Lambda)})$. As expected, the values of θ_∞ and γ depend on the slab depth h and weak spot length a ($\theta_\infty \approx 39.1^\circ$ and $\gamma \approx 0.17$ in the presented case), but the constant k is independent of these parameters ($k \approx 3$). Finally, if the distance between weak spots is less than the characteristic length ($d/\Lambda < 1$), the release angle increases as d decreases and the displacement profile becomes unimodal. This indicates that, in this case, the slab does not “feel the

effect” of the cohesive zone between the two weak spots and only “sees an equivalent weak spot” of length approximately $L \approx 2a + d$.

Hence, it appears that the interaction and progressive bridging between the two weak spots is primarily controlled by the characteristic length Λ . Physically, this characteristic length Λ represents the typical distance over which the stress redistribution induced by slab elasticity is felt. As illustrated in Fig. 9 this stress redistribution actually amounts to smoothing out the effect of the structural heterogeneity of the weak layer as soon as the typical variations of this heterogeneity occur over distances less than Λ . Hence, Λ can be viewed as a characteristic smoothing length associated to slab elasticity. More generally, it shall be noted that this parameter Λ appears to be the main length scale of the system. In particular, we checked that the softening length δ involved in the quasi-brittle weak-layer constitutive law, has essentially no influence on the results as long as it remains much smaller than Λ .

4. RESULTS: INFLUENCE OF WEAK-LAYER HETEROGENEITY

4.1. Simulation protocol

We now consider the case of a spatially heterogeneous weak layer, as described in section 2.4. We conducted simulations for different values of the slab depth h varying between 0.25m and 4m and different values of the correlation length ϵ varying between 0.5m and 40m. For each couple (h, ϵ) , 100 simulations with different realizations of the heterogeneity were performed. In each of the simulations, the release angle θ_r was determined according to the release criterion given by Eq. (5), which yields to release angle distributions. For reasons that will be developed below, the results will be primarily presented in terms of the release factor F defined as:

$$F = \sin \theta_r - \mu \cos \theta_r. \quad (17)$$

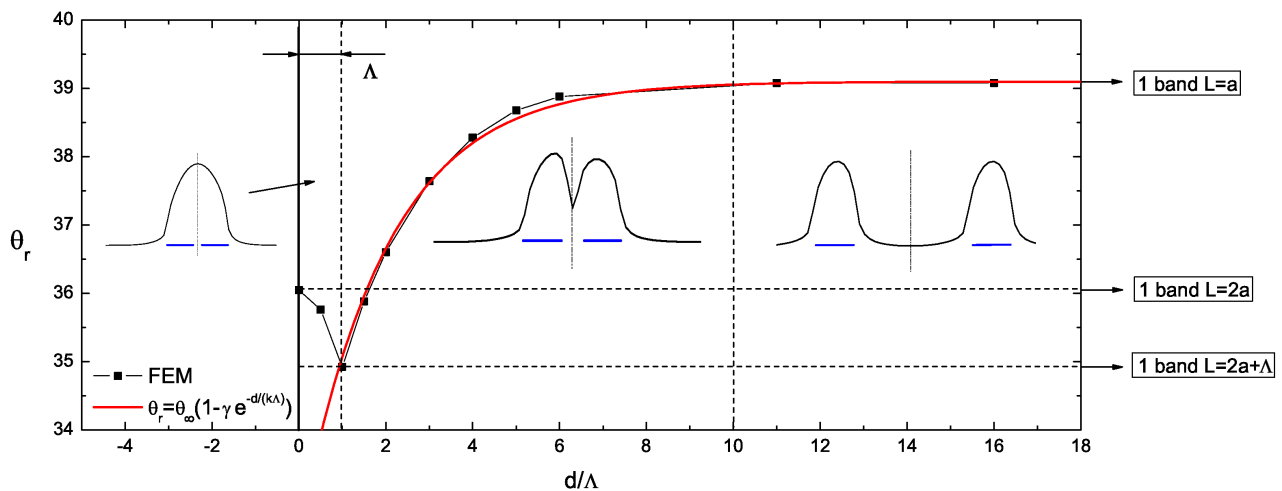


Fig. 9. Evolution of the release angle θ_r with the inter-distance between the two weak spots d (normalized by the characteristic length Λ) for weak-spot lengths $a = 4.5\text{m}$. The black dots are the results of the finite element model. The red curve is an exponential adjustment for $d/\Lambda > 1$. Three different zones are distinguished: $d < \Lambda$, $\Lambda < d \lesssim 10\Lambda$ and $d \gtrsim 10\Lambda$, and the typical displacement profiles recorded a few time-steps before release in each of these zones are represented.

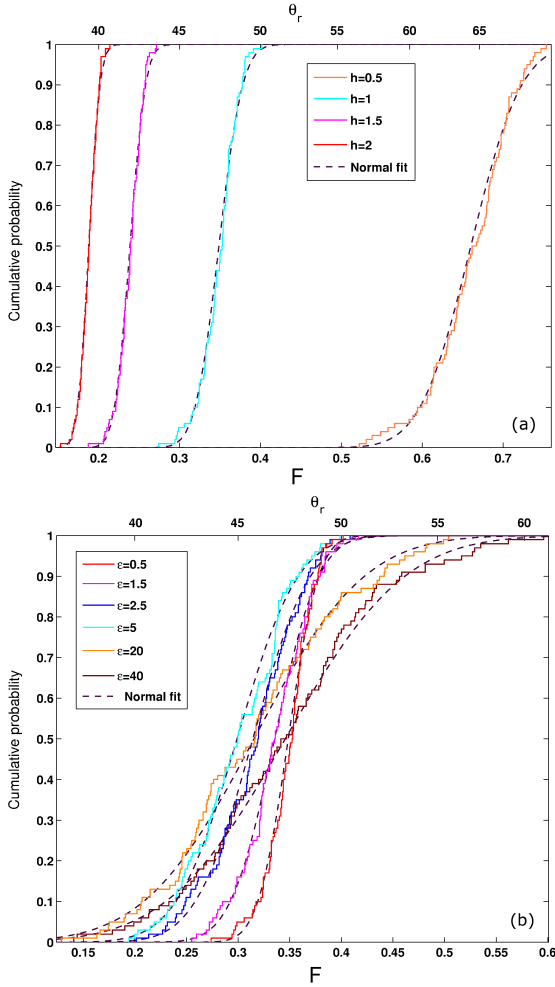


Fig. 10. Cumulative distributions of release angle θ_r (top scale) and release factor F (bottom scale). (a) $\epsilon = 0.5$ m and various values of slab depth h , (b) $h = 1$ m and various values of ϵ . Note that according to Eq. (17), the top scale represented is non linear in terms of release angle θ_r .

4.2. Release angle and release factor distributions

Fig. 10 shows the influence of slab depth h and correlation length ϵ on the cumulative distributions of the release factor F . Note that these distributions can also be interpreted in terms of release angle θ_r . First we observe that all the distributions obtained can be well adjusted by Gaussian laws, which can be interpreted as a consequence of the Gaussian nature of the cohesion heterogeneity. As shown in Fig. 10a, the average and the variance of the release factor distributions decrease with the slab depth h . In addition, the average appears to be approximately independent of the correlation length ϵ , while the variance increases with ϵ (Fig. 10b). These results will now be described in more details.

4.3. Average release factor

In a homogeneous case, the release factor F_h is expected to decrease with h according to $F_h = \langle c \rangle / (\rho gh)$. As shown in Fig. 11a, the numerical results appear to closely follow this prediction. In detail, however, it can be noted that the average release factor is always slightly lower than F_h , the difference tending to vanish as the slab depth h increases. The same

slight difference with F_h is seen in Fig. 11b, where it appears to increase with increasing correlation length ϵ for $\epsilon < 10$ m. Recall that for $\epsilon > 10$ m, the results begin to be influenced by finite size effects. These small discrepancies between the results and the theoretical homogeneous value F_h are due to the heterogeneity and the presence of local cohesion minima. However, globally, we can conclude that the average release factor $\langle F \rangle$ (and the average release angle $\langle \theta_r \rangle$) are almost unaffected by the weak-layer heterogeneity.

4.4. Variability and heterogeneity smoothing

Fig. 11a shows that the release factor variance decreases with slab depth h as a power law. The associated exponent is slightly smaller than -2 (≈ -2.16). In addition, this variance appears to be significantly smaller than the variance $\sigma_\infty^2 = \sigma_c^2(\rho gh)^{-2}$ that would be observed if the stress field in the weak layer exactly followed the heterogeneity variations (case of a completely rigid slab). This illustrates the smoothing of the heterogeneity due to the elastic redistribution of stresses in the slab.

Following section 3, the stress redistribution effects induced by slab elasticity are characterized by the smoothing length $\Lambda = \sqrt{E' h u_p / \tau_p}$. Hence we can assume that the ratio $\sigma_F^2 / \sigma_\infty^2$ can be expressed only in terms of the ratio ϵ / Λ . As shown in

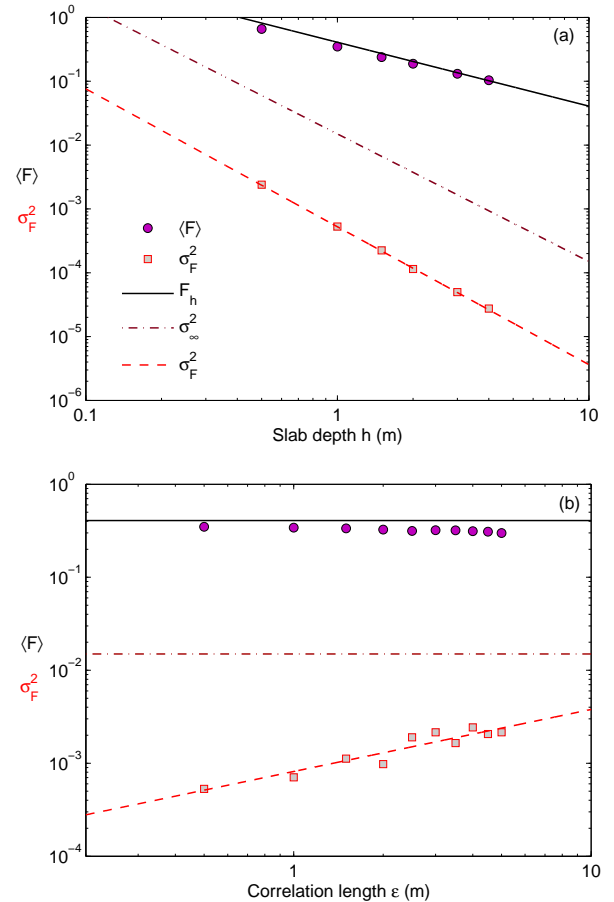


Fig. 11. Evolution of the average release factor $\langle F \rangle$ and release factor variance σ_F^2 as functions of slab depth h for $\epsilon = 0.5$ m (a) and as functions of heterogeneity correlation length ϵ for $h = 1$ m (b). σ_∞^2 represents the release factor variance that would be obtained in the case of a completely rigid slab.

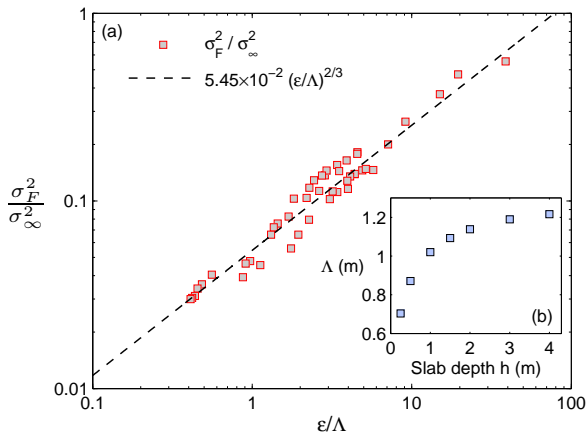


Fig. 12. (a) Ratio between release factor variance σ_F^2 and infinitely rigid slab variance $\sigma_\infty^2 = \sigma_c^2(\rho gh)^{-2}$ (see text) as a function of the ratio between correlation length ϵ and elastic smoothing length Λ for all (h, ϵ) couples (≈ 5000 simulations). (b) Evolution of the elastic smoothing length Λ with slab depth h .

Fig. 12a, all the datapoints corresponding to $\sigma_F^2/\sigma_\infty^2$ obtained from the simulations effectively collapse on a single master curve when plotted in terms of ϵ/Λ . The following power-law expression provides a good fit to the data:

$$\frac{\sigma_F^2}{\sigma_\infty^2} = \delta \left(\frac{\epsilon}{\Lambda} \right)^{\frac{2}{3}} \quad (18)$$

with $\delta = 5.45 \times 10^{-2}$. Note however that one can expect $\sigma_F^2/\sigma_\infty^2 \rightarrow 1$ if $\epsilon/\Lambda \rightarrow \infty$. Hence, the power-law given by Eq. (18) is not expected to remain valid for this limit. In addition, Fig. 12b shows that the elastic smoothing length Λ slightly increases with slab depth h in our simulations. This is consistent with the slightly-less-than 2 power-law exponent observed for the evolution of σ_F^2 with h in Fig. 11.

We can thus conclude that, at the limit of low values of correlation length ϵ and/or high values of the smoothing length Λ (and thus high values of slab depth h), $\sigma_F^2 \rightarrow 0$ and the system behaves as in a homogeneous case. This also explains why the difference between the average release factor $\langle F \rangle$ and the theoretical homogeneous value F_h decreases when h increases or ϵ decreases, as noted in Figs. 11a and 11b. For large correlation lengths, since the effect of ϵ dominates the effect of h in Eq. (18), very thick slabs can be released even for moderate slope angles, which corresponds to the so-called knock-down effect (Kronholm and Schweizer, 2003; Schweizer and others, 2008).

5. COMPARISON WITH FIELD DATA

5.1. La Plagne release depth data

La Plagne, in the French Alps, is one of the largest ski area in the world, covering 100km^2 with 225km of ski tracks. Ski patrollers provided us with release depth data from 14,391 avalanches collected during winters 1998 to 2010. Since avalanche depths cannot always be directly measured, data come from a mix of eyesight estimates and precise measurements. From the complete database, 369 naturally-released slab avalanches were extracted. These data have been analyzed in detail in Gaume and others (2012). Note that the same data were also used by Failletaz and others (2004), but with fewer avalanches

(only three winters). These analyses showed that the release depth cumulative distribution at La Plagne seems to decrease as a power-law for large slab depths ($h > 0.7\text{m}$, corresponding to cumulative exceedance probability lower than about 10%). Similar power-law trends have also been reported in other locations (Rosenthal and Elder, 2002; McClung, 2003). We note however that, due to the error associated to the data, the value of the power-law exponent is poorly constrained and strongly dependent on the cutoff considered for the power-law. Typically, in agreement with McClung (2003), exponents in the $[-3; -5]$ range provide a good fit to the data.

Our objective here is to examine whether our mechanical model is capable of reproducing these release depth data for both the core and the tail of the distribution. This comparison first requires computing the release depth distribution predicted by the model, which can be obtained in two phases: (1) The release factor distributions presented above have to be inverted to obtain release depth distributions for fixed angle values. (2) These release depth distributions must then be integrated over all slopes since data mix avalanche paths of various slope angle. Lastly, to be compared with data, the release depth probability obtained from the mechanical model has to be combined with the local snowfall probability.

5.2. Release depth distributions obtained from mechanical model

Inversion of release factor distributions

We have shown that the distributions of the release factor F are normally distributed with an average $\langle F \rangle \approx \langle c \rangle / (\rho gh)$ and a variance $\sigma_F^2 = f(\epsilon/\Lambda) \sigma_c^2 / (\rho gh)^2$, with $f(\epsilon/\Lambda)$ given by Eq. (18). In addition, since Λ varies only slightly in our results (see Fig. 12b), we assume it to be constant in what follows. This approximation does not significantly influence the results to be presented but allows to obtain analytical solutions. Hence, the variance σ_F^2 can be written as:

$$\sigma_F^2 = \frac{f(\epsilon) \sigma_c^2}{(\rho gh)^2}, \quad (19)$$

with $f(\epsilon) \approx \kappa \epsilon^{2/3}$, and $\kappa = \delta \Lambda^{-2/3}$ assumed constant. Finally, the probability density of having a release factor F for a given slab depth h is given by:

$$p(F|h) = \frac{h}{C_\sigma \sqrt{2\pi}} e^{-\frac{1}{2} \left(\frac{hF - C_\mu}{C_\sigma} \right)^2}, \quad (20)$$

with $C_\mu = \frac{\langle c \rangle}{\rho g}$ and $C_\sigma = \frac{\sigma_c \sqrt{f(\epsilon)}}{\rho g}$.

The Mohr-Coulomb rupture criterion which controls avalanche release in the simulations can be written in terms of release factor $F = \sin \theta_r - \mu \cos \theta_r$ as:

$$\rho gh F = c. \quad (21)$$

Hence, slab depth h and release factor F play similar roles in this criterion. Consequently, it can be shown that, if the probability density of release factor F for a given slab depth h value writes $p(F|h) = g(F, h)$, then the probability density of h for a given value of F writes $p(h|F) = g(h, F)$. Eq. (20) can thus be inverted into:

$$p(h|F) = \frac{F}{C_\sigma \sqrt{2\pi}} e^{-\frac{1}{2} \left(\frac{hF - C_\mu}{C_\sigma} \right)^2}. \quad (22)$$

A more detailed and rigorous demonstration of this inversion is provided in Appendix B.

Integration over all slopes

For the sake of simplicity, we chose, in this study, to consider a uniform probability distribution for the slope factor $F = \sin\theta - \mu\cos\theta$ between F_{min} and F_{max} : $p(F) = 1/(F_{max} - F_{min})$. Once again, this assumption enables us to obtain analytical expressions for the integrated release depth distribution $p_m(h)$:

$$p_m(h) = \int_{F_{min}}^{F_{max}} p(h|F)p(F) dF. \quad (23)$$

From Eq. (22), we obtain:

$$p_m(h) = \frac{1}{h\sqrt{\pi}} [g_1(h) + g_2(h)], \quad (24)$$

with

$$\begin{aligned} g_1(h) &= \int_{U_{min}}^{U_{max}} ue^{-u^2} du \\ &= \frac{\sqrt{2}C\sigma}{2h} \left[e^{-\frac{1}{2}U_{min}^2} - e^{-\frac{1}{2}U_{max}^2} \right], \end{aligned} \quad (25)$$

and

$$\begin{aligned} g_2(h) &= \int_{U_{min}}^{U_{max}} e^{-u^2} du \\ &= \frac{\sqrt{\pi}C\mu}{2h} \left[\operatorname{erf}\left(\frac{U_{min}}{\sqrt{2}}\right) - \operatorname{erf}\left(\frac{U_{max}}{\sqrt{2}}\right) \right], \end{aligned} \quad (26)$$

where we defined $U_{min} = (hF_{min} - C_\mu)/C_\sigma$ and $U_{max} = (hF_{max} - C_\mu)/C_\sigma$. In the following, without loss of generality, we will assume $F_{min} = 0$ and $F_{max} = 1$.

5.3. Coupling mechanical and snowfall distributions

Gaume and others (2012) have shown that the global avalanche release depth probability $p_r(h)$, resulting from the coupling between the mechanical model presented above and snowfall distributions, can be related to $p_m(h)$ as follows:

$$\Rightarrow p_r(h) \approx \frac{p_m(h) p_{sf}(h_{sf} \geq h)}{C}, \quad (27)$$

where $p_{sf}(h_{sf} \geq h)$ is the probability of having a snowfall whose thickness h_{sf} is higher than the depth h , and C a normalization constant given by: $C = \int_0^\infty p_m(h) p_{sf}(h_{sf} \geq h) dh$. This coupling relation expresses that the amount of snowfall represents a limiting factor weighting the mechanical probability density $p_m(h)$ derived from the stability criterion.

To define the snowfall distribution $p_{sf}(h_{sf} \geq h)$, Gaume and others (2012) considered the 3-day snowfall annual maxima in La Plagne (MeteoFrance data: daily measurements from 1966) at the average altitude of 2200m. These maxima follow a generalized extreme value (GEV) distribution so that:

$$p_{sf}(h_{sf} \geq h) = 1 - \exp \left[- \left(1 + \xi \frac{h - \mu}{\sigma} \right)^{-1/\xi} \right], \quad (28)$$

where μ , σ and ξ are, respectively, the location, scale, and form parameters. These parameters assume the following values: $\mu_{sf} = 0.98\text{m}$, $\sigma_{sf} = 0.21\text{m}$ and $\xi_{sf} = 0.214$.

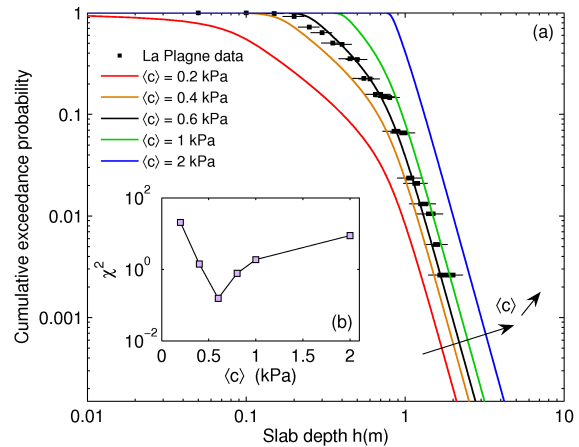


Fig. 13. Slab release depth distributions predicted by the coupled model [Eq. (27)] for different values of average cohesion $\langle c \rangle$, and comparison with field release depths from La Plagne. The numerical results have been obtained for a cohesion standard deviation $\sigma_c = 0.3$ kPa, a correlation length $\epsilon = 2\text{m}$, $F_{min} = 0$ and $F_{max} = 1$, the other parameters being the same as in section 4. (a) Cumulative exceedance probability in logarithmic scale, (b) χ^2 of the model ($\chi^2 = \sum (p_{data} - p_{model})^2 / p_{model}$, where p_{data} and p_{model} are the cumulative exceedance probabilities derived from the data and from the model, respectively).

5.4. Result of the coupling and sensitivity analysis

As shown in Gaume and others (2012) (see also Fig. 13), it is possible to find a set of mechanical parameters for which the coupled model described in Eqs. (24)-(27)-(28) provides a very good adjustment to La Plagne release depth data. The model effectively predicts a power-law behavior of the cumulative exceedance distribution for large slab depths, in good agreement with the empirical distribution, and also well accounts for the data corresponding to lower release depths. In spite of the various assumptions involved, this model is, to our knowledge, the first capable of reproducing release depth data with such a good accuracy. To complement the results shown in Gaume and others (2012), we present below a detailed sensitivity analysis of the predicted distribution to the main mechanical parameters of the model.

Fig. 13 shows the comparison between data and the coupled model for different values of the average cohesion $\langle c \rangle$. The goodness of the fit (Fig. 13b) shows a pronounced minimum for $\langle c \rangle = 0.6$ kPa, which indicates that the agreement between model and data drastically depends on this average cohesion value. In particular, the depth h_m below which no avalanche can occur is strongly dependent on $\langle c \rangle$. This depth can be approximated by (Gaume and others, 2012):

$$h_m \approx [\langle c \rangle - 2\sigma_c f(\varepsilon)] / (\rho g F_{max}). \quad (29)$$

With the value $\langle c \rangle = 1$ kPa retained in section 3 and 4, h_m is slightly overestimated compared to the data. For $\langle c \rangle = 0.6$ kPa, a value still fully consistent with existing studies (Föhn and others, 1998; Jamieson and Johnston, 2001), an excellent agreement between the coupled model and the data is obtained.

The influence of the cohesion standard deviation σ_c is presented in Fig. 14. First, it can be noted that σ_c plays a less

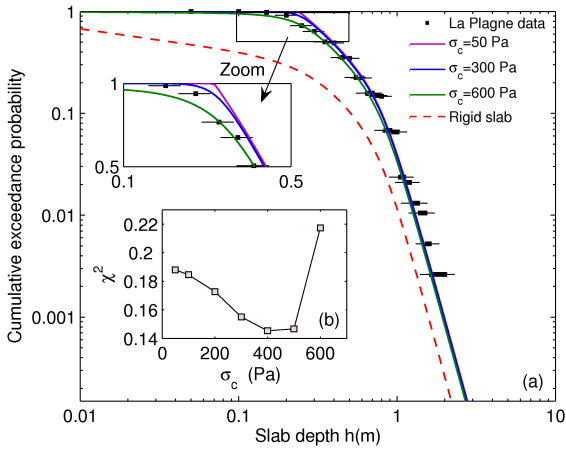


Fig. 14. Slab release depth distributions predicted by the coupled model [Eq. (27)] for different values of the standard deviation σ_c , and comparison with field release depths from La Plagne. The numerical results have been obtained for a cohesion $\langle c \rangle = 0.6$ kPa, a correlation length $\epsilon = 2$ m, $F_{min} = 0$ and $F_{max} = 1$, the other parameters being the same as in section 4. (a) Cumulative exceedance probability in logarithmic scale, (b) χ^2 of the model.

significant role than $\langle c \rangle$ on the goodness of the fit. As shown in Fig. 14b, values of σ_c in the 0.3–0.5 kPa range give similar results for constant values of the other parameters. In fact, the standard deviation σ_c mainly influences the curvature of the coupled cumulative exceedance distribution around the cut-off h_m . Fig. 14a also displays the distribution that would be obtained in the case of a completely rigid slab, which poorly adjusts the data. Even if the tail of this distribution could be adjusted to the data by tuning the other parameters, there would be no way to properly adjust the core of the distribu-

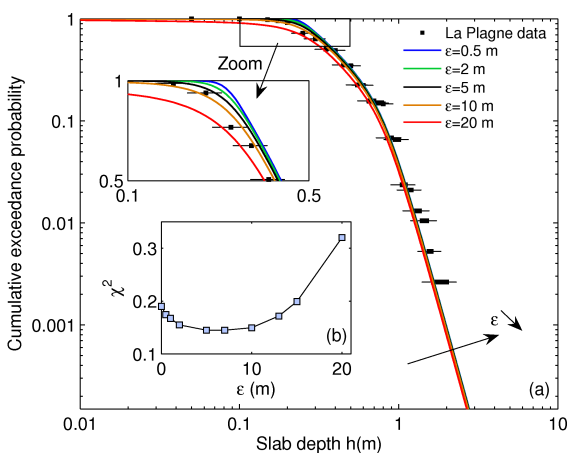


Fig. 15. Slab release depth distributions predicted by the coupled model [Eq. (27)] for different values of the correlation length ϵ , and comparison with field release depths from La Plagne. The numerical results have been obtained for a cohesion $\langle c \rangle = 0.6$ kPa, a cohesion standard deviation $\sigma_c = 0.3$ kPa, $F_{min} = 0$ and $F_{max} = 1$, the other parameters being the same as in section 4. (a) Cumulative exceedance probability in logarithmic scale, (b) χ^2 of the model.

tion. This highlights the major importance of the elasticity of the slab and of stress redistribution effects.

Finally, the influence of the correlation length ϵ is shown in Fig. 15. As well as for the standard deviation σ_c , the correlation length ϵ mainly modifies the curvature of the coupled cumulative exceedance distribution around h_m . Globally, the adjustment to the data remains good for correlation length values in the 0.5–15 m range.

To conclude, in the range of realistic mechanical parameters for snow (for which stress redistribution effects play an important role), it turns out that the average cohesion $\langle c \rangle$ has the most significant influence on slab avalanche release distributions predicted by the coupled model. Hence, provided GEV parameters are known, the adjustment of the model to the data essentially amounts to a one parameter fit. Note also that the value of F_{max} which has been set to 1 in the previous results, plays in fact a role essentially similar to that of $\langle c \rangle$ [see Eq. (29)]. Hence, changing the value of F_{max} would result in straightforward modifications of the best fit value found for $\langle c \rangle$.

6. CONCLUSION AND PERSPECTIVES

This paper investigates the influence of weak layer heterogeneity on slab avalanche release using a finite element model. A shear-softening interface underlying an elastic slab is modeled and the system is loaded by increasing the slope angle until failure and avalanche release. After validating the model on the case of a nil-cohesion weak spot, the effect of a heterogeneous weak-layer cohesion field was studied. The heterogeneity is represented through a Gaussian distribution, with a spherical covariance function characterized by a spatial correlation length. Release angle distributions were analyzed and a heterogeneity smoothing effect due to redistributions of stresses by elasticity of the slab was highlighted. This smoothing effect induces a reduction of the release angle variance compared to the case of a fully rigid slab. However, the average release angle is almost unaffected by this effect. The presented results showed that the smoothing intensity critically depends on the ratio between the correlation length ϵ and a characteristic elastic length of the system Λ . Further work would be required, however, to fully unravel the possible interplay between ϵ and the cohesion variance σ_c^2 on this smoothing effect.

To be compared with field data, the obtained release angle distributions were inverted, yielding a release depth distribution integrated over all slopes. Coupling this mechanical distribution with the distribution of 3-day extreme snowfalls, we were able to reproduce with excellent accuracy field data from 369 natural slab avalanches. A detailed sensitivity analysis showed that this agreement is obtained with only one adjustable parameter, namely the average cohesion $\langle c \rangle$. The mechanically-based probabilistic model thus fulfills the objectives of the study, namely the evaluation of avalanche release depth distributions in any potential release zone, as soon as meteorological data are available. In the future, a straightforward extension to the 3d-case will be developed to predict distributions of avalanche release volumes. However, before being used in operational context, additional tests on other datasets and in other locations would need to be performed to further validate the model. Finally, let us recall that, with the parameters used in our model, the crown fracture always occurs at particular morphological features (such as ridges, rocks, trees, etc.) since the heterogeneity is not sufficient to

directly trigger tensile rupture within the slab. Another interesting perspective for future work would thus be to study the release depth distributions obtained with different sets of parameters leading to other types of failure mechanisms.

APPENDIX A. MODEL VALIDATION: EXPRESSION OF THE PARAMETERS

We give here the expressions of the parameters involved in the weak spot analytical solution derived in section 3.1:

$$r = \frac{\frac{\Lambda}{\Lambda_{ws}} \left(1 - \frac{\Lambda_{ws}^2}{\Lambda^2}\right) \left(\beta e^{a/\Lambda_{ws}^2} - \alpha e^{-a/\Lambda_{ws}^2}\right)}{1 + \frac{\Lambda}{\Lambda_{ws}} \left(\beta e^{a/\Lambda_{ws}^2} - \alpha e^{-a/\Lambda_{ws}^2}\right)} \quad (\text{A1})$$

$$\alpha = \frac{1 - e^{-a/\Lambda_{ws}}}{e^{a/\Lambda_{ws}} - e^{-2a/\Lambda_{ws}}} \quad (\text{A2})$$

$$\beta = \frac{1 - \alpha e^{-a/\Lambda_{ws}}}{e^{a/\Lambda_{ws}}} \quad (\text{A3})$$

$$r' = \frac{\Lambda^2}{\Lambda_{ws}^2} - 1 - r \quad (\text{A4})$$

$$r_2 = \frac{a}{\Lambda} \left(\frac{\tau_r}{\tau_g} - 1\right) \quad (\text{A5})$$

APPENDIX B. INVERSION OF RELEASE FACTOR DISTRIBUTIONS

The objective is to deduce from the distributions $p(F|h)$ derived from the simulations, the distributions $p(h|F)$ that would be obtained in the “dual” experiment (much more difficult to perform numerically) consisting in fixing the slope angle and gradually increasing the slab depth h until rupture. The principle of this inversion lies in that, for a given realization of heterogeneity, the rupture is achieved under the same conditions in both experiments. Hence, the couple (F, h) obtained in both cases must be the same.

It is thus possible to obtain $p(h|F)$ from $p(F|h)$ by generating a large number of couples (F, h) in drawing in $p(F|h)$ distributions for several values of h , and then to reclassify data obtained as a function of F . To this end, values of h can be drawn from a random distribution $p(h)$. Instead of applying this protocol empirically, one can notice that the knowledge of $p(h)$ allows to consider the couple (F, h) as a random vector, and to compute $p(h|F)$ using Bayes formula:

$$p(h|F) = \frac{p(F|h) p(h)}{\int_{-\infty}^{+\infty} p(F|h) p(h) dh} \quad (\text{A6})$$

Then, to avoid biasing the result, it is necessary to sample uniformly all possible values of h . In other words $p(h)$ has to be chosen as constant. Eq. (A6) therefore simplifies to:

$$p(h|F) = \frac{p(F|h)}{\int_{-\infty}^{+\infty} p(F|h) dh} \quad (\text{A7})$$

Knowing the expression of $p(F|h)$:

$$p(F|h) = \frac{1}{\sqrt{2\pi}\sigma_F} e^{-\frac{1}{2}\left(\frac{F-(F)}{\sigma_F}\right)^2}, \quad (\text{A8})$$

with

$$\langle F \rangle = \frac{\langle c \rangle}{\rho gh}, \quad (\text{A9})$$

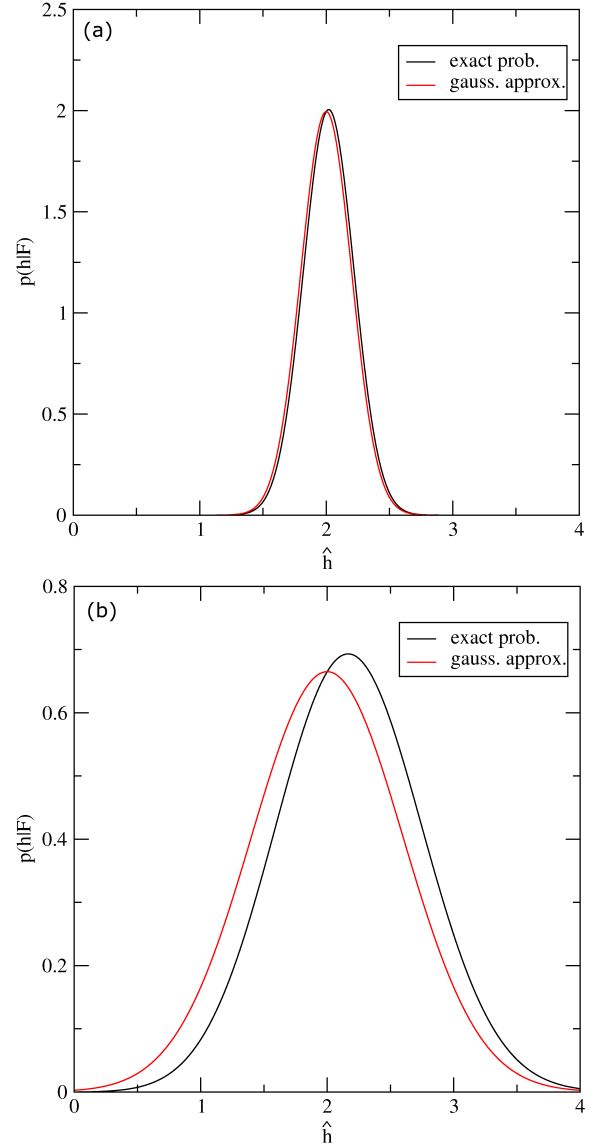


Fig. 16. Comparison between the exact expression (A12) and the Gaussian approximate expression (A13) of the inverted probability $p(\hat{h}|F)$ (case $F = 0.5$): (a) $C_V = 0.1$, (b) $C_V = 0.3$.

and

$$\sigma_F = \frac{\sigma_c}{\rho gh} \sqrt{f\left(\frac{\epsilon}{\Lambda}\right)}, \quad (\text{A10})$$

where Λ is the elastic characteristic length of the system, the inverse distribution $p(h|F)$ can be obtained numerically by applying Eq. (A7). In the present case in which $p(F|h)$ is Gaussian, it is possible to integrate analytically the denominator assuming that $\Lambda = \Lambda_0$ is a constant independent of h . As already mentioned, this assumption is not completely fulfilled, but the error made is negligible since the influence of h on the function $\sigma_F \rho gh / \sigma_c = \sqrt{f(\epsilon/\Lambda)}$ remains low.

For homogeneity reasons, we also define $\hat{h} = \rho gh / \langle c \rangle$ (dimensionless variable). We can then write

$$p(F|\hat{h}) = \frac{\hat{h}}{\sqrt{2\pi}C_V} e^{-\frac{1}{2}\left(\frac{\hat{h}F-1}{C_V}\right)^2}, \quad (\text{A11})$$

with $C_V = (\sigma_c / \langle c \rangle) \sqrt{f(\epsilon / \Lambda_0)}$. We thus obtain:

$$\int_{-\infty}^{+\infty} p(F|\hat{h})d\hat{h} = \frac{1}{\sqrt{2\pi}C_V} \int_{-\infty}^{+\infty} \hat{h} e^{-\frac{1}{2}\left(\frac{\hat{h}F-1}{C_V}\right)^2} d\hat{h} \\ = \frac{1}{F^2}$$

Finally, from Eq. (A7), it comes:

$$p(\hat{h}|F) = \frac{F^2 \hat{h}}{\sqrt{2\pi}C_V} e^{-\frac{1}{2}\left(\frac{\hat{h}F-1}{C_V}\right)^2} \quad (\text{A12})$$

Hence, strictly, the inverted probability distribution $p(\hat{h}|F)$ is not Gaussian. However, as shown in Fig. 16, if the Gaussian contribution to Eq. (A12) is sufficiently sharp, i.e. if C_V is sufficiently small, the variation of \hat{h} in the prefactor remains negligible. We can then replace \hat{h} in the prefactor by the mode of the Gaussian, i.e. $1/F$, which leads to the following approximate expression:

$$p(\hat{h}|F) = \frac{F}{\sqrt{2\pi}C_V} e^{-\frac{1}{2}\left(\frac{\hat{h}F-1}{C_V}\right)^2}, \quad (\text{A13})$$

which is a Gaussian. This approximation is well justified in our case, since for $\epsilon < 10$ m we have $C_V < 10$ % (Fig. 16a). Note that in the case of a completely rigid slab, the coefficient of variation C_V would be equal to that of the cohesion, $\sigma_c / \langle c \rangle = 30$ %, value for which the Gaussian approximation is less valid (Fig. 16b). The role of the variance reduction by elastic effects (i.e. the role of the function $f(\epsilon / \Lambda)$) is thus crucial for this Gaussian approximation of $p(\hat{h}|F)$ to be valid. Returning to the physical variable h , we finally obtain Eq. (22), which simply corresponds to the expression of $p(F|h)$ in which the variables F and h have been inverted (again under the assumption that $\Lambda = \Lambda_0 = \text{const}$).

ACKNOWLEDGMENTS

This work was supported by the European DYNAVAL and MAP³ INTERREG projects and the French ANR MOPERA project. The authors wish to express their gratitude to Claude Schneider, snow scientist in La Plagne, for providing release depth data and to MétéoFrance for providing related snowfall data. An anonymous reviewer and the Scientific Editor P. Bartelt are gratefully acknowledged for their careful reading of the manuscript and their constructive comments.

REFERENCES

- Bader, H. and B. Salm, 1990. On the mechanics of snow slab release, *Cold Reg. Sci. Technol.*, **17**, 287–299.
- Barbolini, M., U. Gruber, C. Keylock, M. Naaim and F. Savi, 2000. Application and evaluation of statistical and hydraulic-continuum dense-snow avalanche models to five real European sites, *Cold Reg. Sci. Technol.*, **31**(2), 133–149.
- Bartelt, P., B. Salm and U. Gruber, 1999. Calculating dense-snow avalanche runout using a Voellmy fluid model with active-passive longitudinal straining, *J. Glaciol.*, **45**(150), 242–254.
- Bazant, Z.P., Zi G and D.M. McClung, 2003. Size effect law and fracture mechanics of the triggering of dry snow slab avalanches, *J. Geophys. Res.*
- Bellaire, S. and J. Schweizer, 2011. Measuring spatial variations of weak layer and slab properties with regard to snow slope stability, *Cold Reg. Sci. Technol.*, **65**(2), 234–241.
- Birkeland, K.W., K. Kronholm and S. Logan, 2004. A comparison of the spatial structure of the penetration resistance of snow layers in two different snow climates, *ISSW*, 3–11.
- Camponovo, C, 1998. Rheometric measurements during winter 1997–98, *Tech. rep.*, Swiss Federal Institute for Snow and Avalanche Research.
- Charras, T and F Di Paola, 2011. Utiliser Cast3m - La procédure PASAPAS, CEA.
- Chiaia, B.M, P. Cornetti and B. Frigo, 2008. Triggering of dry snow slab avalanches: stress versus fracture mechanical approach, *Cold Reg. Sci. Technol.*, **53**, 170–178.
- Chilès, J.P. and P. Delfiner, 1999. Geostatistics: Modelling spatial uncertainty, *Wiley Ser. Probab. Math. Statist.*, 695.
- Conway, H and J. Abrahamson, 1988. Snow-slope stability - A probabilistic approach, *J. Glaciol.*, **34**, No 117.
- De Montmollin, V, 1978. Introduction à la rhéologie de la neige, (PhD thesis), Université Scientifique et Médicale de Grenoble.
- Eckert, N, M. Naaim and E. Parent, 2010. Long-term avalanche hazard assessment with a Bayesian depth-averaged propagation model, *J. Glaciol.*, **56**(198), 563–586.
- Eckert, N., E. Parent, M. Naaim and D. Richard, 2008. Bayesian stochastic modelling for avalanche predetermination: from a general system framework to return period computations, *SERRA*, **22**, 185–206.
- Failletaz, J, F. Louchet and J.R. Grasso, 2004. Two-threshold model for scaling laws of noninteracting snow avalanches, *Phys. Rev. Lett.*, **93**(20), 208001.
- Föhn, P.M.B, C. Camponovo and G. Krst, 1998. Mechanical and structural properties of weak snow layers measured in situ, *Ann. Glaciol.*, **26**, 1–6.
- Fyffe, B and M. Zaiser, 2004. The effects of snow variability on slab avalanche release, *Cold Reg. Sci. Technol.*, **40**, 229–242.
- Fyffe, B and M. Zaiser, 2007. Interplay of basal shear fracture and slab rupture in slab avalanche release, *Cold Reg. Sci. Technol.*, **49**, 2638.
- Gaume, J., G. Chambon, N. Eckert and M. Naaim, 2012. Relative influence of mechanical and meteorological factors on avalanche release depth distributions., *Geophys. Res. Lett.*, **39**, L12401, in prep.
- Gaume, J., G. Chambon, M. Naaim and N. Eckert, 2011. Influence of weak layer heterogeneity on slab avalanche release using a finite element method, *Springer Ser. Geomech. Geoengin.*, **11**(3), 261–266.
- Griffiths, D.V and G.A. Fenton, 2004. Probabilistic slope stability analysis by finite elements, *J. Geotech. Geoenviron.*, **130**, 507; doi:10.1061/(ASCE)1090-0241(2004)130:5(507).
- Heierli, J, P. Gumbsch and M. Zaiser, 2008. Anticrack nucleation as triggering mechanism for snow slab avalanches, *Science*, **321**, 240.
- Heierli, J. and M. Zaiser, 2007. Failure initiation in snow stratifications containing weak layers: Nucleation of whumpfs and slab avalanches, *Cold Reg. Sci. Technol.*, **52**, 385–400.
- van Herwijnen, A and J. Heierli, 2009. Measurements of crack-face friction in collapsed weak snow layers, *Geophys. Res. Lett.*, **36**, L23502.
- Hutter, K., 1996. Chapter 11: avalanche dynamics. Kluwer Academic Publishers, *In Singh, V.P., Hydrology of disasters.*, 317–394.
- Jamieson, B and C. Johnston, 1990. In-situ tensile tests of snowpack layers, *J. Glaciol.*, **36**(122), 102–106.
- Jamieson, B, S. Margreth and A. Jones, 2008. Application and limitations of dynamic models for snow avalanche hazard mapping, *ISSW Proc.*
- Jamieson, B. and J. Schweizer, 2000. Texture and strength changes of buried surface-hoar layers with implications for dry snow-slab avalanche release, *J. Glaciol.*, **46**, 151–160.
- Jamieson, J.B and C.D. Johnston, 2001. Evaluation of the shear frame test for weak snowpack layers, *Ann. Glaciol.*, **32**, 59–69.

- Johnson, B.C., J.B. Jamieson and R.R. Stewart, 2004. Seismic measurements of fracture speed in a weak layer snowpack layer, *Cold Reg. Sci. Technol.*, **40**, 41–45.
- Keylock, C., D. McClung and M Magnusson, 1999. Avalanche risk by simulation, *J. Glaciol.*, **45**, 303–314.
- Kronholm, K., 2004. Spatial variability of snow mechanical properties with regards to avalanche formation, (PhD thesis), University of Zurich.
- Kronholm, K and K.W Birkeland, 2005. Integrating spatial patterns into a snow avalanche cellular automata model, *Geophys. Res. Lett.*, **32**, L19504, doi: 10.1029/2005GL024373.
- Kronholm, K and J Schweizer, 2003. Snow stability variation on small slopes, *Cold Reg. Sci. Technol.*, **37(3)**, 453–465.
- Mahajan, P and S Joshi, 2008. Modeling of interfacial crack velocities in snow, *Cold Reg. Sci. Technol.*, **51**, 98–111.
- Mahajan, P., R. Kalakuntla and C. Chandel, 2010. Numerical simulation of failure in a layered thin snowpack under skier load, *Ann. Glaciol.*, **51(54)**, 169–175.
- McClung, D.M., 1977. Direct simple shear tests on snow and their relation to slab avalanche formation, *J. Glaciol.*, **19(81)**, 101–109.
- McClung, D.M., 1979. Shear fracture precipitated by strain softening as a mechanism of dry slab avalanche release, *J. Geophys. Res.*, **84(B7)**, 3519–3526.
- McClung, D.M., 2003. Size scaling for dry snow slab release, *J. Geophys. Res.*, **108(B10)**, 2465.
- McClung, D., 2009. Dry snow slab quasi-brittle fracture initiation and verification from field tests, *J. Geophys. Res.*, **114**, F01022.
- McClung, D.M., 2011. Analysis of critical length measurements for dry snow slab weak-layer shear fracture, *J. Glaciol.*, **57**, No. 203.
- McClung, D.M. and J Schweizer, 2006. Fracture toughness of dry snow slab avalanches from field measurements, *J. Geophys. Res.*, **111**, F04008.
- Mellor, M, 1975. A review of basic snow mechanics, *IAHS Publ.*, **114**, 251–291.
- Meunier, M and C. Ancely, 2004. Towards a conceptual approach to predetermining high-return-period avalanche run-out distances, *J. Glaciol.*, **50(169)**, 268–278.
- Naaïm, Mohamed, T Faug and F Naaïm-Bouvet, 2003. Dry granular flow modelling including erosion and deposition, *Surv. Geophys.*, **24**, 569–585.
- Narita, H, 1980. Mechanical behaviour and structure of snow under uniaxial tensile stress, *J. Glaciol.*, **26**, No. 94.
- Navarre, J.P., A. Taillefer and Y Danielou, 1992. Fluage et rhéologie de la neige, *Actes de conférence Chamonix*.
- Palmer, A.C and J.R Rice, 1973. The growth of slip surfaces in the progressive failure of over-consolidated clay, *Proc. R. Soc. London*, **332**, 527–548.
- Reiweger, I, J Schweizer, J Dual and H.J Herrmann, 2009. Modelling snow failure with a fibre bundle model, *J. Glaciol.*, **55**, No 194.
- Roch, A., 1965. Les variations de la résistance de la neige, *IASH Publ.*, **No. 69**, 128–140.
- Rosenthal, W. and K. Elder, 2002. Evidence of chaos in slab avalanches, *ISSW*.
- Schweizer, J, 1998. Laboratory experiments on shear failure of snow, *Ann. Glaciol.*, **26**, 97–102.
- Schweizer, J, 1999. Review of dry snow slab avalanche release, *Cold Reg. Sci. Technol.*.
- Schweizer, J, B Jamieson and M Schneebeli, 2003. Snow avalanche formation, *Rev. Geophys.*, **41(4)**, 1016. (10.1029/2002RG000123.).
- Schweizer, J, K Kronholm, J.B Jamieson and K.W Birkeland, 2008. Review of spatial variability of snowpack properties and its importance for avalanche formation, *Cold Reg. Sci. Technol.*, **51(2-3)**, 253–272.
- Sigrist, C, 2006. Measurement of fracture mechanical properties of snow and application to dry snow slab avalanche release, (PhD thesis), ETHZ.
- Stoffel, M., 2005. Numerical modelling of snow using finite elements, (PhD thesis), ETH Zurich.
- Verpeaux, P, T Charras and A. Millard, 1988. CASTEM2000: une approche moderne du calcul des structures, *Calcul des structures et intelligence artificielle (Ed. Pluralis)*, cast3m Website: <http://www-cast3m.cea.fr>.

4.2 Application to the evaluation of the position of avalanche release area

This section is composed of an article entitled “Influence of tensile strength and weak layer heterogeneity on slab tensile rupture” which is still **in preparation** for a submission to *Journal of Glaciology*. The following authors contributed to this paper: Guillaume Chambon, Nicolas Eckert and Mohamed Naaim.

In this paper, the mechanically-based statistical model presented in the last section is used to study the position of the slab tensile rupture. This work aims at helping in the definition of potential avalanche release zones which is also a crucial input ingredient of hazard mapping procedures. To do so, the elastic behaviour of the slab was changed into an elastic-brittle one and the influence of slab tensile strength was studied in a probabilistic framework. We show, in particular, for realistic value of the mechanical parameters, the critical and major influence of morphological and topographical features such as rocks, trees, slope curvature and ridges, etc, on the position of slab tensile rupture. Note that the statistical model developed in this paper is still preliminary.

Influence of tensile strength and weak layer heterogeneity on slab tensile rupture.

Johan GAUME,¹ Guillaume CHAMBON,¹ Nicolas ECKERT,¹ Mohamed NAAIM¹

¹*Irstea, UR ETNA, 2 rue de la Papeterie, 38400 St Martin d'Heres.*

E-mail: johan.gaume@gmail.com

ABSTRACT. The evaluation of the position of slab tensile rupture represents an important concern for the evaluation of the avalanche release area and hence hazard assessment. In this paper, a mechanically-based statistical model of the slab – weak layer system accounting for weak-layer heterogeneity, stress redistribution by elasticity of the slab and the slab possible tensile failure is simulated. Two types of avalanche releases are distinguished in the simulations: (1) full slope releases, where the entire simulated slope is released and the heterogeneity is not sufficient to trigger a tensile failure within the slab; (2) partial slope release, where tensile failure occurs within the slab due to the heterogeneity so that only a part of the slope is released. We present the proportion of these two release types as a function of the different model parameters obtained from finite element simulations, and a simple statistical model capable of reproducing these results. One of the main outcome is that, for slab tensile strength σ_T higher than the average cohesion $\langle c \rangle$, all the releases appear to be full-slope, highlighting the critical and major influence of morphological features such as rocks, trees, slope curvature and ridge, as already pointed out in the litterature. It is also shown that the partial slope releases percentage is significantly increased when the slab depth h is of the same order than the correlation length ϵ and when the standard deviation of cohesion σ_c increases. Finally, phase diagrams of partial slope release percentage are computed to stress out the complex influence of the different parameters involved.

1. INTRODUCTION

For avalanche hazard mapping, coupled statistical–deterministic models see growing popularity so as to evaluate the runout distance distribution and the probability of exceedence of maximal pressure at any location of the runout zone (Barbolini and others, 2000; Naaim and others, 2003; Ancey and others, 2004; Eckert and others, 2007, 2008, 2010). These coupled models require the evaluation of the release volume, combination between the release depth and area. For the evaluation of the release depth, empirical techniques already exist (Swiss guidelines, Salm and others, 1990) and more recently, a coupled statistical – mechanical model was proposed by Gaume and others (2012a) and Gaume and others (2012b) taking into account both mechanical and meteorological factors in a probabilistic framework. On the other hand, the position of the release zone and the evaluation of its spatial extent have been less investigated. Maggioni and others (2002) and Maggioni and Gruber (2003) analyzed a well-documented database of avalanche events with respect to many topographic characteristics and showed that the mean slope angle, the curvature and the distance to the ridge are the most important parameters influencing avalanche release area distribution. Failletaz and others (2006); Fyffe and Zaiser (2004, 2007) used cellular-automata approaches to compute avalanche release area distributions. These models include a source of stochastic variability such as the heterogeneity of weak layer mechanical properties. Interestingly, these models are able, under certain conditions, to reproduce the power-law area distributions observed from field measurements (McClung, 2003; Failletaz and others, 2004).

In this paper, we extend a mechanically-based probabilistic model developed in a previous study (Gaume and others, 2012a,b) to analyze the parameters influencing the position of the slab tensile failure and, hence, the extent of the release area. In a first section, we recall the main characteristics of the model and present the changes made compared to our previous version. Then, in the second section, two rupture types are distinguished and presented. Finally, in the third section, we quantify the influence of weak layer heterogeneity and slab tensile strength on the position of slab tensile failure and we propose a simple statistical model capable of reproducing our results.

2. FORMULATION OF THE MODEL

In this paper, the mechanical model proposed by Gaume and others (2012b) and deeply detailed in Gaume and others (2012a) is used. We recall here its main characteristics.

The simulated system is a uniform slope composed of a slab and a weak layer of length $L = 50$ m. The simulations are carried out using the finite element code Cast3m in 2D (plane stress condition). Gravity is the only applied external force and the system is loaded by progressively increasing the slope angle θ until rupture. The main change compared to Gaume and others (2012b)'s model concerns the constitutive law of the slab. We use here an elastic–brittle law in order to take into account the possible tensile failure of the slab. The Young modulus of the slab is $E = 1$ MPa, the Poisson ratio $\nu = 0.2$, and the density $\rho = 250$ kg.m⁻³. The tensile strength of the slab is denoted σ_T and was varied between 500 and 2000 Pa. The weak layer is modeled as a quasi-brittle (strain-

softening) interface with a Mohr-Coulomb rupture criterion characterized by a cohesion c and a friction coefficient $\mu = \tan 30^\circ$. A spatial heterogeneity of the weak layer is accounted for through a stochastic distribution of the cohesion c with a spherical covariance function of correlation length ϵ . The average cohesion is denoted $\langle c \rangle$ and its standard deviation σ_c .

Besides the evaluation of avalanche release depth distributions, this model enabled to evidence, a heterogeneity smoothing effect caused by stress redistribution due to slab elasticity and characterized by the ratio between correlation length ϵ and a typical length scale of the system Λ associated to elastic effects (see Gaume and others, 2012b,a, for more details).

3. RELEASE TYPES

Two types of avalanche releases were distinguished in the simulations: (1) full slope release, where the entire simulated slope is released without tensile failure within the slab (Fig. 1a); (2) partial slope release, where tensile failure occurs within the slab so that only a part of the slope is released (Fig. 1b).

Importantly, however, for both release types, the primary rupture process observed is always the shear failure of the weak layer. Slab rupture, when existent, systematically constitutes a secondary process. In the case of a full slope release, the heterogeneity magnitude is not sufficient to trigger a tensile failure within the slab. The basal shear failure in the weak layer thus propagates until the top boundary condition which can be seen as an anchor point where slab tensile rupture would occur (Fig. 1a).

Replaced in the context of natural avalanche paths, this boundary condition can represent a strong geomorphological feature susceptible to trigger the tensile failure (ridges, rocks, trees, local convex zone, etc.). On the contrary, for partial slope releases, the cohesion variations in the weak layer are sufficient to generate the tensile failure within the system. Local strong zones can effectively stop the progression of the basal failure and the excess of stress is redistributed in the slab and engenders slab tensile opening.

4. RESULTS: PARAMETRIC ANALYSIS

In this section, we present the results in terms of partial slope release probability also called tensile failure probability and

denoted P_{tf} as a function of the following model parameters: tensile strength σ_T , correlation length ϵ , slab depth h and cohesion standard deviation σ_c . First, the standard deviation is fixed ($\sigma_c = 0.3$ kPa) and the other parameters, tensile strength σ_T , slab depth h and correlation length ϵ are varied to understand their influence. Then ϵ is fixed at 0.5 m and the influence of σ_c is investigated for different values of h .

4.1. Influence of σ_T

Fig. 2 represents the probability of tensile failure P_{tf} within the system as a function of the tensile strength σ_T for different values of the correlation length ϵ and a constant slab depth $h = 1$ m (left) and for different values of the slab depth h and a constant correlation length $\epsilon = 0.5$ m (right). Tensile strength values are varied between 0.5 and 1.5 kPa. As expected, this probability decreases with the tensile strength σ_T from 100% to 0%. The rate of decrease and tensile strength values at 0 and 100 % depend on slab depth h and correlation length ϵ .

4.2. Influence of h

As shown in Fig. 2 (right), the probability P_{tf} decreases globally with slab depth h . The higher h is, the faster the probability decreases with σ_T . The values of σ_T for $P_{tf} = 100\%$ is almost unaffected by the slab depth h while the value for $P_{tf} = 0\%$ is decreasing with increasing slab depth h . In more detail, Fig. 3 reports the tensile failure probability P_{tf} as a function of h for different tensile strength values and a constant correlation length $\epsilon = 0.5$ m. For $\sigma_T < 0.75$ kPa, P_{tf} is approximately equal to 100%, whereas, P_{tf} is approximately equal to 0% for $\sigma_T > 1.5$ kPa. For intermediate values of σ_T , P_{tf} decreases from $h = 0.5$ m to $h = 0.25$ m. A single simulation for $h = 0.25$ m was also performed for $\sigma_T = 1$ kPa to confirm the increase of P_{tf} with h for $h < 0.5$ m that will be highlighted by the statistical model developed in the next section.

4.3. Influence of ϵ

The influence of correlation length ϵ is also noticeable on Fig. 2 (left). The higher ϵ is, the slighter the probability decreases with σ_T . Besides, for constant tensile strength values, P_{tf} globally decreases with ϵ . In contrast with the influence of slab depth h , the values of σ_T for $P_{tf} = 100\%$ is

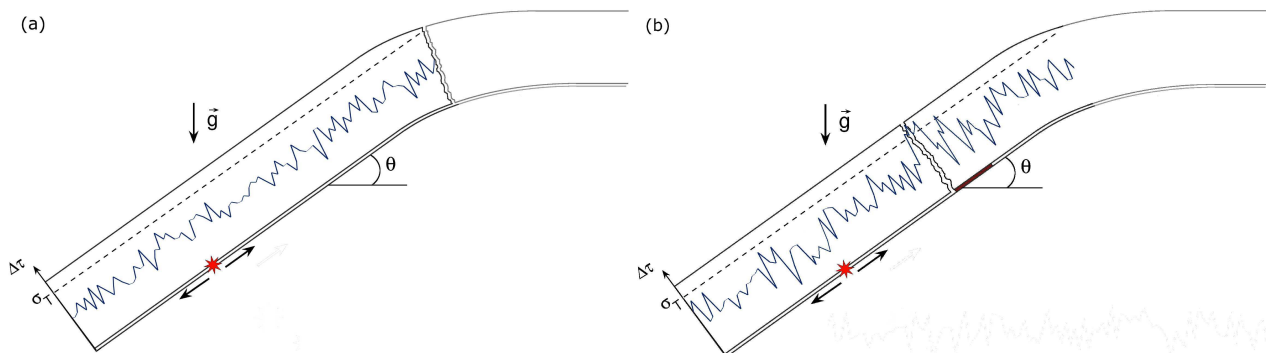


Fig. 1. Diagram representing the two types of failure observed in the simulations. (a) full-slope release: the localization of the slab tensile failure is influenced by morphological features (rocks, trees, ridge, curvature...). (b) partial-slope release: the local heterogeneity is sufficient to trigger the tensile failure within the slab. The red-colored part of the weak layer represents a local zone of important shear strength. The blue curves represent an illustration of the heterogeneity of shear stress difference $\Delta\tau$ and the dotted line represents the tensile strength σ_T .

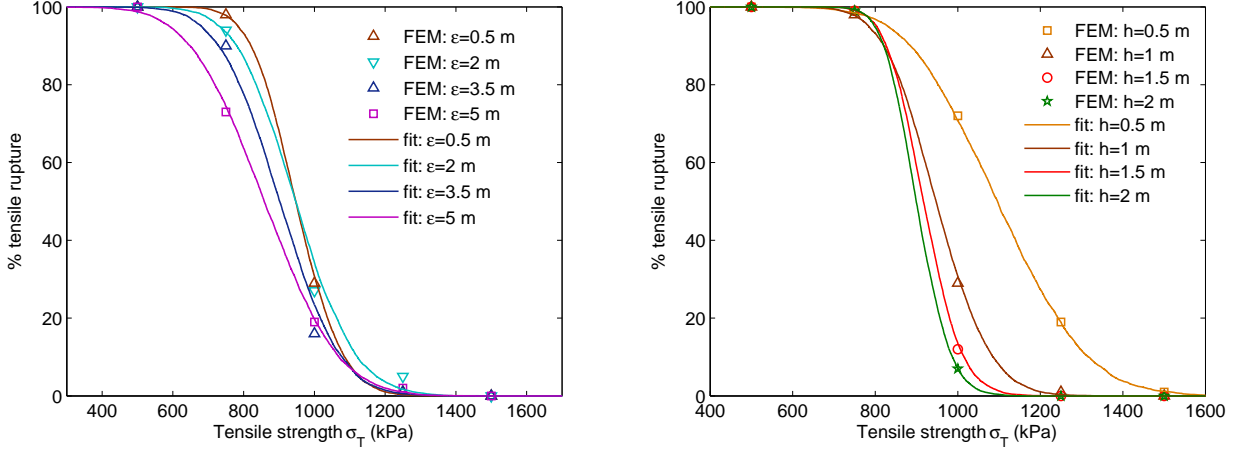


Fig. 2. Probability of slab tensile failure P_{tf} within the simulated system (partial-slope release) as a function of the tensile strength σ_T for different values of ϵ and a constant slab depth $h = 1$ m (left), and for different values of slab depth h and a constant correlation length $\epsilon = 0.5$ m (right). The curves represent the adjustment given by the statistical model presented in Sec. 5.

decreasing with increasing correlation length while the value for $P_{tf} = 0\%$ is almost not affected.

4.4. Influence of σ_c

The influence of the standard deviation σ_c of weak-layer heterogeneity for a constant tensile strength $\sigma_T = 0.75$ kPa and correlation length $\epsilon = 0.5$ m is then investigated for different values of the slab depth h .

Fig. 4 (top) shows the tensile failure probability P_{tf} as a function of the standard deviation σ_c . Globally, whatever the slab depth value, the tensile failure probability increases with σ_c and the rate of increase is all the more important that the slab depth h is low. As shown in Fig. 4 (bottom) all datapoints collapse on a same master curve when the tensile failure probability is plotted against σ_c normalized by $\rho g f(h)$ with $f_c(h) = 0.64h - 0.17$. This adjustment was obtained empirically (Fig. 4, inset).

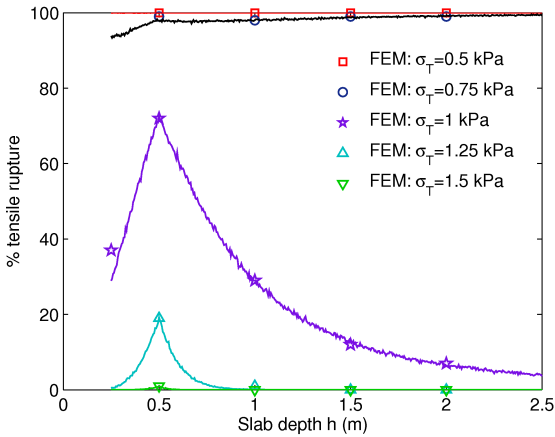


Fig. 3. Probability of slab tensile failure P_{tf} with the simulated system (partial-slope release) as a function of slab depth h for different values of the tensile strength σ_T and a constant correlation length $\epsilon = 0.5$ m. The curves represent the adjustment given by the statistical model presented in Sec. 1.3.

5. STATISTICAL MODEL

5.1. Formulation of the model

In order to estimate the proportion between the two release types, one can define the probability that the tensile stress σ_{xx} in the slab exceeds the tensile strength σ_T . We have shown that, a necessary condition for slab release is the primary rupture in shear of the weak layer. Thus, this probability $P(\sigma_{xx} > \sigma_T)$ is assumed to be equal to $P(\Delta\tau > \sigma_T)$, the probability that the shear stress difference $\Delta\tau$ between two adjacent elements of the weak layer exceeds the tensile strength σ_T . The shear stress difference $\Delta\tau$ is due to weak layer cohesion heterogeneity. Because of the Gaussian character of weak layer heterogeneity, we assume that $\Delta\tau$ also follows a Gaussian law of average $\langle\Delta\tau\rangle$ and standard deviation $\sigma_{\Delta\tau}$. The variance $\sigma_{\Delta\tau}$ will mainly depend on the cohesion standard deviation σ_c and the average $\langle\Delta\tau\rangle$ on the average cohesion $\langle c \rangle$, but also both will depend on other model parameters such as the slab depth h , the correlation length ϵ because of the elastic smoothing effect highlighted in Gaume and others (2012a,b). Let us define these two quantities as:

$$\langle\Delta\tau\rangle = (1 - R) \langle c \rangle, \quad (1)$$

and

$$\sigma_{\Delta\tau} = S \sigma_c, \quad (2)$$

where $R = R(\epsilon, h, \sigma_c)$ is called the reduction parameter and $S = S(\epsilon, h, \sigma_c)$ the smoothing parameter. For instance, for a homogeneous weak layer ($\sigma_c = 0$), the basal failure will occur simultaneously over the entire length of the system without triggering a tensile failure within the slab whatever the value of the tensile strength σ_T . In this case, the average $\langle\Delta\tau\rangle$ is equal to zero and thus $R \rightarrow 1$ to allow $P(\Delta\tau > \sigma_T) = 0$ in any case.

The exceedence probability $P(\Delta\tau > \sigma_T)$ can be analytically computed if one assumes that $\Delta\tau$ follows a Normal distribution. It is then the Normal cumulative exceedence probability and is given by:

$$P(\Delta\tau > \sigma_T) = 1 - \frac{1}{2} \left[1 + \operatorname{erf} \left(\frac{\sigma_T - \langle\Delta\tau\rangle}{\sqrt{2}\sigma_{\Delta\tau}} \right) \right] \quad (3)$$

As will be shown, this model can reproduce with a good accuracy the proportion between release types.

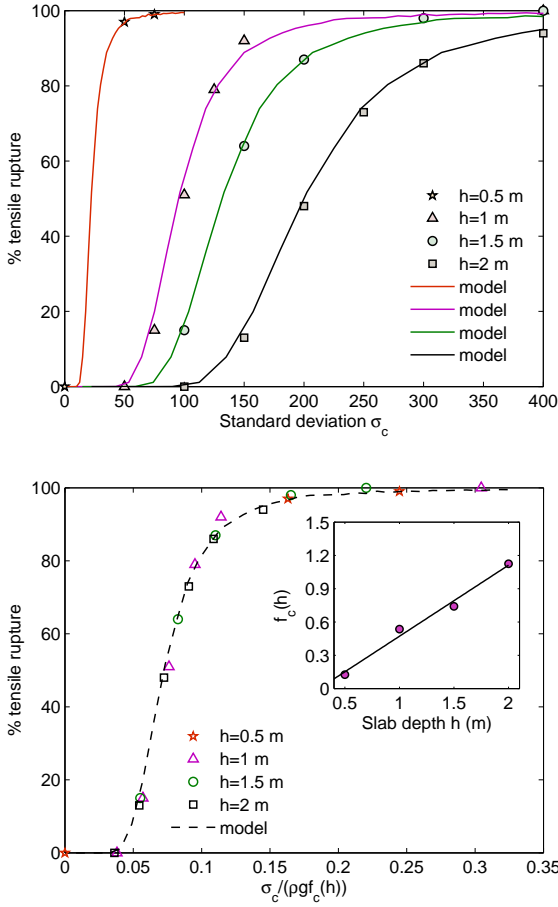


Fig. 4. (a) Tensile failure probability as a function of the standard deviation of weak layer cohesion σ_c and for different values of slab depth h . (b) Tensile failure probability as a function of σ_c normalized by $\rho g f_c(h)$. The function $f_c(h)$ is represented in the inset. Both curves are obtained for a constant correlation length $\epsilon = 0.5$ m and tensile strength $\sigma_T = 0.75$ kPa.

5.2. Application of the model to our results

Evolution with σ_T for different h , ϵ values

A maximum likelihood adjustment of Eq. (3) to the finite element calculations presented on Fig. 2 ($P_{tf}(\sigma_T)$) for different ϵ values) and Fig. 3a ($P_{tf}(\sigma_T)$) for different h values) was performed in order to determine the average and standard deviation of $\Delta\tau$. These adjustments are represented on Fig. 2 with continuous lines. The values of the reduction and smoothing parameters can thus be computed and the obtained values are represented on Fig. 5, as a function of the correlation length ϵ (Fig. 5a), of slab depth h (Fig. 5b) and as a function of the ratio between the correlation length and slab depth ϵ/h (Fig. 5c). In detail, one can note that the smoothing parameter and thus the standard deviation $\sigma_{\Delta\tau} = S\sigma_c$ decreases with h and the reduction parameter R increases with h corresponding to an average $\langle\Delta\tau\rangle = (1 - R)\langle c\rangle$ which decreases with h (Fig. 5b). This result highlights once again the characteristic smoothing effect induced by slab elasticity. Concerning the evolution with the correlation length ϵ , we can remark on Fig. 5a that the smoothing parameter S and thus also the standard deviation $\sigma_{\Delta\tau}$ increase globally with increasing ϵ .

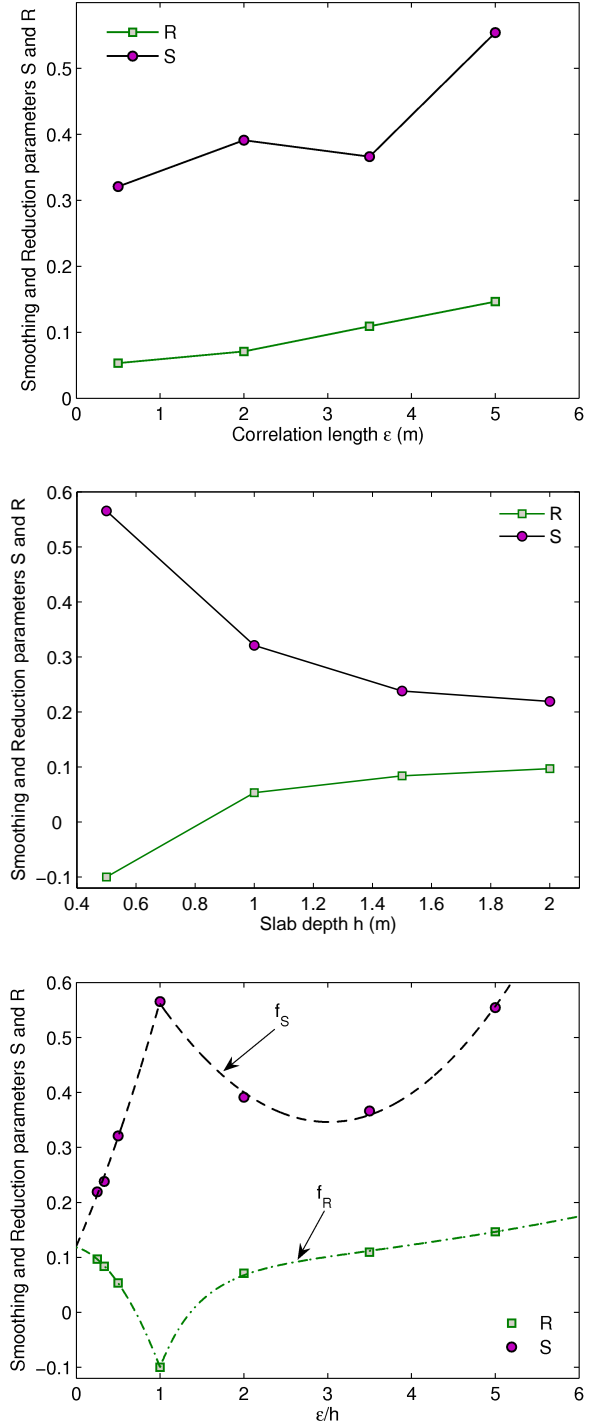


Fig. 5. Evolution of the reduction and smoothing parameters R and S computed by fitting a normal distribution to the results presented in Figs. 2a and 2b as a function of ϵ for a constant slab depth $h = 1$ m (a), as a function of h for $\epsilon = 0.5$ m (b) and as a function of the ratio ϵ/h (c).

Finally, the reduction parameter R increases with ϵ corresponding to an average $\langle\Delta\tau\rangle$ which decreases with ϵ .

In order to predict the evolution of the tensile failure probability for different (h, ϵ) values than those that were simulated, the evolution of these two parameters is plotted against

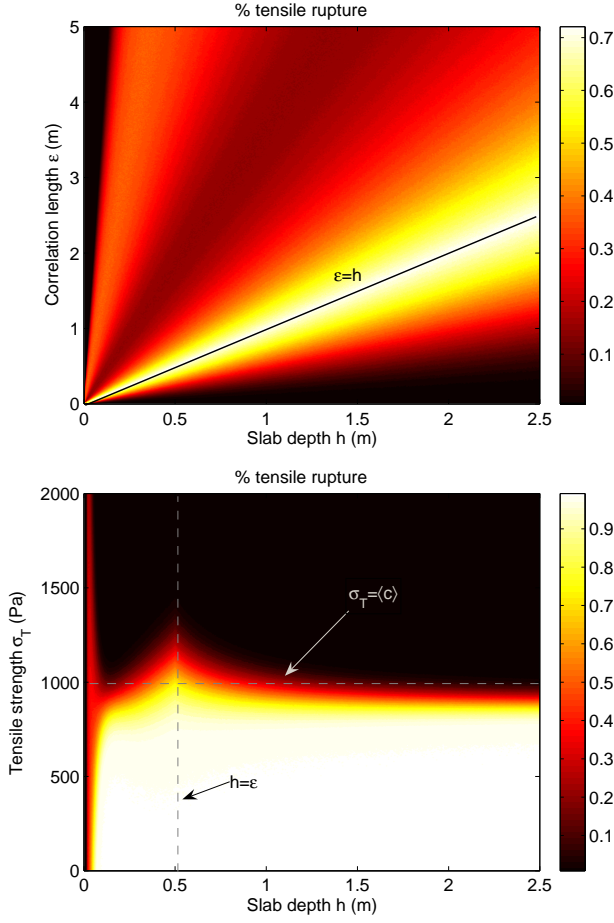


Fig. 6. Phase diagrams of slab tensile failure probability as a function of slab depth h and correlation length ϵ for a constant tensile strength $\sigma_T = 1$ kPa (a) and as a function of tensile strength σ_T and slab depth h for a constant correlation length $\epsilon = 0.5$ m (b).

ϵ/h on Fig. 5c. The two adjustments f_R and f_S are given by:

$$f_R\left(\frac{\epsilon}{h}\right) = \begin{cases} -0.1758\left(\frac{\epsilon}{h}\right)^2 - 0.0424\frac{\epsilon}{h} + 0.1182 & \text{if } \epsilon \leq h \\ 0.061 e^{0.1754\frac{\epsilon}{h}} - 1.551 e^{-2.198\frac{\epsilon}{h}} & \text{if } \epsilon > h \end{cases}, \quad (4)$$

and

$$f_S\left(\frac{\epsilon}{h}\right) = \begin{cases} 0.0965\left(\frac{\epsilon}{h}\right)^2 + 0.3488\frac{\epsilon}{h} + 0.1204 & \text{if } \epsilon \leq h \\ 0.0532\left(\frac{\epsilon}{h}\right)^2 - 0.3202\frac{\epsilon}{h} + 0.8282 & \text{if } \epsilon > h \end{cases} \quad (5)$$

These two adjustments were used to determine the evolution of the tensile failure probability against slab depth h on Fig. 3 (continuous line). The results from the finite element computations are well reproduced by this simple adjusted model for all tensile strength values. For instance, for a tensile strength $\sigma_T = 1$ kPa, the probability first increases between $h = 0$ m and $h = 0.5$ m and then decreases down to zero for slab depths higher than 2 m. Besides, the simulation for a slab depth $h = 0.25$ m was only performed for $\sigma_T = 1$ kPa and thus was not used in the fitting of R and S , which confirms the efficiency of the model, since the quite complex evolu-

tion of tensile failure probability around $h = 0.5$ m is well reproduced.

Lastly, using this model and the evolution of R and S with ϵ/h , phase diagrams representing the probability of tensile failure as a function of different parameters can be built. For example, Fig. 6a represents the diagram of tensile failure probability as a function of ϵ and h for a tensile strength $\sigma_T = 1$ kPa. We observe maxima of tensile strength probability on the $\epsilon = h$ line (around 70%) and a decrease of this probability when receding from this line. Note that this diagram was built by extrapolating the evolutions of R and S to all (h, ϵ) couples while only two directions ($h, \epsilon = 0.5$ m) and ($h = 1$ m, ϵ) have been explored. Other simulations would be necessary to confirm the validity of this diagram. Another diagram was drawn for the evolution of the tensile failure probability with the tensile strength σ_T and slab depth h for a constant correlation length $\epsilon = 0.5$ m (Fig. 6b). For this diagram, simulations on the complete grid were made, ensuring its accuracy. We can clearly note that, globally, for tensile strength values σ_T higher than the average cohesion $\langle c \rangle = 1$ kPa, the tensile failure probability is vanishing indicating that only full slope releases occur.

Evolution with σ_c for different slab depth h values

The adjustment of the evolution with σ_c of the tensile failure probability is more complex to obtain since the simulations have been done for a constant tensile strength value only $\sigma_T = 0.75$ kPa and thus the average $\langle \Delta\tau \rangle$ and the variance $\sigma_{\Delta\tau}$ cannot be determined by adjusting $P(\Delta\tau > \sigma_T)$ using Eq. (3) as it was done in the last section. Consequently, the evolutions of R and S with σ_c need to be anticipated.

We assume that the parameters R and S can be expressed through the following simple functions:

$$R = \frac{1}{rCV + 1} \quad \text{and} \quad S = \frac{1}{sCV + 1}, \quad (6)$$

with $CV = \sigma_c/\langle c \rangle$, r and s adjustment parameters. A good adjustment was found for $r = 16.5$ and $s = 13$ and was represented on Figs. 4a and 4b. Note that other evolutions of R and S with σ_c could also lead to suitable adjustments. Other sets of simulation for different tensile strength values would be necessary to obtain the most accurate adjustment.

These evolutions are represented on Fig. 7a in terms of average $\langle \Delta\tau \rangle = (1 - R)\langle c \rangle$ and standard deviation $\sigma_{\Delta\tau} = S\sigma_c$. Besides, 5 distributions of $\Delta\tau$ are represented in Fig. 7b illustrating the results of tensile failure probability (for $\sigma_T = 0.75$ kPa and $h = 1$ m). When σ_c is very low (e.g. 10 Pa), the whole distribution is far from the tensile strength line and thus the tensile failure probability is equal to 0%. Then, when σ_c increases (e.g. 65 Pa), a part of the right tail of the distribution goes beyond the tensile failure criterion leading to a probability of 8%. When the average of the distribution $\langle \Delta\tau \rangle$ becomes greater than σ_T (e.g. $\sigma_c = 215$ Pa), the tensile failure probability becomes greater than 50% (63%). Finally, for values of σ_c sufficiently high (e.g. 65 Pa), almost the whole distribution is beyond the tensile failure criterion and thus the tensile failure probability is close to 100% (99%). This illustrates the two following necessary constraints to obtain the good agreement with the results presented on Fig. 4:

- $\langle \Delta\tau \rangle$ must increase with σ_c and tend to $\langle c \rangle$ when $\sigma_c \rightarrow \infty$,
- the rate of increase of $\sigma_{\Delta\tau}$ with σ_c must not be too large compared to that of $\langle \Delta\tau \rangle$ for the tensile strength probability to tend to 100% (in this case) when σ_c is very high. In the opposite case, a residual part of the distribution of $\langle \Delta\tau \rangle$ could

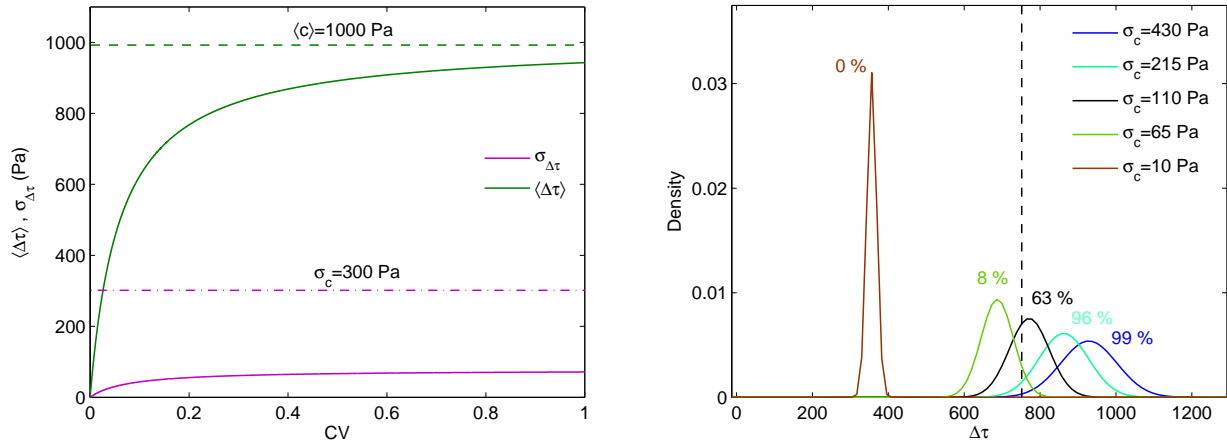


Fig. 7. (Left) Evolution of the average of the shear stress difference $\langle \Delta\tau \rangle = (1 - R)\langle c \rangle$ and of the standard deviation $\sigma_{\Delta\tau} = S\sigma_c$ as a function of the standard deviation of the weak-layer cohesion σ_c ($\epsilon = 0.5$ m, $\sigma_T = 0.75$ kPa). (Right) Evolution of the distribution of shear stress difference $\Delta\tau$ for different values of σ_c ($\epsilon = 0.5$ m, $\sigma_T = 0.75$ kPa, $h = 1$ m). The indicated percentage value corresponds to the probability $P(\Delta\tau > \sigma_T)$.

still be lower than σ_T even for large values of σ_c which would generate a decrease of the tensile failure probability.

6. CONCLUSION AND DISCUSSION

In this article, we presented two different release types observed in our simulations. (1) Full-slope releases are influenced by the morphology of the path since the heterogeneity is not sufficient to trigger a tensile failure. For instance, the tensile failure will be very sensitive to the presence of trees, rocks, ridges and local curvature. (2) Partial-slope releases for which

the local variations of weak-layer cohesion is substantial and can trigger the slab tensile crack on its own. Importantly, for both release types, the primary rupture process observed is always the basal shear failure of the weak layer. Hence slab rupture systematically constitutes a secondary process.

We have shown that the proportion between these two types is extremely dependent on the model parameters such as the tensile strength σ_T , the slab depth h , the correlation length ϵ , the standard deviation of the weak layer cohesion σ_c and probably on other parameters that have not been varied in this study such as the average cohesion $\langle c \rangle$. Besides, we pre-



Fig. 8. Diptych: Avalanche triggered by a snowboarder. The release area is defined by the ridge at the crown and rock and trees at flanks. Left side: before the impact of the snowboarder. Right side: after the impact. ©Rémi Petit.

sented a simple statistical model capable of reproducing the proportion between release types as a function of the model parameters. Two illustrations of this simple model are represented on Fig. 1. In the first case (Fig. 1a), the shear stress difference $\langle \Delta\tau \rangle$ is always lower than the tensile strength σ_T . The basal failure thus propagates over the entire system until the top boundary condition which can be seen as a ridge, a rock, a tree or a local curvature. In the second case (Fig. 1b), a local zone of substantial average $\langle \Delta\tau \rangle$ due to strong variation of the cohesion heterogeneity generates a local tensile failure within the slab since $\Delta\tau > \sigma_T$.

We have demonstrated that for values of σ_T higher than the average cohesion $\langle c \rangle$, the releases are full slope and consequently they are controlled by the morphology of the path. Let us recall that tensile strength values from laboratory tests appear to be globally higher than 1 kPa (Jamieson and Johnston, 1990; Sigrist, 2006) according to many different measurement techniques whereas shear strength values of weak layers are typically lower than 1 kPa. This indicates, for realistic values of the mechanical parameters, the major influence of slope morphology on the position of the tensile failure within the slab and thus on the extent of the release area. It corroborates the results found by Maggioni and Gruber (2003) who analyzed the influence of morphological features of the path on the extend of the release area using a purely data-driven statistical approach, and brings some mechanical justification to the predominance of local geometry in the localization of real avalanches. This result shows in particular that the release area will be extremely dependent on slope topography (local curvature, ridge...), on the presence of rocks and trees for instance. For example, Fig. 8 shows a typical slab avalanche release area defined by the ridge at the crown and by rocks and trees at flanks. This is a very important result than encourages us to pursue with more simulations to study for example the influence of curvature, ridge angle, rocks...

REFERENCES

- Ancey, C., C. Gervasoni and M Meunier, 2004. Computing extreme avalanches, *Cold Reg. Sci. Technol.*, **39**, 161–180.
- Barbolini, M, U Gruber, C Keylock, M Naaim and F Savi, 2000. Application and evaluation of statistical and hydraulic-continuum dense-snow avalanche models to five real European sites, *Cold Reg. Sci. Technol.*, **31(2)**, 133–149.
- Eckert, N, M Naaim and E. Parent, 2010. Long-term avalanche hazard assessment with a Bayesian depth-averaged propagation model, *J. Glaciol.*, **56(198)**, 563–586.
- Eckert, N., E. Parent, M Naaim and D. Richard, 2008. Bayesian stochastic modelling for avalanche predetermination: from a general system framework to return period computations, *SERRA*, **22**, 185–206.
- Eckert, N, E. Parent and D. Richard, 2007. Revisiting statistical-topographical methods for avalanche predetermination: Bayesian modelling for runout distance predictive distribution, *Cold Reg. Sci. Technol.*, **49(1)**, 88–107.
- Failletaz, J, F Louchet and J.R Grasso, 2004. Two-threshold model for scaling laws of noninteracting snow avalanches, *Phys. Rev. Lett.*, **93(20)**, 208001.
- Failletaz, J, F Louchet and J.R Grasso, 2006. Cellular automaton modelling of slab avalanche triggering mechanisms : from the universal statistical behaviour to particular cases, *Proceedings of the ISSW*, 174–180.
- Fyffe, B and M Zaiser, 2004. The effects of snow variability on slab avalanche release, *Cold Reg. Sci. Technol.*, **40**, 229–242.
- Fyffe, B and M Zaiser, 2007. Interplay of basal shear fracture and slab rupture in slab avalanche release, *Cold Reg. Sci. Technol.*, **49**, 2638.
- Gaume, J., G. Chambon, N. Eckert and M. Naaim, 2012a. Influence of weak-layer heterogeneity on snow slab avalanche release: Application to the evaluation of avalanche release depths., submitted to *J.Glaciol.*
- Gaume, J., G. Chambon, N. Eckert and M. Naaim, 2012b. Relative influence of mechanical and meteorological factors on avalanche release depth distributions., *Geophys. Res. Lett.*, **39**, L12401, in prep.
- Jamieson, B and C Johnston, 1990. In-situ tensile tests of snowpack layers, *J. Glaciol.*, **36(122)**, 102–106.
- Maggioni, M. and U Gruber, 2003. The influence of topographic parameters on avalanche release dimension and frequency, *Cold Reg. Sci. Technol.*, **37**, 407–419.
- Maggioni, M., U. Gruber and M. Stoffel, 2002. Definition and characterisation of potential avalanche release areas, *Proceedings of the ESRI Conference, San Diego*.
- McClung, D.M., 2003. Size scaling for dry snow slab release, *J. Geophys. Res.*, **108(B10)**, 2465–2477.
- Naaim, Mohamed, T Faug and F Naaim-Bouvet, 2003. Dry granular flow modelling including erosion and deposition, *Surveys in Geophysics*, **24**, 569–585.
- Salm, B., A. Burkard and H. Gubler, 1990. Berechnung von fließlawinen: eine anleitung fr pratiker mit beispielen, *Internal report EISLF (in German)*, **47**.
- Sigrist, C, 2006. Measurements of fracture mechanical properties of snow and application to dry snow slab avalanche release, (PhD thesis), ETHZ.

Chapter 5

Mapping extreme snowfalls in the French Alps using Max-Stable processes

This chapter is composed of an article entitled “Mapping extreme snowfalls in the French Alps using Max-Stable processes” which was **submitted** to *Water Resources Research*. The following authors helped in the construction of this paper: Nicolas Eckert, Guillaume Chambon, Mohamed Naaïm and Liliane Bel.

Snowfalls intensity and frequency are one of the most important parameters in avalanche hazard mapping procedures. To compute accurate avalanche release depth distributions, a purely mechanical model is insufficient and needs to be coupled with snowfall distributions. In this paper, the formalism of max-stable processes, generalizing extreme value statistics to the multivariate spatial case is used to map snowfall annual maxima in the French Alps. We show in particular how snowfall quantile maps for different return periods can be obtained using smooth spatial evolution models for the GEV parameters implemented within a Brown-Resnick max-stable model taking into account orographic gradients and anisotropy.

Mapping extreme snowfalls in the French Alps using Max-Stable processes.

J.Gaume,¹ N.Eckert,¹ G.Chambon,¹ M.Naaim,¹ and L.Bel²

Abstract. The evaluation of extreme snowfalls is an important challenge for hazard management in mountainous regions. In this paper, extreme snowfall data acquired from 40 meteorological stations in the French Alps since 1966 are analyzed using spatial extreme statistics. They are then modeled within the formal framework of max-stable processes which are the generalization of univariate extreme value theory to the spatial multivariate case. The three main max-stable processes now available are fitted on the data using composite likelihood maximisation, and the most flexible Brown-Resnick one is retained on the basis of the TIC criterion, taking into account anisotropy by space transformation. Furthermore, different models with smooth trends (linear and splines) for the spatial evolution of the GEV parameters are tested to allow snowfall maps for different return periods to be produced. After altitudinal correction that separates spatial and orographic effects, the different spatial models tested are fitted within the max-stable framework, allowing inference of the GEV margins and the extremal dependence simultaneously. Finally a nested model selection procedure is employed to select the best linear and spline models. Results show that the best linear model produces reasonable quantile maps (assessed by cross-validation using other stations) but that it is outperformed by the best spline model which better captures the complex evolution of GEV parameters with space. For a given return period and at fixed elevation of 2000 m, extreme 3-day snowfalls are higher in the NE and SE of the French Alps. Maxima of the location parameter of the GEV margins are located in the North and South while maxima of the scale parameter are located in the SE which corresponds to the Mediterranean influence that tends to bring more variability. Besides, the dependence of extreme snowfalls is shown to be stronger on the local orientation of the Alps in a range of 60° , an important result for meteorological variables confirming previous studies. Computations are performed for different accumulation durations which enables obtaining magnitude – frequency curves and showing that the intensity of the extremal directional dependence effect is all the more important when the duration is short. Finally, we show how the fitted model can be used to evaluate joint exceedence probabilities and conditional return level maps which can be useful for risk management in practice.

1. Introduction

The evaluation of extreme snowfalls is a challenging issue for risk management in mountainous regions. In particular, extreme snowfall constitutes one of the critical parameters for road viability analysis and avalanche risk management [e.g. *Schweizer et al.*, 2009]. For instance, the systematic implementation of avalanche propagation models requires the precise evaluation of the snow input distribution [e.g. *Ancey et al.*, 2004; *Eckert et al.*, 2010b]. In France, the 100-year quantile (quantile corresponding to a return period $T = 100$ years) is widely used for hazard mapping or for the conception of defence structures. However, in practice, the evaluation of this input turns out to be difficult for several reasons:

(i) In mountainous areas, available data are sparse with generally incomplete and short time series very rarely longer than 100 years. Consequently, extrapolating beyond the

highest observed values is necessary. In this context, Extreme Value Theory (EVT) is an adequate formalism to deal with, since it provides solid theoretical basis for extrapolation, namely the convergence of block maxima to the GEV (Generalized Extreme Value) distribution [Fisher-Tippet theorem *Fisher and Tippett*, 1928] and of Peaks Over Thresholds (POT) to the GPD (Generalized Pareto Distribution) via Pickands theorem [*Pickands*, 1975].

(ii) The data consist mostly in chronicles of precipitation measured in water equivalent (w.e.). The distinction rain/snow is not always done, which requires the joint analysis of temperature series.

(iii) Measurement stations are usually located far from avalanches release zones. It is therefore necessary to use spatial interpolation methods adapted to the specificity of extreme values.

(iv) These stations are usually located in the valleys rather than at high altitudes, which requires using an orographic snowfall gradient for the quantification of the water equivalent in avalanche release zones.

In the current engineering practice, all these difficulties are often circumvented by over-simplifying assumptions. The problems of spatial interpolation and orographic effects are sometimes treated by defining “homogeneous zones by altitude band” [*Salm et al.*, 1990; *Bocchiola et al.*, 2006]. Besides the difficulty of zones definition, this method introduces discontinuities at the zone borders that are incompatible with the natural phenomenon. Simple kriging

¹IRSTEA, UR ETGR, 38400 St Martin d’Heres, France.

²AgroParisTech/INRA,UMR 518 Math. Info. Appli., F-75005 Paris, France

interpolation techniques have also been used, for example *Prudhomme and Reed* [1999] for extreme rainfall mapping in Scotland using a Gaussian field. This method has the advantage of allowing smooth spatial prediction but without acknowledging the specificity of extreme values. *Weisse and Bois* [2001] also used kriging for rainfall quantile mapping. In this case, the previous limitation is thus partially overcome by smoothing directly the quantile of interest obtained by fitting adapted EVT-like distributions rather than the process. However, this method has the main drawback of separating two estimation procedures (local GEV distributions and spatial fields) without reporting the local error on the spatial model. Furthermore, it loses estimation power by using one single quantile value per location instead of the full series of maxima. Finally, for extrapolation, the current engineering methods use almost systematically Gumbel laws rather than a more general model of the GEV type. This can result in systematic underestimation of most extreme snowfalls [*Parent and Bernier*, 2003; *Bacro and Chaouche*, 2006].

An important point in spatial extreme approaches is that covariates are often used to infer the spatial dependence of the GEV parameters, the rationale being the capability to predict high quantiles at any point and to reduce the dimension of the problem. *Blanchet and Lehning* [2010] used both altitude and the mean snow depth [“Climate space”, *Cooley et al.*, 2007] to characterize extreme snow depths at the ground level using smooth spatial models for the GEV parameters. These authors have shown the superiority of such an approach over quantile smoothing even without modeling the extremal dependence. Many other studies have already considered the GEV parameters as spatial fields [*Naveau et al.*, 2009], especially in the context of gridded data resulting from climate modeling [*Rust et al.*, 2009; *Maraun et al.*, 2010].

Recently, a solid formalism based on multivariate extreme value theory has been proposed to characterize the spatial dependence of block maxima extreme values. Applied to a set of data series, maps of extremal dependence can be obtained [*Coles et al.*, 1999]. Furthermore, the definition of an extremal function can extend to spatial fields of extreme values the notions of variogram and range; the distance up to which the different series are dependent [*Cooley et al.*, 2006]. This formalism is now beginning to be successfully applied in hydrology. For instance *Bel et al.* [2008] compared different spatial models on extreme temperature and rainfall data and *Blanchet et al.* [2009] analyzed the spatial dependence of extreme snowfalls in the Swiss Alpine region using the χ and $\bar{\chi}$ statistics [*Joe*, 1993; *Coles et al.*, 1999].

To model spatial dependence in extreme values consistently with extreme value theory, Max Stable Processes (MSP) is an approach based on the pioneering work of *Brown and Resnick* [1977]; *DeHaan* [1984] and further developed by *Smith* [1991]; *Schlather* [2002]; *Schlather and Tawn* [2003] and *Kabluchko et al.* [2009]. Their practical use in environmental sciences is very recent. It has been applied with success by *Padoan et al.* [2009] combined with the use of latitude, longitude and altitude as covariates to model rainfall data in the Appalachian mountains. This paper also proposes a practical inferential method for the fitting of max-stable processes to spatial data by maximisation of a composite likelihood [*Lindsay*, 1988; *Xu and Reid*, 2011], since the full likelihood is out of reach. This has been applied by [*Blanchet and Davison*, 2011] for snow depth data with a modified anisotropic Schlather’s MSP, chosen among large classes of Smith and Schlather MSPs.

The aim of this article is the modeling of extreme snowfalls in the French Alps by Max-Stable processes, a crucial ingredient to evaluate avalanche depths distributions in all potential release areas [*Gaume et al.*, 2012]. Snowfalls are measured in water equivalent w.e. and are thus independent

of density effects. In this spirit, a simple method is proposed to apply the spatial extreme formalism at a constant altitude so as to infer “true” spatial effects. With regards to existing approaches, we bridge the work of *Blanchet and Lehning* [2010] and *Blanchet and Davison* [2011] by estimating the GEV parameters as continuous functions of space within the max-stable framework. Furthermore, in addition to the more classical Smith and Schlather MSP, we implement the more flexible Brown-Resnick MSP, more adapted to snowfalls, a less spatially dependent variable than snow depth. We take also into account directional effects related to the local alpine geography. Finally, we show how quantile maps can be obtained and demonstrate the prediction ability of our approach using cross-validation for the used data sets but also for other stations.

As stated in *Segers* [2012] and *Ribatet and Sedki* [2012], max-stable copulas would have been another option to reach similar goals (other copulas, often used in hydrology, would fail in providing a fair representation of the dependence structure). However, this would have implied fitting first the margins at each station (a not necessarily easy task) and the extremal dependence structure in a second time. Our work is one of the firsts that performs the two steps simultaneously. This is for us theoretically preferable, since it takes into account estimation error on the margin parameters in the estimation of the parameters of the extremal model.

This article is organized as follows: Sec. 2 provides theoretical elements about extreme value statistics in the spatial case and more precisely about MSP. The studied data are presented in Sec. 3 in which an empirical analysis is performed. In Sec. 4, a criterion for model selection is defined and the results using linear models and penalized smoothing splines are compared. Finally, in Sec 5, a discussion is dedicated to the comparison of our results to previous approaches, to the study of the influence of the accumulation period on the results and to a joint analysis that uses the available bivariate distributions and conditional levels which can be useful for operational purposes.

2. Extreme value statistics in the spatial case

2.1. Max-Stable Process (MSP)

$\{Z(\mathbf{x})\}_{\mathbf{x} \in \mathcal{X}}$ is a max-stable process if there exist sequences $a_n(\mathbf{x})$ and $b_n(\mathbf{x}) > 0$, such that if for all n , $(Z_i)_{i=1,n}$ are independent copies of Z , then $\{Z(\mathbf{x})\}_{\mathbf{x} \in \mathcal{X}}$ has the same distribution as

$$\left\{ \frac{\max_{i=1,n} Z_i(\mathbf{x}) - a_n(\mathbf{x})}{b_n(\mathbf{x})} \right\}_{\mathbf{x} \in \mathcal{X}}$$

As a consequence, all finite dimensional marginal distributions are max-stable and, in particular, the univariate marginal $Z(x)$ distribution belongs to the GEV family:

$$P(Z(\mathbf{x}) \leq z) = \begin{cases} \exp \left[- (z'(\mathbf{x}))^{-1/\xi(\mathbf{x})} \right] & \text{if } z'(\mathbf{x}) > 0 \\ 1 & \text{otherwise} \end{cases} \quad (1)$$

with

$$z'(\mathbf{x}) = 1 + \frac{\xi(\mathbf{x})(z - \mu(\mathbf{x}))}{\sigma(\mathbf{x})} \quad (2)$$

where $\mu(\mathbf{x})$, $\sigma(\mathbf{x})$ and $\xi(\mathbf{x})$ are respectively the location, scale and shape parameters at location \mathbf{x} . According to the sign of $\xi(\mathbf{x})$, the $Z(\mathbf{x})$ distribution belongs to three different families of distributions known as Frchet ($\xi(\mathbf{x}) > 0$), Weibull ($\xi(\mathbf{x}) < 0$) and Gumbel ($\xi(\mathbf{x}) \rightarrow 0$).

Usually it is convenient to transform the univariate marginals setting:

$$Z^*(\mathbf{x}) = \left(1 + \xi(\mathbf{x}) \frac{(Z(\mathbf{x}) - \mu(\mathbf{x}))}{\sigma(\mathbf{x})}\right)^{1/\xi(\mathbf{x})}. \quad (3)$$

Z^* is thus a max-stable process with unit Frchet margins whose cumulative distribution function is defined as $P(Z^*(\mathbf{x}) \leq z^*) = \exp(-1/z^*)$, $z^* > 0$. Models of max-stable processes have been proposed by several authors. The most popular are those of *Smith* [1991] (extremal Gaussian) a particular case of *DeHaan* [1984] construction, *Schlather* [2002], and *Brown and Resnick* [1977] generalized by *Kabluchko et al.* [2009]. We will focus in this work mainly on the Kabluchko model defined as:

$$Z(\mathbf{x}) = \max_i (\xi_i \exp(W_i(\mathbf{x}) - \sigma^2(\mathbf{x})/2)) \quad \mathbf{x} \in \mathcal{X}, \quad (4)$$

where ξ_i is a Poisson process on \mathbb{R}^{*+} of intensity $\frac{1}{\xi^2} d\xi$ and W_i are independent Gaussian fields, with stationary increments, variance $\sigma^2(\mathbf{x})$ and variogram $\gamma(\mathbf{x} - \mathbf{x}')$.

2.2. Extremal coefficient

Spatial dependence of maxima at two locations \mathbf{x} and \mathbf{x}' is characterized by the extremal coefficient denoted $\theta(\mathbf{x}, \mathbf{x}')$. If Z^* is the limiting process of maxima with unit Fréchet margins then [*Brown and Resnick*, 1977]:

$$\begin{aligned} P(Z^*(\mathbf{x}) \leq z, Z^*(\mathbf{x}') \leq z) &= P(Z^*(\mathbf{x}) \leq z)^{\theta(\mathbf{x}, \mathbf{x}')} \\ &= \exp(-\theta(\mathbf{x}, \mathbf{x}')/z) \end{aligned} \quad (5)$$

Thus, if $\theta(\mathbf{x}, \mathbf{x}') = 1$ there is perfect dependence of the maxima at stations \mathbf{x} and \mathbf{x}' and on the contrary, if $\theta(\mathbf{x}, \mathbf{x}') = 2$ the maxima are independent. For Smith, Schlather and Brown-Resnick models the extremal coefficient can be calculated explicitly. According to these models, the processes are stationary, and the related extremal coefficient only depends on $\mathbf{h} = \mathbf{x} - \mathbf{x}'$. The Smith's model extremal coefficient θ_{Sm} is given by:

$$\theta_{Sm}(\mathbf{h}) = 2\Phi(a(\mathbf{h})/2), \quad (6)$$

with $a(\mathbf{h}) = (\mathbf{h}^t \Sigma \mathbf{h})^{1/2}$ the Mahalanobis distance, Σ a Gaussian covariance matrix with three parameters σ_{11} , σ_{12} , σ_{22} and Φ the standard normal cumulative distribution. The Schlather's extremal coefficient θ_{Sc} is given by:

$$\theta_{Sc}(\mathbf{h}) = 1 + \sqrt{1 - \frac{1}{2}(\nu(\|\mathbf{h}\|) + 1)} \quad (7)$$

with $-1 \leq \nu(\|\mathbf{h}\|) \leq 1$, a valid correlation function (Wittle-Matern, Cauchy, exponential, Bessel, etc.). We tested several forms of correlation functions and we retained the exponential correlation function $\nu(\mathbf{h}) = \exp(-\|\mathbf{h}\|/c_1)$ where c_1 is a range parameter, that gave the best fit to our data on the basis of the TIC criterion (see below)

Finally, the Brown-Resnick's extremal coefficient θ_{BR} is given by:

$$\theta_{BR}(\mathbf{h}) = 2\Phi\left(\sqrt{\frac{\gamma(\|\mathbf{h}\|)}{2}}\right). \quad (8)$$

The behaviour of the extremal coefficient may give an indication for the choice of the model. For instance the Schlather's MSP cannot achieve full independence ($\theta = 2$). This can be useful for applications with extremal dependence that remains strong even at very important distances, but is a major flaw in other cases. Instead, the Smith's MSP imposes full independence at long distances ($\theta_{Sm} \xrightarrow{\infty} 2$) but is quite rigid at short distances. The Brown-Resnick's MSP

is more flexible as the variogram may take a great variety of shapes near 0 and allowing for full independence ($\theta_{BR} \xrightarrow{\infty} 2$) at long distances [Eq. (8)].

The Smith's MSP can directly model the anisotropy in the extremal coefficient by using a modified distance (Mahalanobis), a function of the Gaussian covariance matrix Σ . This covariance matrix plays a very important role because it determines the elliptical shape of the extremal dependence. On the contrary, Schlather's and Brown-Resnick's MSP are primarily isotropic as they involve the Euclidean distance. Thus, to take into account possible directional effects in extreme snowfalls in the case of Schlather's and Brown-Resnick's MSP, we must modify the standard space [*Blanchet and Lehning*, 2010] while inferring the extremal dependence. To do this, we set $\tilde{\mathbf{E}} = V\mathbf{E}$ with $\mathbf{E} = [\text{long lat alt}]^t$ the Euclidean coordinates and V the rotation matrix defined below:

$$V = \begin{pmatrix} \cos \psi & \sin \psi & 0 \\ -\rho \sin \psi & \rho \cos \psi & 0 \\ 0 & 0 & 1 \end{pmatrix}, \quad (9)$$

where ψ represents the anisotropy angle of the transformation and ρ its intensity.

2.3. Spatial models for the GEV parameters

At a given location \mathbf{x} , GEV parameters $\mu(\mathbf{x})$, $\sigma(\mathbf{x})$, $\xi(\mathbf{x})$ can be estimated if there are observations available. If no data are available at \mathbf{x} , these parameters must be inferred from data at nearby locations. This can be done essentially in two ways: (1) estimate first the pointwise GEV parameters at locations with observations, and interpolate or (2) model the spatial evolution of the GEV parameters [*Blanchet and Lehning*, 2010]. We choose the second option and we investigate within the max-stable formalism two classes of spatial models for the GEV parameters. The first model links linearly the GEV parameters at location \mathbf{x} with the spatial coordinates $\mathbf{x}_1 = \text{long}(\mathbf{x})$, $\mathbf{x}_2 = \text{lat}(\mathbf{x})$. If η is one of the 3 GEV parameters

$$\eta(\mathbf{x}) = \beta_0 + \beta_1 \mathbf{x}_1 + \beta_2 \mathbf{x}_2, \quad (10)$$

the second model is non-linear, it decomposes η in an appropriate basis $B = (b_j)_j$:

$$\eta(\mathbf{x}) = \sum_{j=1}^m \beta_j b_j(\mathbf{x}). \quad (11)$$

In the following, we will consider penalized splines with radial basis functions (pr-splines) [*Ruppert et al.*, 2003] of order 3:

$$\eta(\mathbf{x}) = \beta_0 + \beta_1 \mathbf{x}_1 + \beta_2 \mathbf{x}_2 + \sum_{r=0}^{R-1} \beta_{3+r} \|\mathbf{x} - \kappa^r\|^3, \quad (12)$$

where κ^r are the coordinates of the r^{th} knot of the spline and R is the number of knots.

3. Empirical analysis

3.1. Data presentation

MeteoFrance, the French meteorological agency, provided us with daily controlled and homogenized snowfall measurements (in water equivalent w.e.) for 124 Alpine weather stations with different temporal series length. We retained for the modelling 40 weather stations whose measurements were conducted continuously from 1966 to 2009 (i.e. 44 years

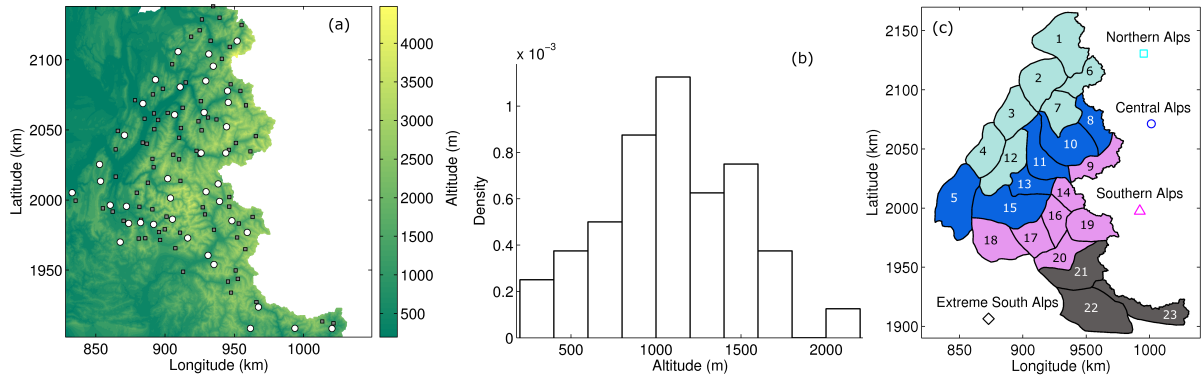


Figure 1. (a) Location of weather stations on the alpine terrain (coordinates in meters extended Lambert II). The circles represent the 40 retained weather stations and the squares the 84 stations with shorter time-series used for model validation. (b) Distribution of the altitudes of the 40 retained stations (in meters). (c) The French Alps divided into 4 Alpine zones. The numbers are massifs index summarized in Table 1.

Table 1. Details of the mountainous massifs of the French Alps presented on Fig. 1c with their highest peak and winter mean snowfall WMS [from Durand et al., 2009]

Index	Massif	Highest peak (m)	WMS (mm w.e.)
1	Chablais	2466 m	941
2	Aravis	2752 m	1006
3	Bauges	2217 m	1003
4	Chartreuse	2082 m	1015
5	Vercors	2341 m	844
6	Mont-Blanc	4810 m	885
7	Beaufortin	2995 m	874
8	Haute-Tarentaise	3747 m	658
9	Haute-Maurienne	3751 m	508
10	Vanoise	3855 m	632
11	Maurienne	3779 m	718
12	Belledonne	2977 m	906
12	Grandes-Rousses	3465 m	708
14	Thabor	3178 m	499
15	Oisan	3983 m	703
16	Pelvoux	4102 m	658
17	Champsaur	3163 m	628
18	Devoluy	2789 m	631
19	Queyras	3385 m	387
20	Parpaillon	3046 m	448
21	Ubaye	3412 m	446
22	Alpes-Azures	3050 m	620
23	Mercantour	3143 m	651

of measurement) and the 84 others with shorter time-series were kept for model validation. Fig. 1a shows the location of all stations on the French alpine terrain. Fig. 1b shows the altitude distribution of the 40 retained stations. One can notice that most weather stations are located around 1000 m of altitude, and that very few stations are available at high altitudes (> 2000 m). Fig. 1c shows the partition of the French Alps into 4 main alpine zones: Northern Alps, Central Alps, Southern Alps and extreme Southern Alps and also 23 massifs. Details on the mountainous massifs with their highest peak and winter mean snowfall [from Durand et al., 2009] are presented in Tab. 1.

We extracted from this database, annual snowfall maxima over different accumulation periods (1 to 7 days) for each weather station. Only the winter period (November 15 to May 15) and snow precipitations were considered. Thus, for the search of maxima, only the days when maximum temperature is below 2°C at the measurement station were considered. This is sufficient to ensure that precipitations fall as snow in avalanche release areas. We will focus mainly in the following on the accumulation period of 3 days since it is

often considered as the best avalanche predictor [Salm et al., 1990; Schweizer et al., 2003; Ancey et al., 2004; Schweizer et al., 2009] for high return period events. In fact, this duration often corresponds to the most intense avalanche cycles [Eckert et al., 2010a]. In accordance with Sec. 2, $Z(\mathbf{x})$ denotes henceforth the annual snowfall maximum over 3 days at the weather station of coordinate \mathbf{x} .

3.2. Altitude consideration

As shown in Fig. 1b, the number of measurement stations above 2000 m is very low, which complicates the interpolation at higher altitudes where most avalanche release zones are located. Hence, we used an orographic gradient $\delta(\mathbf{x})$ by alpine zone from the study of Durand et al. [2009] represented on Fig. 2, to transform the data at the altitude $\text{alt}(\mathbf{x})$ to the same constant altitude level (2000 m):

$$z(\mathbf{x}, 2000) = z(\mathbf{x}, \text{alt}(\mathbf{x})) \underbrace{\left[1 + \delta(\mathbf{x}) \frac{2000 - \text{alt}(\mathbf{x})}{\text{WMS}(\mathbf{x})} \right]}_{G(\mathbf{x})} \quad (13)$$

where $z(\mathbf{x}, 2000)$ and $z(\mathbf{x}, \text{alt}(\mathbf{x}))$ are the snowfall annual maximum data in \mathbf{x} at 2000 m and at altitude $\text{alt}(\mathbf{x})$, respectively.

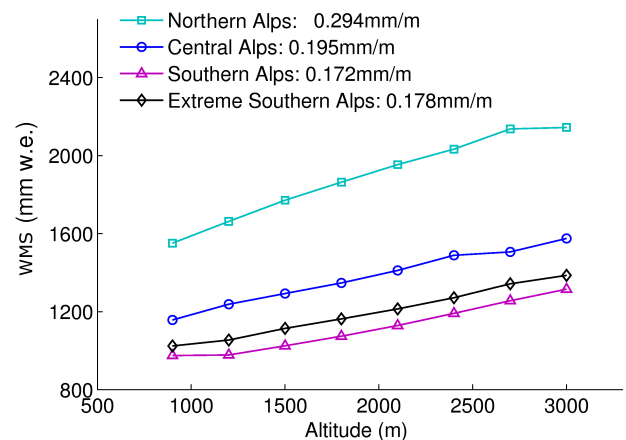


Figure 2. Evolution of mean winter snowfall (WMS) as a function of altitude for the four alpine zones. Figure constructed from Durand et al. [2009].

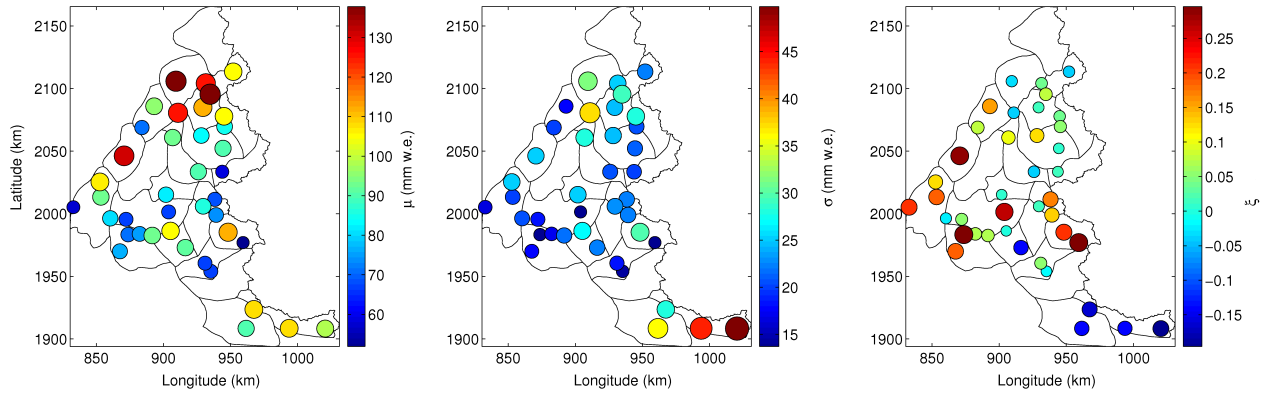


Figure 3. Maps of the GEV parameters estimated pointwise on the transformed data (alt= 2000m). (a) Location parameter μ , (b) scale parameter σ , (c) shape parameter ξ .

This transformation involves the massif's winter mean snowfall $WMS(\mathbf{x})$ (see Tab. 1) for weighting the local annual maximum. We also take into account an attenuation of the gradient above a given threshold altitude $s(\mathbf{x})$ (2700m for the Northern Alps, 3000m in the central Alps, South and extreme South Alps, see Figure 2 [Durand et al., 2009]). This amounts to replacing $alt(\mathbf{x})$ by $s(\mathbf{x})$ in Eq. (13) when $alt(\mathbf{x}) > s(\mathbf{x})$. This consideration of the altitude is equivalent to assuming that the annual maxima varies with altitude as a proportion of the annual accumulation. This assumption is reasonable because the annual accumulation can often be explained by a few extreme events only. It is easily shown that the transformation of annual snowfall maxima using Eq. (13) is equivalent to the transform of the location and scale parameters by multiplying them by G while the shape parameter remains constant i.e. the marginal distribution of $Z(\mathbf{x}, 2000)$ is a $GEV(\mu(\mathbf{x})G(\mathbf{x}), \sigma(\mathbf{x})G(\mathbf{x}), \xi(\mathbf{x}))$. Hence, this simple way of handling orographic gradients enables a full analytical formulation of GEV marginals at the transformed altitude. From the point of view of the spatial analysis, it has the advantage of keeping only longitude-latitude effects in the spatial variation and avoids specifying a distance in the 3D space, which is difficult since 1 m of altitude difference should certainly weight differently than 1 m latitude/longitude. More practically, vertical gradients could not be inferred directly from our data since the altitude range of the stations is too small.

The results obtained in the Swiss Alps [Blanchet et al., 2009] on the evolution of extreme snowfall with elevation support our way of handling altitude. Indeed, with 247 stations in the Swiss Alps including SLF automatic stations between 1600 m and 3000 m, these authors were able to distinguish trends of evolution of the GEV parameters with altitude: the location μ and scale σ parameters are increasing functions of altitude (with a gradient of ≈ 0.015 mm/m for μ and 0.003 mm/m for σ) while the shape parameter ξ is almost not influenced by altitude. In our case, the average location parameter gradient is equal to 0.02 mm/m very close to the Swiss one and the average scale parameter gradient is equal to 0.006 mm/m, slightly higher than the Swiss one.

3.3. Pointwise GEV parameters

The GEV parameters μ , σ and ξ have been estimated pointwise on the transformed data [Eq. 13] by maximization of the marginal likelihood for each station and plotted on maps (Fig. 3) and versus longitude and latitude in Fig. 5.

Firstly, it can be noted that, for the three GEV parameters, there are strong disparities between zones, especially between the extreme Southern Alps and the rest of the Alps. Concerning the location parameter μ , there is a decrease with latitude from the extreme Southern Alps to the Central Alps and then an increase from Southern Alps to Northern Alps. Regarding the evolution with the longitude, it is difficult to distinguish any significant trend, except a slight increase. Thus, at first sight, latitude seems to be a good covariate to explain the location parameter μ . The scale parameter σ decreases generally from the extreme Southern Alps to the Southern Alps, before stabilizing in the Central Alps and the Northern Alps. Hence, as shown in Figs. 5b and 5e, the longitude and latitude appear preliminarily as two good covariates for the scale parameter σ . Finally, from Fig. 3, the shape parameter ξ appears to be generally positive (Frechet domain) except in the extreme southern Alps where it is negative (Weibull domain). It increases with latitude from extreme southern Alps to the Southern Alps by

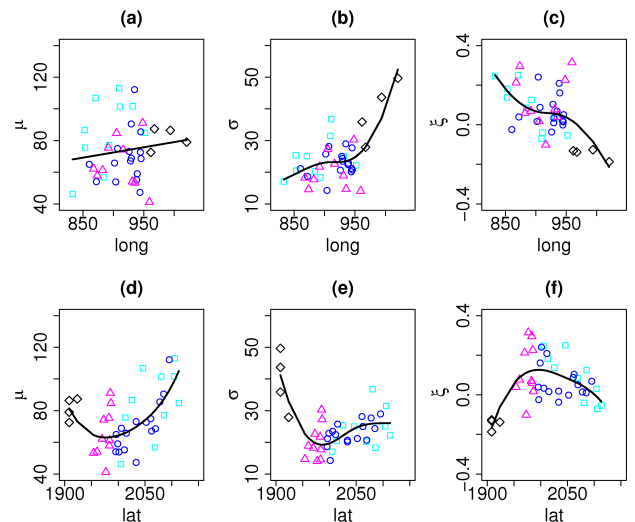


Figure 5. Evolution of the GEV parameters μ , σ and ξ determined pointwise on the transformed data (alt= 2000 m) as functions of longitude and latitude (in km). Cubic pr-splines with two knots have been adjusted on each graph (solid line). The symbols/colors represent the four alpine zones: the Northern Alps, Central Alps, Southern Alps and extreme Southern Alps (see Fig. 1c).

changing its sign, then decreases globally to the Northern Alps. It generally decreases with longitude from the Northern Alps to extreme southern Alps. Again, latitude and longitude thus appear to be two good potential covariates for ξ (Figs. 5c and 5f).

These variations must be taken with care since the GEV parameters (μ , σ , ξ) are correlated and thus some compensation may occur. However, they suggest that there is strong spatial variability of snowfall annual maxima over the whole French Alps. In particular, the extreme southern Alps seem to behave differently than the rest of the Alps. This is probably due to climatic differences between alpine areas, which are submitted to different precipitation regimes. Indeed, Northern and Central Alps are generally affected mainly by westerly flows whereas Southern and more particularly extreme Southern Alps are more often affected by easterly flow patterns which are strongly controlled by the Mediterranean influence.

3.4. Extremal dependence

The spatial dependence of 3-days annual snowfall maxima was studied empirically, by calculating the extremal coefficient for each pair of stations (780 pairs) by likelihood maximisation [Bel et al., 2008]. These values were plotted against the 2D-distance between stations in Fig. 4. Other estimators such as least squares and Cooley-Naveau-Poncet [Cooley et al., 2006] were also tested and gave similar results. Note that values higher than 2 were constrained to 2. We remark that full independence ($\theta = 2$) is achieved only for a very small number of pairs. Distance classes are defined as intervals and averages were then computed within the classes and have been added to Fig. 4 without taking into account directional effects.

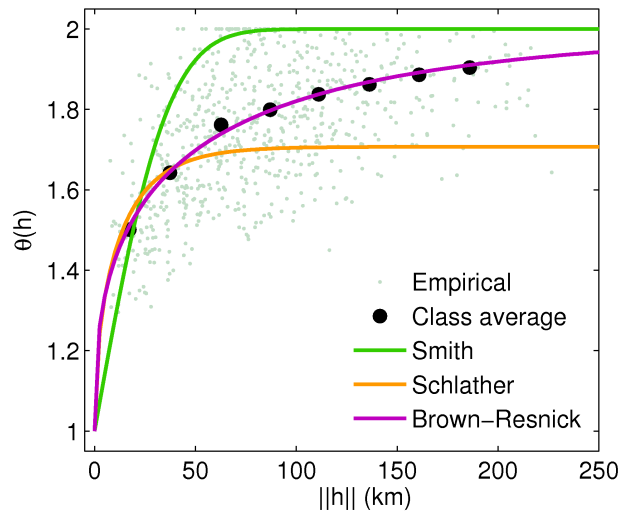


Figure 4. Extremal coefficient estimated for all pairs of stations as a function of the distance between the stations using likelihood maximisation estimation. The black dots represent the averaged extremal coefficient by distance classes. Smith's, Schlather's and Brown-Resnick's extremal coefficients were adjusted to the class averages.

Extremal coefficients of Smith [Eq. (6)], Schlather [Eq. (7)] and Brown-Resnick [Eq. (8)] were fitted to the average extremal coefficient. For the Brown-Resnick MSP, a power variogram $\gamma(\mathbf{h}) = \|\mathbf{h}\|^b/a$ was used to fit the data. It can be noted that the Schlather's and Smith's extremal coefficients provide a poor fit. Indeed, with only one single

parameter (dependence range) both models are very rigid, one imposing the asymptotic independence ($\theta_{Sm}(\mathbf{h}) = 2$ for $\|\mathbf{h}\| \rightarrow \infty$) at large distance and strongly constraining the shape at the origin (Smith), the other imposing a rather strong extremal dependence even at long distances (Schlather: $\theta_{Sc}(\mathbf{h}) = 1 + \sqrt{2}/2$ for $\|\mathbf{h}\| \rightarrow \infty$). Instead, the Brown-Resnick process has an additional smoothing parameter b and thus the shape of the extremal dependence is more flexible than in the case of the previous models which leads to an excellent fit (Fig. 4) of the average extremal coefficient. If we define the range r as the distance corresponding to an extremal coefficient $\theta = 1.9$, the Brown-Resnick model gives a range of $r = 182\text{km}$, identical to the one provided by empirical estimation. Note also that these results remain valid for different accumulation periods (1 to 7 days).

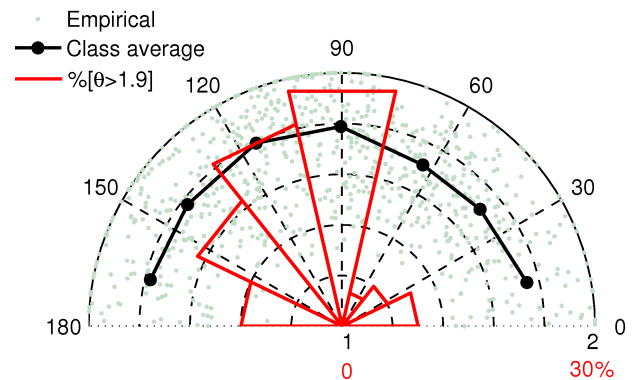


Figure 6. Extremal coefficient estimated for all pairs of stations as a function of α defined as the positive angle between the horizontal and the segment linking the pairs. The black dots represent the averaged extremal coefficient by angle classes (the value of the extremal coefficient is given by the radius). The red bar-plot represents the percentage of extremal coefficient values θ higher than 1.9.

The influence of a potential directional effect was also studied. Let us define α as the positive angle between the horizontal and the segment defined by two pairs of stations. Fig. 6 shows that extreme snowfalls show a strong directional effect. In most cases, the independence ($\theta > 1.9$) is only achieved for pairs of stations whose direction is higher than 90° . Averages by angle classes were also computed showing that, on average, extremal coefficient values are lower if $\alpha < 90^\circ$. In more details, the number of pairs whose extremal coefficient is higher than 1.9 is the lowest in the $[51^\circ - 77^\circ]$ range as well as for the lowest average extremal coefficient. Extremal dependence thus has a greater range along this interval of α than in other directions. Knowing that the main direction of the local Alpine axis is around 60° due to the presence of large valleys in this direction (Isere, Rhone and Durance), this suggests that annual snowfall maxima are very sensitive to the orientation of the mountains and the presence of valleys.

Finally, to investigate the strength of the extremal dependence between regions, 4 stations corresponding to different Alpine zones were chosen as references to compute maps of the interpolated extremal coefficient (Figs. 8b, 8c, 8d, and 8e). Besides, we have selected from the data in Fig. 4, only the pairs of stations for which $\theta(h) < 1.56$ (arbitrary choice to get a good visual) which were represented by a line connecting these pairs of stations in Fig. 8a. We can note a

strong regionalization of the extremal dependence. There is almost no spatial dependence between the extreme Southern Alps and the rest of the Alps. Similarly, the Southern Alps have a strong internal dependence but only a slight dependence with the rest of the Alps, except with a few stations of the Central Alps at the border with the Southern Alps. On the contrary, there is a strong dependence between the Northern Alps and Central Alps accompanied by a significant internal dependence. Finally, in agreement with the last observation, it seems that this dependence has a preferred orientation along the local Alpine axis.

This preliminary study suggests at first that the spatial dependence in extreme snowfall in the French Alps may be better captured by a Brown-Resnick MSP, which is shown to be more flexible than those of Smith and Schlather. In addition, an important directional effect is exhibited by this empirical analysis. The orientation of the Alps and the presence of large valleys are most likely the cause of these directional trends.

4. Application: Adjustment of a MSP to data.

4.1. Composite likelihood

In order to estimate the various parameters of the model (β matrix representing the spatial evolution of the GEV parameters and the dependence parameters), likelihood maximisation is used. However, we cannot calculate the complete likelihood since we only know analytically the expression of the different bivariate distributions according to Eq. (5). *Padoan et al.* [2009] showed that, for MSP, the full log-likelihood can be advantageously replaced by a special case of composite likelihood: the pairwise log-likelihood l_p defined as:

$$l_p(\beta, z) = \sum_{n=1}^N \sum_{i=1}^K \sum_{j=i+1}^{K-1} \log f(z_{n,i}, z_{n,j}; \beta), \quad (14)$$

with N the number of years of measurements, K the number of measurement stations, β the matrix of parameters to estimate and f the bivariate density of the MSP used (Smith, Schlather or Brown-Resnick). In our case, $z_{n,i}$ is the maximum annual precipitation for the year n and station i projected using Eq. (13) at a constant altitude level of 2000 m. One can then find the parameters $\hat{\beta}$ that maximize the composite likelihood by solving the partial differential equation:

$$\frac{\partial}{\partial \beta} l_p(\hat{\beta}, z) \Big|_{\beta=\hat{\beta}} = 0, \quad (15)$$

and derive the associated standard errors from the Hessian and Jacobian information matrices H and J , with

$$H(\hat{\beta}) = - \sum_{n=1}^N \sum_{i=1}^K \sum_{j=i+1}^{K-1} \frac{\partial^2 \log f(z_{n,i}, z_{n,j}; \hat{\beta})}{\partial \beta \partial \beta^t}, \quad (16)$$

and

$$J(\hat{\beta}) = \sum_{n=1}^N \sum_{i=1}^K \sum_{j=i+1}^{K-1} \frac{\partial \log f(z_{n,i}, z_{n,j}; \hat{\beta})}{\partial \beta} \frac{\partial \log f(z_{n,i}, z_{n,j}; \hat{\beta})}{\partial \beta^t}. \quad (17)$$

4.2. Model selection: TIC

To compare different MSP and models of spatial evolution, a criterion weighting the value of the likelihood by the number of model parameters to estimate can be used. The classic AIC [Akaike Information Criterion, *Akaike*, 1981]

cannot be used in our composite case since the complete likelihood is not known. We therefore use a derivative of AIC suitable for composite likelihood, the TIC (Takeuchi Information Criterion) [*Takeuchi*, 1976]:

$$\text{TIC}(\hat{\beta}) = -2l_p(\hat{\beta}, z) + 2\text{tr} \left(J(\hat{\beta}) H(\hat{\beta})^{-1} \right), \quad (18)$$

The best model is the one that minimizes the TIC [Eq. (18)]. Composite likelihood maximisation and TIC computations are carried out under the SpatialExtremes R package [*Ribatet*, 2009] complemented with personal communications.

4.3. Linear models

We choose to describe the parameters $[\mu(\mathbf{x}) \ \sigma(\mathbf{x}) \ \xi(\mathbf{x})]$ firstly through linear evolution models based on the coordinates $\mathbf{X} = [1 \ \text{lon}(\mathbf{x}) \ \text{lat}(\mathbf{x})]^t$. The linear evolution models that we use can be written as:

$$\begin{pmatrix} \mu(\mathbf{x}) \\ \sigma(\mathbf{x}) \\ \xi(\mathbf{x}) \end{pmatrix} = \begin{pmatrix} \beta_{\mu 0} & \beta_{\mu 1} & \beta_{\mu 2} \\ \beta_{\sigma 0} & \beta_{\sigma 1} & \beta_{\sigma 2} \\ \beta_{\xi 0} & \beta_{\xi 1} & \beta_{\xi 2} \end{pmatrix} \begin{pmatrix} 1 \\ \text{lon}(\mathbf{x}) \\ \text{lat}(\mathbf{x}) \end{pmatrix} \quad (19)$$

For the 3-day maxima, we tested 18 different forms for the matrix β , with different numbers of non-zero coefficients in the matrix β . Three models of MSP have also been fitted to the data for these different models of spatial evolution of the GEV parameters. Fig. 7 shows the values of the TIC [Eq. 18] for these different models. These models and the

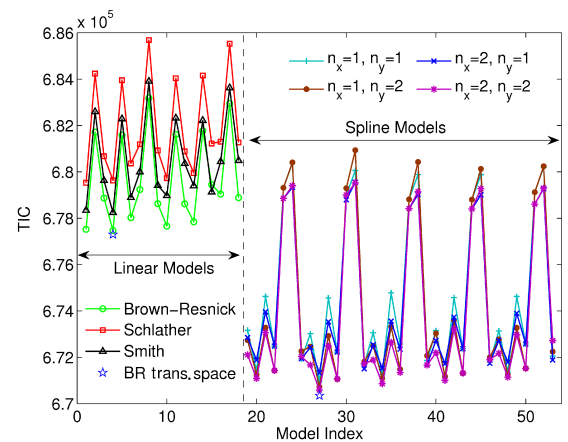


Figure 7. TIC values as a function of the type of linear evolution model for different MSP (Smith, Schlather, Brown-Resnick and Brown-Resnick with a transformed space.) and as a function of the type of pr-spline for different numbers of knots, using a Brown Resnick MSP. Details about the different models used can be found in Appendix 1.

Table 2. Parameters of the $\hat{\beta}$ matrix with the associated standard errors (in brackets) evaluated for the linear model 4 in Fig. 7 with a Brown-Resnick MSP and taking into account anisotropy by space transformation.

μ	$\beta_{\mu 0}$	$\beta_{\mu 1}$	$\beta_{\mu 2}$
	-328.7 (49.56)	0.0845 (0.0216)	0.1598 (0.0213)
σ	$\beta_{\sigma 0}$	$\beta_{\sigma 1}$	$\beta_{\sigma 2}$
	-38.39 (14.81)	0.0726 (0.0163)	0
ξ	$\beta_{\xi 0}$	$\beta_{\xi 1}$	$\beta_{\xi 2}$
	0.0536 (0.0294)	0	0

X - 8

GAUME ET AL.: MAX-STABLE MAPPING OF EXTREME SNOWFALLS

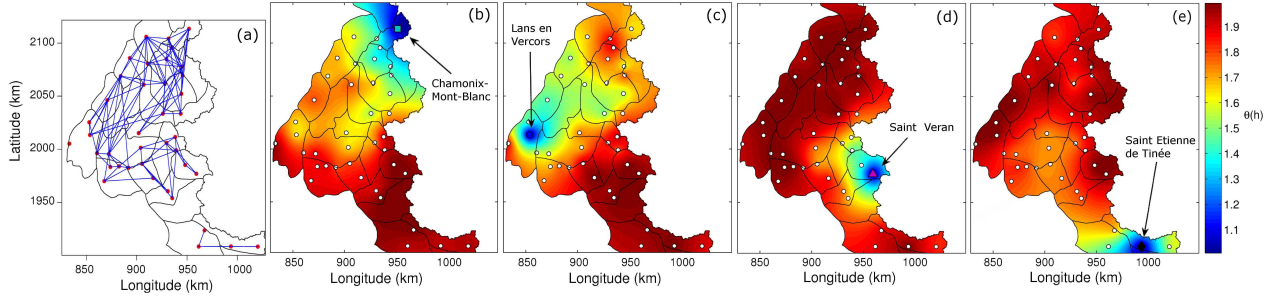


Figure 8. Pairs of stations whose extremal coefficient is less than 1.56 (a). Maps of the interpolated (simple kriging) extremal coefficients with reference to 4 stations belonging to the four alpine zones (Fig. 1c). (b) Chamonix-Mont-Blanc, (c) Lans en Vercors, (d) Saint Veran, (e) Saint Etienne de Tinée.

different used covariates are presented in detail in Appendix 1.

It can be noted that, for all the cases, the Brown-Resnick MSP (with a power variogram $\gamma(\mathbf{h}) = \|\mathbf{h}\|^b/a$) gives better results than the Smith MSP, itself better than Schlather MSP. The superiority of the Brown-Resnick MSP compared to the Smith one is related to its greater flexibility (form of the extremal coefficient) in agreement with the preliminary empirical study. Schlather's MSP gives even worse results since it does not account for complete asymptotic dependence ($\theta = 2$ for large distances). We therefore retain the Brown-Resnick MSP. Initially taken as isotropic, we further

improved it by transforming the standard space according to Eq. (9) in order to take into account the directional effects highlighted in the empirical analysis. This transformation allowed a non-negligible reduction of the TIC of ≈ 200 .

4.3.1. GEV parameters

It appears that models with evolution of μ with both longitude and latitude, and of σ with latitude give minimum TIC values (models 1 and 4 on Fig. 7). Models of evolution with longitude and latitude for both location and scale parameters also give low TIC values (models 1 and 13 on Fig. 7). Note that models with only the longitude as covariate for the location parameter μ are the worst since they lead to the highest TIC values (peaks values: models 2, 5, 8...). The best model corresponds to model 4 on Fig. 7 after transformation of the standard space [Eq. 9]. The resulting value of the different parameters of the matrix $\hat{\beta}$ [Eq. 19] are summarized in Tab. 2.

For this model, the location parameter μ is function of both longitude and latitude while the scale parameter σ

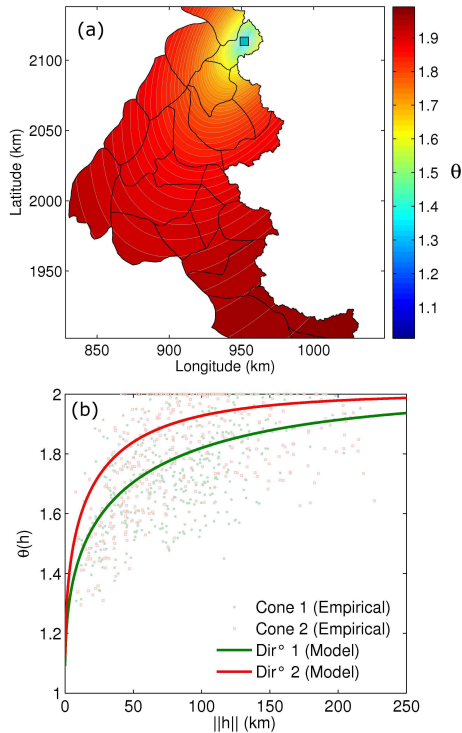


Figure 9. Extremal coefficient provided by the best fitted MSP (Brown-Resnick linear model 4). (a) Spatial evolution with reference station: Chamonix-Mont-Blanc. (b) Evolution with the distance in the ψ direction (Direction 1) and in the orthogonal direction (Direction 2). The dots represent the empirical extremal coefficient of pairs whose direction belongs to a 90° cone around the α -direction (Cone 1: $\alpha \in [\psi - 45; \psi + 45]$) and around the orthogonal direction (Cone 2: $\alpha \in [\psi + 45; \psi + 135]$).

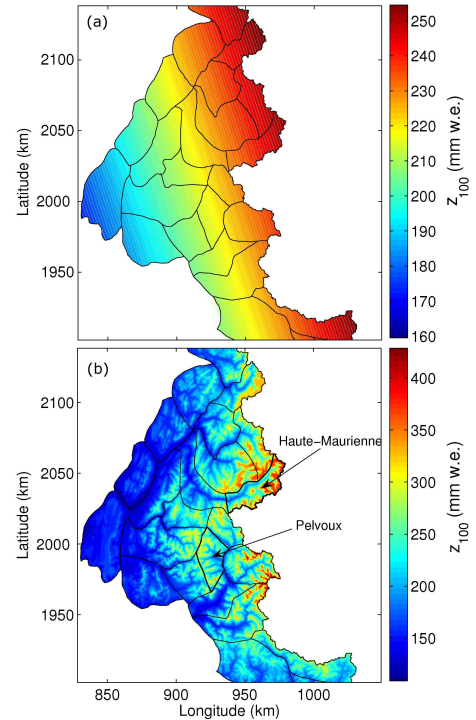


Figure 10. Maps of the 100-year quantile at a fixed altitude of 2000m (a) and projected on the relief (b) using the best linear model from Tab. 2.

depends on longitude only and the shape parameter ξ is constant. At a constant altitude (2000m), we obtain the highest location parameters μ in the Northeast Alps (Mont Blanc) and the highest scale parameters σ in the Southeast (extreme Southern Alps) which corresponds to the Mediterranean effect that tends to bring greater variability. The shape parameter is equal to 0.054 indicating most likely a Frchet domain, hence an increase of the quantile with the return period stronger than predicted by a Gumbel model. However, the 95% CI of ξ contains 0 (Tab. 2) so the Gumbel model could also be a sensible one. This does not fully account for the spatial patterns displayed in Figs. 3 and 5, which justifies the further improvement using spline models, see Sec. 4.4

4.3.2. Directional effect and extremal dependence

Using the elliptic transformation matrix [Eq. (9)], the standard space was transformed iteratively for values of ρ in the 1–4 range and ψ in the 20°–80° range. With model 4, the lowest TIC values were found for transformation parameters $\psi = 62.5^\circ$ and $\rho = 2.05$, leading to extremal dependence parameters [Eq. (8)] equal to $a = 15.5$ and $b = 0.8$. The extremal coefficient obtained by this model is represented on Fig. 9a with reference to Chamonix-Mont-Blanc. A very important directional effect along the $\alpha = \psi = 62.5^\circ$ axis is indeed observed. The range (distance corresponding to $\theta = 1.9$) is maximum (about 185 km) along the direction of the local Alpine axis ($\alpha = 62.5^\circ$), and is only about 85 km along the perpendicular axis (Fig. 9b). This result is in agreement with the empirical analysis which showed that the main dependence direction was belonging to the [51°–77°] range, and thus confirms the importance of mountain

barriers and valleys on extreme snowfalls, the Isere and the Rhone valleys being the widest ones in the French Alps.

4.3.3. Quantile estimation

The estimated GEV parameters [Tab. 2], allow us to compute in any location the quantile $z_T(\mathbf{x})$ for a return period T :

$$P(Z(\mathbf{x}) \leq z_T(\mathbf{x})) = e^{-\left(1 + \frac{\xi(z_T(\mathbf{x}) - \mu(\mathbf{x}))}{\sigma(\mathbf{x})}\right)^{-1/\xi(\mathbf{x})}} = 1 - \frac{1}{T} \quad (20)$$

$$\Rightarrow z_T(\mathbf{x}) = \mu(\mathbf{x}) + \frac{\sigma(\mathbf{x})}{\xi(\mathbf{x})} \left[\left(-\ln \left(1 - \frac{1}{T} \right) \right)^{-\xi(\mathbf{x})} - 1 \right] \quad (21)$$

Fig. 10 shows the maps of 3-day extreme snowfalls for a return period of 100 years at 2000 m and projected onto the local relief taking into account the actual altitude after application of the inverse gradient [Eq. (13)]. We note firstly that 3-day extreme snowfalls are the highest at the border with Switzerland and Italy. However, even if Fig. 10b seems to be mainly governed by altitudinal effects, the strong regional patterns clearly visible in Fig. 10a still significantly influence the 100-year quantile. For instance, the 100-year quantiles predicted in the Haute-Maurienne massif culminating at 3751 m are significantly higher (> 400 mm w.e.) than those in the Pelvoux massif culminating at 4102 m (< 300 mm w.e.).

4.3.4. Standard errors and pointwise/spatial comparison

The relative error of the 100-year quantile at a constant altitude (2000 m) was calculated from the standard errors on the the GEV parameters $\Delta\mu(\mathbf{x})$, $\Delta\sigma(\mathbf{x})$ and $\Delta\xi$:

$$\Delta z_T(\mathbf{x}) = \Delta\mu(\mathbf{x}) + \left| \frac{1}{\xi} (\omega^{-\xi} - 1) \right| \Delta\sigma(\mathbf{x}) + \left| \frac{\sigma(\mathbf{x})}{\xi} \left(\frac{1}{\xi} (\omega^{-\xi} - 1) + \omega^{-\xi} \ln \omega \right) \right| \Delta\xi, \quad (22)$$

with $\omega = -\ln(1 - 1/T)$, $\Delta\mu = \sqrt{\mathbf{X} S_\mu \mathbf{X}^t}$, $\Delta\sigma = \sqrt{(\mathbf{X}) S_\sigma \mathbf{X}^t}$ and $\Delta\xi = \sqrt{\mathbf{X} S_\xi \mathbf{X}^t}$. Matrices S_μ , S_σ and S_ξ are asymptotic covariance matrices of parameters β_{μ_i} , β_{σ_i} and β_{ξ_i} and \mathbf{X} is the “design” vector ($\mathbf{X} = [1 \text{ lon}(\mathbf{x}) \text{ lat}(\mathbf{x})]^t$). The 100-year quantile standard error at 2000 m is represented on Fig. 11a. Note that the relative error does not exceed 26% where the data is available and is the highest in the extreme Southern Alps and in western regions where the spatial interpolation provides less information due to a lower spatial dependence (cf Fig. 8a) and/or to the proximity of the boundary of the studied domain. This error can be considered relatively low given all the assumptions made (linear evolution of the GEV parameters, orographic gradient, etc). For instance, it is lower than if dependence between stations was not accounted for, allowing more confident predictions of high return levels.

A pointwise/spatial comparison at constant altitude of 2000 m is then used to demonstrate the accuracy of our model. Indeed, fitting a MSP with spatial evolutions of the GEV parameters allows us improving the pointwise estimation by “sharing information between stations”. However the results provided are not an exact interpolation of the pointwise quantiles, a large difference with, e.g., smoothed quantiles using kriging techniques [Weisse and Bois, 2001]. Consequently, it must be checked that the spatial model is not “too far” from the pointwise prediction. Fig. 11b shows, for each station, the comparison between the pointwise quantile projected at 2000m using Eq. (13) and the quantile predicted by the spatial model at 2000m for different return periods. We first note that the average curve is very close to the first bissector, which shows that the overall spatial model is not biased. In detail, however, the spatial

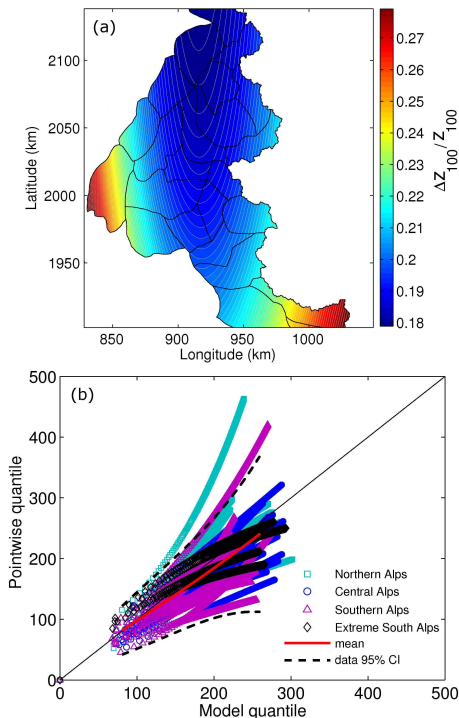
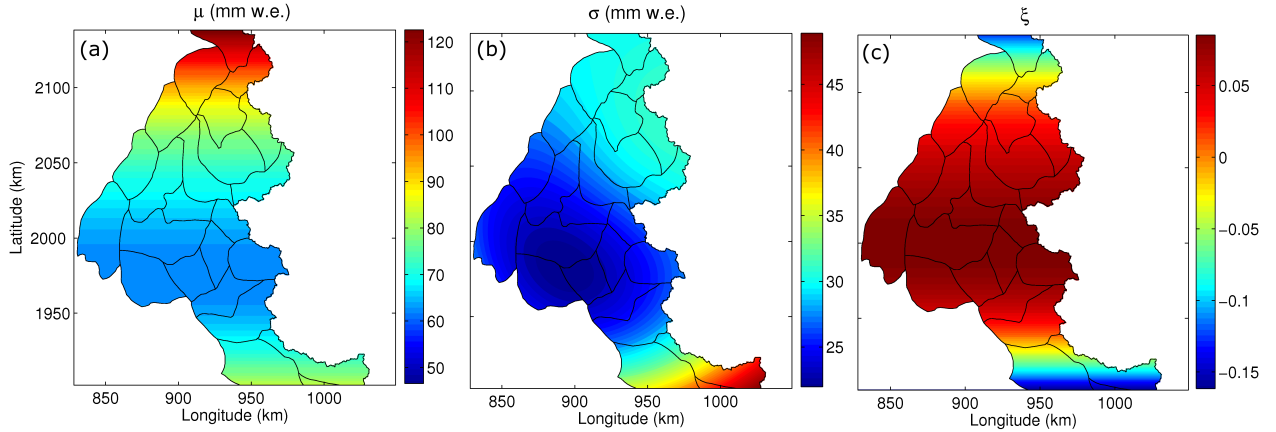


Figure 11. (a) 100-year quantile z_{100} relative error at 2000m. (b) Comparison between the quantile estimated pointwise for a given station and the quantile predicted by the spatial linear model at the location of the station for different return periods. The red curve represents the average curve, the black dashed curves represent 95% confidence interval around the average calculated from the different curves (mean $\pm 2 \times$ standard deviation).

Table 3. Parameters of matrix $\hat{\beta}$ evaluated for the cubic spline model 27 on figure 7 after space transformation.

μ	$\beta_{\mu 0}$ (mm)	$\beta_{\mu 1}$ (mm/km)	$\beta_{\mu 2}$ (mm/km ³)	$\beta_{\mu 3}$ (mm/km ³)		
	-2.705×10^2	1.668×10^{-1}	8.536×10^{-6}	1.05×10^{-5}		
σ	$\beta_{\sigma 0}$ (mm)	$\beta_{\sigma 1}$ (mm/km)	$\beta_{\sigma 2}$ (mm/km)	$\beta_{\sigma 3}$ (mm/km ³)	$\beta_{\sigma 4}$ (mm/km ³)	
	-3.596×10^2	9.562×10^{-2}	1.472×10^{-1}	-5.946×10^{-6}	1.013×10^{-5}	
ξ	$\beta_{\xi 0}$	$\beta_{\xi 1}$	$\beta_{\xi 2}$	$\beta_{\xi 3}$		
	1.586	-7.417×10^{-4}	-1.078×10^{-8}	-1.112×10^{-7}		
Spline knots		κ_{lon}^1 (km)	κ_{lon}^2 (km)	κ_{lat}^1 (km)	κ_{lat}^2 (km)	
		903.9	935.3	1986.3	2046.2	

**Figure 12.** Spatial evolution of the GEV parameters using the spline model [Eq. (12)]. (a) μ , (b) σ , (c) ξ at a constant altitude of 2000 m.

model slightly overestimates the pointwise quantile on average. The most significant errors come from two stations, one in the Northern Alps and one in the Southern Alps. Moreover, we note that the estimation for all extreme South Alpine stations (4 stations in black diamond) is locally biased due to the constant shape parameter $\xi = 0.056$ in the spatial model while the pointwise shape parameter is negative in this region (see Sec. 3.3).

4.4. Spline models

Thirty-six different models (presented in detail in Appendix A) of spatial evolution of the GEV parameters according to Eq. (12) were tested, using in this case only the Brown-Resnick MSP (which outperforms the Smith and Schlather MSP regardless of the model used to estimate the spatial evolution of the GEV parameters) and different numbers of splines knots (Figure 7). The knots of the pr-spline are regularly distributed in the considered interval. It can be firstly noted that models with two knots in both coordinates have the lowest TIC values and therefore correspond to the most efficient models, since they are more flexible. Beyond two knots, the estimation has proved impossible because of too many parameters to be estimated compared to the amount of data available. Consequently, models with two knots in both directions were retained and further improved by transforming the standard space according to Eq. (9) in order to take into account directional effects. Hence, the introduction of splines for the estimation of the evolution of GEV parameters is a drastic improvement, well quantified by the significant TIC reduction (Fig. 7) with regards to the linear models fitted before, since the selected covariates correspond better to the ones assumed preliminarily in the empirical analysis (Fig. 5).

4.4.1. GEV parameters

The best model of spatial evolution is model 27 in Fig. 7 after space transformation:

$$\begin{aligned}
 \mu &= \beta_{\mu 0} + \beta_{\mu 1} \text{lat} + \beta_{\mu 2} (\text{lat} - \kappa_{lat}^1)^3 + \beta_{\mu 3} (\text{lat} - \kappa_{lat}^2)^3 \\
 \sigma &= \beta_{\sigma 0} + \beta_{\sigma 1} \text{lon} + \beta_{\sigma 2} \text{lat} \\
 &\quad + \beta_{\sigma 3} \left(\sqrt{(\text{lon} - \kappa_{lon}^1)^2 + (\text{lat} - \kappa_{lat}^1)^2} \right)^3 \\
 &\quad + \beta_{\sigma 4} \left(\sqrt{(\text{lon} - \kappa_{lon}^2)^2 + (\text{lat} - \kappa_{lat}^2)^2} \right)^3 \\
 \xi &= \beta_{\xi 0} + \beta_{\xi 1} \text{lat} + \beta_{\xi 2} (\text{lat} - \kappa_{lat}^1)^3 + \beta_{\xi 3} (\text{lat} - \kappa_{lat}^2)^3
 \end{aligned} \tag{23}$$

where the parameters of the matrix β and the knots parameters of the spline are summarized in Table 3.

Using these pr-splines, the best covariates are the latitude only for the location parameter μ , both latitude and longitude for the scale parameter σ , and latitude for the shape parameter ξ . The scale parameter σ is thus a 2D-cubic pr-spline depending on both longitude and latitude, while the location μ and shape ξ parameters are only 1D-cubic pr-splines of latitude.

At a constant altitude (2000 m), the map obtained using the linear model is improved. Fig. 12a shows that we obtain the highest location parameters μ in the North (Mont Blanc) but the model also predicts the increase of μ in the extreme Southern Alps (see Fig. 5d) which was not the case with linear models. Similarly, Fig. 12b shows that the highest scale parameters σ are still in the southeast (extreme Southern Alps) but the attenuation of variations of σ in the Northern Alps (Figs. 5b and 5e) is better accounted for. The shape parameter ξ has an evolution with latitude (Fig. 12c): it is negative in the extreme Southern Alps, positive in the rest of the Alps and slightly negative again far

North. This evolution enables to account for the different attraction domains empirically evaluated (Fig. 5f) and controls the spatial variability of the quantile increase rate with the return period. For instance, it is almost zero (in logarithmic scale) in Chamonix-Mont-Blanc (Fig. 17a), positive in Villard-de-Lans and Saint Veran (Figs. 17b and 17c) and negative in Tende (Fig. 17d).

Finally concerning the extremal dependence, there are no significant changes compared to the previous best fitted linear model. The directional effect found has the same direction $\psi = 62.5^\circ$ and intensity $\rho = 2.05$. The only difference is the value of the extremal dependence parameters which are slightly lower than for the linear model: $a = 12.0$ and $b = 0.71$. However this does not significantly change the range of extremal dependence and the extremal coefficient represented on Fig. 9 remains consequently nearly identical for the best spline model.

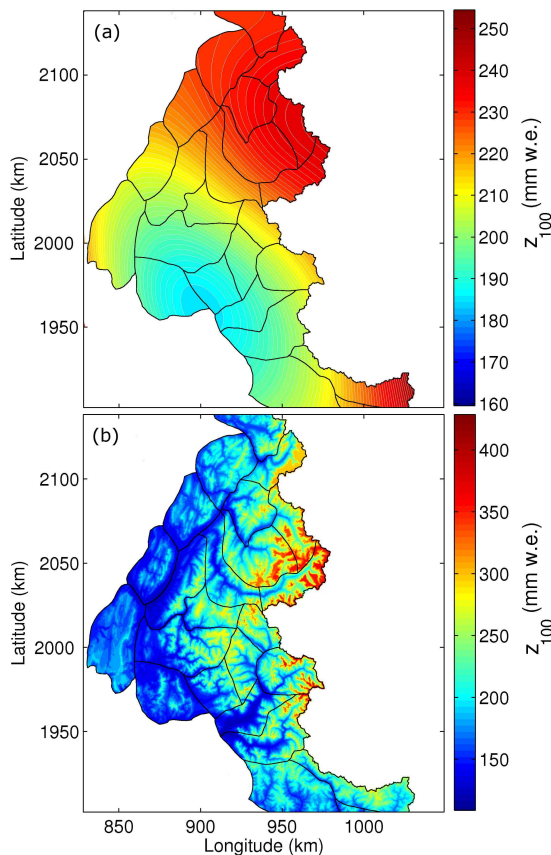


Figure 13. Maps of the 100 year quantile at a fixed altitude of 2000m (a) and projected on the relief (b) using the cubic spline model (23).

4.4.2. Quantile estimation

Eq. (21) is again used to compute the values of the 100-year quantile at 2000m (Fig. 13a) and projected on the Alps relief (Fig. 13b). One can note that the map of the 100-year quantile at 2000 m (Fig. 13a) is close in terms of global evolution to the one obtained with the linear model (Fig. 10a), but locally refined. In particular, low values of the quantile at the west of the Alps predicted by the linear model are increased by the introduction of splines. Fig. 14 represents a map of the ratio between the 100-year quantile from the spline model z_{100}^s and the 100-year quantile from the linear model z_{100}^l . The “spline quantile” is generally higher compared to the “linear quantile” on the west side of the Alps (more than 25% in the Vercors massif for instance). On the

contrary, it is lower on the east side ($\approx 10\%$ lower in the Queyras and Parpaillon massifs for instance).

4.4.3. Pointwise/spatial comparison and improvement compared to the linear model

A comparison between the pointwise quantile at 2000 m and the quantile from the spline spatial model at 2000 m was again performed. We first note (Fig. 15a) that the average curve is even closer to the first bissector than with the linear model. Hence, the spline model is more accurate on average than the linear one. In addition, the bias present in the Southern Alps with the linear model (Fig. 11) has been removed by the introduction of pr-splines. Nevertheless, the two stations already highlighted before (one in the northern Alps, the other in the Southern Alps) still show a significant difference compared to the pointwise estimate.

In order to further characterize the improvement of the model by the introduction of cubic pr-splines, we calculated the NRMSE (Normalized Root Mean Square Estimator), both for all the French Alps, and also for each alpine region to see in which areas the pointwise/spatial agreement has been improved:

$$\text{NRMSE} = \frac{\sqrt{\sum_{T=2}^{N'} \sum_{i=1}^K [z_T(\mathbf{x}_i) - \hat{z}_{T,i}]^2 / [(N' - 1) K]}}{\hat{z}_{max} - \hat{z}_{min}} \quad (24)$$

where $z_T(\mathbf{x}_i)$ is the T -year quantile for station i given by the spatial model, $\hat{z}_{T,i}$ the same quantity estimated pointwise for the station i , $\hat{z}_{max} = \max_{T,i}[\hat{z}_{T,i}]$, $\hat{z}_{min} = \min_{T,i}[\hat{z}_{T,i}]$, $K = 40$ is the number of stations and $N' = 100$ years. One can notice (Fig. 15b) that the spline model improves the results compared to the linear model for all the four alpine zones. In detail, the main source of error of the linear model is the extreme South of the Alps ($\text{NRMSE}_{\text{lin}} = 20\%$). It is significantly reduced ($\text{NRMSE}_{\text{spline}} = 11\%$) by the introduction of pr-splines and more particularly by a spline model for the shape parameter ξ (now accounting for the Weibull domain in this zone). The error in other alpine areas is also reduced (down by 2% approximately). Globally, for all the French Alps, the NRMSE decreases from 13.2% for the linear model to 11.8% for the spline model. This global decrease seems relatively low compared to the drastic improvements in the extreme Southern Alps, but it is mainly due to the low number of weather stations in this zone (only four of 40 total stations).

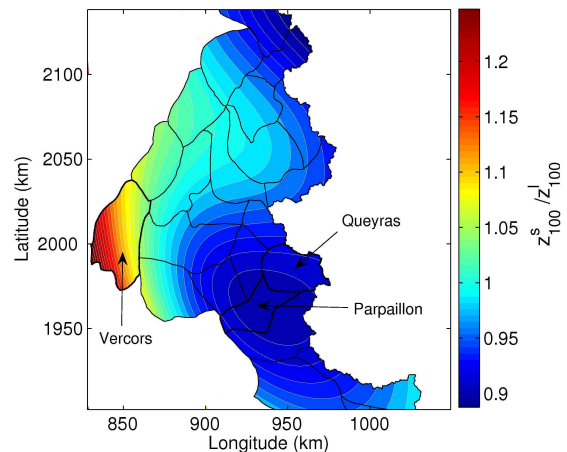


Figure 14. Map of the ratio between the 100-year quantile computed using pr-splines z_{100}^s and the 100-year quantile computed using linear models z_{100}^l .

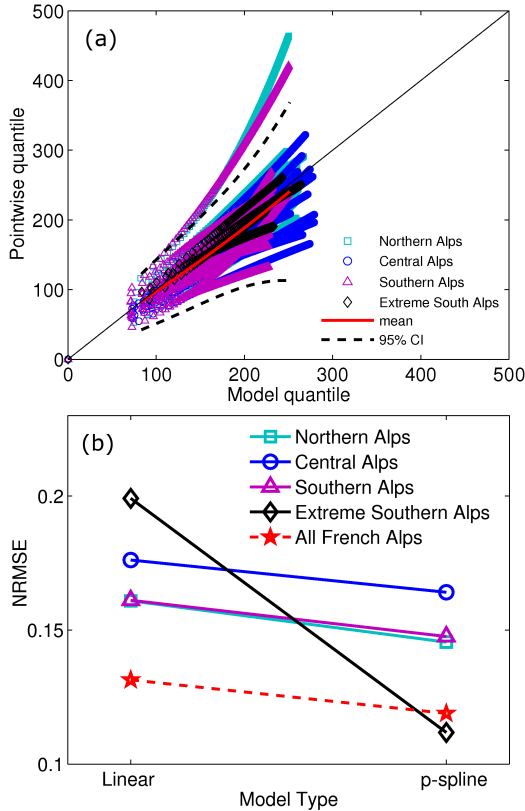


Figure 15. (a) Comparison between the quantile estimated pointwise for a given station and the quantile predicted by the spatial model with cubic pr-splines for different return periods. The red curve represents the average curve, the dashed curves the 95% confidence interval around this average (mean $\pm 2 \times$ standard deviation). (b) Comparison of the NRMSE obtained with the linear and spline models for all the french Alps and for each alpine zone.

4.5. Prediction accuracy: validation on non-used stations

The stations that were not retained for the modelling (squares in Fig 1a) have been used to demonstrate the prediction accuracy of the best spatial model with pr-splines [Eq. 23]. Fig. 16a shows the result of this comparison with the 95% CI determined on the calibration sample at a constant altitude of 2000 m. Fig. 16b shows the same result but projected onto the local altitude using Eq. (13). Only 5 stations on average are out of the 95% CI, for a validation sample of 84 stations which is slightly more than 5% but still very reasonable given the many assumptions made (spatial evolution of the GEV parameters, orographic gradient, etc). The value of the NRMSE at 2000 m is 13.15%, a little more than for the calibration sample, and 11% when projected onto the French Alps relief. This result is quite satisfactory, and confirms the ability of our spatial model to predict high quantiles all over the French Alps. It also suggests that the chosen calibration sample was large enough to be representative of the main spatial patterns over the considered region. Furthermore, the fact that the NRMSE computed for the local altitude is lower than the one in the 2000 m case suggests that our simple way of handling altitude is appropriate. To explain this decrease of the NRMSE, one can note that, for the 2000 m comparison, both the data used for the pointwise fitting and the spatial modeling are

transformed at 2000 m using Eq. (13). However, for the comparison projected onto the local relief, the pointwise fitting is done directly on the non-transformed data while the results from the spatial model at 2000 m are then projected back on the local altitude using the inverse orographic gradient [Eq. (13)]. Apparently, with this last procedure, the error propagation is less important than in the 2000 m comparison.

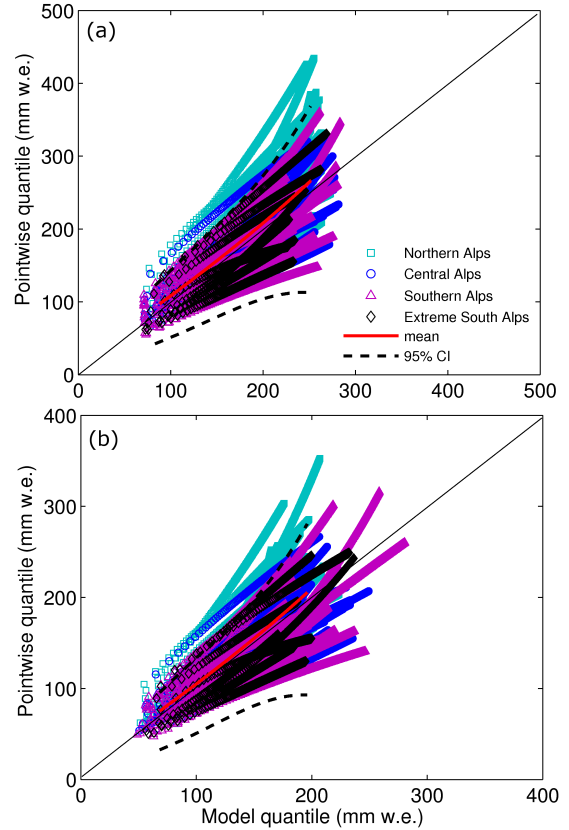


Figure 16. Cross-validation for non-used stations: comparison between the quantile estimated pointwise for a given station and the quantile predicted by the spatial model with cubic pr-splines for different return periods. The red curve represents the average curve and the dashed curves the 95% confidence interval computed from the calibration sample. (a) 2000 m, (b) Local altitude.

5. Discussion

5.1. Comparison with previous work

MSPs have been seldomly used to characterise spatial variations of extreme hydrological quantiles. Thus, a comparison with the few existing applications is worthwhile.

First, we have shown that, for all tested models, Brown-Resnick and Smith MSPs give better results than the Schlather one. On the contrary, *Blanchet and Davison* [2011] show that for extreme snow depth data in Switzerland, the Schlather's MSP gives much lower TIC values than the Smith MSP, without testing the Brown-Resnick one. This shows that there is a significant difference in the spatial structure of extreme snowfalls (in water equivalent) and extreme snow depths at the ground level. This

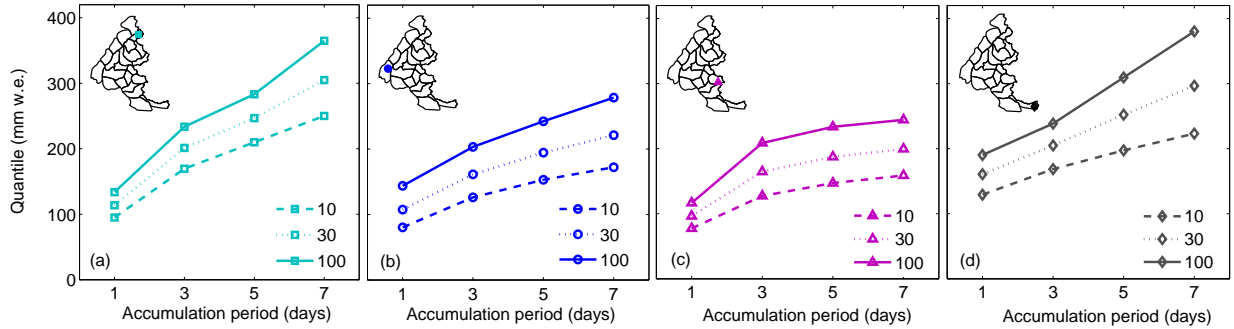


Figure 17. IDF curves for Chamonix-Mont-Blanc (Mont-Blanc massif) (a), Villard-de-Lans (Vercors massif) (b), Saint Veran (Queyras massif) (c) and Tende (Alpes-Azurennes massif) (d). The curves are represented for different return period values (10, 30 and 100 years).

difference is likely to be related to the spatial evolution of snow depth which is much smoother than snowfalls due to cumulative effects involved in the formation of snow cover (successive snowfalls and snow metamorphism). In contrast, the asymptotic independence is necessary for extreme snowfalls, ie $\theta \rightarrow 2$ for large distances, which is not the case with Schlather MSP and explains its poor adjustment in our case.

Second, the anisotropy of the extremal dependence highlighted before is very similar to the one found by *Blanchet and Davison* [2011] in the Swiss Alps for extreme snow depths and to the one shown by *Padoan et al.* [2009] for U.S. precipitation data. Indeed, although the form of dependence highlighted is not the same for extreme snowfalls (Brown-Resnick), extreme snow depths and rainfall (Schlather), it is marked in all cases by an important and similar directional effect related to orography and its main direction. Nevertheless, the local Alps direction in Switzerland is closer to E-W than in France, explaining why *Blanchet and Davison* [2011] found an anisotropy angle $\alpha_{Swiss} = 20^\circ$ which is the direction of the widest valleys in Switzerland, the Rhone and Rhine River valleys. Similarly, in *Padoan et al.* [2009], the main anisotropy corresponded to the orientation of the Appalachian Mountains.

5.2. Influence of the accumulation period

To investigate the influence of the accumulation period, the same procedure of fitting a MSP to data (Sec. 4) was repeated for annual snowfall maxima over 1, 5 and 7 days, using spline models for the GEV parameters and the anisotropic Brown-Resnick MSP.

5.2.1. IDF: Intensity-Duration-Frequency

IDF curves enables the synthesis of snowfall information at given station and thus constitutes an interesting tool for risk management. Four stations in each alpine zone were selected from the maps to produce Intensity-Duration-Frequency (IDF) curves and to compare the evolution of the quantile in these different areas with the duration of accumulation and return period (Fig.17):

- Northern Alps: Chamonix-Mont-Blanc, altitude: 1042m (Mont Blanc massif)
- Central Alps: Villard-de-Lans, altitude: 1050m (Vercors massif)
- Southern Alps: Saint Veran, altitude 2010m (Queyras massif)
- Extreme Southern Alps: Tende, altitude: 650m (Mercantour massif)

First, it can be noted on Fig. 17 that the quantile strongly increases with the duration of accumulation in Chamonix-Mont-Blanc (Fig. 17a) and Tende (Fig. 17d), reaching more than 300 mm w.e. for a return period of 100 years and 7

days of accumulation. The increase is weaker in Villard de Lans (Fig. 17b) where the 100-year quantile reaches 220 mm w.e. for a 7-days accumulation duration. In St-Veran (Fig. 17c), the quantile is attenuating close to 250 mm w.e., this maximum being nearly attained for a 3 day accumulation duration. This result shows the longer persistence of heavy snowfalls in the Northeast (Mont Blanc) and the extreme southeast of the Alps, and, on the contrary, that intense episodes are much shorter in the Queyras massif and a bit shorter in the pre-Alps (low and mid-altitude massifs).

5.2.2. Directional effect

Then to examine if the directional effect highlighted above is influenced by the accumulation period, the ψ -angle and the elongation parameter ρ of the space transformation matrix [Eq. (9)] are represented on Fig. 18 as functions of the accumulation period. We can firstly note that the angle ψ of the transformation is almost constant, varying between 62.5° and 65.2° , hence corresponding to the local Alpine axis whatever the accumulation period. This is presumably explained by the interaction between topography and predominant atmospheric flows, and may therefore be a rather general result for hydrological variables as discussed before.

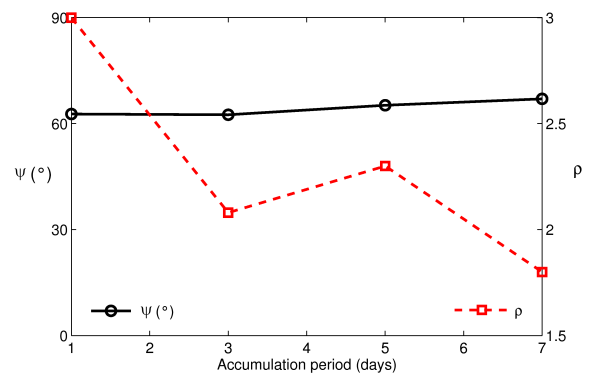


Figure 18. Influence of the accumulation period on the parameters of space transformation ψ (anisotropy angle) and ρ (elongation parameter).

However, the elongation parameter of the matrix ρ and thus the intensity of the transformation is strongly influenced by the accumulation period. The directional effect is globally all the more important that the accumulation period is short ($\rho = 3$ for a 1-day accumulation period and

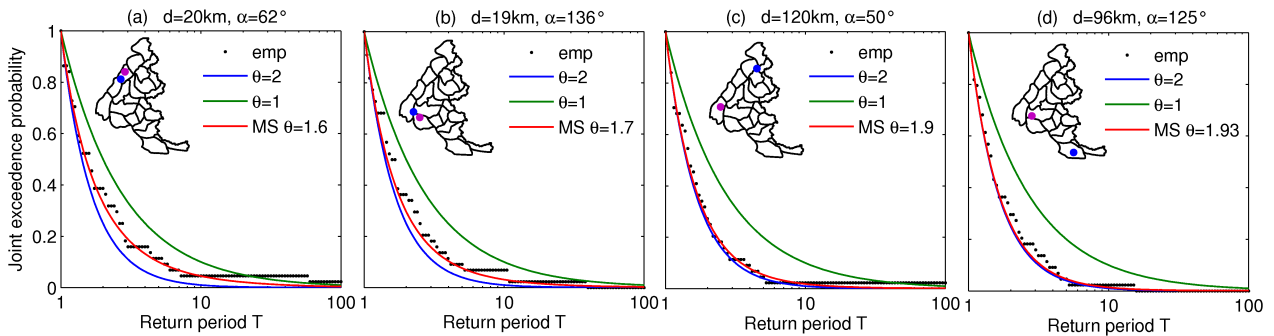


Figure 19. Joint exceedence probability $P(Z^*(\mathbf{x}) > z_T; Z^*(\mathbf{x}') > z_T)$ for 4 couples of stations of the calibration sample. (a) Challes-les-Eaux (291 m, Bauges) – Lescheraines (590 m, Bauges), (b) Monestier de Clermont (800 m, Oisan) – Pellafof (930 m, Devoluy), (c) Megeve (1104 m, Mont-Blanc) – Villard-de-Lans (1050 m, Vercors), (d) La Mure (856 m, Oisan) – Guillaumes (620 m, Alpes-Azureennes)

$\rho = 1.8$ for a 7-day accumulation period). This greater sensitivity to the local relief (presence of valleys, mountainous barriers) of short extreme events with regards to more persistent ones, complements and refines the preliminary results of *Eckert et al.* [2011] obtained with a first version of the model. Physically, it may indicate that persistent snow storms diffuse progressively in all directions while interacting durably with the topographic barriers, reducing the difference between the ranges of the two principal anisotropy axis of the extremal coefficient.

5.3. Joint analysis

Quantifying the joint occurrence of extreme events in different locations can be very useful from an operational perspective. The joint probability of exceeding the T -year quantiles $z_T(\mathbf{x})$ and $z_T(\mathbf{x}')$ in two locations \mathbf{x} and \mathbf{x}' , can be computed by transforming the margins distributions in unit Frchet and using Eq. (5):

$$\begin{aligned} P(Z(\mathbf{x}) > z_T(\mathbf{x}); Z(\mathbf{x}') > z_T(\mathbf{x}')) &= \\ P(Z^*(\mathbf{x}) > z_T^*; Z^*(\mathbf{x}') > z_T^*) &= \\ 1 - 2 \left(1 - \frac{1}{T}\right) + \left(1 - \frac{1}{T}\right)^{\theta(\mathbf{x}, \mathbf{x}')} & \quad (25) \end{aligned}$$

This probability was computed for 4 pairs of stations on Fig. 19 representing different cases: low or large euclidian distances and angles ψ close to the main direction of dependence or almost orthogonal. Globally, we can note that the estimation lies within the case of complete dependence ($\theta = 1$) and total independence ($\theta = 2$) in all cases, but is less close to total independence for low euclidian distances (Figs. 19a and 19b) than for large distances (Figs. 19c and 19d). It is all the more remarkable if the angle α between stations is close to the main dependence direction $\psi = 62.5^\circ$ (Fig. 19a). Indeed, for the same distance between stations ($d \approx 20$ km), the extremal coefficient increases from $\theta = 1.6$ to $\theta = 1.7$ for pairs of stations almost orthogonal one to each other (Fig. 19b). In the case of large distances, the joint probability is very close to the one corresponding to total independence between pairs of stations (Figs. 19c and 19d), with $\theta \rightarrow 2$. However, the influence of the directional effect is still noticeable (dependence a bit stronger in Fig. 19c than in Fig. 19d). This again shows the need of using MSP enabling total asymptotic independence for modeling extreme snowfalls while extreme snow depth at ground level (much smoother than snowfalls) can be modelled with asymptotic dependence $\theta < 2$ at large distance [*Blanchet and Davison*, 2011].

Additionally, we compared the modelled joint exceedence probability P_{mod} to the empirical one P_{emp} (Fig. 20) for

return periods between 1 and 100 years. As well as for the quantile comparison, we remark that the model is just very slightly biased with the mean curve nearly aligned with the first bissector. In detail, the model slightly underestimates the empirical values. This can be explained by the fact that some empirical values of θ have been constrained to 2, while the modelled extremal coefficient is always strictly lower than 2. Beyond that, this graphic confirms the essential contribution of MSPs compared to previous approaches that usually assume independence between stations since, on average, a model with $\theta = 2$ significantly underestimates the empirical values, especially for short distances between pairs of stations and/or high return periods.

5.4. Conditional quantile evaluation

Quickly updating the unconditional quantile maps after an intense snowfall at one location can be very useful from an operational point of view. From the previous joint analysis,

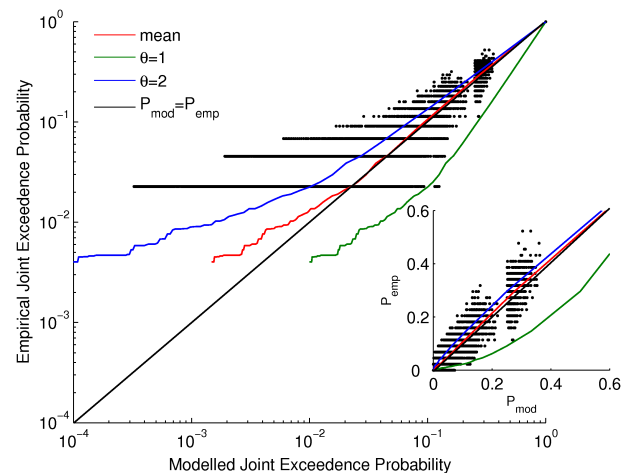


Figure 20. Comparison between the empirical joint exceedence probability P_{emp} and the modeled joint exceedence probability P_{mod} given by Eq. (25) for all the pairs of stations. The red curve represents the average curve, the green one is for a perfect dependence between stations ($\theta = 1$ in P_{mod} [Eq. (25)]) and the blue one for total independence ($\theta = 2$ in P_{mod} [Eq. (25)]). The scale is logarithmic in the main graph and linear in the inset.

conditional return level maps can easily be obtained. We can define the conditional probability of exceeding the T -year return level in location \mathbf{x} knowing that the T' -year return level was exceeded in location \mathbf{x}' as:

$$\begin{aligned} P(Z(\mathbf{x}) > z_T(\mathbf{x}) \mid Z(\mathbf{x}') > z_{T'}(\mathbf{x}')) &= \\ P(Z^*(\mathbf{x}) > z_T^* \mid Z^*(\mathbf{x}') > z_{T'}^*) &= \frac{1}{T} \end{aligned} \quad (26)$$

with $z_{T'}^* = -1/\ln(1 - 1/T')$. Using the general expression of the bivariate probability [Brown and Resnick, 1977; Kabluchko et al., 2009; Davison et al., 2012]:

$$\begin{aligned} -\ln P(Z^*(\mathbf{x}) \leq z_T^*; Z^*(\mathbf{x}') \leq z_{T'}^*) &= \\ \frac{1}{z_T^*} \Phi(c) + \frac{1}{z_{T'}^*} \Phi(c') & \end{aligned} \quad (27)$$

with $c = d/2 + 1/d \ln(z_{T'}^*/z_T^*)$, $d = \sqrt{2\gamma(\mathbf{h})}$ and $c' = d - c$, we can determine the conditional quantile z_T^* by numerically solving the following equation:

$$-\frac{1}{T} + T' \left(\frac{1}{T'} - e^{-\frac{1}{z_T^*}} + e^{-\frac{\Phi(c)}{z_T^*} - \frac{\Phi(c')}{z_{T'}^*}} \right) = 0. \quad (28)$$

An example of this conditional return level for $T = T' = 30$ years is plotted in Fig. 21 for a reference station located in the Champsaur massif. Its spatial pattern is a combination between the shape of the extremal coefficient and of the 30-year quantile map. For instance, knowing that a snowfall has exceeded $z_{30} \approx 150$ mm w.e. in this station, leads to a local increase of the 30-year return level of 35% at 2000 m (conditional quantile $z_{30} \approx 220$ mm w.e.). Moreover, the

directional effect has a major influence on the spatial evolution of the conditional quantile. For instance, 100 km far from the reference station, in the main direction of dependence, an increase of the conditional 30-year return level is still noticeable, whereas almost no influence is observed in the perpendicular direction at 50 km only.

6. Conclusion

In this study, extreme snowfalls have been evaluated in the French Alps by mapping snowfall water equivalent annual maxima at 40 measurement stations. The mathematical formalism of max-stable processes generalizing extreme value theory to the multivariate spatial context has been used. It has been shown in particular that the Brown-Resnick model provides an extremal coefficient that fits the data better than those of Smith and Schlather which are less flexible. Additionally, space transformation has been used to model anisotropy, which has further improved the adjustment. Hence, it appeared that the spatial extremal dependence depends strongly on the local orientation of the alpine axis and the presence of large valleys. For example, for a 3-day accumulation period, the dependence range is more than twice as high in this alpine axis direction in comparison to the orthogonal direction. However, we refined this result important for many hydrological problems and already obtained in other cases by showing that the intensity of the directional effect is all the more important when the duration of accumulation is low.

Linear models and penalized splines with radial basis functions for the evolution of the GEV parameters with space were compared, showing slightly lower NRMSE values in the case of the retained spline model in the whole French Alps but more significantly in the extreme Southern Alps and more generally a better modelling of complex evolutions of GEV parameters with space. At a constant altitude (2000m), the highest location parameters μ are very North (Mont-Blanc, Aravis and Bauges massifs), but significantly high values are also observed far South. The highest scale parameters σ are in the Southeast (extreme Southern Alps) which corresponds to the Mediterranean effect that tends to bring variability. The shape parameter is mainly positive in the Northern, Central and Southern Alps, showing a Frchet attraction domain but becomes negative in the extreme Southern Alps (Weibull domain). From the (μ, σ, ξ) maps, the 100-year snowfall quantile could be determined at any point in the French Alps. In detail, it has also been shown that the 100-year quantile for a 3-days accumulation period is the highest in the Central and Southern Alps at the boarder with Switzerland and Italy. This analysis was also performed for different periods of accumulations, showing the variability of the persistence of heavy snowfall events across the French Alps.

These results, and more particularly quantile maps, constitute a powerful operational tool for long-term managing of avalanche risk, especially to establish hazard maps or as inputs of propagation models [Naaim et al., 2003]. Besides, as shown in Gaume et al. [2012], these results can be rigorously coupled with a mechanical stability criterion to evaluate avalanche release depth distributions and then used to perform statistical-dynamical simulations to evaluate run-out and pressure distributions [e.g. Eckert et al., 2008].

The employed smooth modelling of GEV parameters associated with MSPs and a nested model selection procedure constitutes the methodological strong point of the work. We also studied how a joint analysis can be performed to evaluate the risk of obtaining an extreme event in two different locations within the same year, leading to conditional return level maps which can also be very useful from an operational perspective. Validation on other available data has shown

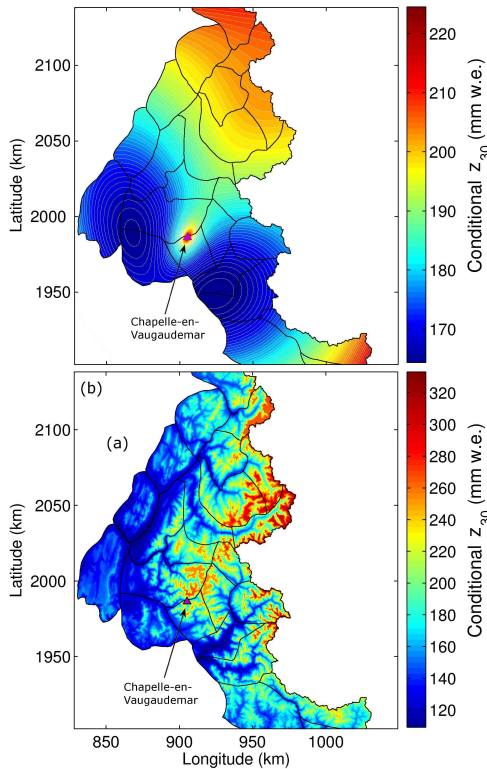


Figure 21. Conditional return level maps, $T = T' = 30$ years. (a) 2000 m, (b) Local altitude. Conditional reference station: Chapelle-en-Valgaudemar (1270 m, Champsaur massif).

the accuracy of the fitted model and of the simple way of handling altitudinal effects which has been proposed. This up-to-date framework could be put in use for various other applications in hydrology such as heavy rainfalls or flood extremes as soon as a sufficient sample of long block maxima series is available.

Finally, since the main objective of our work was prediction as a continuous function of space, we only used the geographical coordinates as covariates. However, additional physical quantities could be further introduced in the model such as the winter mean snowfall (WMS) which has been previously put forward, in order to select the best physical drivers of the spatial trends we highlighted. Another improvement perspective of the model is the test of very recently developed MSPs which were not considered here. Additionally, a pre-selection of the data corresponding to the flux type (NNW / SSE fluxes) would be interesting in order to investigate if dependence patterns in extreme snowfall vary accordingly.

Appendix A: Covariates for the spatial evolution of the GEV parameters

Table A.1. Details about the covariates used for the different evolution models of the GEV parameters with space. The numbers corresponds to the model index in Fig. 7. The last seven models are mixed since they involve spline evolutions of μ and σ and a linear evolution of ξ with space.

Model	Type	Covariates μ		Covariates σ		Covariates ξ	
		lat	long	lat	long	lat	long
1	linear	×	×	×	×		
2	linear		×	×	×		
3	linear	×		×	×		
4	linear	×	×		×		
5	linear		×		×		
6	linear	×			×		
7	linear	×	×	×			
8	linear		×	×			
9	linear	×		×			
10	linear	×	×	×	×	×	×
11	linear		×	×	×	×	×
12	linear	×		×	×	×	×
13	linear	×	×		×	×	×
14	linear		×		×	×	×
15	linear	×			×	×	×
16	linear	×	×	×		×	×
17	linear		×	×		×	×
18	linear	×		×		×	×
19	spline	×	×	×	×		
20	spline	×		×	×		
21	spline	×	×	×			
22	spline	×		×			
23	spline		×		×		
24	spline		×	×			
25	spline	×			×		
26	spline	×	×	×	×	×	
27	spline	×		×	×	×	
28	spline	×	×	×		×	
29	spline	×		×		×	
30	spline		×		×	×	
31	spline		×	×		×	
32	spline	×			×	×	
33	spline	×	×	×	×		×
34	spline	×		×	×		×
35	spline	×	×	×			×
36	spline	×		×			×
37	spline		×		×		×
38	spline		×	×			×
39	spline	×			×		×
40	spline	×	×	×	×	×	×
41	spline	×		×	×	×	×
42	spline	×	×	×		×	×
43	spline	×		×		×	×
44	spline		×		×	×	×
45	spline		×	×		×	×
46	spline	×			×	×	×
47	mixed	×	×	×	×	×	lin
48	mixed	×		×	×	×	lin
49	mixed	×	×	×		×	lin
50	mixed	×		×		×	lin
51	mixed		×		×	×	lin
52	mixed		×	×		×	lin
53	mixed	×			×	×	lin

Acknowledgments. Support from the European Interreg DYNAVAL and MAP3 projects and the ANR MOPERA is acknowledged. MeteoFrance and the French Environment Ministry for data acquisition and supply. We also wish to express our gratitude to M. Ribatet for advices while using the R SpatialExtremes package, to G. Toulemonde and J-N. Bacro for comments about the text, and to three anonymous reviewers and the Associate Editor J. Montanari for their insightful and constructive comments.

References

- Akaike, H., Likelihood of a model and information criteria, *J. Econometrics*, 16(1), 3–14, 1981.
- Ancey, C., C. Gervasoni, and M. Meunier, Computing extreme avalanches, *Cold Reg. Sci. Technol.*, 39, 161–180, 2004.
- Bacro, J., and A. Chaouche, Incertitude destination des pluies extrêmes du pourtour méditerranéen: illustration par les données de marseille, *Hydrolog. Sci. J.*, 2006.
- Bel, L., J. Bacro, and C. Lantuejoul, Assessing extremal dependence of environmental spatial fields., *Environmetrics*, 19(2), 163–182, 2008.
- Blanchet, J., and A. Davison, Spatial modelling of extreme snow depth, *Ann. Appl. Stat.*, 5(3), 1699–1725, 2011.
- Blanchet, J., and M. Lehning, Mapping snow depth return levels: smooth spatial modeling versus station interpolation., *Hydrol. Earth Syst. Sc. Disc.*, 7, 6129–6177, 2010.
- Blanchet, J., C. Marty, and M. Lehning, Extreme value statistics of snowfall in the swiss alpine region., *Water Resour. Res.*, 45, W05424, 2009.
- Bocchiola, D., M. Medagliani, and R. Rosso, Regional snow depth frequency curves for avalanche hazard mapping in central italian alps., *Cold Reg. Sci. Technol.*, 12(4), 204–221, 2006.
- Brown, B., and S. Resnick, Extreme values of independent stochastic processes., *J. App. Prob.*, 14, 732–739, 1977.
- Coles, S., J. Heffernan, and J. Tawn, Dependence measures for extreme value analyses., *Extremes*, 2(4), 339–365, 1999.
- Cooley, D., P. Naveau, and P. Poncet, Variograms for spatial max-stable random fields., *Springer Ed.*, 187(3), 73–390, 2006.
- Cooley, D., D. Nychka, and P. Naveau, Bayesian spatial modeling of extreme precipitation return levels, *J. Amer. Statist. Assoc.*, 102(479), 824–840, 2007.
- Davison, A., S. Padoan, and M. Ribatet, Statistical modelling of spatial extremes, *Statist. Sci.*, unpublished, 2012.
- DeHaan, L., A spectral representation for max-stable processes., *Ann. Probab.*, 12, 1194–1204, 1984.
- Durand, Y., M. Laternser, G. Giraud, and P. e. a. Etchevers, 44 years of climate reanalyses in the french alps (1958–2002). methodology, model validation and temperature-precipitation-snowfall trends., *J. Appl. Meteorol. Clim.*, 48(3), 429–449, 2009.
- Eckert, N., E. Parent, M. Naaim, and D. Richard, Bayesian stochastic modelling for avalanche predetermination: from a general system framework to return period computations, *SERRA*, 22, 185–206, 2008.
- Eckert, N., C. Coleou, H. Castebrunet, M. Deschates, D. Giraud, and J. Gaume, Cross-comparison of meteorological and avalanche data for characterising avalanche cycles: The example of December 2008 in the eastern part of the French Alps, *Cold Reg. Sci. Technol.*, 64, 119–136, 2010a.
- Eckert, N., M. Naaim, and E. Parent, Long-term avalanche hazard assessment with a Bayesian depth-averaged propagation model, *J. Glaciol.*, 56(198), 563–586, 2010b.
- Eckert, N., J. Gaume, and H. Castebrunet, Using spatial and spatial-extreme statistics to characterize snow avalanche cycles., *Procedia Environ. Sci.*, 7, 224–229, 2011.
- Fisher, R., and L. Tippett, Limiting forms of the frequency distribution of the largest and smallest member of a sample, *Proc. Cambridge Phil. Soc.*, 24, 180–190, 1928.
- Gaume, J., G. Chambon, N. Eckert, and M. Naaim, Relative influence of mechanical and meteorological factors on avalanche release depth distributions., *Geophys. Res. Lett.*, 39, L12401, 2012.
- Joe, H., Parametric family of multivariate distributions with given margins, *J. Multivariate Anal.*, 46, 262–282, 1993.
- Kabluchko, Z., M. Schlather, and L. DeHaan, Stationary max-stable fields associated to negative definite functions., *Ann. Probab.*, 37, 2042–2065, 2009.
- Lindsay, B., Composite likelihood methods, *Contemp. Math.*, 80, 221–239, 1988.
- Maraun, D., H. Rust, and T. Osborn, Synoptic airflow and uk daily precipitation extremes, *Extremes*, 13, 133–153, 2010.
- Naaim, M., T. Faug, and F. Naaim-Bouvet, Dry granular flow modelling including erosion and deposition, *Surv. Geophys.*, 24, 569–585, 2003.
- Naveau, P., A. Guillou, D. Cooley, and J. Diebolt, Modelling pairwise dependence of maxima in space, *Biometrika*, 96, 1–17, 2009.
- Padoan, S., M. Ribatet, and S. Sisson, Likelihood-based inference for max-stable processes, *J. Am. Stat. Assoc.*, 105(489), 263–277, 2009.
- Parent, E., and J. Bernier, Encoding prior experts judgments to improve risk analysis of extreme hydrological events via pot modelling, *J. Hydrol.*, 283, 1–8, 2003.
- Pickands, J., Statistical inference using extreme order statistics, *Ann. Statist.*, 3, 119–131, 1975.
- Prudhomme, C., and D. Reed, Mapping extreme rainfall in a mountainous region using geostatistical techniques: A case study in scotland., *Int. J. Climatol.*, 1999.
- Ribatet, M., A user's guide to the spatialextremes package, *Tech. rep.*, EPFL, 2009.
- Ribatet, M., and M. Sedki, Extreme value copulas and max-stable processes, *J. Soc. Fr. Stat.*, 2012.
- Ruppert, D., M. Wand, and R. Carroll, *Semiparametric regression*, Cambridge Series in Statistical and Probabilistic Mathematics, 2003.
- Rust, H., D. Maraun, and T. Osborn, Modelling seasonality in extreme precipitations: A uk case study, *Eur. Phys. J-Spec. Top.*, 174, 99–111, 2009.
- Salm, B., A. Burkard, and H. Gubler, Berechnung von fließlawinen: eine anleitung für praktiker mit beispielen, *Internal report EISLF (in German)*, 47, 1990.
- Schlather, M., Models for stationary max-stable random fields, *Extremes*, 5(1), 33–44, 2002.
- Schlather, M., and J. Tawn, A dependence measure for multivariate and spatial extreme values: Properties and inference, *Biometrika*, 2003.
- Schweizer, J., B. Jamieson, and M. Schneebeli, Snow avalanche formation, *Rev. Geophys.*, 41(4), 1016., 2003.
- Schweizer, J., C. Mitterer, and L. Stoffel, On forecasting large and infrequent snow avalanches, *Cold Reg. Sci. Technol.*, 59, 234–241, 2009.
- Segers, J., Nonparametric inference for max-stable dependence, *Statist. Sci.*, 27(2), 193–196, 2012.
- Smith, R., Max-stable processes and spatial extremes, unpublished, 1991.
- Takeuchi, K., Distribution of informational statistics and a criterion of model fitting., *Suri-Kagaku*, 153, 12–18, 1976.
- Weisse, A., and P. Bois, Topographic effects on statistical characteristics of heavy rainfall and mapping in the french alps., *J. Appl. Meteorol.*, 40(4), 720–740, 2001.
- Xu, X., and N. Reid, On the robustness of maximum composite likelihood estimate, *J. Stat. Plann. Infer.*, 141(9), 3047–3054, 2011.

Chapter 6

Coupling of mechanical and meteorological factors for the evaluation of avalanche release depth distributions

This chapter is composed of an article entitled “Relative influence of mechanical and meteorological factors on avalanche release depth distributions: An application to French Alps” which was **published** in *Geophysical Research Letters* the 20th of June 2012. The following authors helped in the construction of this paper: Guillaume Chambon, Nicolas Eckert and Mohamed Naaim.

This paper presents a rigorous formalism in which avalanche release depth distributions are expressed through a coupling between the mechanical and meteorological ingredients presented in the previous chapters. Considering that an avalanche can occur only if the snowfall depth exceeds a critical value corresponding to a stability criterion, release depth distributions obtained from the slab–weak layer mechanical model (Chapter 4) are coupled with the distribution of 3-day extreme snowfalls (Chapter 5). This coupled model is able to reproduce field data from 369 natural slab avalanches in La Plagne (France) for both the tail and the core of the distribution. Small to medium-sized avalanches are controlled mainly by mechanics, whereas large avalanches are controlled by a strong mechanical–meteorological coupling. Finally, we demonstrate the non-universality of the obtained distribution, which is strongly space-dependent, and, using the consistent interpolation formalism presented in Chapter 5, our model is used to obtain release depth maps for different return periods.

Relative influence of mechanical and meteorological factors on avalanche release depth distributions: An application to French Alps

J. Gaume,¹ G. Chambon,¹ N. Eckert,¹ and M. Naaim¹

Received 9 April 2012; revised 14 May 2012; accepted 17 May 2012; published 20 June 2012.

[1] The evaluation of avalanche release depth distributions represents a major challenge for hazard management. This paper presents a rigorous formalism in which these distributions are expressed through a coupling of mechanical and meteorological factors. Considering that an avalanche can occur only if the snowfall depth exceeds a critical value corresponding to a stability criterion, release depth distributions obtained from a slab–weak layer mechanical model are coupled with the distribution of 3-day extreme snowfalls. We show that this coupled model is able to reproduce field data from 369 natural slab avalanches in La Plagne (France). Not only the power-law tail of the distribution, corresponding to large slab depths, but also the core of the distribution for shallow slab depths, are well represented. Small to medium-sized avalanches appear to be controlled mainly by mechanics, whereas large avalanches and the associated power-law exponent, are influenced by a strong mechanical-meteorological coupling. Finally, we demonstrate that the obtained distribution is strongly space-dependent, and, using a consistent interpolation formalism, our model is used to obtain release depth maps for given return periods.

Citation: Gaume, J., G. Chambon, N. Eckert, and M. Naaim (2012), Relative influence of mechanical and meteorological factors on avalanche release depth distributions: An application to French Alps, *Geophys. Res. Lett.*, 39, L12401, doi:10.1029/2012GL051917.

1. Introduction

[2] The evaluation of avalanche release depth distributions represents a challenging issue for the mapping, zoning and long term management of hazard in mountainous regions. In particular, these distributions constitute one of the essential ingredients (besides friction, terrain, and erosion) to predict accurate run-out distances using avalanche propagation models [Barbolini *et al.*, 2000]. Currently, a strong debate is still ongoing concerning the existence of a possible universal behavior for these distributions. In their pioneering work, Rosenthal and Elder [2003] studied a set of 8000 avalanches mixing artificial and natural triggers at Mammoth Mountain (USA), and showed that the release depth cumulative exceedance distribution (CED) appears to follow a power-law of exponent -2.6 . This led them to postulate that avalanche release depths are scale-invariant and behave as a

chaotic process. They argue that this behavior may be due to the deposition and evolution of snow layers and to the mechanics of slab avalanche release. McClung [2003] reported the same behavior and power-law exponent for a set of 187 slab avalanches in British Columbia (mix of triggers), and points out the possible role of fracture toughness distributions and mechanical size effects. This author also analyzed separately artificial and natural avalanche releases to study the effect of the triggering mechanism. A scale-invariant CED tail was also found on the set of 56 natural avalanches, although on a relatively small range of depths in this case and with an apparent power-law exponent of -4.4 . Failletaz *et al.* [2006] studied 3450 avalanches in Tignes and La Plagne (France) and also reported a power-law CED with a characteristic exponent of -2.4 for artificially released avalanches. Given the similarity of this result with previous studies carried out in different areas, they concluded on the universality of this power-law exponent. Finally, a more recent study by Bair *et al.* [2008] compares the adjustment of different statistical distributions on release depth data from different mountainous areas, and show that GEV (Generalized Extreme Value) and Fréchet distributions seem to provide better fits than power-law distributions for all the analyzed datasets. They also show a significant spatial variation in the power-law exponents of the CED tails and conclude, on the contrary, on a non-universal behavior of avalanche release depth distributions.

[3] In this study, we present a new modeling framework in which the observed avalanche release depth distributions are explained through a coupling of release mechanics and extreme snowfall probabilities. We will show that our approach is capable of satisfactory reproducing release depth data, and supports the conclusions of Bair *et al.* [2008] in that neither the core nor the power-law tail of the CED appear to have universal characteristics.

2. Release Depth Data

[4] Ski patrollers from La Plagne (France) ski resort provided us with a database collecting the release depth of 369 natural and 5323 artificially-triggered slab avalanches that occurred from winters 1998 to 2010. We considered that the typical uncertainty on these data is on the order of 30% (representative error associated to the measurement protocol). Figure 1a shows the obtained release depth CED for both trigger types. In both cases, a power law of exponent α was adjusted to the data for depths higher than a cutoff h_c . As shown in Figure 1b, for artificial releases, the power-law exponent α_a varies only slightly with the chosen cutoff h_c . The best fit, in terms of adjustment error, was found for

¹IRSTEA, UR ETNA, St Martin d'Herès, France.

Corresponding author: J. Gaume, IRSTEA, UR ETNA, 2 rue de la Papeterie, F-38400 St Martin d'Herès CEDEX, France. (johan.gaume@gmail.com)

©2012. American Geophysical Union. All Rights Reserved.

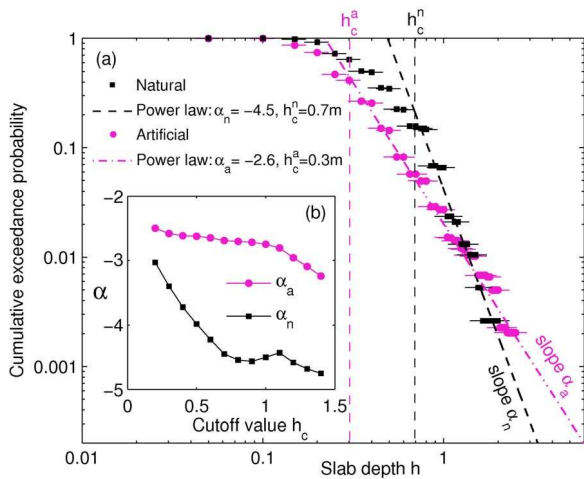


Figure 1. (a) CED of La Plagne slab avalanche release depth data. Natural and artificial avalanches are distinguished and power-laws are adjusted to the tails of the distributions. (b) Power law exponent α as a function of the cutoff value h_c for the two avalanche types.

a relatively low cutoff value $h_c^a = 0.3$ m and leads to an exponent $\alpha_a = -2.6$, very close to the value reported in previous studies [Rosenthal and Elder, 2003; McClung, 2003; Failletaz et al., 2006]. On the contrary, for natural releases, the power-law exponent α_n varies significantly with the cutoff h_c , and the power-law regime tends to be restricted to large avalanches only. The best fit, in this case, was found for a cutoff value $h_c^n = 0.7$ m leading to an exponent $\alpha_n = -4.5$, in agreement with the value reported by McClung [2003]. In view of this relatively large cutoff value, however, it is clear that a complete description of the release depth CED cannot be limited to the power-law tail, but needs to encompass the entire depth range. In the following, we focus specifically on the naturally-released slab avalanches, which are generally the most relevant in terms of hazard zoning applications.

3. Coupled Mechanical-Meteorological Model

3.1. Theoretical Framework

[5] Our approach is based on the assumption that a natural slab avalanche occurs when the recent snowfall exceeds a critical depth corresponding to a mechanical stability criterion. In addition, to account for their spatial variability, both the snowfalls and the critical depth are considered in a stochastic framework. Let us thus define $p_m(h)$ and $p_{sf}(h_{sf})$ as the probability densities of the mechanical critical depth h and of the snowfall depth h_{sf} , respectively. Then, the conditional probability density of having an avalanche release depth h knowing that a snowfall of depth h_{sf} occurred, can be expressed as follows:

$$p(h | h_{sf}) = \begin{cases} \frac{p_m(h)}{\int_0^{h_{sf}} p_m(h') dh'} & \text{if } h \leq h_{sf} \\ 0 & \text{if } h > h_{sf} \end{cases} \quad (1)$$

This amounts to truncating the mechanical distribution $p_m(h)$, retaining only values corresponding to $h \leq h_{sf}$ (see

Figure 3). Finally the global release depth probability density $p(h)$ is obtained by integrating over all values of h_{sf} :

$$p(h) = \int_0^\infty p(h | h_{sf}) p_{sf}(h_{sf}) dh_{sf} = p_m(h) p_{sf/m}(\geq h), \quad (2)$$

$$\text{where } p_{sf/m}(\geq h) = \int_h^\infty \frac{p_{sf}(h_{sf})}{\int_0^{h_{sf}} p_m(h') dh'} dh_{sf}. \quad (3)$$

The avalanche release depth probability is thus expressed through a coupling between mechanical and meteorological factors. As will be shown later, the rigorous coupling equation (2) can be approximated by the following empirical expression:

$$p(h) \approx \tilde{p}(h) = p_m(h) p_{sf}(\geq h) / C, \quad (4)$$

where $p_{sf}(\geq h)$ represents the snowfall CED and $C = \int_0^\infty p_m(h') p_{sf}(\geq h') dh'$ is a normalization constant. In equation (4), we clearly recognize that the global release depth probability $p(h)$ corresponds to the mechanical probability $p_m(h)$ weighted by the probability of having a snowfall h_{sf} greater than h .

3.2. Mechanical Probability Density $p_m(h)$

[6] To determine the probability density $p_m(h)$ of the critical depth h , a mechanical model of slab avalanche release was built. Such avalanches generally result from the rupture of a weak-layer buried under a cohesive slab [Schweizer et al., 2003, and references therein]. In detail, it has also been shown [McClung, 1979; Schweizer, 1999] that the shear rupture generally initiates in local weak spots, from which it then propagates through a stress concentration mechanism. The two essential ingredients taken into account in our model are thus the spatial variability of weak-layer mechanical properties and the redistribution of stresses by elasticity of the overlying slab. At this stage, normal collapse of the weak layer, which has been suggested in some studies [Heierli et al., 2008; van Herwijnen and Heierli, 2009] to play an important role in the propagation of the instability, is not included.

3.2.1. Formulation of the Model

[7] A 2D (plane stress condition) uniform slope of length $L = 50$ m, composed of a slab and a weak layer was simulated (Figure 2a) using the finite element code Cast3m. Gravity is the only applied external force and the system is loaded by progressively increasing the slope angle θ until rupture. The slab is elastic with a Young modulus $E = 1$ MPa, a Poisson ratio $\nu = 0.2$, and a density $\rho = 250$ kg.m⁻³. The weak layer is modeled as a quasi-brittle (strain-softening) interface with a Mohr-Coulomb rupture criterion characterized by a cohesion c and a friction coefficient $\mu = \tan 30^\circ$. The spatial heterogeneity of the weak layer is represented through a stochastic distribution of the cohesion c which, following Jamieson and Johnston [2001] and Kronholm and Birkeland [2005], assumes the form a Gaussian law with a spherical covariance function of correlation length ε . An example of an heterogeneity realization for $\varepsilon = 2$ m is represented in Figure 2a. According to Schweizer et al. [2008], the values of the correlation length ε have been varied in the range 0.5–10 m. The cohesion standard deviation σ_c was fixed at 0.3 kPa while the average $\langle c \rangle$ was varied in the range 0.6–1.5 kPa,

L12401

GAUME ET AL.: AVALANCHE RELEASE DEPTH DISTRIBUTIONS

L12401

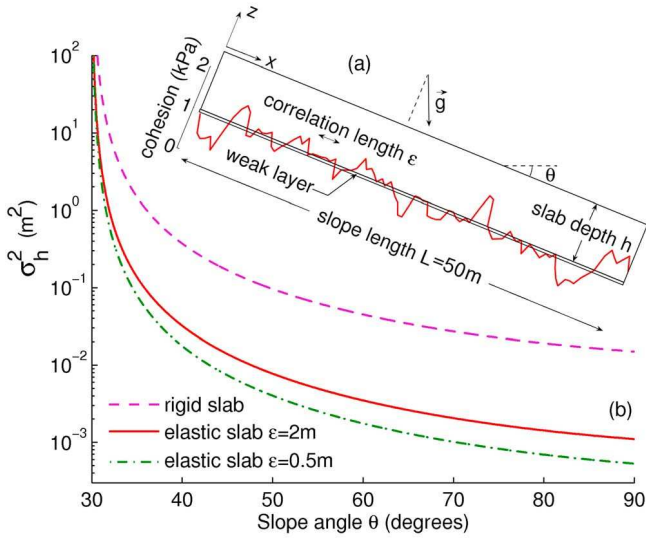


Figure 2. (a) Geometry of the simulated system: a weak layer interface under a cohesive slab of depth h . A realization of the heterogeneity of weak layer cohesion for a correlation length $\varepsilon = 2$ m is represented (average $\langle c \rangle = 1$ kPa, standard deviation $\sigma_c = 0.3$ kPa). (b) Evolution of release depth variance σ_h^2 as a function of slope angle θ for values of correlation length $\varepsilon = 0.5$ m and $\varepsilon = 2$ m. The variance corresponding to a completely rigid slab σ_∞^2 is also shown.

corresponding to coefficients of variation $CV = \sigma_c/\langle c \rangle$ ranging between 20% and 50%.

3.2.2. Release Depth Distributions for a Fixed Slope Angle

[8] More than 5000 simulations were performed for different realizations of the heterogeneity and different sets of model parameters. This allowed us to obtain statistical distributions of release depth h for fixed values of slope angle θ . As a consequence of the Gaussian distribution of the cohesion, these distributions of h are also found to follow Gaussian laws:

$$p(h | \theta) = \frac{1}{\sigma_h \sqrt{2\pi}} e^{-\frac{1}{2} \left(\frac{h - \langle h \rangle}{\sigma_h} \right)^2}, \quad (5)$$

where the average $\langle h \rangle$ and the standard deviation σ_h are related to the model parameters as follows: $\langle h \rangle = \langle c \rangle / (\rho g F)$

and $\sigma_h = \sigma_c f(\varepsilon) / (\rho g F) = \sigma_\infty f(\varepsilon)$, with $F = \sin \theta - \mu \cos \theta$, and $f(\varepsilon) \approx \kappa \varepsilon^{1/3}$ ($\kappa = 0.23 \text{ m}^{-1/3}$). The factor σ_∞ represents the standard deviation that would be observed if the stress field in the weak layer exactly followed the heterogeneity variations (case of a completely rigid slab). As shown in Figure 2b, for realistic values of ε , σ_h^2 is always much lower than the rigid slab variance σ_∞^2 . In addition σ_h^2 decreases with increasing slope angle θ and with decreasing correlation length ε . These evolutions can be explained by a smoothing effect of the weak-layer heterogeneity due to redistributions of stresses by slab elasticity.

3.2.3. Integration Over All Slope Angles

[9] Since release depth data from La Plagne encompass release zones with various slope angles, the mechanical probability $p_m(h)$ is obtained by integrating the release depth distributions $p(h|\theta)$ derived from mechanical modeling over all values of θ . For the sake of simplicity, we chose to consider a uniform slope probability distribution $p(\theta)$ between $\theta_{\min} = 30^\circ$ and $\theta_{\max} = 90^\circ$. This assumption enables us to obtain an analytical expression for $p_m(h)$:

$$p_m(h) = \int_{\theta_{\min}}^{\theta_{\max}} p(h|\theta) p(\theta) d\theta = \frac{\sigma_c f(\varepsilon)}{\rho g h^2 \sqrt{2\pi}} [g_1(h) + g_2(h)], \quad (6)$$

with

$$g_1(h) = e^{-\frac{1}{2} U_1^2} - e^{-\frac{1}{2} U_2(h)^2},$$

and

$$g_2(h) = \sqrt{\frac{\pi}{2}} U_1 \left[\operatorname{erf} \left(\frac{U_1}{\sqrt{2}} \right) + \operatorname{erf} \left(\frac{U_2(h)}{\sqrt{2}} \right) \right],$$

where we defined $U_1 = \langle c \rangle / [\sigma_c f(\varepsilon)]$ and $U_2(h) = (\rho g h - \langle c \rangle) / [\sigma_c f(\varepsilon)]$. As shown in Figure 3a, the mechanical probability density $p_m(h)$ displays negligible values below a characteristic depth h_m . This mechanical cutoff results from a combination of the weak-layer Mohr-Coulomb criterion and the slab heterogeneity smoothing effect, and can be approximated as $h_m \approx [\langle c \rangle - 2\sigma_c f(\varepsilon)] / (\rho g)$. A second important observation is that, for $h > h_m$, the CED $p_m(\geq h)$ follows a power-law trend with a characteristic exponent $\Psi_m = -1$ (Figure 4).

3.3. Snowfall Probability Density $p_{sf}(h_{sf})$

[10] Natural avalanches, which generally occur after or during intense precipitations, can be considered as rare

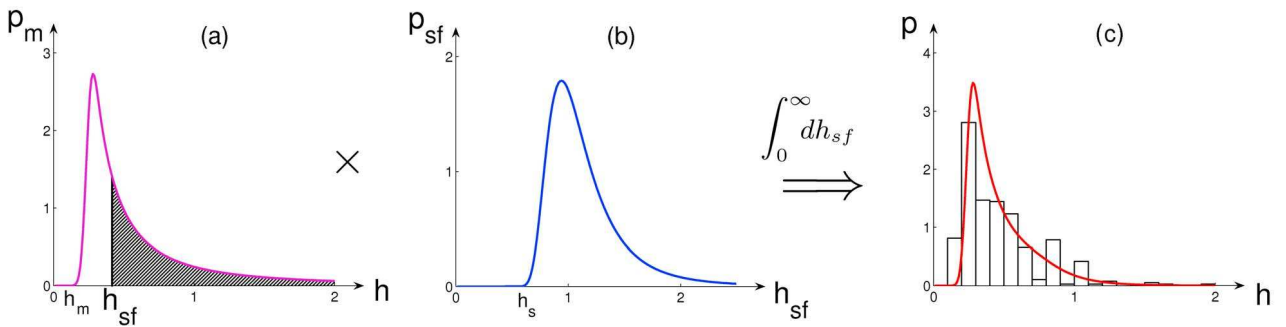


Figure 3. Diagram illustrating the coupling between the mechanical probability p_m and the extreme snowfall probability p_{sf} . (a) Release depth probability density predicted by the mechanical model. The grayed portion corresponds to snow-depth values higher than the available snowfall h_{sf} . (b) Probability density of 3-days extreme snowfalls. (c) Coupled mechanical-meteorological probability density of avalanche release depth. The histogram corresponds to La Plagne data.

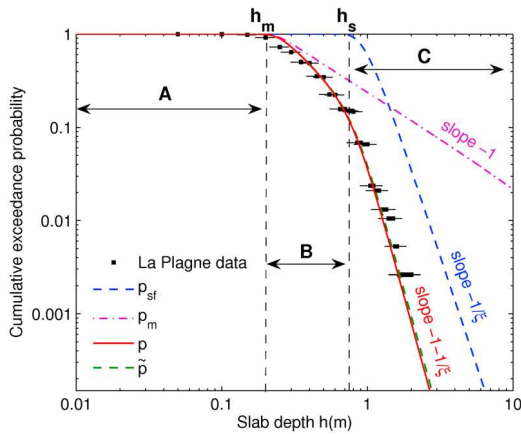


Figure 4. Mechanical release depth CED $p_m(h)$ (equation (6)), extreme snowfall CED $p_{sf}(h)$ (equation (7)), slab release depth CED predicted by the coupled model $p(h)$ (equation (2)), and approximated release depth CED $\tilde{p}(h)$ (equation (4)), compared with field release depth data from La Plagne. The numerical results have been obtained for a correlation length $\varepsilon = 2$ m and an average cohesion $\langle c \rangle = 0.6$ kPa (the other parameters being indicated in text).

events in the statistical sense. In detail, the 3-day extreme snowfall is generally considered as the best avalanche predictor [Schweizer *et al.*, 2003]. Hence, to define the meteorological probability $p_{sf}(h_{sf})$ introduced in equation (2), we analyzed the 3-day snowfall annual maxima in La Plagne (Meteo France data: daily measurements since 1966). These maxima follow a GEV distribution:

$$p_{sf}(\geq h) = 1 - \exp \left[- \left(1 + \xi \frac{h - \mu}{\sigma} \right)^{-1/\xi} \right], \quad (7)$$

where μ , σ and ξ are, respectively, the location, scale, and shape parameters. Taking moreover into account an average snow density of $60 \text{ kg}\cdot\text{m}^{-3}$ (24 h-density from La Plagne data) and a settling of the snowpack after 3 days of 30%, meteorological data in water equivalent can be converted into snow heights, which leads to the following GEV parameters: $\mu = 0.98$ m, $\sigma = 0.21$ m and $\xi = 0.214$. As shown in Figure 3b (density) and Figure 4 (CED), the density $p_{sf}(h_{sf})$ is negligible for $h_{sf} < h_s \approx 0.7$ m in La Plagne (in general, h_s is a function of μ , σ and ξ). For $h_{sf} > h_s$, the CED decreases as a power law whose exponent Ψ_{sf} is directly related to the shape parameter ξ of the GEV: $\Psi_{sf} = -1/\xi \approx -4.68$ in La Plagne. Note that the existence of this power-law tail comes from the fact that the GEV in La Plagne belongs to the Fréchet domain ($\xi > 0$). It would not be the case with Weibull ($\xi < 0$) or Gumbel ($\xi = 0$) distributions.

3.4. Coupling Result

[11] The coupled release depth probability $p(h)$ computed from equation (2) is represented on Figure 3c (density) and Figure 4 (CED). First, it can be noted that, as already mentioned, the approximate probability $\tilde{p}(h)$ (equation (4)) is almost identical to the rigorous coupled probability $p(h)$ for the whole range of depths considered. Concerning the shape of $p(h)$, three different zones can be distinguished (Figure 4). In zone A, for $h < h_m$ no avalanche can occur. Hence, a new

snowfall has to be larger than h_m , after settling, to potentially trigger an avalanche. In zone B, corresponding to $h_m \leq h \leq h_s$ (small to medium-sized avalanches), the coupled CED shows a concave shape (in log-log scales). This zone corresponds to a regime of weak coupling in which the release depth probability $p(h)$ is essentially controlled by the mechanical probability $p_m(h)$, the available amount of snow being sufficient to trigger an avalanche if the mechanical criterion is reached. Lastly, zone C for $h > h_s$ (large avalanches) corresponds to a regime of strong coupling. Snowfall depths larger than h_s become infrequent and thus play the role of a limiting factor on the mechanical probability $p_m(h)$ in the expression of the coupled probability $p(h)$. In this regime, as a direct consequence of the power-law trends displayed both by $p_m(h)$ and $p_{sf}(h)$, the coupled release depth CED also decreases as a power-law. According to equation (4), the corresponding exponent is equal to $\Psi = \Psi_m + \Psi_{sf} = -1 - 1/\xi$.

4. Comparison With Data and Discussion

[12] As shown in Figures 3 and 4, the coupled model presented above is able to reproduce La Plagne data with excellent accuracy. Both the power-law tail, corresponding to large slab depths, and the core of the distribution for shallow slab depths, are well represented. To obtain this result, only the mechanical cutoff h_m was adjusted, which in turn depends on a combination of the average cohesion $\langle c \rangle$, the slab density ρ , the cohesion standard deviation σ_c and the heterogeneity correlation length ε . In our case, the best agreement with the data was obtained for a value $h_m \approx 0.18$ m, which corresponds for instance to $\langle c \rangle = 0.6$ kPa and $\varepsilon = 2$ m (the other parameters being fixed as indicated in Section 3.2). Note also that the obtained agreement critically depends on the fact that, for values of ε in the meter range, the variance σ_n^2 of the mechanical distribution $p_m(h)$ is relatively low due to the elastic smoothing effect (Figure 2b). A less satisfactory data adjustment in zone B would be obtained with values of ε larger than 10–15 m.

[13] Concerning the power-law tail of the CED, it can be noted that, in spite of the good agreement observed in Figure 4, the exponent value $\Psi \approx -5.68$ predicted by the model is lower than $\alpha_n \approx -4.5$ estimated directly from release depth data. This highlights the difficulty of accurately assessing a power-law exponent on the few data corresponding to large avalanches, as already pointed out by McClung [2003]. An important outcome of our coupled model is that the tail exponent Ψ strongly depends on the local meteorological conditions through the shape parameter ξ of the GEV distribution of extreme snowfalls. In the French Alps, ξ -values are generally positive, but present an important spatial variability at regional scale, typically varying between -0.2 and 0.4 . Hence, in agreement with the conclusions of Bair *et al.* [2008], the decay of the tail of natural slab avalanche release depth CED cannot be expected to be universal.

[14] More generally, due to the spatial heterogeneity of the GEV parameters and mechanical properties, it is actually the complete distribution of avalanche release depths which is strongly variable from one location to another. To highlight this point, our model has been used to predict avalanche release depths for a given return period over all French Alps. For that purpose, a spatial interpolation of 3-day extreme snowfall data has been performed using a robust mathematical formalism based on Max-Stable processes and properly

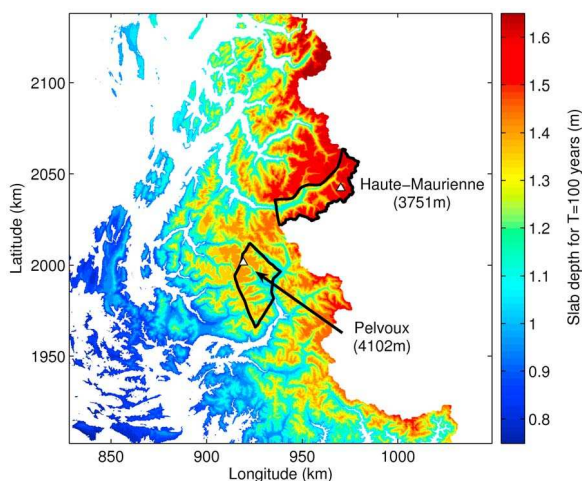


Figure 5. Map of slab avalanche release depth in the French Alps for a return period of 100 years and elevations higher than 1000 m.

accounting for the spatial dependence of the data [Blanchet and Lehning, 2010; Blanchet and Davison, 2011]. A brief description of this spatial model can be found in Eckert *et al.* [2010, 2011]. As shown in Figure 5, the results highlights that, at first order, avalanche release depths are dominated by altitudinal effects. However, in detail, the variation patterns of the GEV parameters with latitude and longitude can also be noticed. For instance, the release depths predicted in the Haute-Maurienne massif culminating at 3751 m are significantly higher (>1.6 m) than those in the Pelvoux massif culminating at 4102 m (<1.4 m). Note that, at this stage, these spatial trends are purely due to snowfall properties since the values of all mechanical parameters have been assumed constant in this interpolation. In a further step, spatialization of the cohesion distributions will also need to be considered, but additional data will be required for that purpose.

5. Conclusion

[15] This paper investigates the relative influence of mechanical and meteorological factors on avalanches release depth distributions. A robust formalism for the coupling of a stochastic stability criterion (resulting from spatial heterogeneity of the mechanical properties) with extreme snowfall distributions has been developed. It has been shown that this coupled mechanical-meteorological model is able to reproduce with excellent accuracy the release depth distribution corresponding to 369 natural slab avalanches in La Plagne (France). Not only the power-law tail, corresponding to large slab depths, but also the core of the distribution for shallow slab depths, are well represented. This agreement does not prove that the physical mechanisms of avalanche release are fully captured in the model proposed. However, the retained ingredients appear sufficient to produce realistic release depth distributions and to provide an interpretation of the distribution parameters (cutoff, exponent, etc.) in terms of clearly-identified nivological properties.

[16] From the model, three avalanche release regimes have been identified. Large avalanches, in particular, are controlled by a strong coupling between mechanical and

meteorological factors. In agreement with previous studies, the release depth CED in this regime behaves as a power-law. However, the corresponding exponent directly depends on the shape parameter of the meteorological GEV distribution and, thus, cannot be considered as universal.

[17] From an operational perspective, the model presented in this paper can be viewed as a powerful tool capable of evaluating avalanche depth distributions at any location, provided snowfall data are available or a suitable spatial interpolation procedure is used. It can be highlighted that, compared to the classical engineering method in which only the 3-day extreme snowfalls are taken into account, the release depth values for a given return period computed with our coupled model generally tend to be lower (see Figure 4).

[18] **Acknowledgments.** Support from the European Interreg DYNAVAL and the ANR MOPERA projects is acknowledged. We also wish to express our gratitude to C. Schneider, snow expert in La Plagne, for providing release depth data and to the two reviewers, M. Lehning and J. Schweizer, for their insightful and constructive comments. Support from the European Interreg DYNAVAL and MAP3 projects and from the ANR MOPERA is acknowledged.

[19] The Editor thanks Michael Lehning for assisting in the evaluation of this paper.

References

- Bair, E. H., J. Dozier, and K. W. Birkeland (2008), Avalanche crown-depth distributions, *Geophys. Res. Lett.*, *35*, L23502, doi:10.1029/2008GL035788.
- Barbolini, M., U. Gruber, C. Keylock, M. Naaim, and F. Savi (2000), Application and evaluation of statistical and hydraulic-continuum dense-snow avalanche models to five real European sites, *Cold Reg. Sci. Technol.*, *31*(2), 133–149.
- Blanchet, J., and A. Davison (2011), Spatial modelling of extreme snow depth, *Ann. Appl. Stat.*, *5*(3), 1699–1725.
- Blanchet, J., and M. Lehning (2010), Mapping snow depth return levels: Smooth spatial modeling versus station interpolation, *Hydrol. Earth Syst. Sci. Discuss.*, *7*, 6129–6177.
- Eckert, N., C. Coleou, H. Castebrunet, M. Deschates, D. Giraud, and J. Gaume (2010), Cross-comparison of meteorological and avalanche data for characterising avalanche cycles: The example of December 2008 in the eastern part of the French Alps, *Cold Reg. Sci. Technol.*, *64*, 119–136.
- Eckert, N., J. Gaume, and H. Castebrunet (2011), Using spatial and spatial-extremes to characterize snow avalanche cycles, *Procedia Environ. Sci.*, *7*, 224–229.
- Faïlletaz, J., F. Louchet, and J. Grasso (2006), Cellular automaton modeling of slab avalanche triggering mechanisms: From the universal statistical behaviour to particular cases, in *Proceedings of the ISSW 2006*, pp. 174–180, Int. Snow Sci. Workshop, Telluride, Colo.
- Heierli, J., P. Gumbsch, and M. Zaiser (2008), Anticrack nucleation as triggering mechanism for snow slab avalanches, *Science*, *321*, 240–243.
- Jamieson, J., and C. Johnston (2001), Evaluation of the shear frame test for weak snowpack layers, *Ann. Glaciol.*, *32*, 59–69.
- Kronholm, K., and K. W. Birkeland (2005), Integrating spatial patterns into a snow avalanche cellular automata model, *Geophys. Res. Lett.*, *32*, L19504, doi:10.1029/2005GL024373.
- McClung, D. M. (1979), Shear fracture precipitated by strain softening as a mechanism of dry slab avalanche release, *J. Geophys. Res.*, *84*(B7), 3519–3526, doi:10.1029/JB084iB07p03519.
- McClung, D. M. (2003), Size scaling for dry snow slab release, *J. Geophys. Res.*, *108*(B10), 2465, doi:10.1029/2002JB002298.
- Rosenthal, W., and K. Elder (2003), Evidence of chaos in slab avalanching, *Cold Reg. Sci. Technol.*, *37*, 243–253.
- Schweizer, J. (1999), Review of dry snow slab avalanche release, *Cold Reg. Sci. Technol.*, *30*, 43–57.
- Schweizer, J., J. Bruce Jamieson, and M. Schneebeli (2003), Snow avalanche formation, *Rev. Geophys.*, *41*(4), 1016, doi:10.1029/2002RG000123.
- Schweizer, J., K. Kronholm, J. Jamieson, and K. Birkeland (2008), Review of spatial variability of snowpack properties and its importance for avalanche formation, *Cold Reg. Sci. Technol.*, *51*(2–3), 253–272.
- van Herwijnen, A., and J. Heierli (2009), Measurement of crack-face friction in collapsed weak snow layers, *Geophys. Res. Lett.*, *36*, L23502, doi:10.1029/2009GL040389.

Chapter 7

Conclusion

In this thesis, a framework for the evaluation of avalanche depths in any potential release zone using a coupled statistical–mechanical approach was proposed. First, the influence of weak layer heterogeneity on slab avalanche release was studied using a finite element model. A shear-softening weak layer underlying an elastic slab was modeled, and the system is loaded by increasing the slope angle until failure and avalanche release. After validating the model on the case of nil-cohesion weak spots, the effect of a heterogeneous weak-layer cohesion field was studied. Its heterogeneity was modeled by Gaussian distribution, with a spherical covariance function characterized by a spatial correlation length. Release angle distributions were analyzed: the average release angle decreases as a power-law with slab depth h but is almost unaffected by the correlation length ϵ and thus by the heterogeneity; the release angle variance decreases as a power-law with slab depth h and increases, also as a power-law, with the correlation length ϵ . Then a heterogeneity smoothing effect due to redistributions of stresses by elasticity of the slab was highlighted. This smoothing effect induces a reduction of the release angle variance compared to the case of a fully rigid slab. The smoothing intensity depends on the ratio between the correlation length ϵ and a characteristic elastic length of the system Λ . The obtained release angle distributions were then rigorously inverted, yielding a release depth distribution integrated over all slopes. We also used this mechanically-based statistical model in the case of an elastic-brittle slab to study the position of slab tensile failure. Two types of releases were observed in the simulations: (1) Full-slope releases for which the heterogeneity is not sufficient to trigger slab tensile failure. These releases are influenced by the topography and the morphology of the path. (2) Partial-slope releases for which the local variations of weak-layer cohesion is substantial and can trigger the slab tensile crack on its own. Importantly, for both release types, the primary process is always the basal shear failure of the weak layer. We showed that, with realistic sets of parameters, the releases are full-slope. Hence, the crown fracture always occurs at particular topographical and morphological features (such as ridges, rocks, trees, etc).

In the future, a straightforward extension of the model to the 3d-case should allow to predict avalanche release volumes.

Then, extreme snowfalls have been evaluated in the French Alps by mapping snowfall water equivalent annual maxima coming from 40 measurement stations. The mathematical formalism of max-stable processes generalizing extreme value theory to the multivariate spatial context has been used. It has been shown in particular that the Brown-Resnick model provides an extremal coefficient that fits the data better than those of Smith and Schlather which are less flexible. Besides, space transformation has been used to model anisotropy, which further improved the adjustment. It appeared that the spatial extremal dependence depends strongly on the local orientation of the alpine axis and the presence of large valleys. For example, for a 3-day accumulation period, the dependence range is more than twice as high in this alpine axis direction in comparison to the orthogonal direction. We refined this result important for many hydrological problems and already obtained in other countries by showing that the intensity of the directional effect is all the more important than the duration of accumulation is low.

Linear models and penalized splines with radial basis functions for the evolution of the GEV parameters with space were compared on the basis of TIC and NRMSE criteria. The best results were obtained with a spline model, showing lower TIC and NRMSE values for the whole French Alps, and more significantly in the extreme Southern Alps. At a constant altitude (2000m), the highest location parameters μ are very North (Mont-Blanc, Aravis and Bauges massifs), but significantly high values are also observed far South. The highest scale parameters σ are in the Southeast (extreme Southern Alps) which corresponds to the Mediterranean effect that tends to bring variability. The shape parameter ξ is mainly positive in the Northern, Central and Southern Alps, showing a Frechet attraction domain, and becomes negative in the extreme Southern Alps (Weibull domain).

The results of our best model, and more particularly the obtained quantile maps, present a clear interest for operational applications. For example, the 100-year snowfall quantile can be determined at any point in the French Alps and for different periods of accumulations. In detail, it has been shown that 100-years quantile for a 3-days accumulation period is the highest in the Central and Southern Alps at the boarder with Switzerland and Italy. Furthermore, the influence of the accumulation period on the intensity and the frequency of extreme events has been analyzed.

It has also been shown how a joint analysis can be performed to evaluate the risk of obtaining an extreme event in two different locations within the same year, leading to conditional return level maps which can also be very useful from an operational perspective. Validation on other available data has shown the accuracy of the fitted model and of the simple way of handling altitudinal effects which has been proposed.

The employed smooth modelling of GEV parameters associated with MSPs and a nested model selection procedure constitutes the methodological strong point of the work. This up-to-date framework could be put in use for various other applications in hydrology.

As improvement perspectives of the model, other MSPs which have been very recently developed could also be tested, and other covariates could be further introduced in the model such as the winter mean snowfall (WMS). Finally, a pre-selection of the data corresponding to the flux type (North–North West / South–South East fluxes) would be an interesting prospect to investigate given the significant regional effects demonstrated in this thesis.

Finally, to obtain avalanche release depth distributions, mechanical and meteorological factors both need to be taken into account. Hence, a robust formalism for the coupling of a stochastic stability criterion (resulting from spatial heterogeneity of the mechanical properties) with extreme snowfall distributions has been developed. It has been shown that this coupled mechanical-meteorological model is able to reproduce with excellent accuracy the release depth distribution corresponding to 369 natural slab avalanches in La Plagne (France). Not only the power-law tail, corresponding to large slab depths, but also the core of the distribution for shallow slab depths, are well represented. A detailed sensitivity analysis showed that this good agreement is obtained with only one adjustable parameter, namely the average cohesion $\langle c \rangle$, and critically depends on the heterogeneity smoothing effect by slab elasticity.

From the coupled model, three avalanche release regimes have been identified. Large avalanches, in particular, are controlled by a strong coupling between mechanical and meteorological factors. In agreement with previous studies, the release depth CED in this regime behaves as a power-law. However, the corresponding exponent directly depends on the shape parameter of the meteorological GEV distribution and, thus, cannot be considered as universal.

From an operational perspective, the model presented in this thesis can be viewed as a powerful tool capable of evaluating avalanche depth distributions at any location, as soon as meteorological data are available. These distributions can be used as inputs of propagation models (Barbolini et al., 2000; Naaim et al., 2003) to establish hazard maps. It can be highlighted that, compared to the classical engineering method in which only the 3-day extreme snowfalls are taken into account, the release depth values for a given return period computed with our coupled model generally tend to be lower. Besides, using the mathematical formalism of max-stable processes, avalanche release depth maps for a given return period can be obtained. At this stage, the spatial trends observed are purely due to snowfall properties since the values of all mechanical parameters have been assumed constant in this interpolation. In a further step, spatialization of the cohesion distributions

will also need to be considered, but additional data will be required for that purpose.

The proposed mechanically-based probabilistic model coupled with extreme snowfalls thus fulfills the objectives of the study, namely the evaluation of avalanche release depth distributions in any potential release zone, provided snowfall data are available or a suitable spatial interpolation procedure is used. However, before being fully used operationally, additional tests on other datasets in other locations should now be performed to further validate this model.

To finish, a GUI (Graphical User Interface) was developed in the Java language in order to simplify the selection of snowfall depth data coming from the max-stable model and avalanche release depth data coming from the coupled model for different return periods for all French Alps massifs. This interface also shows the GEV distribution and the values of its parameters (μ , σ and ξ). A screenshot of this GUI is shown in Fig. 7.1.

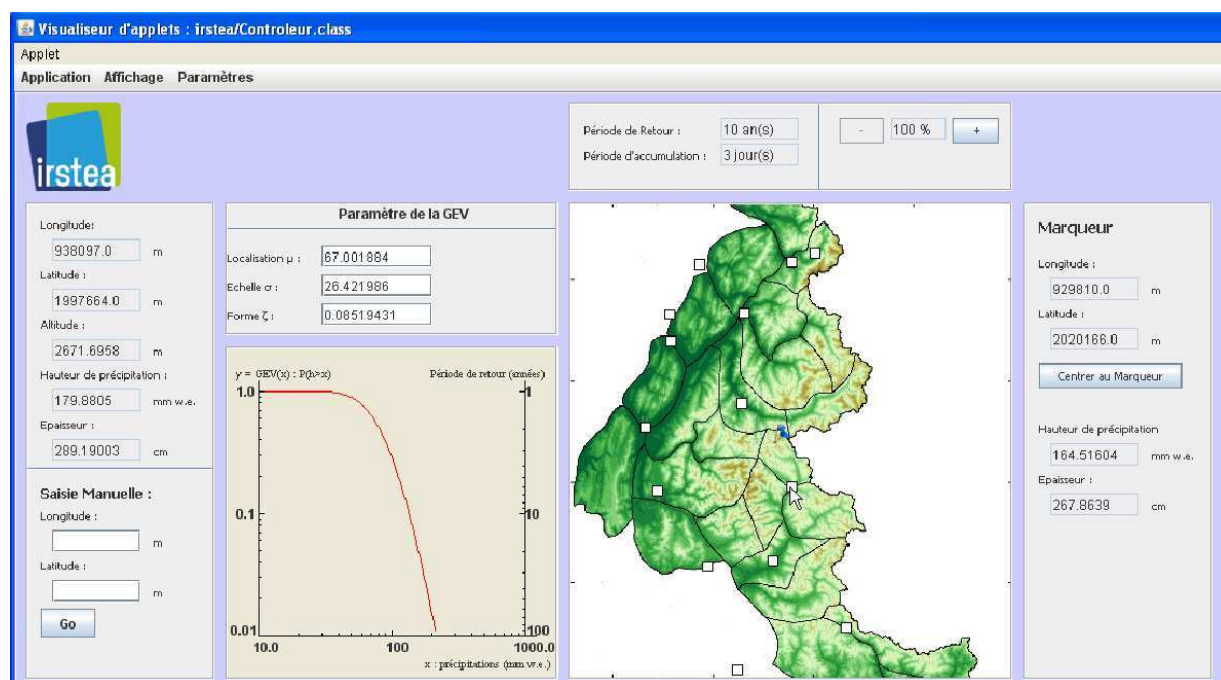


Figure 7.1: Screenshot of the GUI (Graphical User Interface) developed for the selection of snowfall depth data coming from the max-stable model and avalanche release depth data coming from the coupled model for different return periods for all French Alps massifs.

Chapter 8

Conclusion (version française)

Dans cette thèse, la prédétermination des hauteurs d'avalanche dans toute zone de départ potentielle a été réalisée en utilisant une approche couplée statistique–mécanique. Tout d'abord, nous avons étudié l'influence de l'hétérogénéité de la couche fragile sur le départ des avalanches de plaque à l'aide d'une modélisation par éléments finis. Le système simulé est composé d'une couche fragile modélisée comme une interface adoucissante en cisaillement sous une plaque élastique. Le système est chargé en augmentant l'angle de la pente jusqu'à la rupture correspondant au départ de l'avalanche. Après avoir validé le modèle sur le cas de zones faibles de cohésion nulle, l'effet d'une cohésion de la couche fragile spatialement hétérogène a été étudié. L'hétérogénéité est représentée par une distribution gaussienne, avec une fonction de covariance sphérique caractérisée par une longueur de corrélation spatiale. Les distributions d'angle de départ obtenues ont été analysées: l'angle de départ moyen décroît avec l'épaisseur de la plaque h comme une loi puissance mais n'est quasiment pas affecté par la longueur de corrélation ϵ et donc par l'hétérogénéité; la variance de l'angle de départ décroît également avec h comme une loi puissance et augmente avec ϵ . Un effet de lissage de l'hétérogénéité du aux redistributions de contraintes par élasticité de la plaque a été mis en évidence. Cet effet de lissage induit une réduction de la variance de l'angle de départ par rapport au cas d'une plaque complètement rigide. L'intensité du lissage dépend du rapport entre la longueur de corrélation ϵ et une longueur élastique caractéristique du système Λ . Ces distributions d'angle de départ ont ensuite été rigoureusement inversées afin d'obtenir une distribution de hauteur de départ d'avalanche intégrée sur toutes les pentes. Nous avons également utilisé ce modèle mécanique-statistique dans le cas d'une plaque élastique-fragile pour étudier la position de la rupture en traction de la plaque. Deux types de départs ont été observés dans les simulations: (1) Les départs complets pour lesquels l'hétérogénéité n'est pas suffisante pour déclencher une rupture en traction. Ces départs sont influencés par la topographie et la morphologie du couloir. (2) Les départs partiels pour lesquels les variations locales de la cohésion de la couche fragile sont importantes et peuvent déclencher la rupture en traction

de la plaque à elles-seules. Il est important de noter que, pour les deux types de départs, le processus de rupture primaire observé est toujours la rupture en cisaillement de la couche fragile basale. Nous avons aussi montré que, avec un ensemble de paramètres réalistes, les départs sont complets. Ainsi, la zone de départ se situe toujours au niveau de caractéristiques topographiques et morphologiques particulières (ruptures de pentes, rochers, arbres, etc).

Plus généralement, une extension du modèle au cas 3D devrait permettre de prédire les volumes de départ d'avalanche.

Dans un deuxième temps, la prédétermination des chutes de neige extrêmes dans les Alpes françaises a été réalisée en cartographiant les maxima annuels de chutes de neige en équivalent en eau mesurés dans 40 stations nivo-météorologiques. Le formalisme mathématique des processus max-stables généralisant la théorie des valeurs extrêmes au contexte multivarié spatial a été utilisé. Il a été montré en particulier que les coefficients extrémaux prédits par le modèle de Brown-Resnick s'ajustent mieux aux données que ceux de Smith et Schlather qui sont moins souples. Par ailleurs, une transformation elliptique de l'espace a été utilisée pour modéliser l'anisotropie, ce qui a encore amélioré l'ajustement. Il est apparu que la dépendance spatiale des extrêmes était fortement fonction de l'orientation locale de l'axe alpin et de la présence de grandes vallées. Par exemple, pour une période d'accumulation de 3 jours, la portée de la dépendance est deux fois plus élevée dans la direction de l'axe alpin que dans la direction orthogonale. Ce résultat, déjà mis en évidence dans d'autres pays, a été affiné en montrant que l'intensité de l'effet directionnel est d'autant plus important que la durée de l'accumulation est faible.

Pour l'évolution des paramètres de la GEV avec l'espace, des modèles linéaires et des splines pénalisées avec des fonctions de base radiales ont été comparés sur la base des critères TIC et NRMSE et le meilleur modèle s'est avéré être un modèle spline. D'après ce modèle, à altitude constante (2000m), les valeurs les plus élevées du paramètre de localisation μ sont situées très au Nord (massifs du Mont-Blanc, des Aravis et des Bauges), mais des valeurs relativement élevées sont également observées dans les Alpes extrême-sud. Les valeurs du paramètre d'échelle σ sont les plus importantes dans le Sud-Est (Alpes extrême-sud), ce qui correspond à l'effet méditerranéen qui tend à amener de la variabilité. Le paramètre de forme ξ est globalement positif dans les Alpes du Nord, centrales et dans les Alpes du Sud, correspondant à un domaine d'attraction de Fréchet, et devient négatif dans les Alpes extrême-sud (domaine de Weibull).

Les résultats de notre meilleur modèle, et plus particulièrement les cartes de chutes de neige pour différentes périodes de retour, constituent un outil opérationnel puissant pour la gestion à long terme du risque d'avalanche. Par exemple, la chute de neige centennale peut être déterminée en n'importe quel point des Alpes françaises et pour différentes périodes

d'accumulation. En détail, nous avons montré que le quantile centennal pour une période d'accumulation de 3 jours était le plus élevé à la frontière avec la Suisse et l'Italie dans la partie centrale et sud des Alpes. En outre, l'influence de la période d'accumulation sur l'intensité et la fréquence des événements extrêmes a été analysée.

Nous avons montré également qu'une analyse jointe pouvait être réalisée afin d'évaluer la probabilité d'obtenir deux événements extrêmes dans deux endroits différents pendant la même année, donnant lieu à des cartes de niveaux de retours conditionnels qui peuvent aussi être très utiles d'un point de vue opérationnel. La validation sur d'autres données disponibles a montré la précision du modèle ajusté et de la procédure relativement simple qui a été proposée pour gérer les effets d'altitude.

La modélisation lisse des paramètres de la GEV associée aux processus max-stables et à une procédure de sélection de modèles imbriqués constitue le point méthodologique fort de ce travail. Ce cadre pourrait être utilisé pour d'autres applications en hydrologie.

Comme perspectives d'amélioration du modèle, d'autres processus max-stables qui ont été très récemment développés pourraient également être testés, et d'autres covariables pourraient être introduites dans le modèle, comme la moyenne hivernale des chutes de neige par exemple. Enfin, une pré-sélection des données correspondant au type de flux (Nord - Nord Ouest / Sud - Sud Est) serait une perspective d'étude intéressante étant donné les effets régionaux importants démontrés dans cette thèse.

Enfin, afin d'obtenir des distributions de hauteur de départ d'avalanche, les facteurs mécaniques et météorologiques doivent être pris en compte conjointement. Par conséquent, un formalisme robuste pour le couplage d'un critère de stabilité stochastique (résultant de l'hétérogénéité spatiale des propriétés mécaniques) avec les distributions des chutes de neige extrêmes a été développé. Nous avons montré que ce modèle couplé mécanique-météorologique était capable de reproduire avec une excellente précision la distribution de départ d'avalanche correspondant à 369 avalanches naturelles de plaque à La Plagne (France). Non seulement la queue de la distribution en loi de puissance, correspondant à des épaisseurs de plaque élevées, mais aussi le corps de la distribution pour de faibles épaisseurs, sont bien ajustés. Une analyse de sensibilité détaillée a montré que cet accord peut être obtenu avec un seul paramètre ajustable, à savoir la cohésion moyenne $\langle c \rangle$, et que cet accord est possible grâce aux effets de lissages de l'hétérogénéité par élasticité de la plaque.

A partir du modèle, trois régimes de départ d'avalanche ont été identifiés. Les grosses avalanches, en particulier, sont contrôlées par un couplage fort entre les facteurs mécaniques et météorologiques. En accord avec les études précédentes, dans ce régime, la distribution cumulée de hauteur de départ d'avalanche se comporte comme une loi puissance. Toutefois, l'exposant correspondant dépend directement du paramètre de forme de la distribution

GEV des chutes de neiges et, par conséquent, ne peut pas être considéré comme universel.

D'un point de vue opérationnel, le modèle présenté dans cet thèse peut être considéré comme un outil puissant capable de prédéterminer les distributions de hauteur d'avalanche en n'importe quelle zone de départ, à partir du moment où des données météorologiques sont disponibles. Ces distributions peuvent être utilisées pour établir des cartes de risque ou comme entrées de modèles de propagation (Barbolini et al., 2000; Naaim et al., 2003). Nous mettons en évidence également que, par rapport à la méthode d'ingénierie classique, dans laquelle seules les chutes de neige extrêmes sur 3 jours sont prises en compte, les valeurs de hauteur de départ pour une période de retour donnée calculées avec notre modèle couplé ont généralement tendance à être plus faibles. En outre, en utilisant le formalisme mathématique des processus max-stables proposé, des cartes de hauteur de départ d'avalanche pour une période de retour donnée peuvent être obtenues. Néanmoins il faut noter qu'à ce stade, les tendances spatiales sont purement liées aux propriétés des chutes de neige puisque les valeurs de tous les paramètres mécaniques ont été supposées constantes dans cette interpolation. Dans une étape ultérieure, la spatialisation de la distribution de cohésion devra également être envisagée, mais des données supplémentaires seront nécessaires à cette fin.

Le modèle mécanique-statistique proposé couplé avec la probabilité des chutes de neige extrêmes remplit les objectifs de l'étude, à savoir la prédétermination des distributions de hauteur d'avalanche dans toute zone de départ potentielle, en utilisant soit des données des chutes de neige disponibles ou une procédure d'interpolation spatiale appropriée. Toutefois, avant d'être pleinement utilisable sur le plan opérationnel, des tests supplémentaires sur d'autres jeux de données dans d'autres sites doivent maintenant être effectués pour valider complètement ce modèle.

Pour finir, une interface graphique a été réalisée en langage Java afin de simplifier la saisie des données de hauteurs de chutes de neige issues du modèle max-stable et de hauteurs de départ d'avalanche issues du modèle couplé, pour différentes périodes de retour et en tous points des Alpes Françaises. Cette interface renvoie également la distribution GEV et la valeur de ses paramètres (μ , σ and ξ). Une capture d'écran de cette interface est présentée en Fig. 7.1.

Appendix A

Influence of weak layer friction heterogeneity on slab avalanche release

This appendix is composed of a conference proceeding entitled “Influence of weak layer heterogeneity on slab avalanche release using a finite element method”. It was presented in the *International Workshop on Bifurcation and Degradation in Geomaterials* and **published** in *Springer Series in Geomechanics and Geoengineering* in 2011 with the contribution of Guillaume Chambon, Mohamed Naaim and Nicolas Eckert.

The objective of this article is to study the influence of a weak layer friction heterogeneity on slab avalanche release using the mechanically-based statistical model presented in Chapter 4. The main differences with Section 4.1 are thus the choice of the parameter that varies in space, here the friction angle ϕ of the weak layer Mohr-Coulomb criterion, and the constitutive law of the slab which is elastic-brittle with a tensile strength $\sigma_T = 1$ kPa. From this model, avalanche release depth distributions are obtained and the effect of friction heterogeneity on the localization of the slab tensile failure is studied. We showed that, with an heterogeneous friction angle of the weak layer, the obtained release angle distributions were very slightly influenced by the slab depth h , which is not very realistic and which led us to choose an heterogeneous cohesion for the main part of this PhD thesis.

Influence of weak layer heterogeneity on slab avalanche release using a finite element method.

J.Gaume, G.Chambon, M.Naaim and N.Eckert

Abstract Snow avalanches generally result from the collapse of a weak layer underlying a cohesive slab. We use the finite element code Cast3m to build a complete mechanical model of the {weak layer-slab} system including inertial effects. We model the weak layer as a strain-softening interface whose properties are spatially heterogeneous. The softening accounts for the breaking of ice bridges. The overlying slab is represented by a Drucker-Prager elasto-plastic model, with post-peak softening to model the crack opening. The two key ingredients for the mechanical description of avalanches releases are the heterogeneity of the weak layer and the redistribution of stresses by elasticity of the slab. The heterogeneity is modeled through a Gaussian stochastic distribution of the friction angle with spatial correlations. We first study the effect of the weak layer's heterogeneity and the slab depth on the release on a simple uniform slope geometry. We observe two releases types, full slope releases corresponding to a crown rupture and partial slope releases for which the traction rupture occurs inside the slope and thus only a part of the slope is released. The influence of slab depth on the relative proportion of these two rupture types, as well as on the avalanche angle distributions is also studied.

1 Introduction

Recently, several models have been developed to simulate the flow of the various types of snow [Naaim2003, Naaim2004] involved in snow avalanches. Nevertheless, the systematic use of these models in operational applications still faces a number of difficulties including the evaluation of the avalanche release volume which is an input parameter of these models which very strongly influences the results. However, there is currently no clear and well-defined methodology which would enable, for a given avalanche path, to predetermine the initial volume of potential avalanches

J.Gaume, G.Chambon, M.Naaim and N.Eckert
Cemagref, BP 76, 38402 St Martin d'Herès, France. e-mail: johan.gaume@cemagref.fr

for different return periods. Slab avalanches result from the collapse of a thin weak layer underlying a cohesive slab. Recently, some cellular automaton models have been developed providing important insight into the mechanisms of avalanche release [Failletaz2004, Fyffe2004, Fyffe2006]. In particular, they pointed the two basic ingredients that are essential for the mechanical description of avalanche release, namely the heterogeneity of the weak-layer and the stress redistribution effect conveyed by the elasticity of the overlaying slab. However, the treatment of the mechanical behavior of the different layers is very simplified in these models. In addition these models are unable to include a detailed description of topography and geomorphology of release zones. The objective of this study is to develop a complete mechanical model of the {weak layer-slab} system. In this paper, we focus in particular on the role of the weak layer heterogeneity on the avalanche release mode.

2 Formulation of the model

We use the Finite Element code Cast3m to build a complete mechanical model for slab avalanche release including inertial effects. The code solves the mass and momentum balance equations under the small-strain assumption. The used procedure enables to perform non-linear incremental computations with an implicit integration scheme.

2.1 Geometry, boundary conditions and loading

We study a simple 2D uniform slope geometry (figure 1). The system is composed of a weak layer modeled as an interface and an upperlying slab. The gravity is the only external force and we load the system by increasing the slope angle θ . The length of the slope is $L = 30m$ and we perform simulations for different slab depths. The weak layer's base is fixed to the ground. The boundary condition at the base of the slope (BC_2) consists in imposing a nil displacement in the x direction. At the crown of the slope (BC_1) we apply a shear stress varying with the depth in order to avoid bending due to limit size effects.

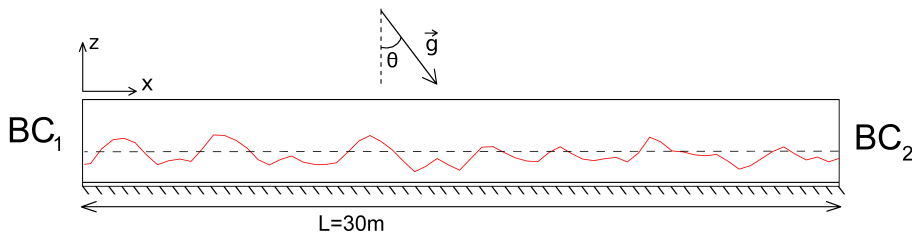


Fig. 1 Geometry of the system. The red curve represents a realization of the heterogeneity (friction angle) of the weak layer.

2.2 Mechanical behavior of snow: constitutive laws

Snow is a very complex material whose mechanical behaviour remains largely unknown. Nevertheless, it has been shown that under certain conditions [McClung1979] snow behaves as an elasto-plastic material. Thus, we model the weak layer as an elasto-plastic interface with shear softening [McClung1979, Fyffe2004, Fyffe2006, Kronholm2005]. This shear softening is justified by the breaking of ice bonds at the micro-scale. In a first step, we have considered a Mohr-Coulomb rupture criterion without cohesion. Once rupture is reached, shear softening occurs over a characteristic tangential displacement $u_c = 2mm$ [McClung1979] after which the shear stress reaches a residual value equal to the half of the peak shear stress.

The slab layer is modeled using a Drucker-Prager constitutive law with a softening post-peak behavior and a very low residual stress in order to represent the opening of the traction crack. The value of the mechanical parameters were chosen according to [Schweizer1999]. We have taken a slab density of $\rho = 250kg/m^3$, a Poisson's ratio $\nu = 0.3$, a Young's modulus $E = 10^6Pa$ and a traction and compression elastic limit $\sigma_t = 1kPa$, $\sigma_c = 10kPa$. Hence, the parameters of the plastic flow law are not important since the plastic limit only account for a slab rupture criterion.

2.3 Spatial heterogeneity of the weak layer

The spatial variability of the weak layer mechanical properties are modeled through an heterogeneous stochastic friction angle ϕ . Several field studies [Jamieson2001, Schweizer2008, Kronholm2005] show that the spatial variability of mechanical properties of snow can be approximated by a Gaussian distribution. Thus, in agreement with the literature, ϕ is modeled as a Gaussian stochastic field with spatial correlations. The associated covariance matrix is expressed as follow: $C_{ij} = s^2 \exp(-0.5(d_{ij}/\varepsilon)^2)$, where s is the standard deviation, d_{ij} is the distance between P_i and P_j and ε is the correlation length. Note that no nugget effect is considered. According to [Conway1984], the typical correlation length of strength variation should be between 0.2m and 1.3m. In this study, we took $\varepsilon = 1m$. According to [Schweizer2008], we have taken a coefficient of variation $CV = \tan s / \tan \langle \phi \rangle = 15\%$ and the mean friction angle $\langle \phi \rangle = 30^\circ$. One realization of this heterogeneity is represented on figure 1.

3 First results and discussion

For different slab depths ($h \in \{0.3m, 0.6m, 0.9m, 1.2m, 1.5m, 2.1m\}$) we performed 100 simulations with different realizations of the heterogeneity. This gives us some distributions of release angle. For each slab depths, we then studied these distributions and the release type. Knowing the evolution of the mean and the standard

deviation of release angle distributions in function of the slab depth, we will be able to determine the distributions of release depths for different slope angles.

3.1 Release types and criteria

By looking at the plastic deformation in the slab for each simulation, we can distinguish two kinds of releases: Full slope releases (the entire slope is released without traction rupture) and partial slope releases (only a part of the slope is released with a traction rupture). Both of them are induced by a shear rupture in the weak layer. Indeed, the slab rupture is a secondary process and always results from an instability inside the weak layer ($u > u_c$). Partial releases are generally associated to an important local heterogeneity (difference of shear strength between adjacent elements) around the weakest zone. In the case of a global release, the shear rupture propagates in the whole weak layer since the local heterogeneity is not sufficient to make the slab rupture ($\varepsilon_{pl}^{slab} = 0$). According to these rupture modes, we defined two release criteria. The first one is based on the plastic deformation of the slab and is only relevant for partial releases. The second one is based on the displacement of the base of the slab and can be used for both full and partial releases.

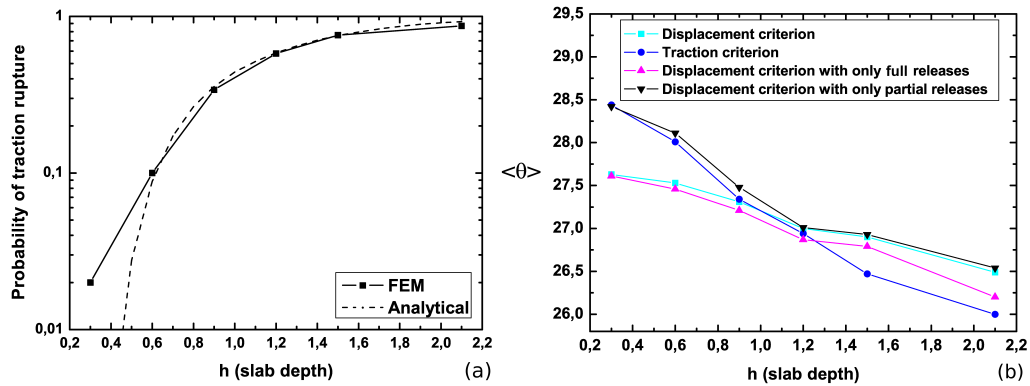


Fig. 2 Probability of traction rupture (a) and mean release angle (b) as a function of the slab depth.

Figure 2a shows the evolution of the probability of traction rupture with the slab depth h calculated from the finite element method. The traction rupture probability is very low for $h < 0.5m$ and then increases almost linearly until $h \approx 1.2m$ where it starts to level off to 1 more slowly. This means that for very thick slabs ($h > 1.2m$), we will have a significant proportion of partial slope releases. On the contrary, full slope releases will be more frequent for thin slabs ($h < 0.5m$). This evolution can be interpreted with a simple small model. We considered the occurrence of traction rupture is directly related to the shear-stress difference $\Delta\tau = |\tau_2 - \tau_1|$ between two neighboring elements 1 and 2 and occurs when $\Delta\tau$ is greater than the slab traction rupture limit σ_T (neglecting spatial correlations). We calculated this probability $P(\Delta\tau > \sigma_T)$ by computing many independent realizations of ϕ_1 and ϕ_2 . The results of this model

are represented on figure 2a (dotted line) and show very good agreement with the results from the finite element method.

3.4 Release angle distributions

Figure 3 shows the distributions of release angles obtained using the traction and the displacement criterion. We first note that for both rupture criteria, the distributions are normally distributed with a variance independent of h . This particular shape is presumably a direct consequence of the Gaussian heterogeneity.

Figure 2b reports the average of these distribution and we also separate full and partial slope releases from the displacement criterion. We can firstly note that the slab depth does not strongly influence the slope stability since the release angle variations remain low. This is due to the frictional rupture criterion used for the weak-layer. This criterion also explains why we observe that the slab traction rupture is more sensitive to the slab depth h . Moreover, the mean release angle is always lower than the mean friction angle $\langle \phi \rangle$ since the rupture occurs around weakest spots. Finally, the rupture type (full slope or partial slope) has a greater influence on the release angle for thin slabs ($h < 1.2m$) than for thick ones ($h > 1.2m$).

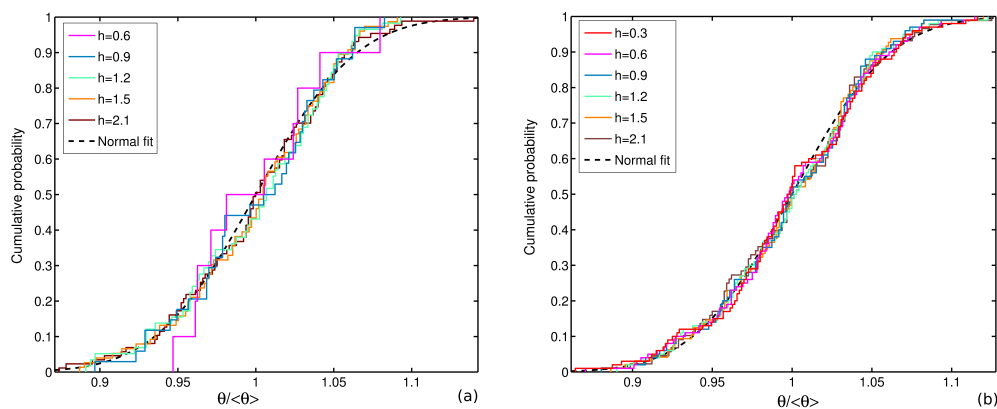


Fig. 3 Distributions of release angle: traction criterion (only partial releases) (a) and displacement criterion (all releases) (b).

4 Conclusions and perspectives

Slab snow avalanches are triggered by the rupture of a weak layer underlying an elasto-plastic slab. In this paper, we study the influence of the heterogeneity of the weak layer mechanical properties on avalanche release using a finite element method. We have shown that the slab rupture always results from an instability inside the weak layer. We have seen that the slab depth has an important influence on

the release type but almost no influence on the release angle. Finally, the distributions of release angles have the same shape as the distribution of the heterogeneity (Gaussian). As perspectives, we will first repeat this study in the cohesive case. Indeed, the slab depth has a little influence on the release angle because of the frictional rupture criterion. Then we will analyse the influence of the correlation length ε on the release type.

References

- [Conway1984] Conway, H. and Abrahamson, J.: Snow slope stability - A probabilistic approach. *Journal of Glaciology* (1984).
- [Failletaz2004] Failletaz, Louchet, F. and Grasso, J-R.: Two-Threshold Model for Scaling Laws of Noninteracting Snow Avalanches. *Physical Review Letters* (2004)
- [Fyffe2004] Fyffe, B. and Zaiser, M.: The effects of snow variability on slab avalanche release. *Cold Region Science and Technology* (2004).
- [Fyffe2006] Fyffe, B. and Zaiser, M.: Interplay of basal shear fracture and slab rupture in slab avalanche release. *Cold Region Science and Technology* (2006).
- [Jamieson2001] Jamieson, J.B. and Johnston, C.D.: Evaluation of the shear frame test for weak snowpack layers. *Annals of Glaciology* (2001).
- [Kronholm2005] Kronholm, K. and Birkeland, K.: Integrating spatial patterns into a snow avalanche cellular automata model. *Geophys. Res. Lett* (2005).
- [McClung1979] McClung, D.: Shear fracture precipitated by strain softening as a mechanism of dry slab avalanches. *Journal of Geophysical Research* (1979).
- [Naaim2003] Naaim, M., Faug, T. and Naaim-Bouvet, F.: Dry granular flow modelling including erosion and deposition. *Surveys in Geophysics* (2003).
- [Naaim2004] Naaim, M., Gurer, I.: Two-phase Numerical Model of Powder Avalanche Theory an Application. *Natural Hazards* (2004).
- [Schweizer1999] Schweizer, J.: Review of dry snow slab avalanche release. *Cold Region Science and Technology* (1999).
- [Schweizer2008] Schweizer, J., Kronholm, K., Jamieson, B. and Birkeland, K.: Review of spatial variability of snowpack properties and its importance for avalanche formation. *Cold Region Science and Technology* (2008).

Appendix B

Application of the max-stable model for the retro-analysis of the December 2008 avalanche cycle in the Eastern part of the French Alps

This appendix is composed of an article entitled “Cross-comparison of meteorological and avalanche data for characterising avalanche cycles: The example of December 2008 in the eastern part of the French Alps”. It was **published** in *Cold Region Science and Technology* in 2010 by Nicolas Eckert as first author.

My contribution to this article was the computation of the return period of the December 2008 snowfall event using the outputs of the max-stable model presented in Chapter 5 (paragraph 2.6 and Fig. 13 of this appendix article mainly). In detail, once the three parameters of the GEV distribution were obtained as continuous functions of space using max-stable processes, and after altitude correction of the cycle data, the exceedance probabilities were evaluated, not only at the locations on which the max-stable model calibration was performed, but also at all locations for which precipitation measurements were made during the cycle. Finally, these exceedance probabilities were interpolated by kriging (exponential covariance model) and inverted to obtain the return period of the 3-day snowfall cycle over the region being studied.

In the rest of the paper, the retro-analysis of this event is also performed using different techniques which are cross-compared. It is shown that the 3-day snowfall return period calculated using the max-stable approach globally corresponds to the one computed using Safran outputs at the massif scale. The relatively good agreement between the two approaches is very encouraging and emphasizes the ability of our model to achieve retro-expertise of past extreme snowfall events.



Contents lists available at ScienceDirect

Cold Regions Science and Technology

journal homepage: www.elsevier.com/locate/coldregions

Cross-comparison of meteorological and avalanche data for characterising avalanche cycles: The example of December 2008 in the eastern part of the French Alps

N. Eckert^{a,*}, C. Coleou^b, H. Castebrunet^{a,b}, M. Deschatres^a, G. Giraud^b, J. Gaume^a

^a UR ETNA, Cemagref Grenoble, BP 76, 38 402 Saint Martin d'Hères, France

^b Centre d'Etudes de la Neige, 1441 rue de la Piscine, 38400 Saint Martin d'Hères, France

ARTICLE INFO

Article history:

Received 4 November 2009

Accepted 19 August 2010

Keywords:

Avalanche cycle

Case study

French Alps

Spatio-temporal scale

Spatial structure

Return period

ABSTRACT

In December 2008, an intense avalanche cycle occurred in the eastern part of the southern French Alps. Southerly atmospheric fluxes that progressively evolved into an easterly return caused important snowfalls with return periods up to 10 years. Cold temperatures and drifting snow had important aggravating effects. The return period for the number of avalanches was above 50 years in two massifs and some of the avalanche had very long runouts that exceeded historical limits recorded in the French avalanche atlas. Using this case study, this paper illustrates and discusses how avalanche reports, snow and weather data and results from numerical modelling of the snow cover can be combined to analyse abnormal temporal clusters of snow avalanches. For instance, it is shown how statistical techniques developed in other fields can be used to test the significance of different explanatory factors, extract spatio-temporal patterns, compare them with previous cycles and quantify the magnitude/frequency relationship at different scales.

© 2010 Elsevier B.V. All rights reserved.

1. Introduction

The concept of avalanche cycle is often used to highlight an abnormal temporal cluster of avalanche events at a given spatial scale: the mountain range, the district, etc. An avalanche cycle is generally caused by a severe storm bringing high snowfalls accompanied by substantial drifting snow, but strong temperature variations causing snowmelt and/or fluctuations of the freezing level can also be involved. Studying avalanche cycles therefore mainly aims at understanding their relations with climatic factors, such as precipitation, temperature, wind effects (e.g. Birkeland et al., 2001; Höller, 2009). Operationally, these studies are valuable to improve avalanche forecasting models (e.g. Gassner and Brabec, 2002), so as to close ski resorts and evacuate the threatened mountain communities when a critical level is reached. Land use planning policies and hazard zoning can also benefit, since major avalanches generally occur during the most extreme cycles. For example, the Montroc avalanche, which killed 12 people in their homes, occurred during the February 1999 avalanche cycle (Ancey et al., 2000) that caused widespread damage in a large part of the European Alps (SLF Davos, 2000).

While it is relatively straightforward to precisely evaluate the magnitude/frequency relationship on given paths (e.g. Meunier and Ancey, 2004; Eckert et al., 2008a), quantifying the magnitude of an avalanche cycle that affects a mountain range over several days is more difficult. First, an appropriate quantitative definition of an avalanche

cycle must be given. The existing definitions are sometimes based on the number of recorded events, but more generally on cumulative indexes taking into account one or several magnitude variables such as total mass of avalanche debris (Birkeland and Mock, 2001; Laternser and Schneebeli, 2002). This has the advantage of lowering the bias induced by the non-observation of small avalanche events, but generally involves estimating the mass from the size classes of the avalanches. A second consideration is that the spatial and temporal scales that provide the best description of the phenomenon have to be found to make historical comparisons. This is particularly tricky because of the strong spatio-temporal variability of avalanche activity during cycles. Moreover, statistical techniques such as magnitude–duration–frequency curves that are currently used in the hydrological community (e.g. Lang et al., 1999; Katz et al., 2002) remain poorly developed in the avalanche field, except for snowfall analysis (e.g. Parent and Bernier, 2003; Bocchiola et al., 2006). The third major difficulty lies in the limitations of data quality, quantity and homogeneity. Indeed, avalanche cycles are characterised by harsh winter conditions making it very difficult and sometimes dangerous to collect enough snow, weather and avalanche data to properly evaluate the strong altitudinal and orographic gradients that may exist. Homogeneity problems can also arise while trying to compare spatially averaged data to point measurements, as well as local measurements to weather data used by a snow cover model.

The goal of this paper is to exemplify and discuss how different information sources can be compared and combined to extract and better understand the spatio-temporal patterns characterising an avalanche cycle. For instance, spatial indexes and spatial regression tools are used to quantify aggregation and gradients during the cycle.

* Corresponding author.

E-mail addresses: nicolas.eckert@cemagref.fr (N. Eckert), cecile.coleou@meteo.fr (C. Coleou).

Additionally, it is shown how the return period concept can be used not only for snowfalls, but also for avalanche counts, so as to fully characterise the cycle at different spatial scales. We focus on data available in France for this study, i.e. snow and weather data collected by Météo-France, avalanche records, and results from snow cover modelling including instability indexes. Most of the analyses are performed at the spatial scale of the massif (Fig. 1), which is used for data assimilation, snow cover modelling and avalanche forecasting in an operational context (see Section 2.1). However, the method can easily be adapted to other countries where data collection protocols and/or modelling approaches are different.

As an illustrative case study, we analyse the recent remarkable avalanche cycle that occurred in December 2008 in the French Alps. Two massifs of the southern French Alps were strongly affected: Queyras and Mercantour, where important roads were closed over several consecutive days. Villages such as Ristolas (Queyras massif) and ski resorts such as Isola 2000 (Mercantour massif) were thus isolated. A few buildings were partially destroyed, for instance in Saint Etienne de Tinée (Mercantour massif), and ski lifts as well as forests were damaged. There were no human casualties, even though several people were buried by an avalanche that occurred on December 16th 2008 in Ristolas (Fig. 2). This cycle was remarkable because of its precocity in the season, especially in the most northerly areas affected. It was generated by large southeasterly fluxes, so that it also affected the western Piedmont Alps (Maggioni et al., 2009), and, to a lesser extent, most of the French massifs situated close to the French–Italian border.

The paper is organised as follows: Section 2 presents the different data used in terms of quantity and limitations, as well as the statistical methodology employed. Section 3 details the events of the cycle and relates them to the prevailing constraining factors. Section 4 offers an extensive historical comparison of the cycle with previous situations.

Section 5 discusses the main results obtained for the analysed cycle, the generic outcomes for the analysis of avalanche cycles, and perspectives for further developments.

2. Data and methods

2.1. Snow and weather data

The snow and weather data came from the different observation networks of Météo-France including surveys and observations of synoptic stations, radiosondes and pilot balloon networks, climatological stations and automatic weather stations. All these data have been quality controlled and, in some cases, local expertise was used to estimate missing data. The automatic weather stations in the French Alps (Nivôse network) are situated at different elevations and provide hourly temperature, wind speed and snow depth data. A human network, mainly ski patrollers, provided more detailed weather and snowpack information: weather and snow surface conditions twice a day, and weekly detailed profiles of the snowpack. The main limitation for this study was that around half sites, mainly ski resorts, were still closed when the December 2008 cycle occurred. Among all the data collected during the cycle, only precipitation data were used directly. However, all the available snow and weather data were used indirectly as inputs to Météo-France's SCM model chain (Durand et al., 1999), presented below, to provide modelled snow cover results.

2.2. Snow cover modelling

The SCM model chain is a system of three numerical models: Safran, Crocus and Mepra. It simulates the evolution of the snow cover and its stability at a massif scale. The different French massifs are

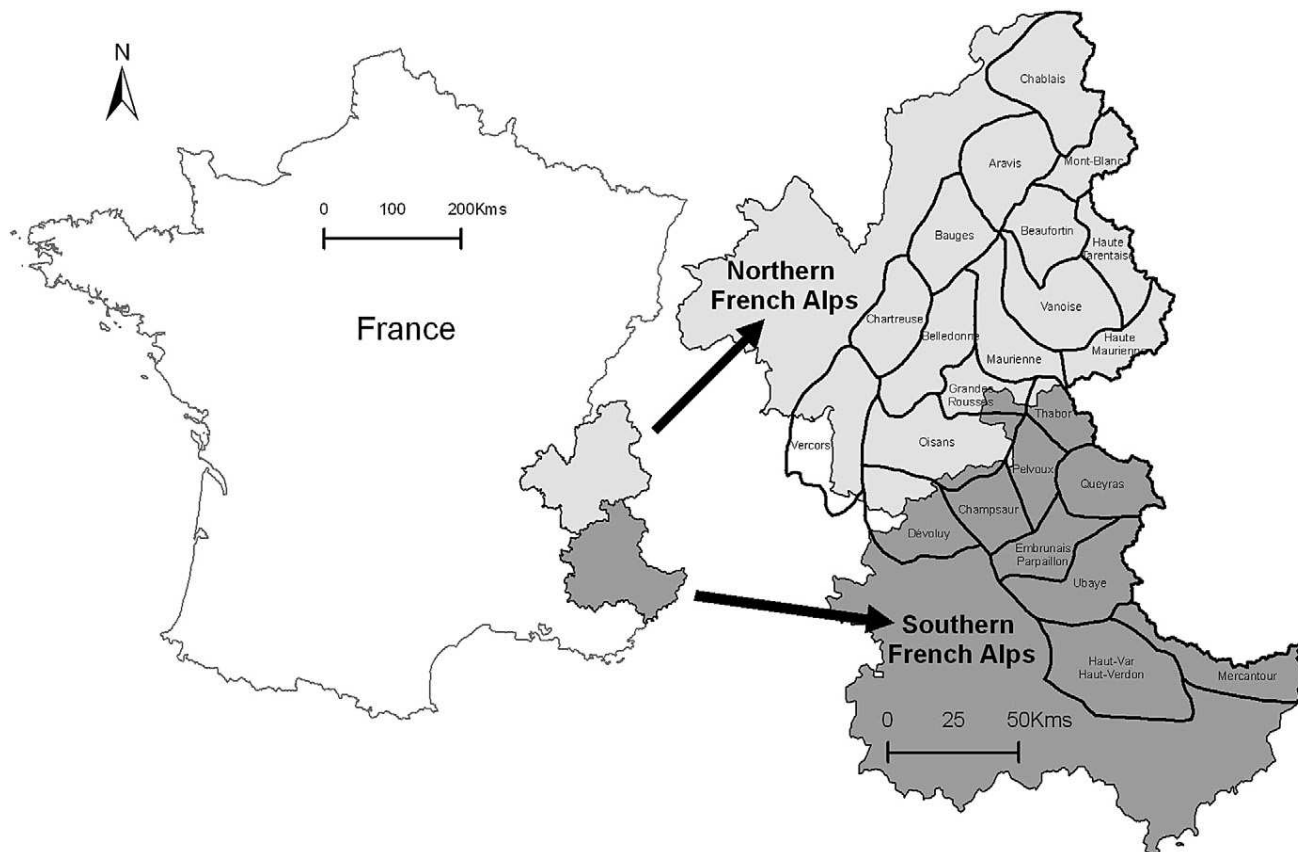


Fig. 1. Studied area and massifs. The French Alps can be roughly divided into Northern (Rhône–Alpes) and Southern (Provence–Alpes–Côte-d’Azur) sections. The massifs are much smaller spatial units that are used for operational avalanche forecasting.



Fig. 2. Avalanche in Ristolas, December 16th 2008. La Combette avalanche path, Queyras massif, France. Avalanche flow path and runout area are marked with a red outline. Two houses were hit and damaged (upper panels). Several people were buried outside the houses, but were rescued. Pictures M. Deschatres/Cemagref.

shown in Fig. 1. The surface area of each massif is about 500 km² and the key assumption is their spatial homogeneity, especially for precipitation. However, for each massif, six aspects, two slopes (20 and 40°), and different elevations with 300-m steps are considered. Safran computes meteorological variables (temperature, precipitation, radiation, wind speed..., etc.) for the different elevations, slopes and aspects. Then Crocus calculates the corresponding changes in the snowpack. Finally, Mepra performs a diagnosis of the snowpack stability for each simulated snow profile.

To compare real avalanche activity (daily number of avalanche events) and Mepra's diagnoses, a "modelled daily spontaneous avalanche activity" index can be used (Martin et al., 2001). It represents the daily maximum of the weighted mean by aspect and altitude in each massif of these indexes. This daily index, denoted "Instability Index" (*II*) in the rest of the paper, is a useful result from the SCM model chain in operational avalanche forecasting. It varies from 0 to 8 in each massif, with a local distribution that is somewhat dependent on the massif's characteristics, e.g. systematically higher values in higher massifs in relation with higher amounts of snow at high elevations. Note that, rather than the raw indexes that have been computed for avalanche forecasting, we use indexes that were recomputed, which allow us to include additional snow and weather data that were not available in real time. Furthermore, since a detailed temporal analysis is not undertaken, we focus mainly on the mean and maximal index over the full cycle, noted mean(*II*) and max(*II*), respectively.

Finally, as shown by Durand et al. (2009a,b), the SCM chain can also be used for retrospective snow and weather climate analyses, using as input different initial meteorological fields (air temperature, humidity, wind speed....) or numerical guess fields provided by atmospheric General Circulation Models (GCM). From mid-1957 to 2001, the retrospective analyses from ERA-40 (ECMWF, 2004) were used as input, whereas Météo-France's numerical weather prediction model ARPEGE (Courtier et al., 1991) provided guess fields since 2001, every 6 h. In this study, the results of this work were used to compare the snow and weather characteristics and instability indexes at the massif scale to previous occurrences over the last few decades.

2.3. Avalanche data from the EPA database

The *Enquete Permanente sur les Avalanches* (EPA) is a report describing the avalanche events on approximately 3800 determined paths in the French Alps and Pyrenees. Avalanche occurrences have been recorded since the beginning of the 20th century (Mougin, 1922), along with quantitative (runout altitudes, deposit volumes, etc.) and qualitative (flow regime, release cause, etc.) data (Jamard et al., 2002). The field observations are collected by forest rangers and stored by the Cemagref research institute. The data collection protocol and observation network has seen several changes since the beginning of the report, including a major update in 2002, which considerably increased the reliability of the information (Bélangier and Cassayre, 2004).

The EPA report was originally devoted to the evaluation of forest damage. Nevertheless, two aspects of its observation protocol make it highly valuable for various other applications. First, the data series, even if some of them are incomplete, are unusually long. They are now routinely used for local predetermination using physical modelling (e.g. Naaim et al., 2004), combined statistical–dynamical approaches (e.g. Ancey et al., 2004; Eckert et al., 2007a) and risk analyses (Eckert et al., 2008b; 2009). Second, the EPA database's objective is to be as exhaustive as possible on a sample of paths situated in all the Alpine massifs rather than recording only certain avalanches on all the French paths. Even if the path selection was originally not based on scientific arguments, it gives a relatively accurate view of the spatio-temporal fluctuations of avalanche activity over the last century. Eckert et al. (2007b) have highlighted coherent spatial patterns in the northern French Alps. Jomelli et al. (2007) found relations between the local probability of avalanching and weather data. Finally, Eckert et al. (2010a) have highlighted large-scale temporal fluctuations possibly related to climate change.

Since the quality of records depends to a large extent on rangers' careful data recording, the EPA suffers, like all avalanche databases, from uncertainty and error sources. Some local avalanche series are poor, with numerous missing events. For intense avalanche cycles, irregularities at large spatial scales are present. Certain events were missed when rangers were busy with other things. Moreover, other events were recorded significantly later than their actual time of occurrence because of the inability to safely reach remote areas during the cycle. In that case, standard observation protocol, since 2002, is to record a time window of two dates to help define the event's true date. These two points are critical while using the EPA data for relating avalanche activity to snow and weather conditions. Indeed, the real magnitude and extension of a cycle may be somewhat underestimated if many events have been missed. Moreover, the relationship with snow cover and meteorology may be hard to establish when the true date of many events remains uncertain.

In this study, to compare avalanche activity from one massif to another, we use the number f_i of events per path (or relative activity) defined as:

$$f_i = \frac{n_i}{c_i} \quad (1)$$

where n_i is the number of avalanche and c_i the number of paths under survey in each massif $i, i \in [1, N]$, known at least since the 2002 protocol update.

The length of the report is used to evaluate, at the massif scale, empirical return periods and magnitude–frequency–duration curves for the number of events per cycle. This allows comparison between the studied cycle and previous ones, and between return periods for precipitation and avalanche activity. For these historical comparisons, the number of events n_i is used rather than the number of events per path f_i because of the uncertainty related to c_i before 2002. Note also that we do not discriminate avalanche events by trigger, mainly because the vast majority of the recorded events are naturally released, which makes sub-sampling unnecessary (see Section 3.1). Furthermore, for many old events, the release cause was not recorded and so the more recent human-triggered avalanches were included in the database to retain consistency.

When there is uncertainty related to the date of the event, we use the later date of the time window proposed by the ranger. This likely biases the results towards extending the cycle beyond its actual end, but at least the onset of the avalanche cycles is captured accurately. Using a weighted mean of the two recorded dates was rejected for two reasons: first, the time window of the two dates is available in the EPA report since the 2002 protocol update only. Second, the events of the cycle studied for which the date range is larger than the duration of the cycle are only 13%, and they are for the most part limited to one massif (see Section 3.1).

Other variables from the EPA report were also considered: the amount of new snow during the 3 days preceding the events in the release zone, the flow regime of the events, the deposit volume, which is estimated from the registered three dimensions of the deposits (mean length, width and depth), and the runout altitude, i.e. the elevation of further reach. For the latter one, we use the Runout Altitude Index (RAI) defined as:

$$RAI_{kj} = \frac{1}{e} \exp \left(1 - \frac{z_{stop_{kj}} - z_{min_j}}{z_{min_j}} \right) \quad (2)$$

where $z_{stop_{kj}}$ denotes the runout altitude corresponding to the avalanches $k \in [1, n(j)]$ recorded in the avalanche path j , $n(j)$ the total number of avalanches recorded in the path j , z_{min_j} the minimal runout altitude possible in the path j (often the valley floor), and RAI_{kj} the corresponding index value. By definition, the RAI equals 1 if z_{min_j} is reached. Otherwise, the RAI is a continuous and decreasing function of the runout altitude belonging to $]0, 1[$.

The RAI is far from perfect. For instance, it gives more weight to paths where the runout altitudes reached are far above the reference value z_{min} . To limit this bias, minimal altitudes z_{min_j} as realistic as possible have been chosen (see Section 4.4). On the contrary, the RAI has the advantage of using no other extra data information. Furthermore, being scaled, it allows the comparison of runouts between avalanche paths of different sizes, aspects, altitudes..., etc. From this point of view, it is relatively similar to the runout index computed using abscissas and used in avalanche engineering to evaluate high-return-period avalanches (McClung and Lied, 1987). Further detailed discussions regarding its advantage and intrinsic limits can be found in Eckert et al. (2010b), where it is used to investigate temporal changes of the runout regime under climate fluctuations.

For the 3 day snowfall, flow regime, deposit volume and RAI data, rather than the full available EPA data, we chose the five winters 2001/2002 to 2005/2006 as a comparison sample for the December 2008 cycle because of the significant improvement in terms of reliability since 2002. Since these variables are generally estimated using binoculars, from a distant and safe observation point, they remain highly uncertain, even after 2002. However, they may still be used to make relative statements about the character of avalanche cycles, e.g. to show that the proportion of powder snow avalanches was higher during an intense cycle than the mean (see Section 3.2).

2.4. Spatial patterns, Moran's index and spatial regression

To characterise spatial patterns of avalanche events, precipitation and instability indexes at the massif scale, the Moran index I (e.g. Cressie, 1993) has been used. It is a measure of spatial autocorrelation and characterizes proximity in two-dimensional space:

$$I_k = \frac{N \times \sum_{i=1}^N \sum_{j=1}^N (\omega_{ij}^{(k)} (y_i - \bar{y})(y_j - \bar{y}))}{\sum_{i=1}^N \sum_{j=1}^N (\omega_{ij}^{(k)}) \times \sum_{i=1}^N (y_i - \bar{y})^2} \quad (3)$$

where N is the number of massifs, y is the variable of interest, \bar{y} is the mean of y and ω_{ij} is a matrix of spatial weights (inverse distances). The notation I_k and $\omega_{ij}^{(k)}$ denotes that the index can be computed for different distance classes (lags), so as to produce a spatial autocorrelogram to investigate how spatial autocorrelation varies with distance.

The expected value of Moran's I under the null hypothesis of no spatial autocorrelation is $E(I_k) = \frac{-1}{N-1}$, which depends on the number of massifs considered. Values lower than the expected value indicate a negative spatial autocorrelation, i.e. anti-clustering. Conversely, values

higher than the expected value indicate the presence of clusters in the observed spatial patterns. Significance of the observed aggregation/repulsion patterns can be tested against the null hypothesis of random spatial sampling. Computations were made using a very simple weight matrix based on a minimal number of nearest neighbours at a given lag (Fig. 5, left).

To explain the patterns observed at the massif scale, different explicit regressions were performed using the generic linear model:

$$y_i = \beta_0 + \sum_{k=1}^P x_{ik}\beta_k + \varepsilon_i \quad (4)$$

where y_i is the explained variable (for example the number of events n_i), x_{ik} the matrix of the P covariates considered, and (β_0, β_k) the $P+1$ regression parameters to be estimated. The ε_i are the local residuals which are assumed to be independent and Gaussian. Spatial gradients were obtained while fitting the model with $x = \{lat, long\}$, where $lat, long$ denotes the latitude and longitude of the centre of each massif respectively, following the Lambert II convention. The explanatory power of the different models was evaluated by computing the (multiple) R^2 statistics, and the marginal significance of each parameter β using t -tests. The presence of a remaining spatial structure in the residuals was investigated by computing, after suitable correction (Cliff and Ord, 1981), Moran's I and testing its significance for the residuals.

2.5. Return period and cycle threshold

The return period, T , is the inverse of the annual exceedance probability p :

$$T = \frac{1}{p}. \quad (5)$$

Evaluating the return period of the snowfall is the most usual way to obtain a return period for an avalanche (e.g. Salm et al., 1990). Two complementary approaches were considered here. First, the return period of the Safran modelled snowfall at the massif scale was obtained by comparison with the back-calculated data of Durand et al. (2009a,b). Computations were made for daily maxima and cumulated snowfalls over 2 to 5 days. Since Safran data were available at different elevations, 1800 masl was chosen to be sure to consider only snow. Second, the continuous precipitation field corresponding to the cycle was analysed using a spatial extreme approach (see Section 2.6).

We also evaluated return periods for the number of avalanche events for durations ranging from 1 to 7 days. The cumulated numbers of events corresponding to each duration were evaluated by considering moving windows centred on the daily maxima. For paired windows, the moving window was centred on the first of the 2 days considered, e.g. day 2 for a 4-day moving window. Since the true number of events occurring is systematically slightly underestimated during cycles, the assumption of a similar underestimation in the past must be made to consider the frequential characterisation as correct. This is unverifiable, but is for us not unrealistic over the last few decades.

A cycle threshold of $T=2$ years for the number of recorded events was used to discriminate the mountain massifs affected by the avalanche cycle. It means that an avalanche cycle can be considered significant if it does not occur more often than once every 2 years on average. The simple definition has the advantage of offering a relative threshold for inclusion as an avalanche cycle. It is independent from the chosen spatial scale and can be applied to different types of data, to allow comparisons between regions and variables. With this definition, a few events may be considered as a significant avalanche cycle in an area where avalanche activity is usually low; conversely, a particularly high number of avalanches are required in an area that normally sees high avalanche activity. This is advantageous for operational purposes,

because in areas where high avalanche activity is usual, operational services are generally well prepared, whereas a few events can cause considerable problems in areas where avalanche activity is usually low.

Evaluating return periods involves evaluating the exceedance probability p in Eq. (5). This can be done empirically, by sorting the data, or with recourse to a parametrical statistical model. In the latter case, Extreme Value Theory (EVT, Coles, 2001) is generally used. As EPA data are discrete, the theoretical justification is not valid and EVT cannot be used rigorously. Thus, an empirical estimation has been employed. The same estimation has been employed for the Safran snowfalls at the massif scale to provide a preliminary evaluation of the return period at the massif scale, for different durations, with a low computational cost.

2.6. Spatial extreme analysis of precipitations

The continuous precipitation field was analysed at the most appropriate duration (3-day) using a fully rigorous but much more computationally intensive spatial extreme approach which can be seen as a mixture of EVT and geostatistics, i.e. how spatial dependence between distribution tails can be captured and modelled. The proposed analysis is based on the work of Schlather (2002), who explored how the concept of max-stability on which EVT is based can be applied to continuous fields. In our work, we used the extremal dependence formulation proposed by Smith (1990). Furthermore, following the ideas of Padoan et al. (2010), we modelled the available long winter (mid-November to end of April) precipitation series $y_{lat, long}$ as Generalized Extreme Value (GEV) distributions whose location $\mu_{lat, long}$ and scale $\sigma_{lat, long}$ parameters are explicit functions of space coordinates ($lat, long$). The shape parameter ξ was modelled as constant for the entire zone studied because there was not enough information in the calibration data set to infer a possible variation with space. The cumulative distribution $P(Y_{lat, long} \leq y_{lat, long})$ of the annual maximum $Y_{lat, long}$ is then:

$$P(Y_{lat, long} \leq y_{lat, long}) = \exp\left(-\left[1 + \xi \frac{(y_{lat, long} - \mu_{lat, long})}{\sigma_{lat, long}}\right]^{-\frac{1}{\xi}}\right) \text{ if } \xi \neq 0 \text{ and,} \quad (6.1)$$

$$P(Y_{lat, long} \leq y_{lat, long}) = \exp\left(-\exp\left(\frac{-(y_{lat, long} - \mu_{lat, long})}{\sigma_{lat, long}}\right)\right) \text{ if } \xi = 0. \quad (6.2)$$

Differences in altitude between the local series were taken into account by making all computations at a constant elevation of 2000 masl using the gradients inferred by Durand et al. (2009a) from the Safran reanalyses. Only snowfalls were considered by retaining only the past episodes for which temperature at 2000 m was under 0 °C. After several trials, simple linear models $\mu_{lat, long} = \mu_0 + \mu_1 lat + \mu_2 long$ and $\sigma_{lat, long} = \sigma_0 + \sigma_1 lat + \sigma_2 long$ were retained on the basis of a model selection criterion derived from the Akaike Information Criterion (Akaike, 1981).

Once the three parameters of the GEV distribution were obtained ($\mu_{lat, long}$ and $\sigma_{lat, long}$ as continuous functions of space, and ξ as its best regional estimate), and after altitude correction of the cycle data, the exceedance probabilities $p_{lat, long} = 1 - P(Y_{lat, long} \leq y_{lat, long})$ were evaluated, not only at the locations with long series on which model calibration was performed, but also at all locations for which precipitation measurements were made during the cycle. Finally, these exceedance probabilities were interpolated by kriging (exponential covariance model) and inverted using Eq. (5) to obtain the return period of the 3-day snowfall cycle over the region being studied.

3. The December 2008 avalanche cycle

3.1. Recorded avalanche events

The EPA report was used for evaluating the duration of the cycle. In the full database, the avalanche events were highly concentrated around mid-December. The highest activity was recorded on 16 December, with a total number of 54 events, but activity was already very significant on 15 December with 46 events, and remained intense on 17, 18 and even 19 December, with 46, 38 and 25 events, respectively (Fig. 3, top left). Initially, it can therefore be considered that the avalanche cycle lasted 5 days, with a total of 209 avalanches and a mean activity of 0.05 events per path recorded during the cycle. This is very high, since 209 avalanches correspond to about 20% of the usual winter occurrences in the EPA report. Consequently, the cycle threshold is exceeded for this 5-day period for the full EPA database, which means that 209 events were recorded in the EPA report for 5 consecutive days less often than every 2 years on average. The 209 cycle events were recorded on 207 paths. This indicates that only two paths were affected by 2 events during the cycle. More than 80% were recorded as naturally released with certainty. 10 events resulted from control measures (artificial release from helicopter). The remainder have unknown triggers. As already mentioned in Section 2.3, we chose not to consider only events that were naturally released with certainty, which would have made historical comparisons more difficult.

Fig. 3 (top right) shows that the size of the time window provided by the rangers is generally shorter than 5 days. This suggests that it is appropriate to treat the cycle as a block to investigate spatio-temporal patterns. For the Queyras massif, the date of all the events (except one) was recorded with an uncertainty lower than 2 days (Fig. 3, middle right), suggesting that the avalanche cycle was concentrated on 15–17

December in this massif (Fig. 3, middle left). In the Mercantour massif, the data were partially collected after the storm because of bad weather conditions, so that the release date is highly uncertain (6–7 days) for about one-third of the events recorded (Fig. 3, bottom right). Consequently, few events were recorded on 15–17 December with certainty, and none at all on 16 December (Fig. 3, bottom left). On the other hand, EPA reports 4 definite events released on 18 December in this massif, and 9 others that were given a range between December 15th and December 18th. This allows us to postulate that the true time scale of the avalanche cycle might be closer to 4 days in this massif.

During the cycle, avalanche activity was spatially very heterogeneous (Fig. 4). The Queyras and Mercantour massifs, which are both relatively high (highest summits above 3000 m), and situated near the Italian border, were by far the most affected. In the Queyras massif, 42 events were recorded between 15 and 19 December, with an activity of 0.21 events per path. This indicates that, in this massif, one EPA path out of five was affected by an event during the cycle. The Mercantour massif, which is the most southeasterly one of the French Alps, was also strongly affected, with 46 events and 0.24 events per path.

Avalanche activity was considerable in five other massifs where the cycle threshold (2-year return period) was significantly exceeded: Haute-Tarentaise, Haute-Maurienne and Thabor massifs, situated northward from Queyras along the French–Italian border, and Ubaye and Haut Var–Haut Verdon massifs situated between Queyras and Mercantour. In these five massifs, activity ranged from 0.12 to 0.15 events per path. In Embrunais–Parpaillon, the cycle threshold was just attained, with 4 events in 5 days and an activity of 0.05 events per path. In Vanoise, activity was slightly below the cycle threshold, with 7 events but only 0.03 events per path, and very small to null in all the other massifs. Hence, the cycle threshold was reached or attained in 8 massifs, where 172 events were recorded in 4 days, i.e.

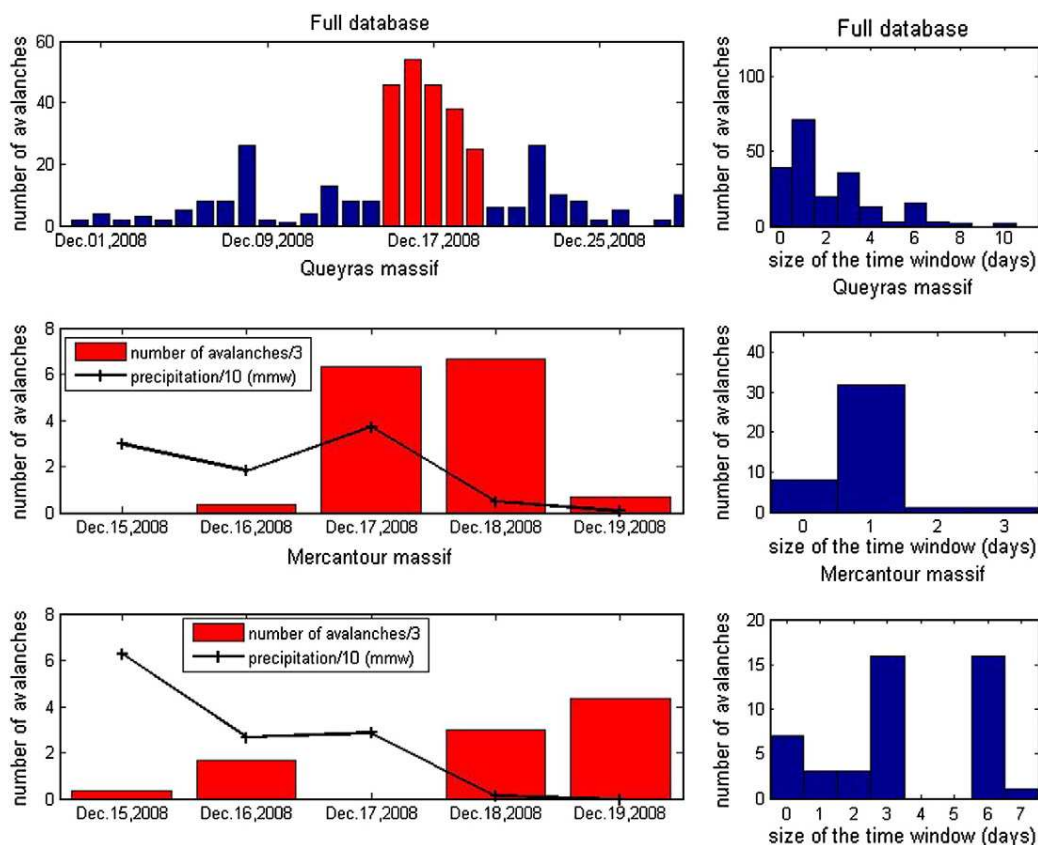


Fig. 3. Number of events per day recorded in the EPA database. Left, daily counts using the second date of the time windows provided by the rangers. In red, the 5 days defined as the avalanche cycle. Right, size of the time windows given by the rangers for the events of the cycle. The different lines correspond to the full database and to the two most affected massifs, Queyras and Mercantour.

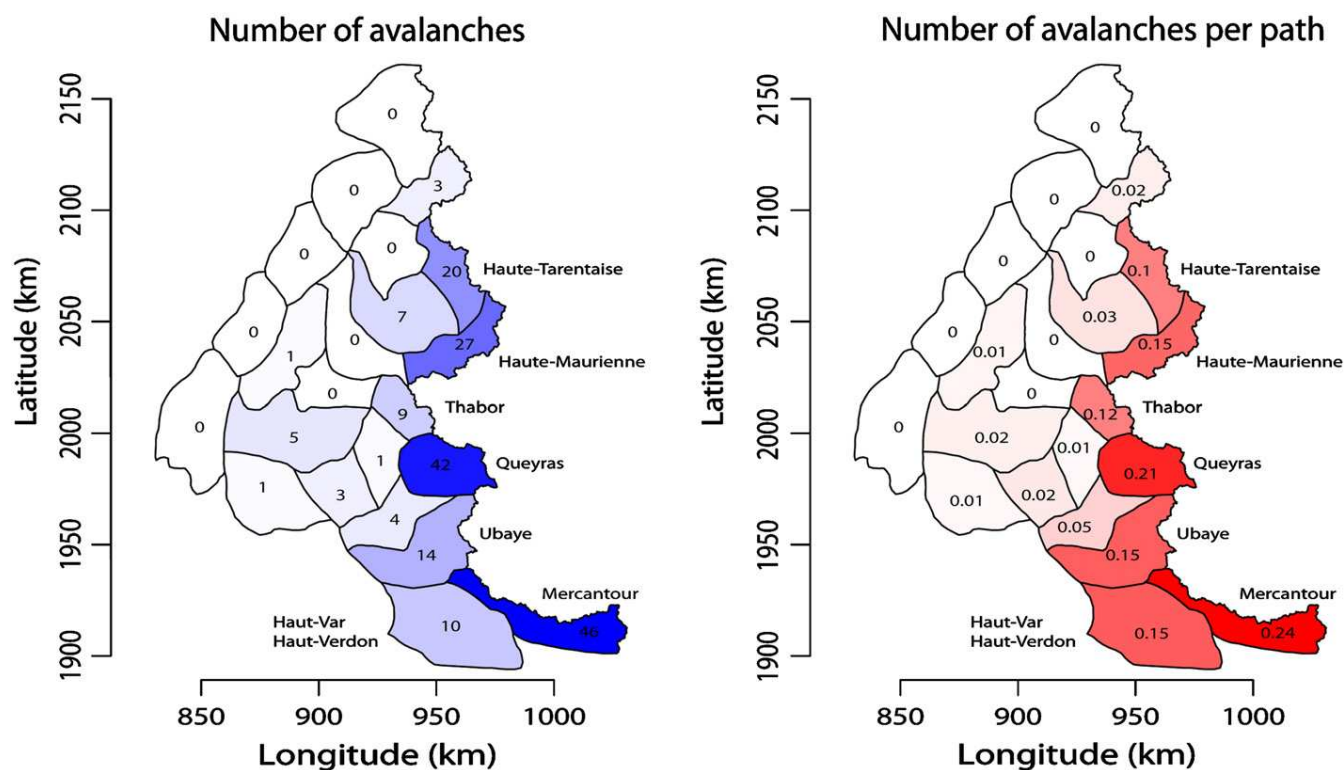


Fig. 4. Number of avalanches per massif during the cycle.

82% of the total number of events recorded between 15 and 19 December for the full database. In the rest of the study, we will therefore consider that the cycle only affected these eight massifs, with a special intensity in Queyras and Mercantour. Note that, at the massif scale and for a duration of 5 consecutive days, the cycle threshold corresponds to an activity of around 0.05 events per path, or 1 path under survey out of 20.

Even if the massifs of Haute-Maurienne and Haute-Tarentaise were involved, it is clear that the southern French Alps were more severely affected than the northern French Alps. Also evident is a strong east–west gradient (Fig. 4). As a consequence, the Moran's I indicates a highly significant clustering of the number of events and of the number of events per path at a low distance (Table 1), with p -values below 0.05 indicating that the null hypothesis of random spatial sampling is rejected. Clustering is no longer significant for both the number of events and number of events per path for lags ranging between 2 and 4 (Fig. 5, centre and right), indicating that spatial autocorrelation is limited to short distances. The spatial autocorrelogram indicates a significant repulsion between the numbers of events per path at lag 5. This is consistent with the existence of strong spatial gradients, since 4 boundaries are about the size (in the west–east direction) of the complete region studied.

Spatial gradients can be quantified using the spatial regression of Eq. (4). For the number of events and the number of events per path,

Table 1
Moran's I for the different variables.

Variable	Moran's I	p -value
Number of events n_i	0.23	0.009
Number of events per path f_i	0.47	0.00002
Safran cumulated snowfall over the cycle h_i	0.4	0.0001
Averaged instability index over the cycle mean (II_i)	0.19	0.02

Moran's I is computed using first order neighbourhood (see Fig. 5). Bold values indicate a significant clustering at the 95% confidence level (null assumption of random spatial sampling is rejected).

the direction of maximal gradient is around -14° and -20° , i.e. in the south-east direction. For the number of events, only the west–east gradient is significant at the 95% confidence level, with a strong value of 0.25 avalanches per km (Table 2). For the number of events per path, both gradients are significant at the 95% confidence level: 0.002 avalanches per path and km in the west–east direction and -0.001 avalanches per path and km in the south–north direction (Table 3). Spatial regression is reasonable for the number of events ($R^2 = 0.59$, Table 4) and good for the number of events per path ($R^2 = 0.76$).

Overall, the more relative metric of the number of avalanches per path shows a stronger spatial structure compared with the number of avalanches in the massif, with more significant Moran indexes for different lags, significant correlations with the two spatial coordinates, and hence a better agreement between data and spatial regression. Note that for both the number of events and the number of events per path, linear spatial gradients are sufficient to explain the observed spatial clustering since the residuals of the spatial regression are no longer spatially correlated (null hypothesis of random spatial sampling is not rejected by Moran's I test, Table 4).

3.2. Meteorological context and consequences for the events

From 14 to 17 December 2008, a large depression formed over the Mediterranean Sea. It maintained a southerly flow of cold air that evolved into a southeasterly flow in the east of France. Heavy precipitation occurred in Italy and extended to France. Heavy snowfalls therefore occurred in the French Alps situated close to the Italian border from 14 December to the morning of 17th, with a break during the 15th. Fig. 6 shows the interpolated cumulated precipitation in millimetres of water from 13 December at 06 UTC to 17 December at 06 UTC. The black crosses mark the location of the different data used.

Rain temporarily occurred at the beginning of the storm below 1200 m in the Mercantour massif, and from 1200 to 1400 m in the Queyras massif. However, because of the coldness of the southeasterly

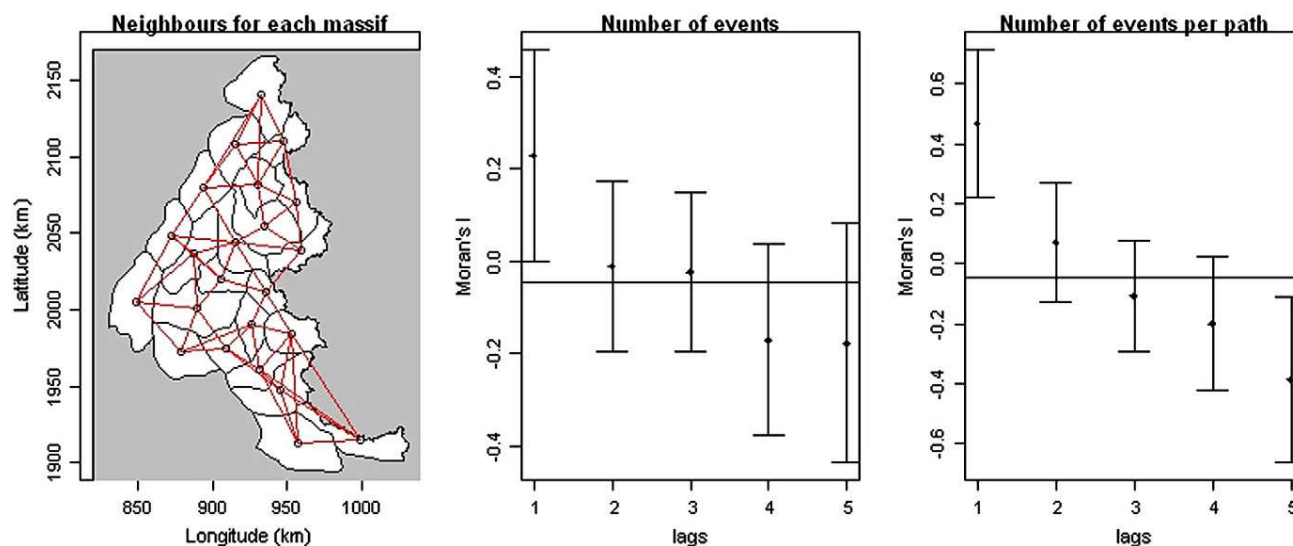


Fig. 5. Spatial structure of avalanche activity during the cycle. Left, graphical representation of the chosen adjacency matrix. Centre and right, spatial autocorrelogram for the number of events per massif and the number of events per massif and path, respectively. Lags represent distance classes measured in terms of nearest neighbours at a given order. Horizontal lines represent Moran's I expectation under random spatial sampling, and vertical bars, computed 95% confidence intervals for Moran's I at each lag.

flow, nearly all precipitations fell as snow throughout the affected massifs during the whole cycle, which is quite remarkable for these elevations in France. The north–south and east–west gradients visible in Fig. 4 are even clearer here. Note that the east–west gradient of precipitation is stronger for the Haute-Maurienne and Queyras massifs than for the Mercantour massif where the first part of the precipitation occurred under a southerly flow. Such spatial patterns typically correspond to a snow and meteorological episode caused by a perturbation coming from the south and having evolved as an easterly return. These intense snowfalls were the main release factor of the cycle's avalanches. However, they were accompanied by strong wind gusts of up to 100 km h^{-1} . Winds blew consistently from east to south-east in the Queyras massif and north to north-east in the Mercantour massif. Considerable drifting snow was observed, and field observations reported that it locally doubled or tripled the accumulated snowfall.

These snow and weather conditions are in very good agreement with those recorded in the EPA report. 82% of the 172 events recorded in the eight massifs where the cycle threshold was attained were preceded by at least 50 cm of new snow in 3 days, and 66% of them by

more than 1 m of new snow in 3 days (Table 5). Due to the prevailing cold temperatures, this increased the proportion of mixed and powder snow avalanches with regard to the 2001–2005 sample (Table 6). Note that this classification refers to the flow regime, and not to the type of release.

To allow cross-comparison between snow and weather data and avalanche activity, modelled Safran snowfall at the massif scale is considered (h_i in each massif $i, i \in [1, N]$). Cumulated snowfalls over 3 or 5 days are quite similar (Fig. 7), indicating that the true duration of the cycle in terms of snowfalls is close to 3 days, with very small snowfalls on 18 and 19 December. Given that a few avalanches were recorded on 18 December in the Mercantour massif, this is a bit shorter than the full duration of the avalanche activity period.

Spatial patterns in Safran cumulated snowfalls are similar to those obtained for the number of events, and very similar to those obtained for the number of events per path. This is indicated by a strongly significant Moran's I at small distances (Table 1). Moreover, the spatial autocorrelogram on Fig. 7 (right for the 3-day snowfall, nearly identical for 5 days) does not present significant autocorrelations between lags 2 and 4 but a significant repulsion at lag 5. No more spatial structure in spatial regression's residuals remains (p -value

Table 2
Spatial regression for the number of events.

Variable x_k /coefficient β_k	$\hat{\beta}_k$	$\hat{\beta}_k$ std. error	p -value
β_0	−96.6	90.3	0.3
lat/ β_1	−0.06	0.03	0.06
long/ β_2	0.25	0.06	0.0002

Bold values indicate coefficients which are significant at the 95% confidence level (t -test).

Direction of the maximal spatial gradient is given by $A \tan \left(\frac{\hat{\beta}_2}{\hat{\beta}_1} \right) = -14.2^\circ$.

Table 3
Spatial regression for the number of events per path.

Variable x_k /coefficient β_k	$\hat{\beta}_k$	$\hat{\beta}_k$ std. error	p -value
β_0	−0.24	0.40	0.55
lat/ β_1	−0.001	0.0001	0.001
long/ β_2	0.002	0.0003	0.000007

Bold values indicate coefficients which are significant at the 95% confidence level (t -test).

Direction of the maximal spatial gradient is given by $A \tan \left(\frac{\hat{\beta}_2}{\hat{\beta}_1} \right) = -19.7^\circ$.

Table 4
Summary of the different linear models tested.

Explained variable y_i	Covariates x_k	Significant covariates (95%)	R^2	Moran's I for residuals	p -value for Moran's I
n_i	lat, long	long	0.59	−0.15	0.62
f_i	lat, long	lat, long	0.76	−0.02	0.19
h_i	lat, long	lat, long	0.68	0.06	0.05
$\max(I_i)$	lat, long	intercept, long	0.48	−0.02	0.17
$\text{mean}(I_i)$	lat, long	intercept, long	0.53	0.04	0.07
n_i	h_i	intercept, h_i	0.79	−0.17	0.80
f_i	h_i	intercept, h_i	0.89	0.13	0.05
f_i	$\max(I_i)$	$\max(I_i)$	0.61	0.32	0.001
f_i	$\text{mean}(I_i)$	$\text{mean}(I_i)$	0.68	0.37	0.0003
f_i	lat, long, h_i	lat, h_i	0.92	−0.14	0.56
f_i	lat, long, h_i	lat, long, h_i	0.86	−0.05	0.25
$\text{mean}(I_i)$	h_i	h_i	0.79	0.14	0.05

Intercept refers to the constant term β_0 in the regression model of Eq. (4). Bold values indicate a significant clustering at the 95% confidence level of the regression residuals (null assumption of random spatial sampling is rejected).

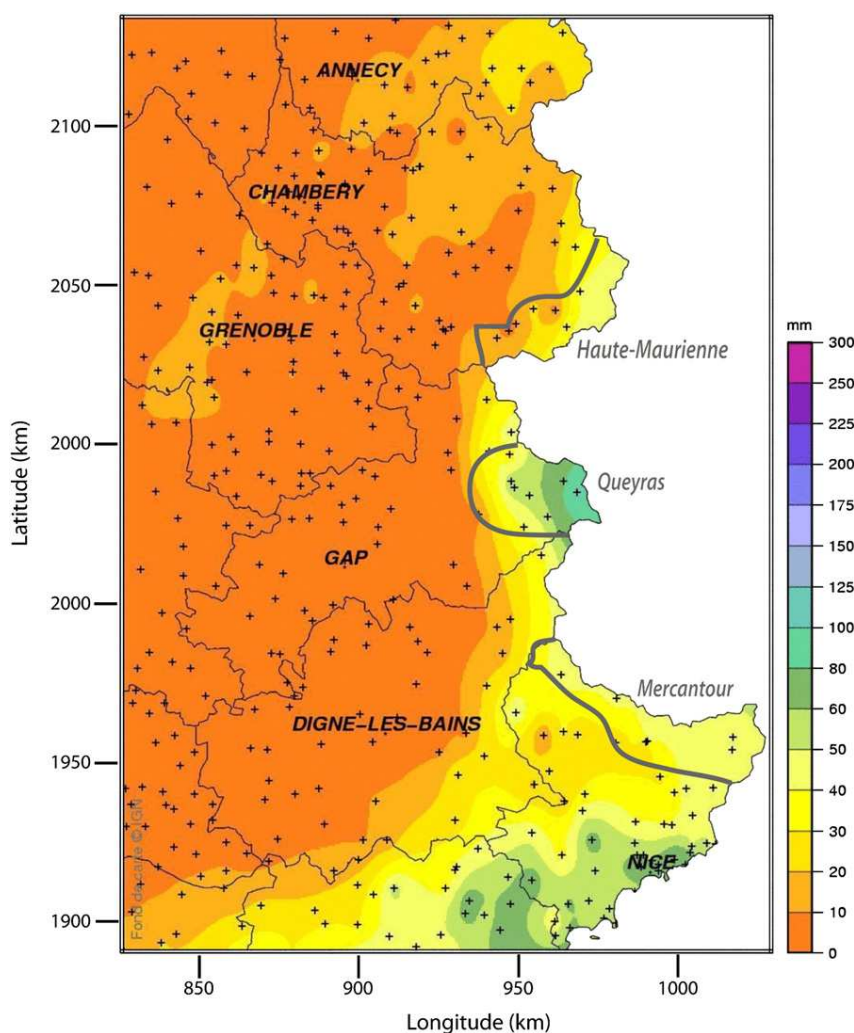


Fig. 6. Cumulated precipitation (mm water equivalent) during the cycle. Black crosses correspond to measurement stations. Interpolation is performed by kriging. The indicated massifs are those most affected by the cycle. The map focuses on the French Alpine space.

below 0.05, Table 4) and gradients are significant in both directions: 0.66 mm km^{-1} in the west–east direction and -0.17 mm km^{-1} in the south–north direction. Consequently, the cumulated snowfall over the cycle h_i as a single covariate explains avalanche activity very well ($R^2 = 0.79$ with the number of events n_i and $R^2 = 0.89$ with the number of events per path f_i , Table 4) and is sufficient for the residuals to be no longer spatially correlated. The latter point indicates that the spatial structure in snowfalls fully explains the spatial structure in avalanche activity at the massif scale. This all quantitatively confirms the predominant role of snowfalls (amount of precipitation and cold temperatures) in the analysed cycle.

Table 5
3-day snowfall preceding the recorded avalanches.

	Events from the cycle	Mean 2001–2005
0 cm	2%	27%
1–20 cm	2%	15%
21–50 cm	4%	28%
51–100 cm	26%	25%
>100 cm	66%	5%

The events from the cycle are the 172 events recorded between December 15th and 19th 2008 in the eight massifs where the cycle threshold is attained. All the events of the 2001–2005 winters are used as a comparison sample.

3.3. Snow cover and snow instability index

Snowfalls started early during the 2008 winter season, and the snowpack began to develop in November. Results of the SCM model chain indicate that, at the beginning of the cycle, the snow depth was already above the average in most of the southern French Alps. As pointed out in Section 2.1, few weather and snow observations exist at this early period of the season. However, a snow profile was made at Auron, Mercantour massif, at an altitude of 2000 m on a 15° north-east slope by a local observer (Fig. 8). Although not fully of professional quality, it shows well the structure of the snowpack at the end of the cycle. The last snowfalls, from 120 cm up to the snow surface, correspond to a water equivalent of 120 mm which is in good agreement with the modelled Safran snowfall amount for the mid-December storm. Below the fresh layers, the snowpack consists of weak snow, partly faceted crystals, with a low density. This snowpack

Table 6
Flow regime of the recorded avalanches.

	Events from the cycle	Mean 2001–2005
Powder snow avalanches	23%	6%
Dense snow avalanches	51%	80%
Mixed avalanches	26%	14%

weakness is confirmed by modelled results of the SCM model chain (not shown here). Thus, the depth of snow that was potentially movable in an avalanche was constituted by the fresh snow brought by the recent snowfalls and the existing weak snowpack which was another clear aggravating factor explaining the cycle studied.

The mean instability index, $\text{mean}(I_i)$, over the cycle is plotted in Fig. 9 (left), showing similar spatial patterns to the Safran cumulated snowfall and avalanche activity. Moran's I indicates a slightly weaker (though significant) clustering of $\text{mean}(I_i)$ than of h_i and avalanche activity (Table 1). Although the spatial gradients are somewhat lower (only longitude is significant) than for avalanche activity and h_i , spatial regression remains reasonable ($R^2 = 0.53$, Table 4).

The correlation between relative avalanche activity f_i and the mean instability index $\text{mean}(I_i)$ is similar, though slightly lower than between relative avalanche activity f_i and Safran cumulated snowfall h_i . The residuals of the regression of f_i on $\text{mean}(I_i)$ are still spatially correlated (Table 4), whereas the null hypothesis of random spatial sampling is no longer rejected for the residuals of the regression of f_i on h_i . However, considering the different uncertainty sources concerning observations and modelled data, it can be considered that the two covariates, h_i and $\text{mean}(I_i)$ have a similar explanatory power for relative avalanche activity in this case. It is confirmed by the regression of $\text{mean}(I_i)$ on h_i ($R^2 = 0.79$) indicating that snowfall patterns explain nearly 80% of the variability and nearly the entire spatial structure of the mean instability index (Table 4). This is logical, since Safran snowfall is included in the instability index calculations, but shows again the predominant role of snowfalls in the cycle. Finally, the relative avalanche activity f_i can be nearly entirely explained with three covariates: the spatial coordinates ($lat, long$) describing the spatial patterns corresponding to the cycle, and h_i or $\text{mean}(I_i)$, with $R^2 = 0.92$ and 0.86 respectively. These high determination coefficients obtained with very few covariates confirm that the avalanche cycle was generated by strong and simple snow and weather patterns.

Similar results are obtained with the maxima instability index over the cycle $\text{max}(I_i)$ instead of $\text{mean}(I_i)$, though they are slightly worse in terms of spatial structure ($R^2 = 0.48$ instead of 0.53 for spatial regression, Table 4), and correlation with avalanche activity f_i ($R^2 = 0.61$ instead of 0.68 , Table 4). This illustrates/confirms that the persistence of unstable conditions over several days is more important for explaining observed avalanche activity than a short and sharp instability peak.

Fig. 9 (right) shows the residuals of the regression of the number of events per path f_i on $\text{mean}(I_i)$. The residuals are generally low, except for a few massifs. Instability has been overestimated compared to the number of avalanches observed per path for the Pelvoux, Haute-Maurienne and Mont-Blanc massifs. On the other hand, the large positive residuals (between 0.06 and 0.12 events per path) for the Haut Var–Haut Verdon, Ubaye and Queyras massifs reflect an underestimation of the modelled instability compared to the number of avalanches observed. There are several possible explanations for these discrepancies. First, the linear regression concerns 15 massifs with a weak activity and only 8 massifs strongly affected by the avalanche cycle, but a statistical study based on the 8 most affected massifs only would have been meaningless. Second, as stated in Section 2, the index takes higher values in higher massifs, which explains in part the high negative residuals in the higher elevation Pelvoux, Haute-Maurienne and Mont-Blanc massifs. This is critical here since, on the contrary, EPA reports mainly avalanche activity at low elevations (human observation). Third, the regression does not take into account intra-massif gradients in snow stability and avalanche activity, see Section 4.3.

The fact that the instability index is not clearly a better predictor of avalanche activity than the Safran snowfall alone may be surprising and somewhat disappointing. One reason is that one of the main advantages of the instability index is to summarise the influence on avalanche activity of several generating factors. Using the index is therefore not fundamental in this case because instability was mainly governed by snowfalls. On the other hand, it can be very useful for other cycles (Martin et al., 2001), for example, those of wet snow avalanches coupled with a positive energy balance, or those discontinuous in terms of precipitations with a variable rain/snow limit. A second crucial advantage of the Mepra outputs with regard to rough snowfall data is to evaluate release probability with a thin spatio-temporal resolution. This also was not beneficial for this study, since the data were mainly considered at the scale of the massif, and cumulated over the full cycle's duration.

4. Historical comparisons

4.1. Return period of the avalanche cycle

Fig. 10 (right) presents the empirical return period of the December 2008 cycle for n_i , the cumulated number of events over 5 days per massif. The spatial patterns appear to agree with those

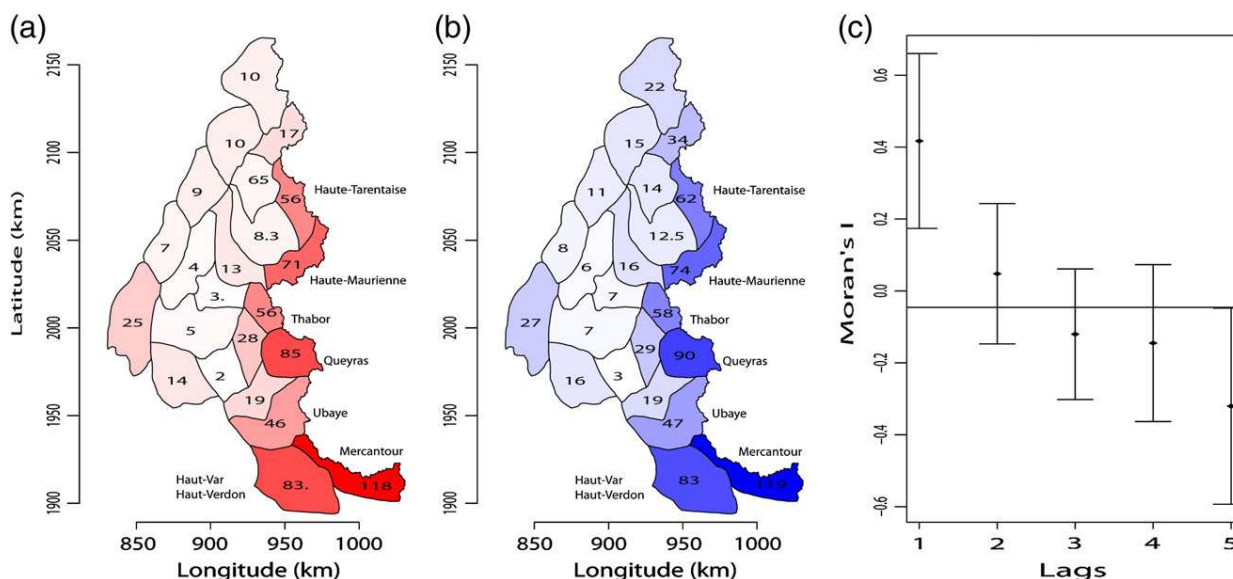


Fig. 7. Cumulated Safran snowfall (mm water equivalent) over three (a) and five (b) days at the massif scale, and spatial autocorrelation for three-day snowfall (c).

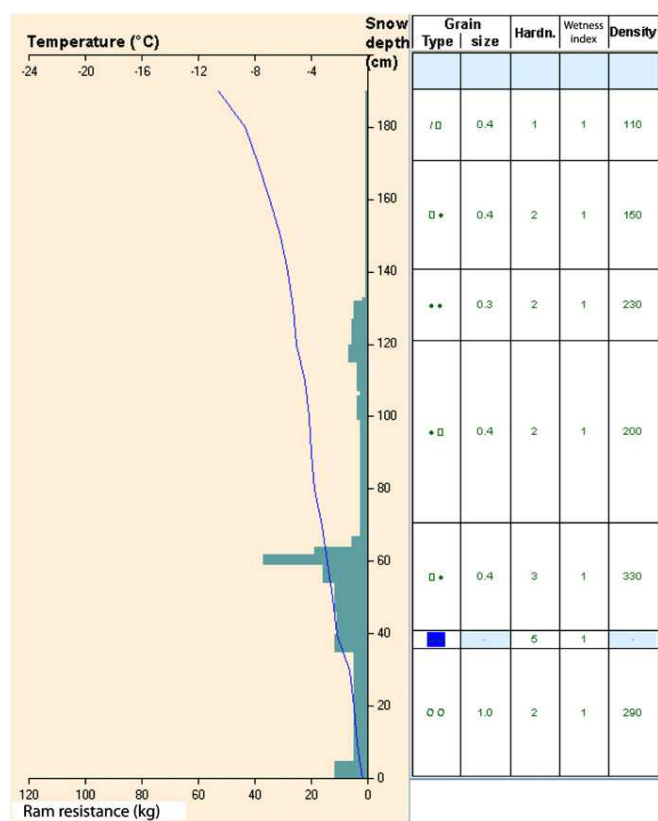


Fig. 8. Snow cover profile at Auron, Mercantour massif, France, December 18th 2008 at an altitude of 2000 m on a 15° north-east slope. The profile presents snow resistance and temperature as a function of depth. For each layer, grain type (from International Classification), grain size (mm), hardness (from 1 to 5), humidity (Wetness index, from 1 to 5) and density (kg m^{-3}) is provided.

obtained for avalanche activity (Fig. 4), Safran snowfalls (Fig. 7) and instability indexes (Fig. 9). In the Queyras and Mercantour massifs, the number of recorded events corresponds to the historical maximum over 5 days since the beginning of the EPA records. The empirical return period of the cycle is therefore at least 50 years in these massifs, but with a high uncertainty because of the empirical estimation procedure used and the relatively short reference period considered. In the Haut-Haut Verdon massif, the return period is around 10 years. It is around 8 years in Haute-Maurienne and around 5 years in all the other massifs affected by the cycle. Interestingly, the return period is an increasing function of the number of events per path at the massif scale: the cycle threshold (Fig. 10, left) corresponds roughly to 0.05 events per path, a return period of 5–8 years to approximately 0.12–0.15 events per path, and historical maxima to 0.2–0.25 events per path.

The maximal instability indexes corresponding to the December 2008 cycle were compared with previous high values encountered over the last 50 years. For Queyras and Mercantour, even if historical maxima were not exceeded, December 2008 was one of the most critical situations in terms of snow instability over the last few decades. In the Mercantour massif, the maximal value of the instability index was 5.3 during the cycle. This value was already attained in December 1983, and exceeded in January 2008 when it reached 5.7. In the Queyras massif, the index reached 4.2 in December 2008. This was a bit less than 5.7 in March 1971 and far beyond in December 1978 where the index reached its maximum possible value of 8.

4.2. Magnitude–frequency–duration quantification

Fig. 11 shows the return period for n_i for durations ranging from 1 to 7 days for the full database, and for a few massifs affected by the cycle.

The different plots can be seen as magnitude–frequency–duration curves, where, for a given duration, the magnitude is defined as the number of cumulated events and the frequency by the corresponding return period. At the scale of the full database (Fig. 11, top), the return period increases for events cumulated over 1–5 days, reaches a maximum for events cumulated over 5 days and then slightly decreases. Relatively similar results are obtained for Haute-Tarentaise and Haute-Maurienne (Fig. 11, middle), with the magnitude–frequency–duration curve reaching a maximum for durations of 3–5 days.

The historical maximum number of events and the highest empirical return period of 54 years is reached for 3–7 days for the Queyras massif, and for 5–7 days only for the Mercantour massif because of the events recorded December 19th with delay (Fig. 11, bottom). In these two massifs, the return period decreases only if much longer time scales of several weeks are considered. The link between weather conditions and avalanche occurrences is then lost, since the events corresponding to one cycle are compared with the events generated by different smaller cycles that successively occurred.

The existence of maxima for time scales ranging from 3 to 5 days in all the magnitude–frequency–duration curves except those corresponding to Mercantour and Queyras confirms that the December 2008 avalanche cycle is remarkable rather because of the succession of several days of high avalanche activity than because of a very intense but short activity. However, the determination of the most critical time scale for the cycle remains difficult: (1) variations exist from one massif to another, depending on the local evolution of the snow and weather constraining factors; (2) the above-mentioned problem of certain events having been recorded after their occurrence in the Mercantour massif makes that an irreducible uncertainty remains. However, such artefacts may also have existed in the past because the uncertainty about the release date is recorded since 2002 only. As a consequence, historical comparisons only allow the time scale of the biased natural process to be rigorously inferred, without possible subtraction of the human factor.

4.3. Snowfall return period

Fig. 12 presents the return periods obtained for Safran snowfalls cumulated over 1 to 5 days, i.e. the magnitude–frequency–duration curve in each massif. Daily maxima were relatively normal, but cumulated snowfalls were much more unusual. The highest return periods are obtained for 3-day snowfalls, thus confirming the 3-day time scale of the snowfall event. For this duration, the return periods obtained are around 4 years in the Haute-Maurienne massif, 6 years in the Mercantour massif and 10 years in the Queyras massif. Note that a much longer return period is obtained in the Queyras massif than in several other massifs for a relatively similar amount of cumulated precipitation. This arises because Queyras is usually the driest French massif, seeing intense snowfalls more rarely.

Fig. 13 shows the 3-day snowfalls return period calculated by the spatial extreme approach described in Section 2.6. It highlights the large intra-massif snowfall variability. The highest return periods are located in the extreme east of the Queyras massif and in the Mercantour massif, with very strong intra-massif gradients. The return period for the mean Safran snowfall at the massif scale (Fig. 12) roughly corresponds to the maximum local value provided in each massif by the spatial extreme approach (Fig. 13). To analyse this result, the substantial differences between the two approaches must be remembered: the spatial extreme approach is based on local precipitation data processed with advanced statistical interpolation tools, whereas the Safran approach is based on simpler statistical tools, but also on assimilation and processing of a large amount of data (not only precipitations) at the massif scale using physical rules. Relatively good agreement between the maximum values provided by the two approaches is therefore already encouraging.

The most extreme snowfalls corresponded well to the massifs where the highest numbers of avalanches were recorded. Moreover, the spatial

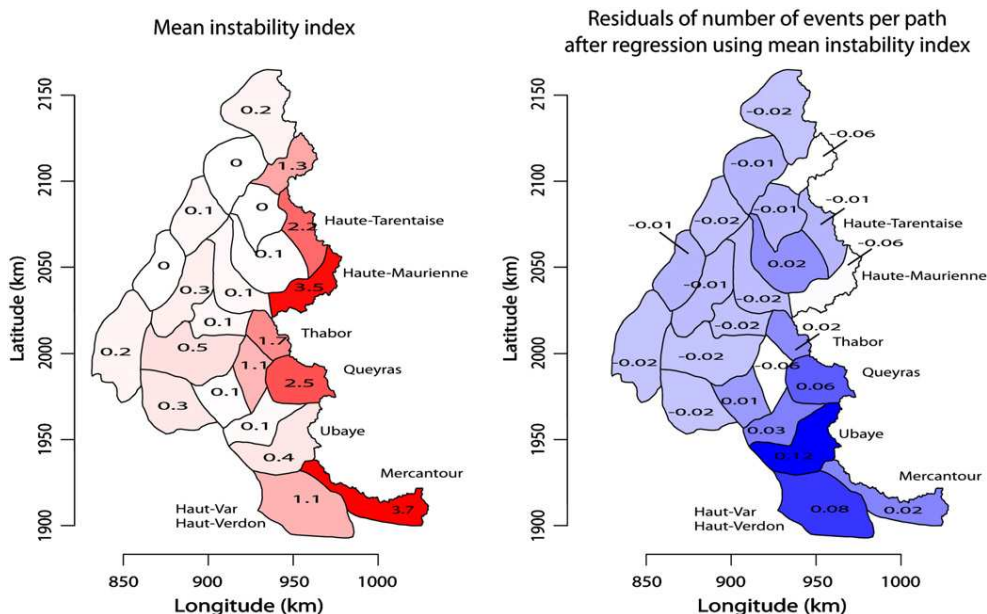


Fig. 9. Instability index over the cycle. The instability index is computed by the SCM chain. Left, the mean instability index mean(*I*) over the cycle. Right, residuals from the regression model of Eq. (4), with mean(*I*) as unique covariate to explain the observed number of events per path.

patterns in snowfall return periods and in the return periods of avalanche numbers during the cycle are quite similar. However, the highest return periods are much higher for avalanche counts (Fig.10, right) than for the cumulated snowfalls (Fig. 12): around 50 years versus around 10 years. This has been reported for other cycles including February 1999 (Schweizer et al., 2009), but with avalanche return periods based on runout distances and impact pressures rather than on the number of events. The most likely explanation for the difference in return period between snowfalls and avalanche numbers is provided by the aggravating effects highlighted previously (drifting snow, thick snowpack at the beginning of the cycle..., etc.) that have induced more avalanches than predicted by snowfalls only. Another possible explanation is that the high intra-massif spatial gradients in snowfall intensity have led to a high intra-massif clustering of the EPA paths on which the

avalanche events were recorded. Indeed, in the Haute-Maurienne, Thabor and Queyras massifs, nearly all the paths located very close to the French–Italian border were active during the cycle (Fig. 14), which corresponds well to the position of local maxima in the snowfall return period (Fig. 13). Since EPA paths are not uniformly spatially distributed and are especially numerous close to the French–Italian border because of a high mountain ridge at this location, this may also explain the fact that a relatively large and infrequent snowfall was able to generate an even more extreme number of avalanches.

4.4. Magnitude of the events

Except in Tables 5 and 6, historical comparisons have been up to here mainly based on avalanche counts. Understanding why the

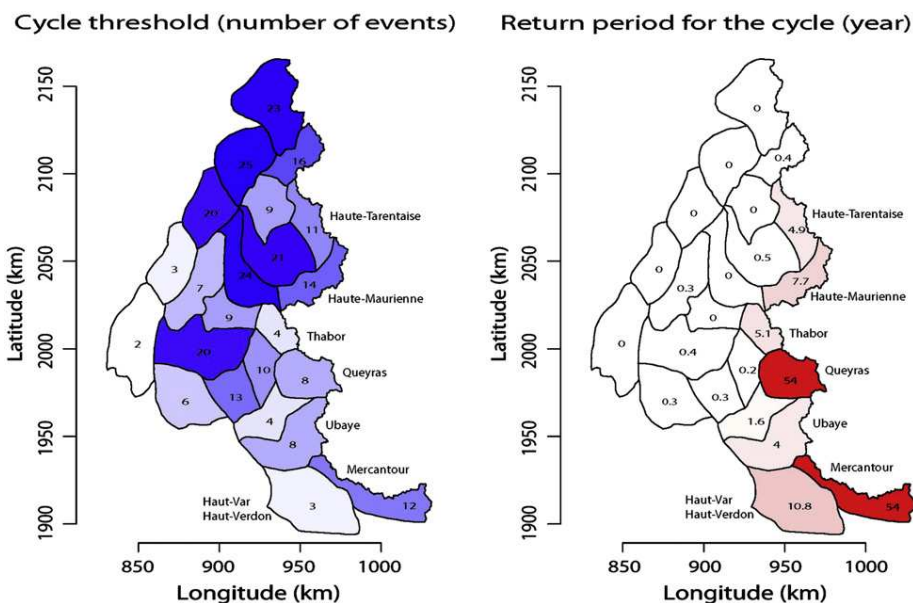


Fig. 10. Return period of the number of events per massif for the cycle. The cycle threshold corresponds to a 2-year return period, i.e. to the number of avalanches over 5 days which has been exceeded only one time in 2 years on average.

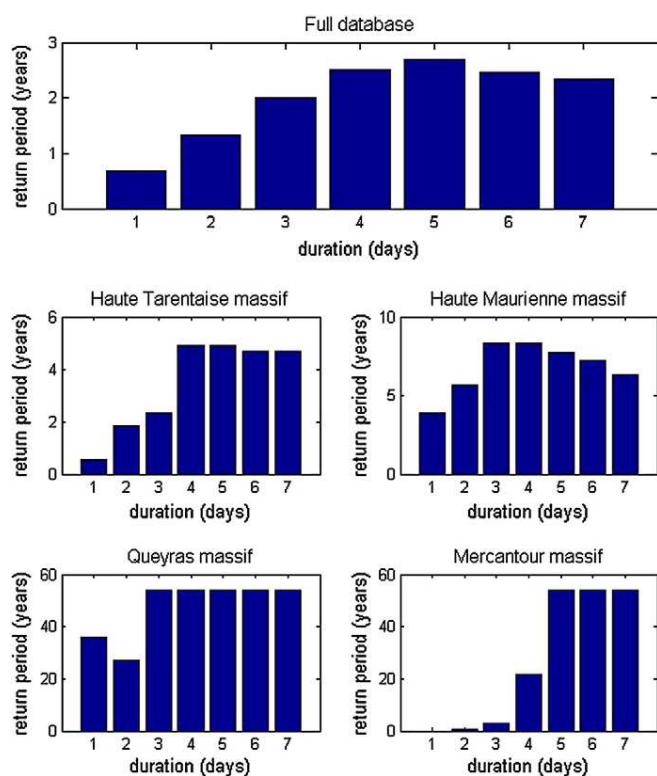


Fig. 11. Magnitude–frequency–duration curves for the number of events for the full database and selected massifs.

December 2008 avalanche cycle caused substantial damage involves more precise evaluation of the magnitude of the cycle events in their runout zones, where the elements at risk are situated. For both the 2001–2005 comparison sample and the 172 events corresponding the December 2008 avalanche cycle, *RAI*'s distribution is strongly skewed on the right (Fig. 15, right). This common shape occurs because of the enhancing effect of the exponential transformation, and because the differences between the observed and minimal runout altitudes are always small. For instance, the mean runout altitude during the cycle was 1643 m (with values ranging roughly between 1200 and 2100 m, Fig. 15, left), to be compared to 1638 m, the mean minimal altitude of the paths which were active during the reference period in the 8 massifs affected by the cycle. This small difference indicates that the reference values are well chosen, making the use of the *RAI* possible.

For a given probability, the cumulative distribution function of the *RAI* is systematically higher for the December 2008 cycle than for the 2001–2005 sample. This remains true to a lesser extent, but still with a significant *p*-value, if the comparison sample is limited to the 8 massifs where the cycle occurred. For instance, the valley floor was reached by 19% of the cycle events (i.e. nearly twice as many as for the 2001–2005 total and partial samples), and seven of them climbed up the opposite slope of the valley. All this suggests that this cycle's avalanches generally reached long runouts, which is coherent with the high proportion of dry snow avalanches (with or without a powder part) during the cycle, and with the cold temperatures that existed (friction is reduced with cold snow). Note that the absence of intense avalanche cycles in the 2001–2005 sample may also explain the systematic difference with the 2001–2005 sample, but it is not sufficient, since several historical extensions based on much longer records were exceeded during the 2008 cycle. As a consequence, the French avalanche atlas had to be significantly updated, mainly in the Queyras and Mercantour massifs.

The maximum deposit volume recorded during the cycle was 180,000 m³. This is much smaller than the maximum over the

2001–2005 comparison sample (900,000 m³). However, for a large range of probabilities including those corresponding to the 50%–90% percentile, the cumulative distribution function of deposit volumes is significantly higher for the December 2008 cycle than for the 2001–2005 sample (Fig. 16, left). Even if no real exceptional deposit volume was observed during the cycle, volumes higher than in mean were therefore encountered, especially if it is considered that the deposit volumes corresponding to the numerous powder snow avalanches having occurred during the cycle were very likely underestimated. Both the cycle and the comparison sample's distributions have a similar log-normal shape, but with different mean and standard deviations. The two samples are no longer statistically different after log-scaling (i.e. after dividing the deviation from the mean by the standard deviation), which is in good agreement with the assumption generally made of log-normally distributed avalanche masses (e.g., McClung, 2003).

5. Discussion, conclusion and outlooks

5.1. The December 2008 cycle

In mid-December 2008, an intense avalanche activity was observed during southeasterly fluxes over the eastern regions of southern French Alps and in the nearby region of Italian Piedmont. It was one of the most critical situations in terms of snow instability over 50 years, and even the historical maxima in terms of the number of events since the beginning of the systematic avalanche observation in the Queyras and Mercantour massifs. Over a smaller time scale, it was the most intense avalanche cycle in the French Alps since the westerly induced cycle of February 1999. A significant correlation between the number of events and their magnitude was also present, since the cycle events on average had higher volumes and reached much longer runouts than during a mean winter.

The detailed analysis proposed in this paper is useful to better understand links between synoptic circulation patterns and avalanche activity in the French Alps. The most important factors explaining the very high number of avalanches observed were the duration of the episode and the abundant snowfalls brought by southerly and westerly fluxes. Significant east–west and south–north gradients of precipitation have existed, and it was shown that they were sufficient to explain nearly all the spatial structure of the avalanche activity at the massif scale. Cold temperatures made the snow–rain limit to be unusually low, and caused long runouts and an important proportion of powder snow avalanches. The weakness of the thick snowpack at the beginning of the cycle also played a role, and wind and drifting snow aggravating effects were observed locally.

From a temporal point of view, magnitude–frequency–duration curves helped in demonstrating that an approach based only on daily maxima of number of events was insufficient for fully characterising the studied cycle, and that 3 to 5 days was more likely the critical time scale. This critical time scale may differ from a purely snow and weather point of view than from the EPA report's point of view. However, the inherent uncertainty around the precise time of occurrence of the avalanche events made it impossible to relate avalanche activity to the available snow and weather data at short time steps. As a consequence, for most of the regression and spatial analyses of Section 3, the avalanche cycle was considered as a block, and avalanches and precipitations were cumulated over 5 days (for precipitations, this makes very little difference with 3 days), so as to avoid underestimation of the cycle's intensity.

5.2. The question of scales

Our relative definition of an avalanche cycle based on the 2-year return period has the advantage of being independent of the duration

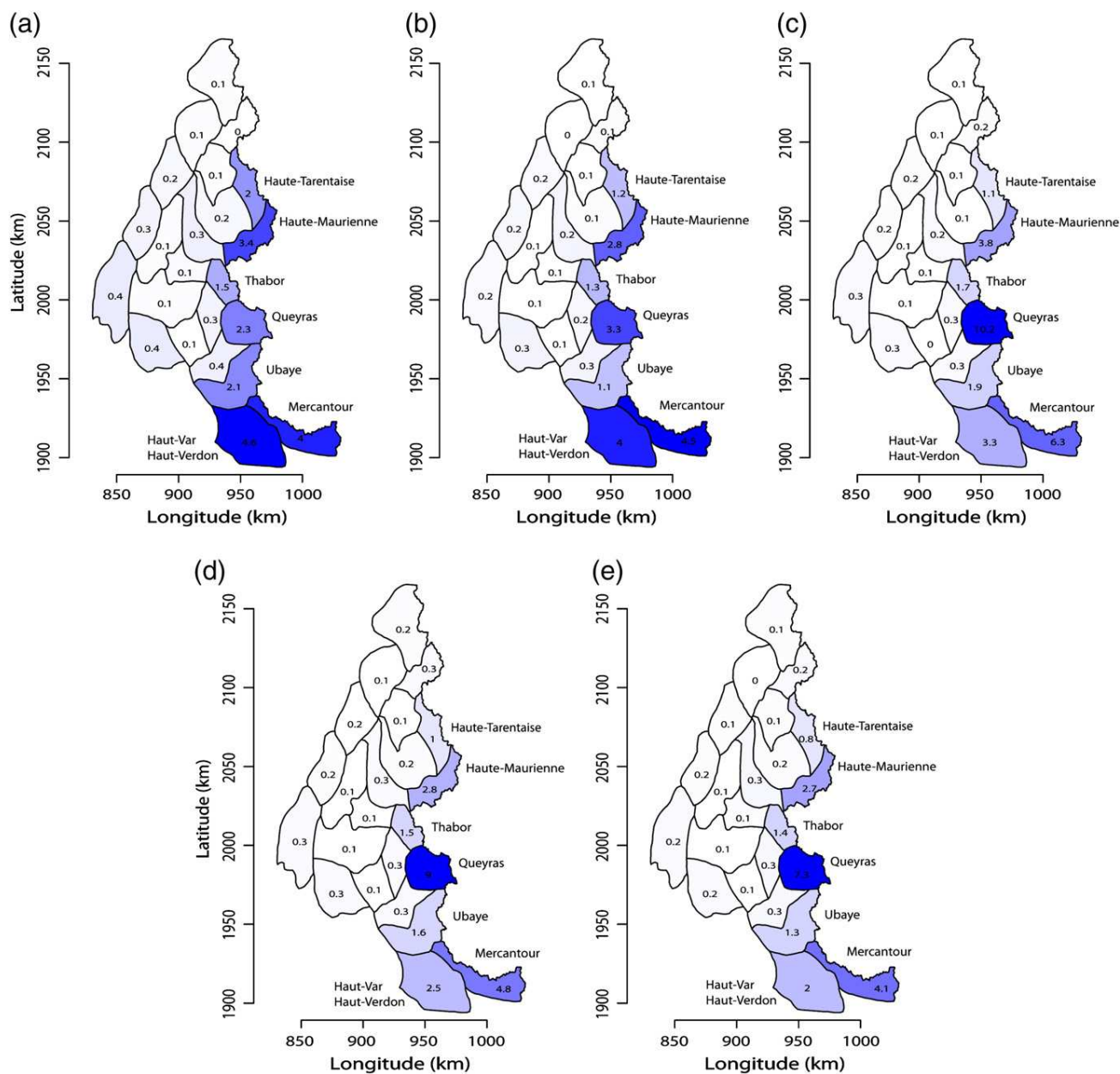


Fig. 12. Return period (year) of Safran snowfall at the massif scale for different durations: (a) daily maximum, (b) 2-day, (c) 3-day, (d) 4-day, and (e) 5-day. Considered altitude is 1800 masl.

on which the events are cumulated, as well as of the spatial scale. It can therefore be used to detect avalanche cycles of various length, and at any spatial scale, for example at the administrative level (*département*) at which the EPA avalanche data are collected. Since such a spatial scale is less relevant to understand the physical characteristics of the factors controlling avalanche cycles, the smaller and more physically-based scale of mountain massifs devoted to operational avalanche forecasting was preferred.

However, characterising the spatial and temporal scales that best describe the studied cycle was very difficult because of its particular generating weather conditions (easterly return) that made the number of avalanche releases high very close to the French–Italian border. For instance, the strong local gradients in snowfall intensity and avalanche activity shown in Figs. 14 and 15, respectively, demonstrate inhomogeneity within massifs. This presumably partially explains the difference

in return periods between snowfalls and avalanche counts. Similarly, as exemplified by the differences in magnitude–frequency–duration curves, the time scale which is the most appropriate to describe the cycle varies from one massif to another.

All these points highlight that defining zones and periods that are homogeneous in terms of avalanche activity remains extremely tough. Since no snow cover model is for the moment able to define a release probability at the path scale, this indicates that the effort of joint analyses of avalanche and weather data during avalanche cycles must be pursued, to better understand the space and time clustering of avalanche events during the most critical situations, and thus improve avalanche forecasting.

It must be noted that a specific detailed study of the most destructive events of the cycle has been conducted at the path scale (Gaucher et al., 2009). However, such an approach does not allow

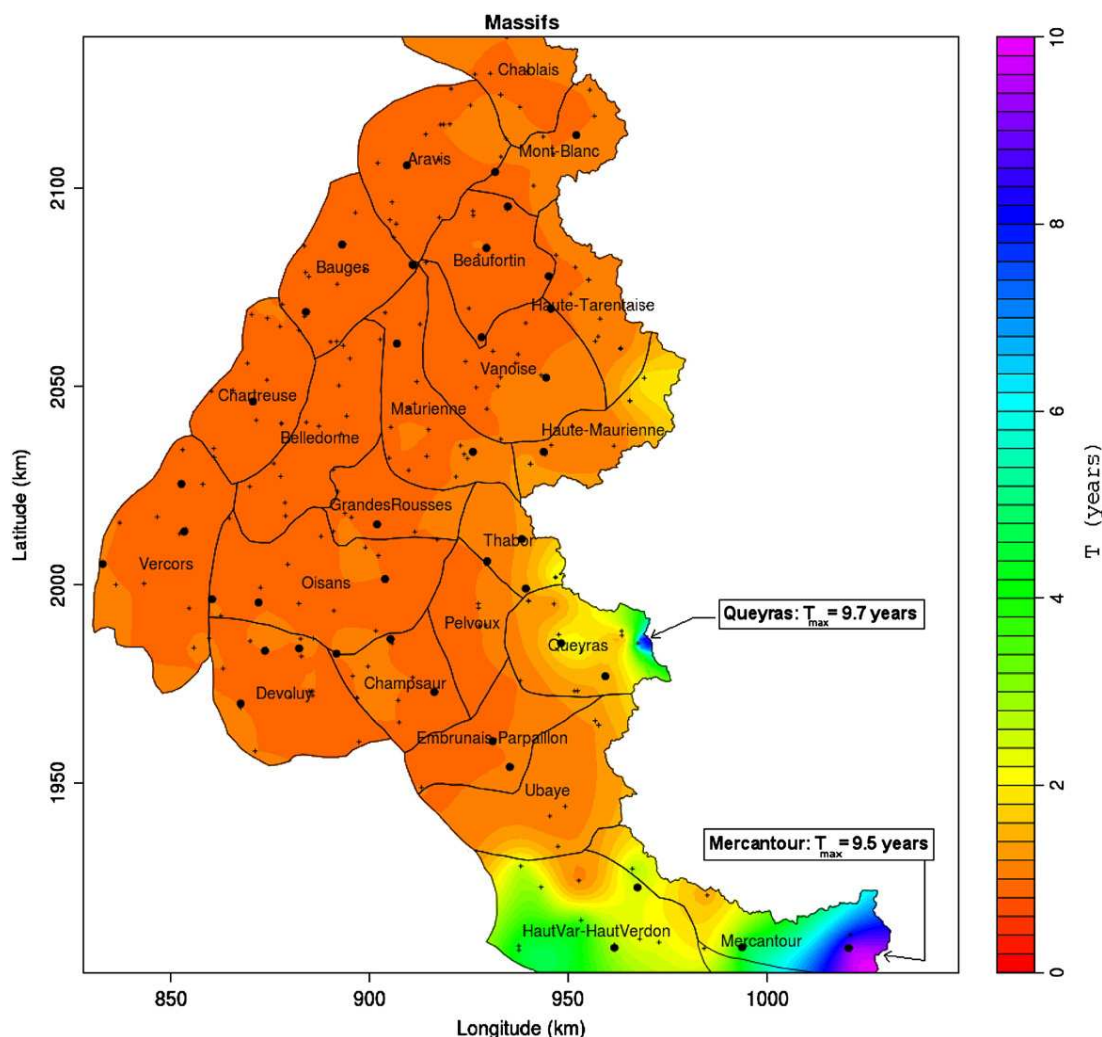


Fig. 13. Return period of the three-day snowfall as a function of space. Black dots correspond to measurement stations with long series that have been used for model calibration. Black crosses correspond to other measurement stations for which data were available for the December 2008 cycle. Return period is evaluated at 2000 masl.

much inference of the global response of a mountain system to a weather signal. Our work at the massif scale can therefore be seen as a reasonable compromise between having enough information to obtain robust estimators of a mean behaviour during an avalanche cycle and choosing regions with a relative homogeneity of the considered events. Going into greater detail would involve computing return periods at the path scale, so as to precisely position the different recorded events on the local magnitude frequency curve corresponding to each path. This would be appealing in terms of long-term hazard assessment and zoning. However, it is difficult to do so systematically because only runout elevations are recorded in the EPA database, so that substantial field work is necessary to convert them into distances and extensions with reasonable uncertainty levels.

5.3. Cross comparison of data

The work aimed at comparing the information conveyed by different data sources. Analyses showed for the case study good coherence between the spatial (Moran's I , gradients, regressions) and temporal (return periods, magnitude–frequency–duration curves) patterns in snow and weather data, snow instability index and avalanche activity. The different snow and weather categorical variables recorded in the EPA database were in good agreement with weather conditions, and the cycle had the most destructive effects where the magnitude of the cycle

was the highest (Queyras and Mercantour massifs). All this is encouraging in terms of the quality and coherence of the different data sources.

Some discrepancies between the information conveyed by the different data sets analysed and methods were though noted. Certain of them are linked with the lack of homogeneity in terms of data scale and type, for example avalanche events at the path scale recorded mainly at low elevations, versus snow and weather data assimilated and processed by the SCM model chain at the massif scale, with greater importance given to high elevations. Others are related to the limitations of each data set, for example missing and delayed avalanche events in the EPA report. These are for us unavoidable during the analysis of a real avalanche cycle for which all information acquired over a large area is used. For instance, in such a context, everything cannot be fully proven quantitatively and a certain credit must be given, after quality checking and/or cross-comparison, to partial, uncertain, or qualitative information provided by experienced local observers. Finally, certain discrepancies arise presumably simply because snow avalanches are integrated and nonlinear responses to snow and weather patterns interacting with topography, which for example induces delay between snowfalls and certain avalanches, or even response/non response to a given loading. Nevertheless, the study has shown that databases, constructed separately, perform relatively well in illustrating different aspects of an avalanche cycle.

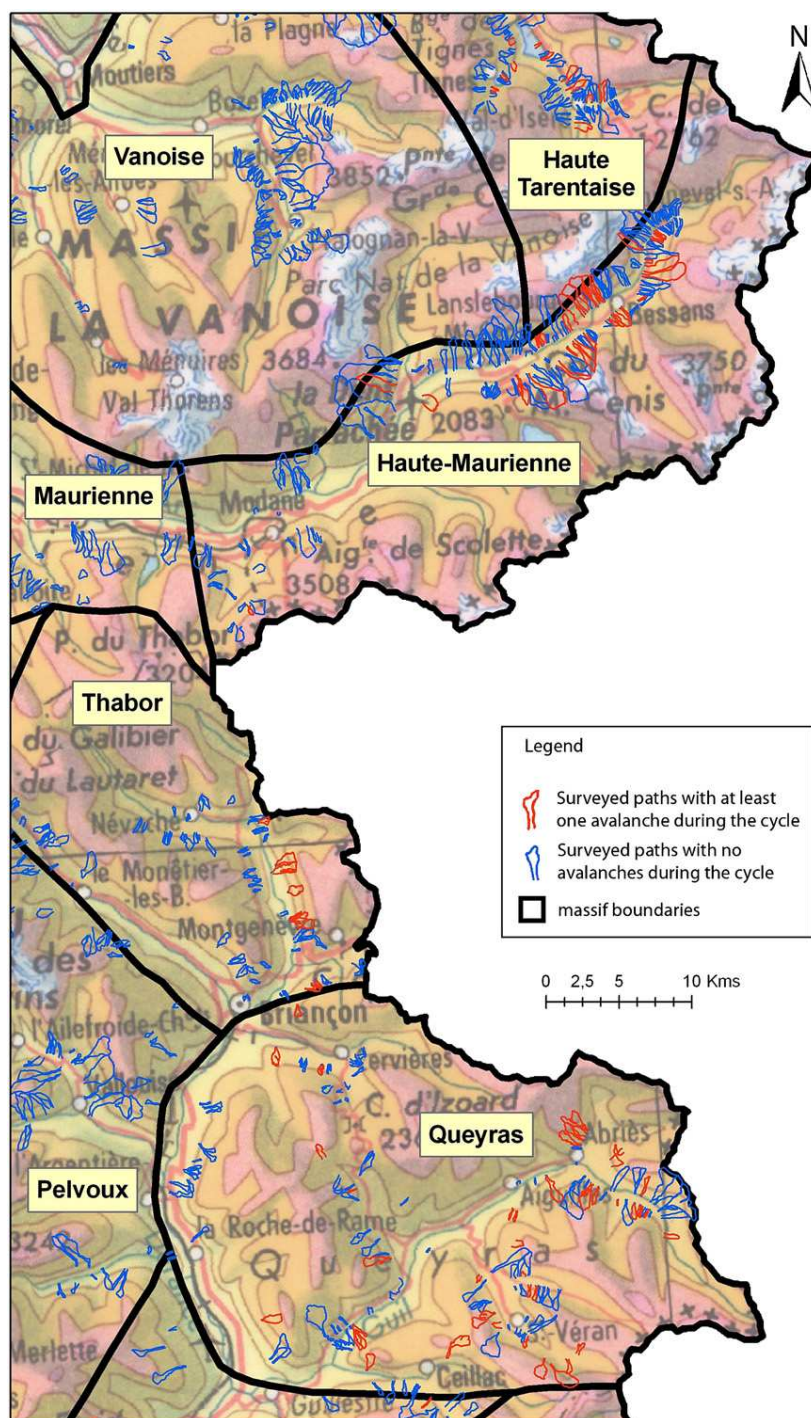


Fig. 14. Activity at the path scale during the cycle.

Furthermore, making them work together somewhat compensates the limitations of each of them: missing values, uncertainties around certain quantitative values..., etc.

An important outcome of this study is that the spatial structure and correlations of avalanche activity with snow and weather data were systematically higher for the relative activity f_i than for the raw number of events n_i . This pleads in favour of the EPA protocol that monitors certain paths as exhaustively as possible rather than as many avalanches as possible on all paths. Sadly, for the historical comparisons, the number of events per path could not be used because the number of paths under survey is too uncertain for older data.

Avalanche activity and the modelled instability index have also been found to be globally consistent. However, the predictive power of the instability index remained limited (relatively high residuals, results not better than with snowfall alone) in the specific cycle studied because of its particularity (predominance of snowfalls as the main explanatory factor, even at low elevations), and the way the study was conducted (without a high spatio-temporal resolution). Even if this study did not aim at assessing the employability of modelled instability index for analysing avalanche cycles, this highlights the interest of including more data and/or recently developed statistical methods in a physically-based forecasting

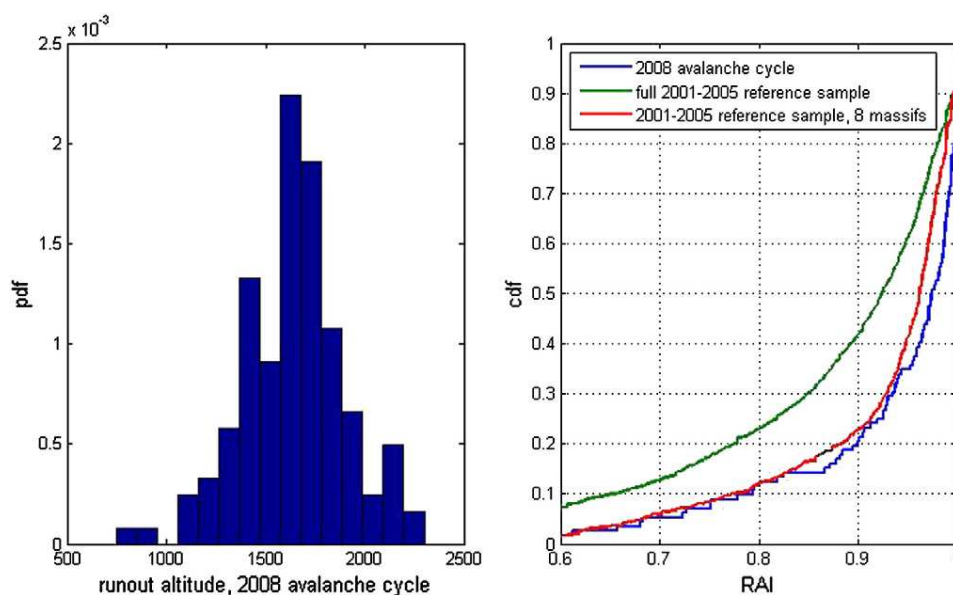


Fig. 15. Runout altitude of the cycle events. Left, distribution of runout altitudes of the 172 events recorded between December 15th and 19th 2008 in the eight massifs where the cycle threshold is exceeded. Right compares the RAI of these events to the RAI of the 2001–2005 comparison sample. The 2008 cycle is statistically different from the full reference sample (Kolmogorv–Smirnov test, p -value $< 10^{-7}$), and from the reference sample in the 8 massifs where the cycle occurred (p -value = 10^{-3}).

procedure such as the SCM model chain employed by Météo-France at the massif scale.

For the historical analysis, rather than focusing only on the traditional 3-day snowfall, we introduced a recent spatial extreme approach to compute spatialised return periods, magnitude–frequency–duration curves, and statistics concerning previous high instability index occurrences. We also proposed using adapted statistical tools to characterise spatial clustering/anti-clustering and quantify spatial gradients of avalanche activity and constraining snow and weather factors. All this is relatively new in the snow and avalanche community. It constitutes an appropriate methodological basis for a deepened analysis of the spatio-

temporal structure of an avalanche cycle with cross-comparison of different data sources which could be put to use for analysing other exceptional episodes.

In further work, other variables, such as avalanche extension at the path scale, orientation of the starting zone of the active paths to better take into account the local wind effects (drifting snow, orographic effects..., etc.) could be considered. Methodological developments remain also necessary in terms of replacing certain empirical approaches that have been used by explicit modelling procedures. For instance, lowering the uncertainty around the return period for the number of avalanche events corresponding to rare avalanche cycles

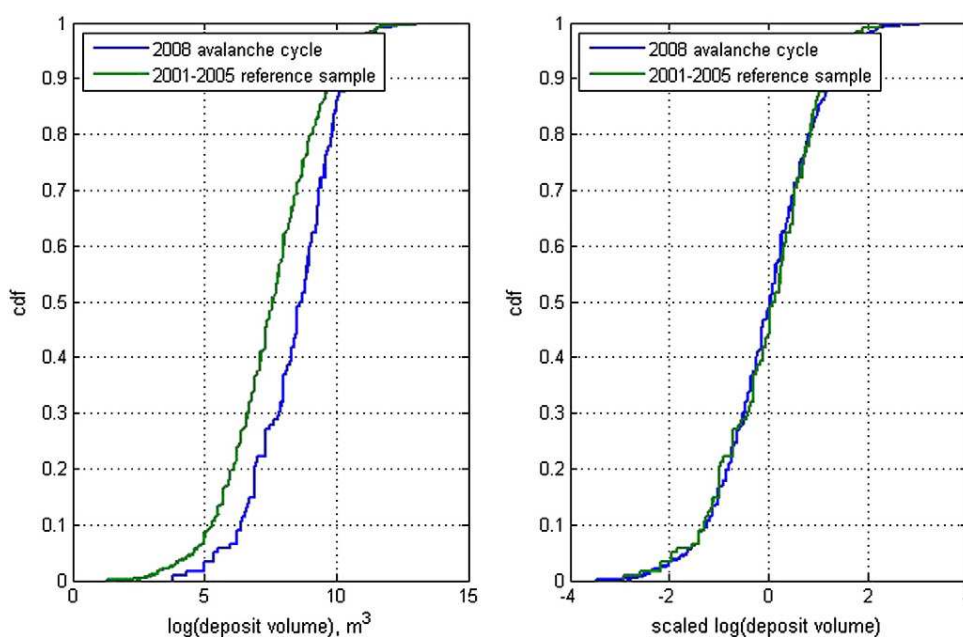


Fig. 16. Deposit volume of the 2008 cycle events versus comparison sample. Left compares the deposit volumes of the 172 events recorded between December 15th and 19th 2008 in the eight massifs where the cycle threshold is exceeded to the deposit volumes of the 2001–2005 comparison sample. The two samples are strongly statistically different (Kolmogorv–Smirnov test, p -value $< 10^{-7}$). Right compares the two scaled samples which are no longer statistically different (p -value = 0.65).

would imply replacing our empirical approach with an extreme value model. This highlights the need for future development of extreme value statistical models adapted to discrete observations, which for the moment do not exist. In the same vein, empirical assessment tools of a spatial structure such as Moran's I could potentially be replaced with explicit spatial models (Banerjee et al., 2003), so as to undertake the analysis within a fully explicit spatio-temporal modelling framework. The underlying assumption of stationarity that was present in all the historical avalanche cycle comparisons that have been provided would then be withdrawn, so as to take into account the growing evidence of changes in avalanche activity over the last several decades and their repercussions on intense avalanche cycles.

Acknowledgements

This work was partially done within the joint Meteo-France–Cemagref ECANA project funded by the French Ministry of the Environment (Risk Division-DGPR). The authors are also grateful to the many people that collected the data during the cycle, to the two anonymous referees for their useful comments that helped improve the paper and to L. Bel for her assistance.

References

- Akaike, H., 1981. Likelihood of a model and information criteria. *Journal of Econometrics* 16, 3–14.
- Ancey, C., Rapin, F., Martin, E., Coleou, C., et al., 2000. L'avalanche de Péclerey du 9 février 1999. *Houille Blanche* 5, 45–53.
- Ancey, C., Gervasoni, C., Meunier, M., 2004. Computing extreme avalanches. *Cold Regions Science and Technology* 39, 161–184.
- Banerjee, S., Carlin, B., Gelfand, A. E. (2003). *Hierarchical Modeling and Analysis for Spatial Data*. Chapman & Hall ed. 472p.
- Bélanger, L., Cassayre, Y., 2004. Projects for past avalanche observation and zoning in France, after 1999 catastrophic avalanches. *Proceedings of the International Snow Survey Workshop*, 19–24 September 2004. Jackson Hole, Wyoming, pp. 416–422.
- Birkeland, K.W., Mock, C.J., Shinker, J.J., 2001. Avalanche extremes and atmospheric circulation patterns. *Annals of Glaciology* 32, 135–140.
- Birkeland, K.W., Mock, C.J., 2001. The major snow avalanche cycle of February 1986 in the western United States. *Natural Hazards* 24, 75–95.
- Bocchiola, D., Medagliani, M., Rosso, R., 2006. Regional snow depth frequency curves for avalanche hazard mapping in central Italian Alps. *Cold Regions Science and Technology* 46 (3), 204–222.
- Cliff, A.D., Ord, J.K. (1981). *Spatial processes: models and applications*. Taylor & Francis ed. 266p.
- Coles, S. (2001). *An introduction to statistical modelling of extreme values*. Springer ed. 208p.
- Courtier, P., Freydl, C., Geleyn, J.F., Rabier, F., Rochas, M., 1991. The ARPEGE project at Météo-France. *Proc. Seminar on Numerical Methods in Atmospheric Models*, Vol. 2, Reading, ENMWF, United Kingdom, pp. 191–212.
- Cressie, N. (1993). *Statistics for spatial data*. Wiley ed. 928p.
- Durand, Y., Giraud, G., Brun, E., Merindol, L., Martin, E., 1999. A computer based system simulating snowpack structures as a tool for regional avalanche forecasting. *Journal of Glaciology* 45 (151), 469–484.
- Durand, Y., Laternser, M., Giraud, G., Etchevers, P., Lesaffre, L., Méridol, L., 2009a. Reanalysis of 44 year of climate in the French Alps (1958–2002): methodology, model validation, climatology, and trends for air temperature and precipitation. *Journal of Applied Meteorology and Climatology* 48 (3), 429–449.
- Durand, Y., Laternser, M., Giraud, G., Etchevers, P., Méridol, L., Lesaffre, B., 2009b. Reanalysis of 47 years of climate in the French Alps (1958–2005): climatology and trends for snow cover. *Journal of Applied Meteorology and Climatology* 48 (12), 2487–2512.
- Eckert, N., Parent, E., Richard, D., 2007a. Revisiting statistical–topographical methods for avalanche predetermination: Bayesian modelling for runout distance predictive distribution. *Cold Regions Science and Technology* 49, 88–107.
- Eckert, N., Parent, E., Bélanger, L., et al., 2007b. Hierarchical modelling for spatial analysis of the number of avalanche occurrences at the scale of the township. *Cold Regions Science and Technology* 50, 97–112.
- Eckert, N., Parent, E., Naaim, M., Richard, D., 2008a. Bayesian stochastic modelling for avalanche predetermination: from a general system framework to return period computations. *Stochastic Environmental Research and Risk Assessment* 22, 185–206.
- Eckert, N., Parent, E., Faug, T., Naaim, M., 2008b. Optimal design under uncertainty of a passive defense structure against snow avalanches: from a general Bayesian framework to a simple analytical model. *Natural Hazards and Earth System Sciences* 8, 1067–1081.
- Eckert, N., Parent, E., Faug, T., Naaim, M., 2009. Bayesian optimal design of an avalanche dam using a multivariate numerical avalanche model. *Stochastic Environmental Research and Risk Assessment* 23, 1123–1141.
- Eckert, N., Parent, E., Kies, R., Baya, H., 2010a. A spatio-temporal modelling framework for assessing the fluctuations of avalanche occurrence resulting from climate change: application to 60 years of data in the northern French Alps. *Climatic Change* 101 (3), 515–553.
- Eckert, N., Baya, H., Deschâtres, M., 2010b. Assessing the response of snow avalanche runout altitudes to climate fluctuations using hierarchical modelling: application to 61 winters of data in France. *Journal of Climate* 23, 3157–3180.
- ECMWF, 2004. ERA-40: 45 years reanalysis of the global atmosphere and surface conditions 1957–2002. In: Uppala, S., et al. (Ed.), *ECMWF Newsletter*, N°101, ENMWF, Reading, United Kingdom, pp. 2–21.
- Gassner, M., Bräber, B., 2002. Nearest neighbour models for local and regional avalanche forecasting. *Natural Hazards and Earth System Sciences* 2, 247–253.
- Gaucher, R., Pasquier, X., Bonnefoy, M., Escande, S., Eckert, N., Deschâtres, M., 2009. Quelques exemples d'avalanches exceptionnelles. Neiges et avalanches 126, 10–14.
- Höllner, P., 2009. Avalanche cycles in Austria: an analysis of the major events in the last 50 years. *Natural Hazards* 48 (N° 3), 399–424.
- Jamard, A.L., Garcia, S., Bélanger, L., 2002. L'enquête permanente sur les Avalanches (EPA). *Statistique descriptive générale des événements et des sites*. DESS Ingénierie Mathématique option Statistique. Université Joseph Fourier, Grenoble, France (Available online at <http://www.avalanches.fr/>. 101 p).
- Jomelli, V., Delval, C., Grancher, D., et al., 2007. Probabilistic analysis of recent snow avalanche activity and climate in the French Alps. *Cold Regions Science and Technology* 47, 180–192.
- Katz, R.W., Parlange, M.B., Naveau, P., 2002. Statistics of extremes in hydrology. *Advances in Water Resources* 25, 1287–1304.
- Lang, M., Ouada, T.B.M.J., Bobée, B., 1999. Towards operational guidelines for over-threshold modelling. *Journal of Hydrology* 225 (3–4), 103–117.
- Laternser, M., Schneebeli, M., 2002. Temporal trend and spatial distribution of avalanche activity during the last 50 years in Switzerland. *Natural Hazards* 27, 201–230.
- McClung, D., Lied, K., 1987. Statistical and geometrical definition of snow-avalanche runout. *Cold Regions Science and Technology* 13, 107–119.
- McClung, D., 2003. Size scaling for dry snow slab release. *Journal of Geophysical Research* 108 (B10), 2465. doi:10.1029/2002JB002298.
- Maggioli, M., Caimi, A., Godone, D., Freppaz, M., et al., 2009. The avalanche events of December 2008 in Ceresole Reale (Piedmont Western Italian Alps). *Proceedings of the International Snow Science Workshop*, Davos, Switzerland, 27 Septembre–2 October 2009, pp. 25–29.
- Martin, E., Giraud, G., Lejeune, Y., Boudart, G., 2001. Impact of climate change on avalanche hazard. *Annals of Glaciology* 32, 163–167.
- Meunier, M., Ancey, C., 2004. Towards a conceptual approach to predetermining high-return-period avalanche run-out distances. *Journal of Glaciology* 50–169, 268–278.
- Mougin, P., 1922. *Les avalanches en Savoie*. Ministère de l'Agriculture, Direction Générale des Eaux et Forêts, Service des Grandes Forces Hydrauliques, Paris, pp. 175–317.
- Naaim, M., Naaim-Bouvet, F., Faug, T., Bouchet, A., 2004. Dense snow avalanche modelling: flow, erosion, deposition and obstacle effects. *Cold Regions Science and Technology* 39, 193–204.
- Padoan, S.A., Ribatet, M., Sisson, S.A., 2010. Likelihood-based inference for max-stable processes. *Journal of the American Statistical Society* 105 (489), 263–277.
- Parent, E., Bernier, J., 2003. Bayesian P.O.T. modelling for historical data. *Journal of Hydrology* 274, 95–108.
- Salm, B., Burkard, A., Gubler, H.U., 1990. Calcul des avalanches: une méthode pour le praticien avec des exemples. *Communication de l'institut fédéral suisse pour l'étude de la neige et des avalanches*, C. Ancey traducteur.
- Schlather, M., 2002. Models for stationary max-stable random fields. *Extremes* 5, 33–44.
- Schweizer, J., Stoffel, L., Mitterer, C., 2009. On forecasting large and infrequent snow avalanches. *Cold Regions Science and Technology* 59 (2–3), 234–241.
- SLF Davos, 2000. *Der Lawinenwinter 1999*. Ereignisanalyse (588 p).
- Smith, R. L. (1990). Max-stable processes and spatial extremes. Unpublished manuscript. 32p. Available online at <http://www.stat.unc.edu/postscript/rs/spatex.pdf>.

Appendix C

Quasistatic to inertial transition in granular materials and the role of fluctuations

This appendix is composed of an article entitled “Quasistatic to inertial transition in granular materials and the role of fluctuations”. It was **published** in *Physical Review E* in 2011 with Guillaume Chambon and Mohamed Naaim.

This article was written during the thesis, although focused on the subject of my master thesis. It consists in the numerical modeling of discrete elements in a Couette cell, in order to characterize the rheology of granular materials in quasistatic and inertial regimes. The transition between these two regimes is deeply discussed and a new constitutive law valid in both regimes is proposed. This constitutive law involves the friction coefficient (normalized shear stress), the inertial number (normalized shear strain rate) and normalized velocity fluctuations.

Quasistatic to inertial transition in granular materials and the role of fluctuations

Johan Gaume, Guillaume Chambon,* and Mohamed Naaim

Cemagref, UR ETGR, 2 rue de la Papeterie, FR-38402 St. Martin d'Hères Cedex, France

(Received 16 July 2010; revised manuscript received 30 September 2011; published xxxxx)

On the basis of discrete element numerical simulations of a Couette cell, we revisit the rheology of granular materials in the quasistatic and inertial regimes, and discuss the origin of the transition between these two regimes. We show that quasistatic zones are the seat of a creep process whose rate is directly related to the existence and magnitude of velocity fluctuations. The mechanical behavior in the quasistatic regime is characterized by a three-variable constitutive law relating the friction coefficient (normalized stress), the inertial number (normalized shear rate), and the normalized velocity fluctuations. Importantly, this constitutive law appears to remain also valid in the inertial regime, where it can account for the one-to-one relationship observed between the friction coefficient and the inertial number. The abrupt transition between the quasistatic and inertial regimes is then related to the mode of production of the fluctuations within the material, from nonlocal and artificially sustained by the boundary conditions in the quasistatic regime, to purely local and self-sustained in the inertial regime. This quasistatic-to-inertial transition occurs at a critical inertial number or, equivalently, at a critical level of fluctuations.

DOI: [10.1103/PhysRevE.00.001300](https://doi.org/10.1103/PhysRevE.00.001300)

PACS number(s): 83.80.Fg, 47.57.Gc

I. INTRODUCTION

One of the most fascinating properties of granular materials is their ability to either sustain stresses as solids, or to flow as fluids, depending on the applied solicitation. It has been shown in several studies [1–3] that, at any given point within the material, this solid-to-fluid transition is primarily controlled by the local value of the inertial number $I = \dot{\gamma}d(\rho/P)^{0.5}$. This number represents the ratio between a microscopic inertial timescale $d(\rho/P)^{0.5}$ (P being the pressure, d the grain diameter, and ρ the grain density) and the macroscopic time scale $\dot{\gamma}^{-1}$ associated with the shear rate $\dot{\gamma}$. Fluidlike behavior is obtained for large enough values of I and corresponds to the so-called inertial regime. In this regime, the constitutive law of the material is characterized by a one-to-one relationship, of the viscoplastic type, between the friction coefficient $\mu = \tau/P$ and the inertial number I [4,5]. For low values of I , on the contrary, the $\mu(I)$ relationship loses its validity and solidlike behavior is recovered. In this so-called quasistatic regime, and in agreement with the plastic constitutive laws classically used in soil mechanics for $I \rightarrow 0$ [6], the mechanical behavior is generally described as becoming rate independent and characterized by a constant friction coefficient μ_s (critical state theory).

The transition between the inertial and quasistatic regimes typically occurs for values of I in the range 10^{-3} – 10^{-2} . In detail, however, the reported I value at the transition appears to vary between existing studies, and possibly depends on system size [1,2]. Furthermore, from these studies, it is still not clear whether this transition occurs sharply at a given value of I , or progressively as $I \rightarrow 0$. More generally, the real nature of the quasistatic-to-inertial transition in granular materials, and the physical processes involved, still remain largely unknown. Recently, the mechanical behavior in the quasistatic regime has been shown to be significantly more complex than described by classical soil mechanics. In particular, continuous

creep in quasistatic zones, incompatible with a supposedly rate-independent mechanical behavior, has been reported in several configurations (such as free-surface flows and Couette cells) [3,7,8]. Several studies have also evidenced the existence, in the quasistatic regime, of strong and intermittent fluctuations characterized by collective particle motions with large correlation lengths (nonlocal processes) [9–13]. Yet, and although it is reasonable to think these fluctuations may play an important role in the macroscopic rheology of the material [12,14,15], the link between fluctuations and creep has never been formally proved. Similarly, although the existence of creep in the quasistatic regime could lead one to think that the transition toward the “true” solid behavior is in fact progressive, this issue, as well as the potential connection between the quasistatic creep and the viscoplastic rheology in the inertial regime, remains to be properly addressed.

The objective of this paper is precisely to explore the links between creep, fluctuations, and viscoplastic rheology in order to propose a more consistent description of the quasistatic-to-inertial transition in granular materials. We will prove that the creep is effectively related to the existence of fluctuations within the sample, and that a three-variable constitutive law between shear rate, friction coefficient, and fluctuation level can be formulated in the quasistatic regime. In addition, we will show that this constitutive law remains valid in the inertial regime, where it can account with good accuracy for the viscoplastic behavior observed, thus opening the way toward a unified treatment of both quasistatic and inertial regimes.

Our work is based on numerical simulations using the discrete element method (DEM) [16]. This method allows us to perform veritable numerical experiments on granular materials. The configuration simulated is a Couette cell (or annular shear cell), which presents the specificity of placing locally the tested sample in a state of simple shear, but with a shear stress $\sigma_{r\theta}$ that decreases from the inner wall to the outer sample boundary according to $\sigma_{r\theta}(r) = \sigma_{r\theta}(R_i) R_i^2/r^2$ (where R_i is the inner cylinder radius and r the radial position of the point considered) [3,10,15,17–19]. This setting is thus

*guillaume.chambon@cemagref.fr

JOHAN GAUME, GUILLAUME CHAMBON, AND MOHAMED NAAIM

PHYSICAL REVIEW E **00**, 001300 (2011)

particularly well suited to studying the quasistatic-to-inertial transition, since coexistence between quasistatic and inertial zones can be observed within the same sample. It is important to mention that our simulations are very similar to those reported in [3]. This latter study actually presents a complete overview of the mechanical response of a granular sample placed in a Couette cell, which we shall obviously not reproduce here. In the present paper, we take one step forward and, building from the results of [3], our analysis of the simulation data is specifically focused on insights concerning sample rheology and the quasistatic-to-inertial transition.

This paper is organized as follows. Section II presents the simulated system and defines the mechanical quantities considered. In Sec. III, after having evidenced the existence of the quasistatic-to-inertial transition, we revisit the rheological properties of the inertial regime and propose a new approach to the rheology of the quasistatic regime. In Sec. IV, an empirical three-variable constitutive law valid in both the quasistatic and the inertial regimes is derived. Lastly, conclusions regarding the physical nature of these two regimes and of the transition between them are discussed in Sec. V.

II. SIMULATED SYSTEM

The discrete element simulations were performed using the commercial software PFC2D (by Itasca) which implements the original soft-contact algorithm described in [20]. The simulated Couette cell is two dimensional (Fig. 1), with inner and outer cylinder radii $R_i = 0.4$ m and $R_e = 0.6$ m. The granular samples are composed of about 7000 circular particles of average diameter $d = 4.7$ mm [thus $(R_e - R_i)/d \approx 43$], with a grain size distribution polydispersity of $\pm 30\%$ (diameters ranging from 3 to 6 mm) in order to prevent crystallization. Shear is applied by rotation of the inner cylinder at an imposed rotation velocity Ω which was varied between 0.05 and 20 rad s^{-1} . The outer cylinder is fixed, but consists of a flexible membrane through which a constant radial pressure $P = 10$ kPa is imposed onto the sample. This setting is preferable to a rigid wall, in order to accommodate the density variations undergone by the granular material during shear.

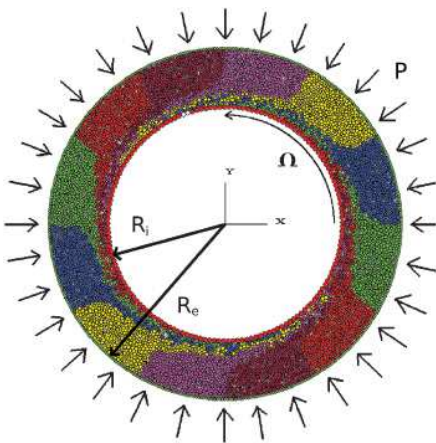


FIG. 1. (Color online) Simulated shear cell. Zones of different colors within the sample illustrate the shear deformation.

TABLE I. Mechanical parameters used in the simulations. k_n : normal contact stiffness; k_t : tangential contact stiffness; μ_g : intergranular friction; e : normal restitution coefficient; ρ : particle density.

k_n/P	k_t/k_n	μ_g	e	ρ
10^4	0.5	0.5	0.1, 0.9	300 kg m^{-3}

Both boundaries are constituted by grains of diameter d to represent wall roughness.

The interparticle contact laws used in the simulations are classical [16]. The normal force is the sum of a linear-elastic and of a viscous contribution (spring-dashpot model), and the tangential force is linear-elastic with a Coulombian friction threshold. The corresponding mechanical parameters are summarized in Table I. Let us mention that the value of the normal stiffness k_n was chosen in order to keep low normal interpenetrations δ at contacts, $\delta/d \ll 10^{-3}$, i.e., to work in the quasirigid grain limit [2,6]. Concerning the normal restitution coefficient e , we checked that the results presented below, and more generally all the macroscopic mechanical quantities obtained from the simulations, are actually independent of this parameter (in the range 0.1–0.9), in agreement with previous studies [2].

One of the main interests of DEM simulations is that mechanical quantities such as stresses, shear rates, etc., can be computed at each material point within the sample. Hence, the rheological behavior of the material can be explored locally, regardless of the spatial heterogeneities possibly displayed by these mechanical quantities. In our case, the shear rate $\dot{\gamma}$ is obtained from the orthonormal velocity profile $v(r)$ according to $\dot{\gamma} = r[d(v/r)/dr]$. The stress tensor is derived using the classical Love homogenization formula [21]. In the following, only mechanical responses obtained in steady state will be considered, disregarding the transients that occur

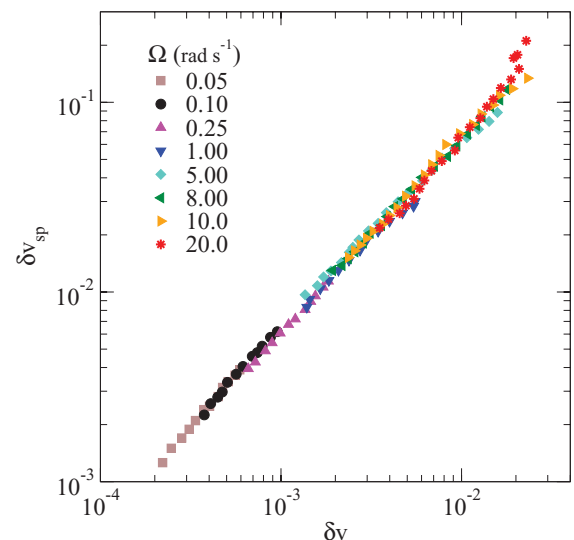


FIG. 2. (Color online) Correlation between the spatiotemporal velocity fluctuations δv_{sp} and the temporal velocity fluctuations δv in the simulated samples. The different symbols refer to the imposed values of inner cylinder rotation velocity Ω .

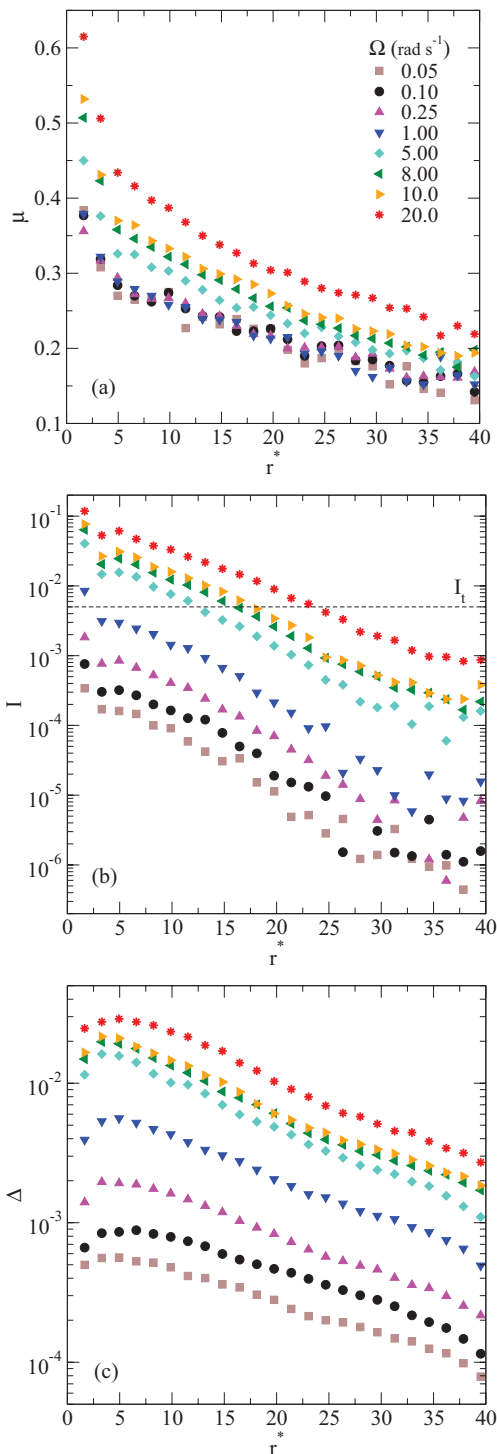


FIG. 3. (Color online) Radial profiles of (a) friction coefficient μ , (b) inertial number I , and (c) fluctuation number Δ for the different imposed values of inner cylinder rotation velocity Ω . The profiles are plotted as a function of the reduced radius $r^* = (r - R_i)/d$.

at the initiation of shear. Acknowledging this steady-state condition and the cylindrical symmetry of the system, all the mechanical quantities computed are subjected to a double, spatiotemporal averaging procedure $\langle \cdot \rangle_{\theta,t}$ over annuli having a

thickness of $1.6d$ and over time windows that are sufficiently long to integrate both individual and correlated particle motions.

In addition to average quantities, we will also consider the orthoradial velocity fluctuations $\delta v = (\langle \langle v \rangle_{\theta}^2 \rangle_t - \langle v \rangle_{\theta,t}^2)^{1/2}$. Note that defined as such, the quantity δv only accounts for the temporal fluctuations of the spatially averaged velocity $\langle v \rangle_{\theta}$. We chose this fluctuation measure by analogy with the common practice in fluid turbulence. In addition, as shown in Fig. 2, we observed that the spatiotemporal velocity fluctuations defined as $\delta v_{sp} = (\langle v^2 \rangle_{\theta,t} - \langle v \rangle_{\theta,t}^2)^{1/2}$ appear strongly correlated to the temporal fluctuations δv in our system. Hence, and although this result would deserve further discussion beyond the scope of this paper, we argue that the quantity δv can actually be considered as a good proxy for all types of fluctuations within our samples.

Compared to the simulations described in [3], the only notable specificity of our study lies in the consideration of complete annular samples, instead of orthoradial periodic boundary conditions. As a validation of our work, we checked that the global response of the samples observed in our simulations, such as the evolutions with r and Ω of the velocity, density, and stresses, fully agrees with the results presented in [3]. As already mentioned, the reader is thus referred to this previous study to get an overall view of the mechanical behavior of a granular sample in a Couette cell. In what follows, we only focus on the variables relevant to describing the macroscopic rheology of the granular material, namely, the inertial number I (dimensionless shear rate), the friction coefficient μ (dimensionless shear stress), and a dimensionless measure of the velocity fluctuations Δ defined as $\Delta = \delta v (\rho/P)^{0.5}$.

The radial profiles within the sheared samples of the quantities I , μ , and Δ are shown in Fig. 3. The observed decrease of the friction coefficient μ with r is fully explainable by the geometrical heterogeneity of the shear stress inside the Couette cell: $\mu \propto (r/R_i)^{-2}$ (the pressure being constant in the sample; see [3]). In parallel, both the inertial number I and the velocity fluctuations Δ also decrease with r . These two quantities display roughly exponential trends, with characteristic lengths that remain quasiconstant for all tested values of the rotation velocity Ω . (In detail, however, the localization width, i.e., the characteristic length associated with the exponential decrease of I , may show a slight increase with Ω ; see [3].)

III. GRANULAR RHEOLOGY

A. A marked quasistatic-to-inertial transition

The mechanical behavior of the tested material is highlighted when representing directly the friction coefficient μ or the fluctuation number Δ as a function of the inertial number I for all locations within the sample and all rotation velocities Ω (Fig. 4). As already noted in [3], the plot of μ versus I [Fig. 4(a)] clearly evinces the existence of a marked rheological transition at a given value of I , $I_t \approx 5 \times 10^{-3}$ in our case. For $I > I_t$, all the obtained data points collapse on a master curve and, therefore, define a single $\mu(I)$ relationship regardless of the values of rotation velocity Ω and radius r . For $I < I_t$, on the contrary, there appears to be no one-to-one relationship

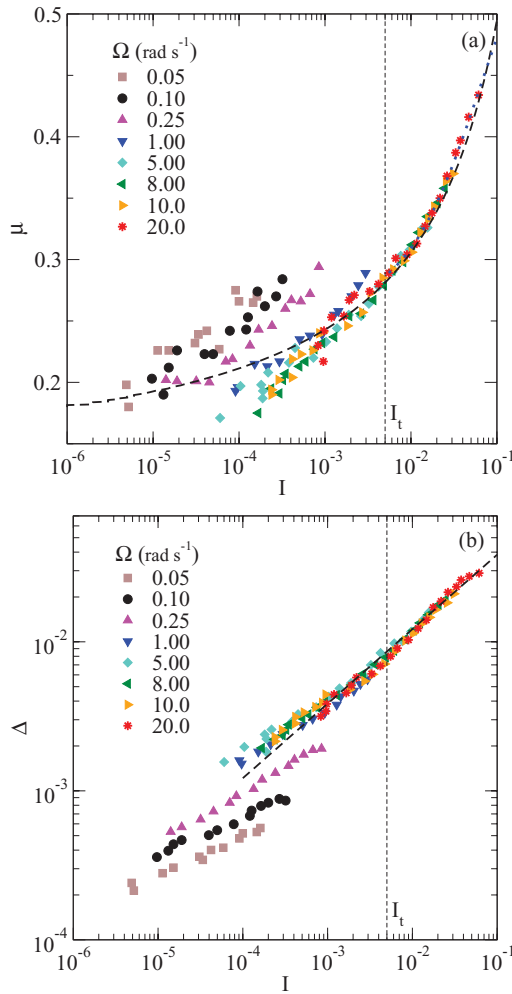


FIG. 4. (Color online) (a) Friction coefficient μ as a function of inertial number I . The different symbols refer to the imposed values of inner cylinder rotation velocity Ω . The blue dotted curve represents Eq. (1), while the black dashed one corresponds to Eq. (6). (b) Fluctuation number Δ as a function of inertial number I . The dashed line represents Eq. (2).

between μ and I . Interestingly, this transition at $I = I_t$ is also clearly visible on the evolution of the fluctuation number Δ with I [Fig. 4(b)]. Similarly, a one-to-one relationship $\Delta(I)$ is obtained for $I > I_t$, while no such relationship exists for $I < I_t$.

Following [3], we identify this transition observed at $I = I_t$ with the quasistatic-to-inertial transition. The data points corresponding to the inertial ($I > I_t$) and to the quasistatic ($I < I_t$) regime will now be examined independently, in order to exhibit the rheological properties of each of these regimes. Let us recall that due to the decrease of the inertial number I with r , zones lying in the inertial and in the quasistatic regime may simultaneously coexist within our samples. In what follows, these cases of coexistence between inertial and quasistatic zones will prove to be particularly informative in terms of rheological behavior. In detail, Fig. 3(b) shows that such a coexistence is actually observed only above a particular value of the rotation velocity, $\Omega_t \approx 1$ rad s⁻¹. For $\Omega > \Omega_t$,

$I > I_t$ at the sample's inner boundary and an inertial zone thus develops around the inner cylinder, surrounded by a quasistatic zone outside. The thickness of the inertial zone progressively decreases with Ω , and vanishes at Ω_t . For $\Omega < \Omega_t$, the whole sample lies in the quasistatic regime. Note that a quasistatic zone, either alone or in coexistence with an inertial zone, was always present in all our simulations.

B. Inertial regime

The rheological behavior observed for $I > I_t$ is fully consistent with the results obtained in previous studies dedicated to the inertial regime of granular materials [1,2]. In particular, the $\mu(I)$ relationship in Fig. 4(a) can be well fitted by the empirical expression proposed in [4]:

$$\mu = \mu_s + \frac{\mu_l - \mu_s}{I_0/I + 1}, \quad (1)$$

with parameters on the same order as those obtained from experimental data ($\mu_s = 0.26$, $\mu_l = 0.62$, $I_0 = 0.07$). Note that a simpler, alternative expression to describe this $\mu(I)$ relationship will be proposed hereinafter. Independent of the particular fitting law used, the existence of such a one-to-one relationship between the friction coefficient μ and the inertial number I indicates that the inertial regime is characterized by a rate-dependent rheological behavior similar to that of a complex fluid. As a macroscopic signature of this rate-dependent behavior, Fig. 3(a) shows that as soon an inertial zone exists around the inner cylinder, the friction coefficient profile in the sample (and thus the global torque on the inner cylinder) increases with the rotation velocity Ω .

In parallel, and also in good agreement with previous studies [1,2], the relationship between the fluctuation and inertial numbers Δ and I observed for $I > I_t$ is well fitted by a power law with an exponent of 0.5 [Fig. 4(b)]:

$$\Delta = C_I I^{1/2}, \quad (2)$$

where $C_I \approx 0.12$. The existence of this one-to-one relationship $\Delta(I)$ can be interpreted as the fluctuations being created locally by the granular agitation resulting from the shear rate [2,15]. Actually, as will be discussed later, we propose that it is precisely this property of locality for the fluctuations that constitutes the ‘‘intrinsic’’ definition of the inertial regime.

C. Quasistatic regime

In contrast to the inertial regime, the quasistatic regime is characterized by the absence of one-to-one relationships between μ and I and between Δ and I . We also observe in Fig. 3(a) that the friction coefficient radial profiles are independent of the rotation velocity Ω for $\Omega < \Omega_t$, i.e., when the whole sample lies in the quasistatic regime. Nevertheless, these properties do not imply that the mechanical behavior in this regime is rate independent, as would be predicted by classical soil mechanics constitutive laws. First, Fig. 3(b) clearly shows that significant deformation rates exist within the quasistatic zones, both for $\Omega > \Omega_t$ and for $\Omega < \Omega_t$. When coexistence between inertial and quasistatic zones occurs (for $\Omega > \Omega_t$), the radial profiles of I are actually completely continuous across the two zones. Hence, as already noted in [3], the quasistatic zones in the Couette cell appear to undergo a continuous creep

which is incompatible with a rate-independent mechanical behavior. (With a rate-independent behavior, we would rather expect the material to remain immobile in the quasistatic zones, except in particular localization layers concentrating all the deformation [19].)

Second, even if there is no unique relationship between μ and I for $I < I_t$, these two variables do nevertheless show clear correlations [Fig. 4(a)]. In particular, all data points obtained in quasistatic zones that coexist with an inertial zone (case $\Omega > \Omega_t$) appear to collapse on a master curve which smoothly connects with the $\mu(I)$ relationship obtained for $I > I_t$. For $\Omega < \Omega_t$, the data points follow distinct paths in the μ - I space according to the value of Ω , but all these paths remain globally parallel to the master curve just described for $\Omega > \Omega_t$. Similar correlations are observed between Δ and I in Fig. 4(b). In fact, the evolution of the fluctuation number Δ with I in the quasistatic regime strongly resembles that of the friction coefficient μ . Data points corresponding to $\Omega > \Omega_t$ collapse on a master curve, while data points obtained for $\Omega < \Omega_t$ follow distinct but approximately parallel paths.

These correlations and the similarity between the evolutions of μ and Δ with I suggest the existence, in the quasistatic regime, of a unique relationship between these three quantities. To check this hypothesis, the three variables are represented in a three-dimensional (3D) plot in Fig. 5. Although not clearly evident on a planar representation, we observe that all the data points obtained in the quasistatic regime effectively appear to define a single surface in this plot. More quantitatively, a principal component analysis of the data set made of the triplets $[\log_{10}(I), \log_{10}(\Delta), \mu]$ has been performed. It shows that more than 99.9% of the data dispersion is explained by the two largest eigenvalues of the correlation matrix (Fig. 5). This constitutes a formal proof that the three variables are effectively linked by a unique relationship.

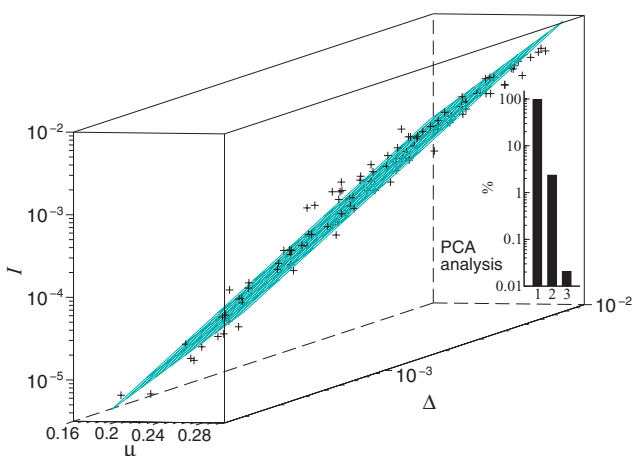


FIG. 5. (Color online) 3D plot representing the triplets constituted by the values of inertial number I (\log_{10} scale), fluctuation number Δ (\log_{10} scale), and friction coefficient μ obtained in the quasistatic regime ($I < I_t$). The histogram represents the three eigenvalues of the data-set correlation matrix inferred through principal value analysis (PCA). The surface plotted as an eyeguide corresponds to the plane defined by the two largest eigenvalues of the PCA.

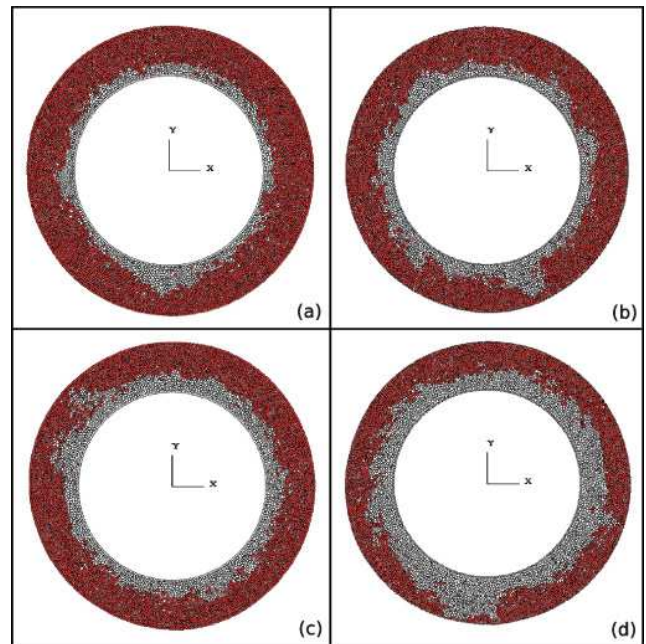


FIG. 6. (Color online) Instantaneous snapshots of particle velocities in the simulated Couette cell. White (light) particles are characterized by a velocity that exceeds a fixed threshold (0.4 m s^{-1} in this example), whereas red (dark) particles have a velocity below this threshold. (a) $\Omega = 5$, (b) $\Omega = 8$, (c) $\Omega = 10$, and (d) $\Omega = 20 \text{ rad s}^{-1}$.

Hence, in spite of the absence of one-to-one relationships between μ and I and Δ and I in the quasistatic regime, these quantities are nevertheless strongly correlated through a three-variable relationship of the form $I = f(\mu, \Delta)$. Since it only involves local variables, this relationship, for which we shall propose an empirical expression in what follows, can be viewed as a local constitutive law characteristic of the quasistatic regime. Note, however, that the existence of this law does not imply that the rheology of the material is local. Indeed, and unlike in the inertial regime, the fluctuations in the quasistatic regime appear to be essentially produced by nonlocal processes. Qualitative observation of the particle velocities shows that fluctuations tend to organize into short-lived “bursts” that emerge at the boundary of the quasistatic zone (either at the inner cylinder or at the interface with the inertial zone) and then “propagate” into the material (Fig. 6). We also remark that when the fluctuation level at the boundary of a quasistatic zone is fixed, i.e., when the quasistatic zone coexists with an inertial zone, then the complete radial profile of the fluctuations inside this quasistatic zone is also fixed (cf. the collapse of the data points corresponding to $\Omega > \Omega_t$ in Fig. 4(b)). These observations indicate that fluctuations in the quasistatic regime are in fact essentially sustained by the boundary conditions applied at the periphery of the quasistatic zones.

IV. EMPIRICAL CONSTITUTIVE RELATIONS

A. Derivation of a three-variable relationship

From the principal component analysis presented above, it can be deduced that a linear function in terms of the

JOHAN GAUME, GUILLAUME CHAMBON, AND MOHAMED NAAIM

PHYSICAL REVIEW E **00**, 001300 (2011)

variables $\log_{10}(I)$, $\log_{10}(\Delta)$, and μ would constitute a good approximation for the three-variable constitutive relationship characterizing the quasistatic regime (at least for the values of I , μ , and Δ covered in our simulations). However, an even better empirical expression for this relationship can be derived by analyzing the dependence between I and Δ at constant values of μ . Such an analysis is possible for $\Omega < \Omega_t$, i.e., when the whole sample lies in the quasistatic regime, owing to the fact that the friction coefficient μ is independent of Ω in this case. Therefore, studying the dependence between I and Δ for data determined at constant values of radius r is equivalent to considering constant values of μ .

Figure 7(a) shows that for each value of friction coefficient μ , the evolution of the fluctuation number Δ as a function of the inertial number I approximately follows a power-law of the form

$$\Delta = C_{QS} I^{\beta(\mu)}, \quad (3)$$

with a prefactor $C_{QS} \approx 0.59$ independent of μ , and an exponent β increasing with μ . Furthermore, the dependence of this exponent β with μ appears to be essentially linear [Fig. 7(b)]:

$$\beta(\mu) = \beta_0 + \beta_1 \mu, \quad (4)$$

with $\beta_0 \approx 0.29$ and $\beta_1 \approx 1.80$. Quantitatively, in terms of least-squares error, these empirical expressions (3) and (4) provide a fit to the surface defined by the quasistatic data points in Fig. 5 which is 20% better than the fit obtained with the linear relationship derived from principal component analysis.

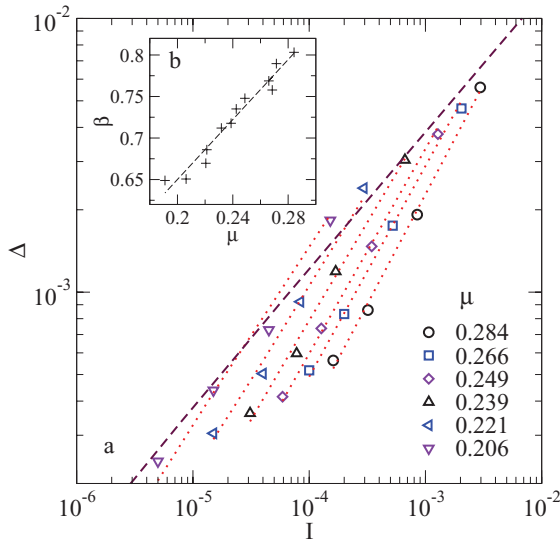


FIG. 7. (Color online) (a) Fluctuation number Δ as a function of inertial number I at fixed values of friction coefficient μ (see legend). The represented data come from simulations in which the whole sample lies in the quasistatic regime ($\Omega < \Omega_t$). Dotted lines correspond to the best power law fits Eq. (3) obtained for each value of μ . The dashed line represents the extrapolation of the relationship between Δ and I established in inertial regime Eq. (2). (b) Evolution of power-law exponent β with friction coefficient μ . The dashed line represents the best linear fit Eq. (4).

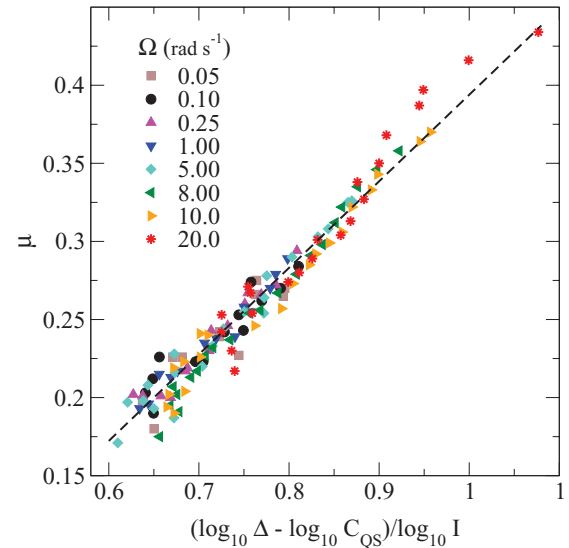


FIG. 8. (Color online) Friction coefficient μ as a function of the composite variable $(\log_{10} \Delta - \log_{10} C_{QS}) / \log_{10} I$. All data points determined from the simulations are represented, the different symbols referring to the values of imposed rotation velocity Ω . The dashed line represents the prediction of Eq. (5).

Equations (3) and (4) can be rewritten in a more compact form as

$$\mu = \frac{1}{\beta_1} \left(\frac{\log_{10} \Delta - \log_{10} C_{QS}}{\log_{10} I} - \beta_0 \right). \quad (5)$$

As a further validation of this expression, Fig. 8 shows that all data points determined in the quasistatic regime, including those corresponding to $\Omega > \Omega_t$ which were not taken into account in the establishment of Eqs. (3) and (4), effectively collapse on a single master curve when plotted in terms of μ versus $(\log_{10} \Delta - \log_{10} C_{QS}) / \log_{10} I$. Hence, we argue that Eq. (5), or equivalently Eqs. (3) and (4), can be regarded as good approximations of the three-variable constitutive relationship characterizing the quasistatic regime. We emphasize, however, that these equations are purely empirical at this stage, and that we cannot rule out the possible existence of alternative expressions that would produce an even better fit to the data.

B. Extrapolation to the inertial regime

An important point not mentioned above is that Fig. 8 also includes the data determined in the inertial regime. Interestingly, these data appear to collapse on the same master curve as those corresponding to the quasistatic regime. This unexpected result seems to indicate that Eq. (5), established in the quasistatic regime, would also remain valid in the inertial regime. To check this prediction, Eq. (5) can be combined with Eq. (2) relating Δ and I in the inertial regime, to yield the following relationship between the variables μ and I alone:

$$\mu = \mu_0 - \frac{\mu_1}{\log_{10} I}, \quad (6)$$

with $\mu_0 = (1/2 - \beta_0) / \beta_1 \approx 0.12$ and $\mu_1 = (\log_{10} C_{QS} - \log_{10} C_I) / \beta_1 \approx 0.38$. As shown in Fig. 9, this expression

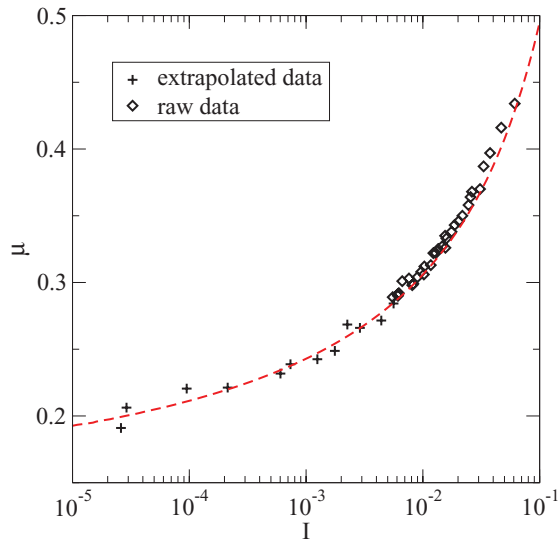


FIG. 9. (Color online) Relationship between friction coefficient μ and inertial number I for the data points obtained in the inertial regime ($I > I_t$) and for the data points extrapolated from the quasistatic regime (see text). The dashed curve represents Eq. (6).

effectively provides an excellent fit to the $\mu(I)$ relationship observed in the inertial regime, with fewer parameters than Eq. (1) used previously [see also Fig. 4(a)]. Furthermore, we emphasize that in this case, the two parameters μ_0 and μ_1 were not adjusted on the inertial data, but directly derive from Eqs. (2) and (5), the latter having been established using quasistatic data only.

Hence, the three-variable constitutive law between I , μ , and Δ characteristic of the quasistatic regime turns out to be also valid in the inertial regime. This three-variable law actually includes the $\mu(I)$ relationship characterizing the inertial regime, which emerges as soon as fluctuations begin to be governed by the local law (2). In consequence, a virtual continuation in the quasistatic regime of the inertial $\mu(I)$ relationship can be drawn assuming that Eq. (2) remains valid for $I < I_t$. This continuation is shown in Fig. 9 using directly Eq. (6), and through extrapolated data points which have been computed from quasistatic results as the intersects, for each value of friction coefficient μ , between relationships (3) and (2) (see Fig. 7). Note that the value of the exponent β used to compute these intersects was the best-fitting value obtained for each friction coefficient, and not the linear approximation given by Eq. (4). It is interesting to note that these extrapolated data points figure in the exact continuity of the data points obtained in the inertial regime, which constitutes further evidence that the quasistatic and inertial regimes are effectively governed by the same underlying constitutive law.

V. DISCUSSION AND CONCLUSIONS

The analysis presented in this paper sheds new light on the rheological behavior of granular materials in the quasistatic regime. Our results clearly show that this regime is characterized both by a friction coefficient independent of the shear rate, and by a local, three-variable constitutive relationship

between the inertial number, the friction coefficient, and the normalized velocity fluctuations. Importantly, this constitutive law directly relates the occurrence of creep in quasistatic zones to the existence of fluctuations. It is only in the absence of fluctuations that the material is jammed and $I = 0$ for whatever the level of stress. As soon as fluctuations exist, the material can flow even under very small applied stresses, with an apparent viscosity that is a direct function of the fluctuation amplitude [see Eq. (3)]. The key role played by the fluctuations in the rheology of quasistatic granular materials has already been hypothesized by several authors [13,15,22,23]. Our study thus formally demonstrates this assumption by showing, directly from local mechanical data, that fluctuations must be accounted for in the constitutive relationship. An interesting perspective for future work would now be to go beyond the purely empirical approach presented here, and develop a theoretical framework capable of yielding a three-variable constitutive law compatible with our results.

Another important outcome of this study is the fact that the three-variable constitutive law obtained in the quasistatic regime appears to be also valid in the inertial regime. When combined with the expression governing the fluctuations in the inertial regime Eq. (2), this constitutive law yields a one-to-one $\mu(I)$ relationship which, though of a different form from the relationships previously proposed in the literature [2,4], provides an excellent fit to the inertial data. Hence, the distinction between the quasistatic and inertial regimes cannot be related to the rate-dependent or rate-independent character of the mechanical behavior. Both regimes are in fact characterized by the same underlying constitutive law involving the variables I , μ , and Δ .

In spite of this similarity in mechanical behavior, the quasistatic and inertial regimes are nevertheless separated by an abrupt transition at $I = I_t$. Elaborating from our results, we propose that the “true” origin of this transition is in fact related to the mode of production of the fluctuations within the material. As already pointed by other workers [1,2], in the inertial regime the fluctuations necessary for the flow are created locally by the flow itself. This is the meaning of Eq. (2), and explains the possibility of reducing the three-variable constitutive law to a local relationship between μ and I alone. On the contrary, in the quasistatic regime, the fluctuations result from nonlocal processes [9–11] and, as shown by our results, are essentially sustained by sources localized at the boundaries of the quasistatic zones (either at the wall or at the interface with the neighboring inertial zone). In particular, when a quasistatic zone coexists with an inertial one, the fluctuations within the former and, as a consequence, its apparent rheology (namely, the apparent relationship between μ and I), are completely controlled by the latter. In the absence of boundary sources, on the contrary, the fluctuations in the bulk would rapidly die off, and I would tend to 0. Eventually, the three-variable relationship presented in this paper will thus need to be complemented by a nonlocal evolution equation for the fluctuations in quasistatic regime.

As a conclusion, the quasistatic-to-inertial transition in granular materials thus appears to correspond to a transition between a regime where the fluctuations are governed by nonlocal processes and a regime where fluctuations are produced locally. This transition occurs at a critical value of

JOHAN GAUME, GUILLAUME CHAMBON, AND MOHAMED NAAIM

PHYSICAL REVIEW E **00**, 001300 (2011)

I or equivalently [according to Eq. (2)], at a critical value of Δ , $\Delta_t \approx 8 \times 10^{-3}$ in our case, which can be interpreted as the fluctuation level above which the mechanisms for long-range propagations of the fluctuations become inefficient. Following this interpretation, the parameters Δ , and I_t should thus represent intrinsic characteristics of the material, whose value should be independent of the considered system. This prediction tends to be confirmed by the results reported in [2,3], in which different system sizes and system geometries result to apparently constant values of I at the quasistatic-to-inertial

transition. Yet, the uncertainties associated with the determination of I_t and the different methods employed to define this parameter (from global or local measurements) render difficult the comparisons among existing studies; further work would be needed to conclude on the intrinsic nature of I_t .

ACKNOWLEDGMENT

Financial support from the French National Agency for Research is acknowledged (ANR project MONHA).

-
- [1] G. D. R. MiDi, *Eur. Phys. J. E* **14**, 341 (2004).
 - [2] F. da Cruz, S. Emam, M. Prochnow, J. N. Roux, and F. Chevoir, *Phys. Rev. E* **72**, 021309 (2005).
 - [3] G. Koval, J. N. Roux, A. Corfdir, and F. Chevoir, *Phys. Rev. E* **79**, 021306 (2009).
 - [4] P. Jop, Y. Forterre, and O. Pouliquen, *Nature* **441**, 727 (2006).
 - [5] Y. Forterre and O. Pouliquen, *Annu. Rev. Fluid Mech.* **40**, 1 (2008).
 - [6] J. N. Roux and G. Combe, *C.R. Phys.* **3**, 131 (2002).
 - [7] T. S. Komatsu, S. Inagaki, N. Nakagawa, and S. Nasuno, *Phys. Rev. Lett.* **86**, 1757 (2001).
 - [8] P. Jop, Y. Forterre, and O. Pouliquen, *Phys. Fluids* **19**, 088102 (2007).
 - [9] F. Radjai and S. Roux, *Phys. Rev. Lett.* **89**, 064302 (2002).
 - [10] G. Chambon, J. Schmittbuhl, A. Corfdir, J.-P. Vilotte, and S. Roux, *Phys. Rev. E* **68**, 011304 (2003).
 - [11] O. Pouliquen, *Phys. Rev. Lett.* **93**, 248001 (2004).
 - [12] P. Mills, P. G. Rognon, and F. Chevoir, *Eur. Phys. Lett.* **81**, 64005 (2008).
 - [13] O. Pouliquen and Y. Forterre, *Phil. Trans. Math. Phys. Eng. Sci.* **367**, 5091 (2009).
 - [14] L. Bocquet, W. Losert, D. Schalk, T. C. Lubensky, and J. P. Gollub, *Phys. Rev. E* **65**, 011307 (2001).
 - [15] G. I. Tardos, S. McNamara, and I. Talu, *Powder Technol.* **131**, 23 (2003).
 - [16] F. Radjai and F. Dubois, *Discrete-Element Modeling of Granular Materials* (ISTE, London, and Wiley, New York, 2011).
 - [17] C. T. Veje, D. W. Howell, and R. P. Behringer, *Phys. Rev. E* **59**, 739 (1999).
 - [18] D. M. Mueth, G. F. Debregeas, G. S. Karczmar, P. J. Eng, S. R. Nagel, and H. M. Jaeger, *Nature* **406**, 385 (2000).
 - [19] A. Zervos, I. Vardoulakis, M. Jean, and P. Lerat, *Mech. Cohes. Frict. Mat.* **5**, 305 (2000).
 - [20] P. A. Cundall and O. D. L. Strack, *Géotechnique* **29**, 47 (1979).
 - [21] B. Cambou and M. Jean, *Micromécanique des Matériaux Granulaires*, Traité MIM, Série Géomatériaux (Hermes Science, London, 2001).
 - [22] L. Bocquet, J. Errami, and T. C. Lubensky, *Phys. Rev. Lett.* **89**, 184301 (2002).
 - [23] K. A. Reddy, Y. Forterre, and O. Pouliquen, *Phys. Rev. Lett.* **106**, 108301 (2011).

Bibliography

- Akaike, H., 1981: Likelihood of a model and information criteria. *J. Econometrics*, **16(1)**, 3–14.
- Akitaya, E., 1974: Studies on depth hoar. *Contributions from the Institute of Low Temperature Science*, **A26**, 1–67.
- Ancey, C., C. Gervasoni, and M. Meunier, 2004: Computing extreme avalanches. *Cold Reg. Sci. Technol.*, **39**, 161–180.
- Bacro, J. and A. Chaouche, 2006: Incertitude d'estimation des pluies extrêmes du pourtour méditerranéen: illustration par les données de marseille. *Hydrological Sciences Journal des Sciences Hydrologiques*.
- Bader, H., B. Hansen, J. Joseph, and M. Sandgren, 1951: Preliminary investigations of some physical properties of snow. *USA SIPRE Report 7*.
- Bader, H. and B. Salm, 1990: On the mechanics of snow slab release. *Cold Reg. Sci. Technol.*, **17**, 287–299.
- Bailard, G. and R. McGaw, 1965: A theory of snow failure. Technical report, USA CRREL Research Report 137.
- Bair, E., J. Dozier, and K. Birkeland, 2008: Avalanche crown depth distributions. *Geophys. Res. Lett.*, **35**, L23502.
- Barbolini, M., F. Cappabianca, and F. Savi, 2003: A new method for the estimation of avalanche distance exceeded probabilities. *Surveys in Geophysics*, **24(5-6)**, 587–601.
- Barbolini, M., F. Cappabianca, and F. Savi, 2004: Risk assessment in avalanche prone areas. *Ann. Glaciol.*, **38**, 115–122.
- Barbolini, M., U. Gruber, C. Keylock, M. Naaim, and F. Savi, 2000: Application and evaluation of statistical and hydraulic-continuum dense-snow avalanche models to five real European sites. *Cold Reg. Sci. Technol.*, **31(2)**, 133–149.

- Barbolini, M., L. Natale, and F. Savi, 2002: Effect of release conditions uncertainty on avalanche hazard mapping. *Nat. Hazard*, **25**, 225–244.
- Bartelt, P., U. Gruber, and B. Salm, 1997a: Modelling dense snow avalanche flow as a crinale-ericksen-filby fluid without cohesion. *SFISAR Internal Report*, No. 717.
- Bartelt, P., U. Gruber, and B. Salm, 1997b: Numerical modelling of dense snow avalanches using a voellmy-fluid flow law solved by a finite difference method. *SFISAR Internal Report*, No. 716.
- Bartelt, P., M. Kern, and M. Christen, 2000: A mixed flowing/powder snow avalanche model. *ISSW Proc.* 280–289.
- Bel, L., J. Bacro, and C. Lantuejoul, 2008: Assessing extremal dependence of environmental spatial fields. *Environmetrics*, **19(2)**, 163–182.
- Bellaire, S. and J. Schweizer, 2011: Measuring spatial variations of weak layer and slab properties with regard to snow slope stability. *Cold Reg. Sci. Technol.*, **65(2)**, 234–241.
- Birkeland, K., 1990: The spatial variability of snow resistance on potential avalanche slopes. Master's thesis, Department of Earth Sciences, Montana State University.
- Birkeland, K., B. Hansen, and R. Brown, 1995: The spatial variability of snow resistance on potential avalanche slopes. *J. Glaciol.*, **41(137)**, 183–189.
- Birkeland, K., K. Kronholm, and S. Logan, 2004: A comparison of the spatial structure of the penetration resistance of snow layers in two different snow climates. *ISSMA Proc.* 3–11.
- Birkeland, K., K. Kronholm, M. Schneebeli, and C. Pielmeir, 2004: Changes in shear strength and micropenetration hardness of a buried surface-hoar layer. *Ann. Glaciol.*, **38**, 223–228.
- Blanchet, J. and M. Lehning, 2010: Mapping snow depth return levels: smooth spatial modeling versus station interpolation. *Hydrol. Earth Syst. Sc. Disc.*, **7**, 6129–6177.
- Bocchiola, D., M. Medagliani, and R. Rosso, 2006: Regional snow depth frequency curves for avalanche hazard mapping in central Italian Alps. *Cold Reg. Sci. Technol.*, **46(3)**, 204–221.
- Brown, B. and S. Resnick, 1977: Extreme values of independent stochastic processes. *Journal of Applied Probability*, **14**, 732–739.
- Bucher, E., 1948: Beiträge zu den theoretischen Grundlagen des Lawinenverbau. *Beiträge zur Geologie der Schweiz, Geotechnische Serie, Hydrologie*, **6**.

- Butkovich, T., 1956: Strength studies of high-density snow. Technical report, USA SIPRE Research Report 18.
- Campbell, C., 2004: Spatial variability of slab stability and fracture properties in avalanche start zones. Master's thesis, University of Calgary, Canada.
- Campbell, C. and B. Jamieson, 2007: Spatial variability of slab stability and fracture characteristics within avalanche start zones. *Cold Reg. Sci. Technol.*, **47(1-2)**, 134–147.
- Chiaia, B., P. Cornetti, and B. Frigo, 2008: Triggering of dry snow slab avalanches: stress versus fracture mechanical approach. *Cold Reg. Sci. Technol.*, **53**, 170–178.
- Coles, S., 2001: An introduction to statistical modelling of extreme values. *Springer Ed.*, **208p**.
- Coles, S., J. Heffernan, and J. Tawn, 1999: Dependence measures for extreme value analyses. *Extremes*, **2(4)**, 339–365.
- Conway, H. and J. Abrahamson, 1984: Snow stability index. *J. Glaciol.*, **30(106)**, 321–327.
- Conway, H. and J. Abrahamson, 1988: Snow-slope stability - A probabilistic approach. *J. Glaciol.*, **34**, No 117.
- Cooley, D., P. Naveau, and P. Poncet, 2006: Variograms for spatial max-stable random fields. *Springer Ed.*, **187(3)**, 73–390.
- Cooley, D., D. Nychka, and P. Naveau, 2007: Bayesian spatial modeling of extreme precipitation return levels. *J. Amer. Statist. Assoc.*, **102(479)**, 824–840.
- Cressie, N., 1993: Statistics for spatial data. *Wiley ed.*, **928p**.
- De Montmollin, V., 1978: *Introduction à la rhéologie de la neige*. PhD thesis, Université Scientifique et Médicale de Grenoble.
- De Quervain, M., 1966: On the snow pressure at rest. *Proceedings of International Symposium on Scientific Aspects of Snow and Ice Avalanches, Davos*.
- DeHaan, L., 1984: A spectral representation for max-stable processes. *The Annals of Probability*, **12**, 1194–1204.
- Durand, Y., M. Laternser, G. Giraud, and P. e. a. Etchevers, 2009: 44 years of climate re-analyses in the french alps (1958-2002). methodology, model validation and temperature-precipitation-snowfall trends. *Journal of Applied Meteorology and Climatology*, **48(3)**, 429–449.

- Eckert, N., H. Baya, and M. Deschatres, 2010: Assessing the impact of climate change on snow avalanche runout altitudes in France over the last 61 years using a hierarchical change point model. *J. Climate*, **23**, 3157–3180.
- Eckert, N., C. Coleou, H. Castebrunet, M. Deschatres, D. Giraud, and J. Gaume, 2010: Cross-comparison of meteorological and avalanche data for characterising avalanche cycles: The example of December 2008 in the eastern part of the French Alps. *Cold Reg. Sci. Technol.*, **64**, 119–136.
- Eckert, N., M. Naaim, and E. Parent, 2010: Long-term avalanche hazard assessment with a Bayesian depth-averaged propagation model. *J. Glaciol.*, **56(198)**, 563–586.
- Eckert, N., E. Parent, M. Naaim, and D. Richard, 2008: Bayesian stochastic modelling for avalanche predetermination: from a general system framework to return period computations. *SERRA*, **22**, 185–206.
- Faillietaz, J., F. Louchet, and J. Grasso, 2004: Two-threshold model for scaling laws of noninteracting snow avalanches. *Phys. Rev. Lett.*, **93(20)**, 208001.
- Faillietaz, J., F. Louchet, and J. Grasso, 2006: Cellular automaton modelling of slab avalanche triggering mechanisms : from the universal statistical behaviour to particular cases. *Proceedings of the ISSW* 174–180.
- Fierz, C., R. Armstrong, Y. Durand, P. Etchevers, E. Greene, D. McClung, K. Nishimura, P. Satyawali, and S. Sokratov, 2009: The international classification for seasonal snow on the ground. *UNESCO-International Hydrological Program. (Technical Documents in Hydrology)*, **83**, 90 pp.
- Föhn, P., 1989: Snow cover stability tests and the areal variability of snow strength. *ISSW Proc., Whistler, BC, Canada* 262–273.
- Föhn, P., C. Camponovo, and G. Krüst, 1998: Mechanical and structural properties of weak snow layers measured in situ. *Ann. Glaciol.*, **26**, 1–6.
- Fukuzawa, T. and H. Narita, 1993: An experimental study on the mechanical behavior of a depth hoar under shear stress. *ISSW Proc., Colorado, USA* 171–175.
- Fyffe, B. and M. Zaiser, 2004: The effects of snow variability on slab avalanche release. *Cold Reg. Sci. Technol.*, **40**, 229–242.
- Fyffe, B. and M. Zaiser, 2007: Interplay of basal shear fracture and slab rupture in slab avalanche release. *Cold Reg. Sci. Technol.*, **49**, 26–38.
- Griffiths, D. and G. Fenton, 2004: Probabilistic slope stability analysis by finite elements. *J. Geotech. Geoenviron.*, **130(5)**, 507–518.

- Habermann, 2008: Influence of snowpack layering on human-triggered snow slab avalanche release. *Cold Reg. Sci. Technol.*, **54(3)**, 176–182.
- Haefeli, R., 1939: Snow mechanics with references to soil mechanics. *Beiträge zur Geologie der Schweiz, Geotechnische Serie, Hydrologie*, **3**.
- Haefeli, R., 1966: Considérations sur la pente critique et le coefficient de pression au repos de la couverture de neige. *Proceedings of International Symposium on Scientific Aspects of Snow and Ice Avalanches, Davos*.
- Hagenmuller, P., M. Schneebeli, and T. Theile, 2012: A microstructure-based model of snow tensile failure. *In Prep*.
- Hawkes, I. and M. Mellor, 1972: Deformation and fracture of ice under uniaxial stress. *J. Glaciol.*, **11(61)**.
- Heffernan, J. and J. Tawn, 2004: A conditional approach for multivariate extreme values. *J. R. Stat. Soc.*, **B66**, 26–38.
- Heierli, J., P. Gumbsch, and M. Zaiser, 2008: Anticrack nucleation as triggering mechanism for snow slab avalanches. *Science*, **321**, 240.
- Heierli, J. and M. Zaiser, 2007: Failure initiation in snow stratifications containing weak layers: Nucleation of whumpfs and slab avalanches. *Cold Reg. Sci. Technol.*, **52**, 385–400.
- Hutter, K., Y. Wang, and S. Pudasaini, 2005: The savage-hutter avalanche model: how far can it be pushed? *Phil. Trans. R. Soc. London*, **A 363**, 203–309.
- Jamieson, B. and C. Johnston, 1990: In-situ tensile tests of snowpack layers. *J. Glaciol.*, **36(122)**, 102–106.
- Jamieson, B. and C. Johnston, 1992: Snowpack characteristics associated with avalanche accidents. *Can. Geotech. J.*, **29**, 862–866.
- Jamieson, B. and J. Schweizer, 2000: Texture and strength changes of buried surface-hoar layers with implications for dry snow-slab avalanche release. *J. Glaciol.*, **46**, 151–160.
- Jamieson, J. and C. Johnston, 2001: Evaluation of the shear frame test for weak snowpack layers. *Ann. Glaciol.*, **32**, 59–69.
- Johnson, B., J. Jamieson, and R. Stewart, 2004: Seismic measurements of fracture speed in a weak layer snowpack layer. *Cold Reg. Sci. Technol.*, **40**, 41–45.
- Kabluchko, Z., M. Schlather, and L. DeHaan, 2009: Stationary max-stable fields associated to negative definite functions. *The Annals of Probability*, **37**, 2042–2065.

- Kaempfer, T., M. Hopkins, and D. Perovich, 2007: A three-dimensional microstructure-based photon-tracking model of radiative transfer in snow. *J. Geophys. Res.*, **112**, D24113.
- Keeler, C., 1969: Some physical properties of alpine snow. Technical report, USA CRREL Research Report 271.
- Keeler, C. and W. Weeks, 1967: Some mechanical properties of alpine snow. Technical report, USA CRREL Research Report 227.
- Kovacs, A. and W. Weeks, 1969: Variation of some mechanical properties of polar snow. Technical report, USA CRREL Research Report 276.
- Kronholm, K., 2004: *Spatial variability of snow mechanical properties with regards to avalanche formation*. PhD thesis, University of Zurich.
- Kronholm, K. and K. Birkeland, 2005: Integrating spatial patterns into a snow avalanche cellular automata model. *Geophys. Res. Lett.*, **32**, L19504.
- Kronholm, K., J. Schweizer, and M. Schneebeli, 2004: The effect of spatial variability on snow avalanche formation. *Geophys. Res. Abstr.*, **6**, 06272.
- Lachamp, P., T. Faug, M. Naaim, and D. Laigle, 2002: Simulation of the effects of defence structure on granular flows using sph. *Nat. Hazard Earth Sys.*, **2** (3/4), 203–209.
- Landry, C., 2002: Spatial variations in snow stability on uniform slopes: Implications for extrapolation to surrounding terrain. Master's thesis, Montana State university, USA.
- Landry, C., K. Birkeland, K. Hansen, J. Borkowski, R. Brown, and R. Aspinall, 2004: Variations in snow strength and stability on uniform slopes. *Cold Reg. Sci. Technol.*, **39**(2-3), 205–218.
- Lindsay, B., 1988: Composite likelihood methods. *Contemp. Math.*, **80**, 221–239.
- Logan, S., 2005: Temporal changes in the spatial patterns of weak layer shear strength and stability on uniform slopes. Master's thesis, Montana State University, USA.
- Logan, S., K. Birkeland, K. Kronholm, and K. Hansen, 2007: Temporal changes in the slope-scale spatial variability of the shear strength of buried surface hoar layers. *Cold Reg. Sci. Technol.*, **47**(1-2), 148–158.
- Louchet, F., 2001: Creep instability of the weak layer and natural slab avalanche triggerings. *Cold Reg. Sci. Technol.*, **33**, 141–146.
- Maggioni, M. and U. Gruber, 2003: The influence of topographic parameters on avalanche release dimension and frequency. *Cold Reg. Sci. Technol.*, **37**, 407–419.

- Maggioni, M., U. Gruber, and M. Stoffel, 2002: Definition and characterisation of potential avalanche release areas. *Proceedings of the ESRI Conference, San Diego*.
- Mahajan, P. and S. Joshi, 2008: Modeling of interfacial crack velocities in snow. *Cold Reg. Sci. Technol.*, **51**, 98–111.
- Mahajan, P., R. Kalakuntla, and C. Chandel, 2010: Numerical simulation of failure in a layered thin snowpack under skier load. *Ann. Glaciol.*, **51(54)**, 169–175.
- Martinelli, M. J., 1974: Snow avalanche sites, their identification and evaluation. Technical report, Agriculture Information Bulletin 360. U.S. Forest Service.
- Marty, C. and J. Blanchet, 2011: Long-term changes in annual maximum snow depth and snowfall in switzerland based on extreme value statistics. *Climatic Change*, **1**, 1–17.
- McClung, D., 1975: Creep and the snow-earth interface condition in the seasonal alpine snow-pack. *IAHS Publ*, **114**, 235–248.
- McClung, D., 1977: Direct simple shear tests on snow and their relation to slab avalanche formation. *J. Glaciol.*, **19(81)**, 101–109.
- McClung, D., 1979a: In situ estimates of the tensile strength of snow utilizing large sample sizes. *J. Glaciol.*, **22(87)**, 321–329.
- McClung, D., 1979b: Shear fracture precipitated by strain softening as a mechanism of dry slab avalanche release. *J. Geophys. Res.*, **84(B7)**, 3519–3526.
- McClung, D., 2003: Size scaling for dry snow slab release. *J. Geophys. Res.*, **108(B10)**, 2465–2477.
- McClung, D., 2009: Dry snow slab quasi-brittle fracture initiation and verification from field tests. *J. Geophys. Res.*, **114**, F01022.
- McClung, D., 2011: Analysis of critical length measurements for dry snow slab weak-layer shear fracture. *J. Glaciol.*, **57(203)**, 557–566.
- McClung, D. and K. Lied, 1987: Statistical and geometrical definition of snow-avalanche runoff. *Cold Reg. Sci. Technol.*, **13**, 107–119.
- McClung, D. and P. Schaerer, 2006: *The Avalanche Handbook*.
- McClung, D. and J. Schweizer, 2006: Fracture toughness of dry snow slab avalanches from field measurements. *J. Geophys. Res.*, **111**, F04008.
- Mellor, M., 1975: A review of basic snow mechanics. *IAHS Publ*, **114**, 251–291.

- Mellor, M. and J. Smith, 1966: Strength studies on snow. *Proc. of the International Symposium on Scientific Aspects of Snow and Ice Avalanches*.
- Meunier, M. and C. Ancey, 2004: Towards a conceptual approach to predetermining high-return-period avalanche run-out distances. *J. Glaciol.*, **50(169)**, 268–278.
- Naaïm, M. and C. Ancey, 1992: Dense avalanche model. *European Summer University, Chamonix, Cemagref Publications*. 173–181.
- Naaïm, M., T. Faug, and F. Naaïm-Bouvet, 2003: Dry granular flow modelling including erosion and deposition. *Surveys in Geophysics*, **24**, 569–585.
- Naaïm, M., T. Faug, F. Naaïm-Bouvet, and N. Eckert, 2008: Dispositif paravalanche de taconnaz. note à propos de la validation du projet final par simulations numériques des pressions exercées sur les digues intermédiaires et terminale et du risque lié à l'aérosol. Technical report, Irstea.
- Naaïm, M. and F. Naaïm-Bouvet, 1999: Two-layers model for dry mix snow avalanches. *La Houille Blanche*, **5**, 54–69.
- Nakamura, T., O. Abe, R. Hashimoto, and T. Ohta, 2010: Instruments and methods. a dynamic method to measure the shear strength of snow. *J. Glaciol.*, **56**, No. 196.
- Narita, H., 1980: Mechanical behaviour and structure of snow under uniaxial tensile stress. *J. Glaciol.*, **26(94)**, 275–282.
- Navarre, J., A. Taillefer, and Y. Danielou, 1992: Fluage et rhéologie de la neige. *Actes de conférence Chamonix*.
- Norem, H., F. Irgens, and B. Schieldrop, 1989: Simulation of snow-avalanche flow in run-out zones. *Ann. Glaciol.*, **13**, 218–225.
- Padoan, S., M. Ribatet, and S. Sisson, 2009: Likelihood-based inference for max-stable processes. *J. Am. Stat. Assoc.*, **105(489)**, 263–277.
- Palmer, A. and J. Rice, 1973: The growth of slip surfaces in the progressive failure of over-consolidated clay. *Proc. R. Soc. London*, **332**, 527–548.
- Parent, E. and J. Bernier, 2003: Encoding prior experts judgments to improve risk analysis of extreme hydrological events via pot modelling. *Journal of Hydrology*, **283**, 1–8.
- Perla, R., 1969: Strength tests on newly fallen snow. *J. Glaciol.*, **8(54)**, 427–440.
- Perla, R., 1977: Slab avalanche measurements. *Can. Geotech. J.*, **14**, 387–462.

- Perla, R., T. Cheng, and D. McClung, 1980: A two-parameter model of snow-avalanche motion. *J. Glaciol.*, **26(94)**, 197–207.
- Perla, R. and R. Sommerfeld, 1987: On the metamorphism, morphology and microstructure of snow. *ISSW Proc. Lake Tahoe, USA* 98–102.
- Pinzer, B., 2009: *Dynamics of temperature gradient snow metamorphism*. PhD thesis, ETH Zürich.
- Podolskiy, E., K. Nishimura, O. Abe, and P. Chernous, 2010: Earthquake-induced snow avalanches: Ii. experimental study. *J. Glaciol.*, **56**, No. 197.
- Ramseier, R., 1963: Some physical and mechanical properties of polar snow. *J. Glaciol.*, **4(36)**.
- Reiweiger, I., 2010: Failure of a layer of buried surface hoar. *Geophys. Res. Lett.*, **37**, L24501.
- Reiweiger, I., 2011: *Failure of a layer of buried surface hoar*. PhD thesis, ETH Zürich.
- Reiweiger, I., J. Schweizer, J. Dual, and H. Herrmann, 2009: Modelling snow failure with a fibre bundle model. *J. Glaciol.*, **55(194)**, 997–1002.
- Ribatet, M., 2009: A user's guide to the spatialextremes package. Technical report, Chair of statistics. Ecole Polytechnique Fédérale de Lausanne.
- Roch, A., 1965: Les variations de la résistance de la neige. *IASH Publ.*, **69**, 128–140.
- Roch, A., 1966: Les déclenchements d'avalanches. *Proceedings of International Symposium on Scientific Aspects of Snow and Ice Avalanches, Davos*, **69**, 182–195.
- Rosenthal, W. and K. Elder, 2002: Evidence of chaos in slab avalanches. *Proceedings of the ISSW*.
- Rosso, R., 1987: In situ strength measurements of the snowpack. *Proceedings of the ISSW at Lake Tahoe, Homewood, CA* 210–215.
- Salm, B., A. Burkard, and H. Gubler, 1990: Berechnung von fließlawinen: eine anleitung für pratiker mit beispielen. *Internal report EISLF (in German)*, **47**.
- Savage, S. and K. Hutter, 1991: The dynamics of granular avalanche from initiation to runoff. part i: analysis. *Acta Mechanica*, **86**, 201–223.
- Scapozza, C., 2004: *Entwicklung eines dichte und temperaturabhängigen stoffgesetzes zur Beschreibung des visko-elastischen verhaltens von schnee*. PhD thesis, ETH Zürich.

- Schlather, M., 2002: Models for stationary max-stable random fields. *Extremes*, **5(1)**, 33–44.
- Schlather, M., 2010: Brown-resnick processes. Oral presentation, Toledo, March 2010.
- Schneebeli, M. and S. Sokratov, 2004: Tomography of temperature gradient metamorphism of snow and associated changes in heat conductivity. *Hydrological Processes*, **18**, 3655–3665.
- Schweizer, J., 1998: Laboratory experiments on shear failure of snow. *Ann. Glaciol.*, **26**, 97–102.
- Schweizer, J., 1999: Review of dry snow slab avalanche release. *Cold Reg. Sci. Technol.*, **30**, 43–57.
- Schweizer, J. and C. Camponovo, 2002: The temperature dependence of the effective elastic shear modulus of snow. *Cold Reg. Sci. Technol.*, **35**, 55–64.
- Schweizer, J., B. Jamieson, and M. Schneebeli, 2003: Snow avalanche formation. *Rev. Geophys.*, **41(4)**, 1016.
- Schweizer, J., K. Kronholm, J. Jamieson, and K. Birkeland, 2008: Review of spatial variability of snowpack properties and its importance for avalanche formation. *Cold Reg. Sci. Technol.*, **51(2-3)**, 253–272.
- Sigrist, C., 2006: *Measurements of fracture mechanical properties of snow and application to dry snow slab avalanche release*. PhD thesis, ETHZ.
- Smith, J., 1963: Crushing strength and longitudinal wave velocity in processed snow. Technical report, USA CRREL Technical Report 137.
- Smith, J., 1965: The elastic constants, strength, and density of greenland snow as determined from measurement of sonic wave velocity. Technical report, USA CRREL Technical Report 167.
- Smith, R., 1991: Max-stable processes and spatial extremes.
- Sommerfeld, R. and R. King, 1979: A recommendation for the application of the rock index for slab avalanche release. *J. Glaciol.*, **22(87)**, 402–404.
- Stewart, K., 2002: Spatial variability of slab stability within avalanche start zones. Master's thesis, University of Calgary, Canada.
- Stewart, K. and B. Jamieson, 2002: Spatial variability of slab stability within avalanche start zones. *ISSW Proc., Penticton BC, Canada* 544–548.

- Stoffel, M., 2005: *Numerical modelling of snow using finite elements*. PhD thesis, ETH Zurich.
- Takeuchi, K., 1976: Distribution of informational statistics and a criterion of model fitting. *Suri-Kagaku*, **153**, 12–18.
- van Herwijnen, A. and J. Heierli, 2009: Measurements of crack-face friction in collapsed weak snow layers. *Geophys. Res. Lett.*, **36**, L23502.
- van Herwijnen, A. and B. Jamieson, 2005: High speed photography of fractures in weak snowpack layers. *Cold Reg. Sci. Technol.*, **43(1-2)**, 71–82.
- Yamanoi, K. and Y. Endo, 2003: Dependence of shear strength of snow cover on density and water content. *Japanese journal*.
- Yosida, Z., 1963: *Physical properties of snow*. MIT Press, Cambridge, Mass.

Johan Gaume

IRSTEA Grenoble

Natural hazard research unit (ETNA)

Phone: +33 (0) 4 76 76 28 14

Mobile: +33 (0) 6 74 82 35 47

Email:

Date of birth: 18/09/1985

Nationality: French

Skills

- Fluid mechanics and hydraulics
- Geomechanics, soil and solid mechanics
- Statistical/Probabilistic analysis and modeling
- Computational mathematics
- Top level snowboard practitioner

Areas of applications

- Natural hazards
- Mechanics of avalanche release
- Hydrology
- Granular materials

Education

2009 - 2012: PhD (Geomechanics) - University Joseph Fourier (Grenoble I) - Doctoral school TUE (Terre Univers Environnement) - Title: *"Evaluation of avalanche release depths - Combined statistical and mechanical modeling"*.

2007 - 2008: Master Rheology Mechanics Physics of Fluid Materials obtained with **high honors** (mention très bien) - Grenoble Institute of Technology.

2005 - 2008: Engineering degree from ENSHMG (Ecole Nationale Supérieure d'Hydraulique et de Mécanique de Grenoble) - Grenoble Institute of Technology - Département: Fluid Engineering and Mechanics (IFM), Option: Energy and Processes (EP), obtained with **honors** (mention bien)

2004 - 2005: Post-secondary special preparatory school ("Classes Préparatoires Mathématiques Spéciales") - Option: Physics, Engineering Sciences (PSI) - **Major**.

2003 - 2004: Post-secondary superior preparatory school ("Classes Préparatoires Mathématiques Supérieures") - Option: Maths, Physics, Engineering Science (MPSI).

2002 - 2003: Scientific Baccalauréat - Option: Physics, obtained with **high honors** (mention très bien).

Relevant experiences

2009 - 2012: PhD - Research experience on snow slab avalanche release (PhD at IRSTEA, Grenoble, France)

- Finite Element Modeling
- Statistical analysis and modeling (extreme value statistics in the spatial case)
- Hazard analysis and mapping
- Publications in peer-reviewed journals: 4 accepted publications [2][3][6][7]

- Vulgarization by publishing in non-scientific journals [18 – 22]

2009 - 2012: Teaching experience. Hydraulic and heat transfert practical course. 40 hours/year.

2011: Master internship supervisor. Influence of morphological features on snow slab avalanche release. 3 months.

2007 - 2008: Master of science - Research experience on the quasi-static/inertial transition in dense granular materials (CEMAGREF, Grenoble, France)

- 2D Discrete Element Modeling with PFC2D (Itasca).
- New constitutive law highlighted
- Multiscale analysis
- Publication in peer-reviewed journals: 1 accepted article [1]

Publications

Accepted Journal Articles

- [1] **Gaume J**, Chambon G, Naaim M. 2011. Quasi static to inertial transition in granular materials and the role of fluctuations, *Phys-Rev-E*, Vol. 84(5), No. 051304.
- [2] **Gaume J**, Chambon G, Eckert N, Naaim M. 2012. Relative influence of mechanical and meteorological factors on slab avalanche release depth distributions, *Geophysical Research Letters*, Vol. 39, L12401.
- [3] **Gaume J**, Eckert N, Chambon G, Naaim M. 2012. Predetermination of avalanche release depths. A spatial extreme approach, *La Houille Blanche*.
- [4] Eckert N, Coleou C, Castebrunet H, Dechatres M, Giraud G, **Gaume J**. 2011. Cross comparison of meteorological and avalanche data for characterizing avalanche cycles: the example of December 2008 in the eastern part of the southern French Alps, *Cold Regions Science and Technology*, Vol. 64, pp 119-136.
- [5] Eckert N, **Gaume J**, Castebrunet H. 2011. Using spatial and spatial-extreme statistics to characterize snow avalanche cycles, *Procedia Environmental Sciences*, Vol. 7, pp 224-229.
- [6] **Gaume J**, Chambon G, Eckert N, Naaim M. 2012. Influence of weak layer heterogeneity on slab avalanche release: Application to the evaluation of avalanche release depths, *Journal of Glaciology*.
- [7] **Gaume J**, Eckert N, Bel L, Chambon G, Naaim M. 2012. A spatial-extreme method for extreme snowfall mapping in the French Alps, *Water Resources Research*.

Journal Articles in preparation

- [8] **Gaume J**, Chambon G, Eckert N, Naaim M. 2012. Influence of tensile strength and weak layer heterogeneity on slab tensile rupture., in prep for *Journal of Glaciology*.
- [9] Podolskiy E, Chambon G, Naaim M, **Gaume J**. Evaluation of rupture Mohr-Coulomb parameters through finite element modelling of shaking platform experiments. In prep for *Journal of Geophysical Research*.

Proceedings

- [10] **Gaume J**, Chambon G, Eckert N, Naaim M. 2011. Influence of weak layer heterogeneity on slab avalanche release using a finite element method. *International Workshop on Bifurcation and Degradation in Geomaterials*, in *Springer Series in Geomechanics and Geoengineering*, Vol. 11(3), pp 261-266.
- [11] **Gaume J**, Eckert N, Chambon G, Naaim M. 2011. Predetermination of avalanche release depths. A spatial extreme approach, *SHF*, Lyon 2011.
- [12] Podolskiy E, Chambon G, Naaim M, **Gaume J**. 2012. Mechanics of weak layer snow under cyclic conditions by FEM, *International Snow Science Workshop*, Anchorage 2012.

Conferences

- [13] **Gaume J**, Chambon G, Eckert N, Naaim M. Coupling mechanical and meteorological factors to evaluate avalanche release depth distributions. Application to the French Alps. *EGU General Assembly*, Vienna, April 27 2012, Oral presentation.
- [14] **Gaume J**, Chambon G, Eckert N, Naaim M. Influence of weak-layer heterogeneity on slab avalanche release using a finite element method. *EGU General Assembly*, Vienna, April 27 2012. Poster.
- [15] **Gaume J**, Eckert N, Chambon G, Naaim M. Predetermination of snow avalanche release depths using a spatial extreme statistical approach. *EGU General Assembly*, Vienna, May 2-7 2010. Oral presentation.
- [16] **Gaume J**, Chambon G, Eckert N, Naaim M. Relative influence of mechanical and meteorological factors on avalanche release depth distributions: An application to the French Alps. *International Snow Science Workshop*, Anchorage, September 17-21 2012. Poster.
- [17] Bacher M, Naaim M, Faug T, **Gaume J**. Numerical Investigations of cohesive granular material using an anular geometry. *EGU General Assembly*, Vienna, May 19-24 2009. Poster.

Vulgarization Articles

- [18] **Gaume J**, Chambon G, Eckert N, Naaim M. 2011. Modélisation mécanique du déclenchement des avalanches de plaques, *ANENA*.
- [19] **Gaume J** 2011. Où va-t'on skier dans 50 ans. Les Alpes face au réchauffement climatique, *ACT snowboarding*.
- [20] **Gaume J** 2011. Enjoy the Glaciers. La gestion des glaciers face au réchauffement climatique, *ACT snowboarding*.
- [21] **Gaume J** 2011. Le déclenchement des avalanches de plaques, *ACT snowboarding*.
- [22] **Gaume J** 2011. Avalanches, évaluation du risque sur le terrain, *ACT snowboarding*.

Technical skills

Langages: French (Native), English (fluent, TOFEL), German (Basics)
 FEM codes: Cast3m, Abaqus, Fluent
 DEM codes: PFC2D (Itasca)
 Computer codes: Matlab, Octave, R, L^AT_EX
 Programming: Python, Esope

